Electronic Thesis and Dissertation Repository

7-28-2016 12:00 AM

Aging comets and their meteor showers

Quanzhi Ye, *The University of Western Ontario*

Supervisor: Peter Brown, *The University of Western Ontario*

A thesis submitted in partial fulfillment of the requirements for the Doctor of Philosophy degree in Astronomy
© Quanzhi Ye 2016

Abstract

Comets are thought to be responsible for the terrestrial accretion of water and organic materials. Comets evolve very quickly, and will generally deplete their volatiles in a few hundred revolutions. This process, or the *aging* of comets, is one of the most critical yet poorly understood problems in planetary astronomy. The goal of this thesis is to better understand this problem by examining different parts of the cometary aging spectrum of Jupiter-family comets (JFCs), a group of comets that dominates the cometary influx in the near-Earth space, using both telescopic and meteor observations.

We examine two representative JFCs and the population of dormant comets. At the younger end of the aging spectrum, we examine a moderately active JFC, 15P/Finlay, and review the puzzle of the non-detection of the associated Finlayid meteor shower. We find that, although having been behaving like a dying comet in the past several 10^2 years, 15P/Finlay have produced energetic cometary outbursts without a clear reason. Towards the more aged end of the spectrum, we examine a weakly active JFC, 209P/LINEAR. By bridging telescopic observations at visible and infrared wavelength, meteor observations and dynamical investigations, we find that 209P/LINEAR is indeed likely an aged yet long-lived comet. At the other end of the spectrum, we examine the population of dormant near-Earth comets, by conducting a comprehensive meteor-based survey looking for dormant comets that have recently been active. We find the lower limit of the dormant comet fraction in the near-Earth object (NEO) population to be $2.0 \pm 1.7\%$. This number is at the lower end of the numbers found using dynamical and telescopic techniques, which may imply that a significant fraction of comets in the true JFC population are weakly active and are not yet detected.

These results have revealed interesting diversity in dying or dead comets, both in their behavior as well as their nature. An immediate quest in the understanding of cometary aging would be to examine a large number of dying or dead comets and understand their general characteristics.

Keywords: asteroid, comet, meteor, meteoroid

Co-Authorship Statement

This thesis dissertation is based on several published or submitted manuscripts which are listed as follows:

- **Chapter 2**: *Bangs and Meteors from the Quiet Comet 15P/Finlay*, published in the Astrophysical Journal (2015), Volume 814, Number 1, with the authors being Quan-Zhi Ye, Peter G. Brown, Charles Bell, Xing Gao, Martin Mašek, and Man-To Hui. The contribution of each coauthor is: Peter Brown provided extensive advice and suggestions to improve the manuscript; Charles Bell, Xing Gao and Martin Mašek operated the telescopes at Vickburg, Xingming Observatory and Pierre Auger Observatory and provided the data; Man-To Hui helped with the preliminary reduction of the data from Xingming Observatory.

- **Chapter 3**: *When comets get old: A synthesis of comet and meteor observations of the low activity comet 209P/LINEAR*, published in Icarus (2016), Volume 264, p. 48–61, with the authors being Quan-Zhi Ye, Man-To Hui, Peter G. Brown, Margaret D. Campbell-Brown, Petr Pokorný, Paul A. Wiegert, and Xing Gao. The contribution of each coauthor is: Man-To Hui provided extensive suggestions on the development of the dust model; Peter Brown and Paul Wiegert provided extensive suggestions and reviews of the manuscript; Margaret Campbell-Brown provided the meteor ablation code; Petr Pokorný helped with the determination of the mass indices of the meteor shower; Xing Gao operated the telescope at Xingming Observatory and provided the data.

- **Chapter 4**: *Dormant Comets Among the Near-Earth Object Population: A Meteor-Based Survey*, in press at the Monthly Notices of the Royal Astronomical Society, with the authors being Quan-Zhi Ye, Peter G. Brown and Petr Pokorný. Peter Brown and Petr Pokorný provided extensive suggestions and reviews of the manuscript.

As the author of this thesis and the lead author of these papers, I initiated the original

research ideas, wrote and led the manuscripts as well as relevant telescope proposals, integrated the cometary dust and meteoroid model, and performed measurements and analysis of the telescopic and meteor data. However, it is only fair to point out that my supervisor, Peter Brown, provided extensive guidance, suggestions and comments throughout my research. All radar meteor observations presented in this thesis were obtained by the Canadian Meteor Orbit Radar (CMOR), developed and maintained by the Western Meteor Physics Group at the University of Western Ontario.

Acknowledgments

First and foremost, I thank my advisor, Peter Brown, for all his guidance and support that help me reach my potential as a scientist. As a stargazer at heart I consider myself extremely fortunate to be able to work with a great mind who is both passionate and knowledgeable. I am constantly amazed by his ability to convoy a difficult concept in a straight and lighthearted way.

I thank my advisory committee, Margaret Campbell-Brown and Paul Wiegert, for their support and for many helpful discussions that took place on or off their duty. For countless times they (together with Peter) encouraged me to bravely take the challenges and be better.

Thanks to all the members of the Western Meteor Physics Group, as well as to the students, postdocs, staffs and faculties at the Department of Physics and Astronomy, who helped me progress and made my time at Western enjoyable. I couldn't possibly acknowledge everyone here, but the following people deserve special mention: Abedin Abedin, Pubuditha Abeyasinghe, Sayantan Auddy, Sebastián Bruzzone, Pauline Barmby, Clara Buma, David Clark, Tushar Das, Jason Gill, Jodi Guthrie, Renjie Hou, Bushra Hussain, Mahdia Ibrahim, Sina Kazemian, Shayamila Mahagammulla, Stanimir Metchev, Petr Pokorný, Fereshteh Rajabi, Sahar Rahmani, Edward Stokan, Dilini Subasinghe, Robert Sica, Aaron Sigut, Maryam Tabeshian, and Robert Weryk. Thanks also to all my badminton and table tennis buddies, whom I had a lot of fun with.

Thanks to the many amateur and professional astronomers, who inspired and helped me over the years I love and study astronomy. These include Eric Christensen, Xing Gao, Alan Harris, Song Huang, Man-To Hui, Matthew Knight, Jian-Yang Li, Chi Sheng Lin, Hung-Chin Lin, Robert Matson, Robert McNaught, Nalin Samarasinha, Liaoshan Shi, Tim Spahr, Jin Zhu, and many others.

Thanks to all the great composers, notably Bach, Beethoven, Schubert, Dvoǒák and Sibelius, for writing the great music and lighting up us followers. For many times their great sounds re-

To the Great Inhabitants of H.C.

Contents

List of Figures

List of Tables

List of Appendices

List of Abbreviations and Symbols

AAVSO   American Association of Variable Star Observers

ACO   Asteroid in cometary orbit

APASS   AAVSO All-Sky Photometric Survey

ASGARD   All Sky and Guided Automatic Real-time Detection

AU   Astronomical Unit, equals to mean Sun-Earth distance

CAMO   Canadian Automated Meteor Observatory

CMOR   Canadian Meteor Orbit Radar

Dec.   Declination

FRAM   F(/Ph)otometric Robotic Atmospheric Monitor

FWHM   Full-width-half-maximum

HTC   Halley-type comet

JFC   Jupiter-family comet

KBO   Kuiper belt object

LPC   Long period comet

MOID   Minimum orbital intersection distance

NEA   Near-Earth asteroid

NEACO   Near-Earth asteroid in cometary orbit

NEC   Near-Earth comet

NEO   Near-Earth object

NEV   Normalized error variance

R.A.   Right ascension

SOHO   Solar and Heliospheric Observatory

SWAN   Solar Wind ANisotropies, an instrument on-board the SOHO spacecraft

SKiYMET   All-Sky Interferometric Meteor Radar

WMPG   Western Meteor Physics Group

$Af\rho$	An indicator of the dust production of comets
$Af\rho_0$	$Af\rho_0$ scaled to $r_h = 1$ AU
A_B	Bond albedo
A_d	Dust albedo
A_p	Geometric albedo
A_x	The xth non-gravitational parameter
$A_\lambda(\alpha)$	Phase angle corrected geometric albedo
$\bar{a}$	Mean dust diameter
a_d	Diameter of the interplanetary dust
a_J	Semimajor axis of Jupiter
C_e	Effective scattering cross-section
c	Speed of light
D_{SH}	Southworth & Hawkins' D-criterion
$D_{threshold}$	Threshold of D-criterion
d_{min}	Close approach distance
e	Eccentricity
$\mathcal{F}$	Meteoroid flux
$\mathcal{F}_C$	Photometric flux of the comet
$\mathcal{F}_{coma}$	Photometric flux of the coma
$\mathcal{F}_\odot$	Photometric flux of the Sun
$\mathcal{F}_{CMOR}$	Meteoroid flux for CMOR
F_G	Solar gravity
$\mathcal{F}_{nucleus}$	Photometric flux of the nucleus
F_{PR}	Poynting-Robertson force
$\mathcal{F}_{tail}$	Photometric flux of the tail
G	gravitational constant

H	Absolute magnitude of a small solar system body
I	Ionisation coefficient
i	Inclination
$L_\odot$	Solar luminosity
$\mathbf{M}_i$	Modeled brightness profile
$\overrightarrow{MOID}$	Vector of MOID
M_1	Total magnitude
M_d	Total dust mass
M_n	Normalized nuclear magnitude **OR** total mass of nucleus
$M_\odot$	Solar mass
m	Apparent magnitude **OR** mass
m_d	Meteoroid mass
m_n	Apparent nuclear magnitude
m_λ	Apparent magnitudes of the comet at wavelength λ
$m_{\odot,\lambda}$	Apparent magnitudes of the Sun at wavelength λ
N_0	Mean dust production rate of 1 μm particles
$\mathcal{N}_{CMOR}$	Number of CMOR-detectable meteor showers
$\mathcal{N}_{dc}$	True number of dormant comets
N_m	Meteoroid production of the parent body
n	Brightening rate **OR** number of pixels
$\mathbf{O}_i$	Observed brightness profile
P	Orbital period
q	Perihelion distance **OR** differential size distribution index
R_G	Characteristic distance that gas drag become negligible
R_n	Effective radius of cometary nucleus
r_D	Heliocentric distance of the meteoroid at the MOID point

r_E	Heliocentric distance of the Earth at the MOID point
r_h	Heliocentric distance of a solar system body
s	Mass distribution index
s_{od}	Mass distribution index in the overdense regime
s_{ud}	Mass distribution index in the underdense regime
T_J	Tisserand's parameter
t_p	Epoch of perihelion passage
ΔT	First time criterion
δT	Second time criterion
Δt_{shower}	Duration of meteor shower
U	Uncertainty parameter
V_0	Mean ejection speed of a dust particle of $\beta_{rp} = 1$
v	Speed
v_{ej}	Dust ejection speed
v_{esc}	Dust escape speed
v_g	Geocentric speed
v_m	In-atmosphere speed
v_{rel}	Relative velocity between the meteoroid and the Earth
$V_\oplus$	Orbital speed of the Earth
X	Number of better parents
X_1	Purity
ΔX	Space criterion
α_g	Geocentric R.A.
α_ϕ	Phase angle
β	Ecliptic latitude
β_{rp}	Ratio between the radiation pressure and solar gravity that acts on the interplanetary dust

$\beta_{\mathrm{rp,max}}$	Upper β limit of dust
δ_{g}	Geocentric Dec.
$\varDelta$	Geocentric distance of a solar system body
η	Fraction of potentially visible meteoroids
η_{CMOR}	Detection efficiency of CMOR
η_{NEACO}	Detection efficiency of NEACOs
η_{shr}	Selection efficiency of NEACOs that produce visible meteor showers
λ	Ecliptic longitude
$\lambda_{\odot}$	Solar longitude
ν	Lagging function
ρ	Linear radius of photometric aperture
ρ_{d}	Bulk density of the interplanetary dust
ρ_{n}	Bulk density of cometary nucleus
σ_{rad}	Spatial probe size
σ_{v}	Speed probe size
σ_{ν}	Standard deviation of ν
τ	Lead time
τ_{enc}	Encircling time
τ_{parent}	Diverging timescale of the clones of a parent body
τ_{stream}	Age of meteoroid stream
ϕ	Normalized phase function
ψ	Wavelet coefficient
Ω	Longitude of the ascending node
ω	Argument of perihelion

Chapter 1

Introduction

"武王伐纣，东面而迎岁，至汜而水，至共头而坠，彗星出而授殷人其柄。"

《淮南子》

"When King Wu undertook the chastisement of Chou[1], he met with discouraging omens in his enterprise, such as great rains, when he came to Fan: the head of the Kung mountain collapsed into the river when he came near. A comet appeared, with its tail pointing to the east, which seemed to be an omen favourable to Yin (Chow) and indicating that Wu would be routed."

Writings of the Masters of Huai-Nan; translation by Evan S. Morgan[2].

1.1   Basics

A *comet* is a small, icy body in the Solar System that can display a fuzzy atmosphere (*coma*) and/or one or several "tail(s)" usually when it gets close to the Sun (Figure 1.1). Coma and cometary tails are mostly composed of dust particles (*meteoroids*), which are lifted from the

---

[1]Circa 1045 B.C.
[2]`http://www.sacred-texts.com/tao/tgl/index.htm`, retrieved 2016 May 2.

cometary surface due to outgassing. The meteoroids are mainly composed of silicates and iron with small amounts of Mg, Na, Ca and Al (e.g. Ceplecha et al., 1998, § 5.3). The meteoroids released at each perihelion passage of the comet undergo a slightly different dynamical evolution compared to their parent bodies due to their own size and bulk density as well as different time of ejection, forming a set of *meteoroid trails*. Differential effects such as radiation force and planetary perturbation lead to the gradual dispersion of the trails to a point that they become *meteoroid streams* that encircle the entire orbit (Figure 1.2). If the comet is a Near-Earth Comet (NEC; comets with perihelion distance $q < 1.3$ AU), these trails/streams have a chance of intercepting the Earth's orbit and producing *meteor showers* when the Earth passes through them. A *meteor*, or more commonly known as a "shooting star", is the light phenomenon caused by the impact of a *meteoroid* (an interplanetary dust particle) into Earth's atmosphere. Meteors are usually more easily noticeable during a meteor shower, in which a significant number of meteors radiate from a virtual point (the *radiant*) in the sky.

It has been proposed that comets are one of the primary sources of Earth's water (e.g. Delsemme, 1997). Recent observations and in-situ exploration have challenged this theory, as the deuterium/hydrogen ratio (D/H ratio) of most measured comets are different from the water on the Earth (e.g. Hartogh et al., 2011; Bockelée-Morvan et al., 2012; Altwegg et al., 2015). The D/H ratio acts as a fingerprint for the origin of the water, as stable atoms like hydrogen (and deuterium, an isotope of hydrogen) do not change over time. The population of asteroids, on the contrary, appears to be a better candidate as the D/H ratio in carbon-rich chondrites (which are believed to be mainly from asteroids) agrees with the D/H ratio of the Earth's water (Morbidelli et al., 2000; Genda & Ikoma, 2007). However, we note that only a tiny fraction of comets have been measured, usually with non-trivial uncertainties, therefore it is unclear whether the measured comets are representative to the entire cometary population. Also, as we will investigate in this Thesis, the transition between comets to asteroids (or asteroids to comets) is a continuum rather than discrete, which makes it difficult to attribute the origin of the Earth's water to either population.

Figure 1.1 Morphological evolution of comet C/2007 N3 (Lulin). Lower-right: Comet Lulin (center dot) at the time it was discovered by the author and Chi Sheng Lin (2007 July 11; r_h = 6.4 AU), credit: Lulin Observatory/National Central University. Full image: Comet Lulin near perihelion (2009 February 28; r_h = 1.4 AU), taken by Johannes Schedler (Panther Observatory), used with permission.
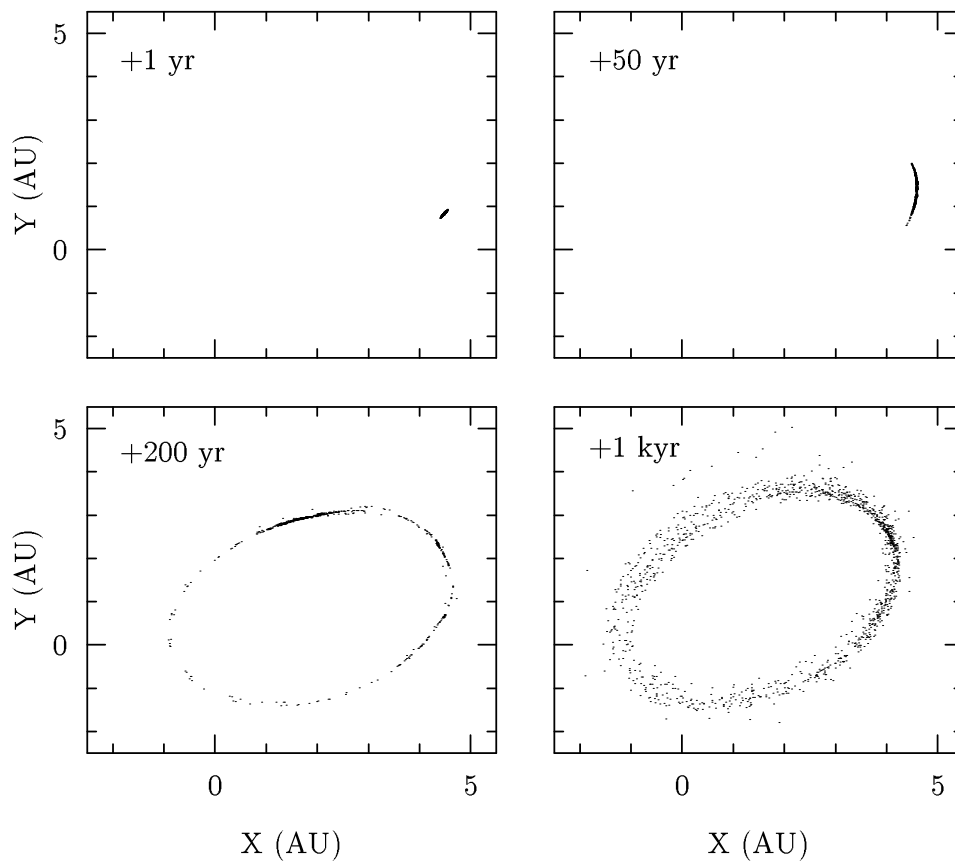
Figure 1.2 Evolution from meteoroid trail into stream: meteoroid ejection from comet 209P/LINEAR after 1 (a short arc of meteoroid trail), 50 (a longer arc of meteoroid trail), 200 (spread to the entire orbit) and 1000 years (a more spread, dispersed stream). Meteoroids drift away from their initial position on the orbit due to ejection velocity as well as differential perturbation.
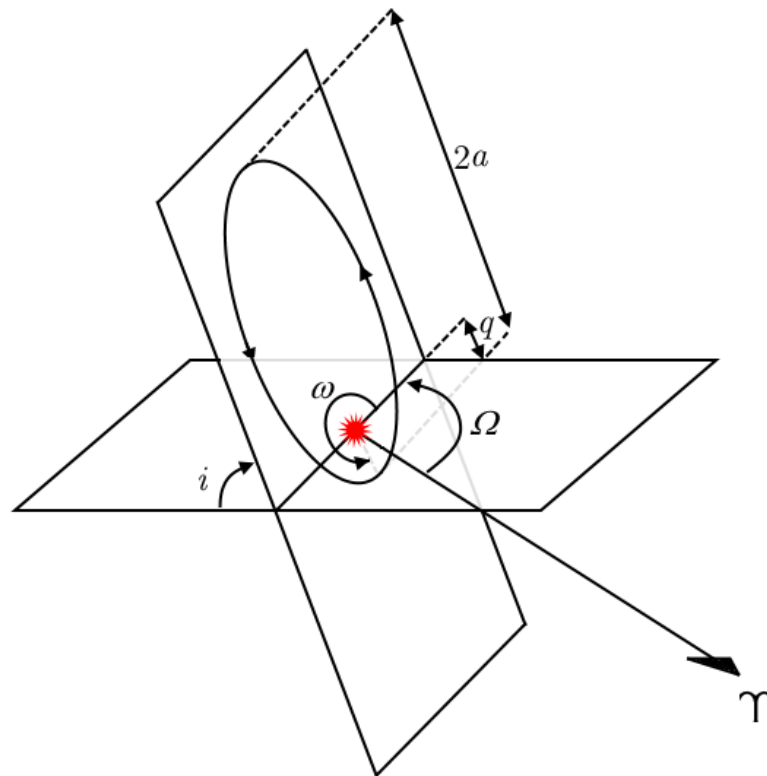
Figure 1.3 Elements that define an orbit: perihelion distance q, semimajor axis a (note that for clarity, the quantity of $2a$ is shown in the figure), longitude of ascending node Ω, and argument of perihelion ω. The eccentricity e is not explicitly shown, but can be derived through the relation $q = a(1 - e)$. The symbol of Υ stands for the First Point of Aries. The horizontal plane is the ecliptic plane (the orbital plane of the Earth) and the central red point is the Sun.

The detection of organic, complex molecules among comets also implies that they may have brought the precursors of life, even life itself, to the Earth (e.g. Chyba & Sagan, 1992; Napier et al., 2007; Furukawa et al., 2009). Thus, understanding the properties and evolution of comets helps understanding the biological and geological history of the early Earth as well as the dynamical evolution of the Solar System as a whole. The study of comets is also significant for protecting our planet from impacts by these icy bodies. Although asteroids are thought to be responsible for 99% of impact events on Earth (Yeomans & Chamberlin, 2013), cometary impacts are potentially more destructive, as they are more difficult to discover and track, and their arrival speeds tend to be higher than their asteroidal counterparts. Comets also release meteoroids into space, which can present a hazard to human activity (particularly space-based) without a direct impact at the Earth's surface. The most recent example is C/2013 A1 (Siding Spring), a long-period comet that approached Mars at a record-breaking 1/3 lunar distance in October 2014 (Ye & Hui, 2014) and triggered emergency maneuvers of all Mars-orbiting spacecraft.

A fundamental question in cometary science concerns the aging process of cometary nuclei. This refers to the effects that have altered the physical properties of the cometary nucleus since its formation. Since sublimation is the primary mechanism for cometary mass loss, comets that stay closer to the Sun (e.g. short-period comets) are more susceptible to the aging process. The dominant cometary population in the inner solar system is Jupiter-family comets (JFCs). JFCs, as the name suggests, are dynamically controlled by Jupiter, and spend their time in the inner solar system until being dynamically removed or impact the Sun or a major planet (see § 1.3 for a more quantitative description of the cometary populations based on dynamical criteria). An interesting observation made by Fernández et al. (2002); Di Sisto et al. (2009); Emel'yanenko et al. (2013) and others is that the physical lifetime (the time that it is physically active) of a typical JFC is only a fraction of its dynamical lifetime. This implies that JFCs should spend the majority of their life behaving like asteroids before their dynamical removal from the inner Solar System or impact with the Sun or major planets. The most common reason

for comets to cease activity (other than physical disruption) is because the reservoir of volatiles that supplies the activity is either depleted or is permanently locked under the crust. Such a comet is typically called a *dormant* comet. It is believed that two main mechanisms can lead to the dormancy of a comet (Jewitt, 2004): crust-over, in which the crust builds up an outer rind of debris and locks up the volatiles into the interior of the nucleus; and devolatilization, in which the volatiles are drained after many revolutions around the Sun. Unfortunately, with current observational techniques, we cannot tell which mechanism is acting on any particular comet.

While younger and more active comets are relatively easy to observe and study, the population of near-dormant and dormant comets presents a non-trivial challenge to observers as they are faint and hard to detect. Additionally, the population is further contaminated by asteroidal bodies that shed dust due to various effects unrelated to the sublimation of volatile ices (spin-up, collision, etc.) or achieve cometary orbits due to dynamical mechanisms (Bottke et al., 2002). These difficulties, together with the short age of modern observational astronomy (that spans less than $\sim$ 10% of the typical active lifetime of a JFC, even less for comets with longer periods) all make it very challenging to construct a clear chronological profile of the aging process of a comet.

1.2 History of Comet and Meteor Studies

The earliest known record of comets dates back to 1045 B.C. as made by Chinese diviners (i.e. the opening quote of this Chapter). The Greeks are known to be the first to explore the nature of comets. Pythagoras (ca. 570–ca. 495 B.C.) considered comets to be planets that were rarely seen, while Aristotle (384–322 B.C.) argued that comets are "dry and warm exhalations" in the atmosphere (Festou et al., 2004).

The modern study of comets started in the 16th century. Tycho Brahe (1546–1601) observationally demonstrated that comets are indeed celestial objects by measuring the parallax of

the Great Comet of 1577 and confirming its extraterrestrial origin. Isaac Newton (1642–1727) used his celebrated inverse square law of universal gravitation to show that the Great Comet of 1680 has a parabolic orbit (Newton, 1760). Edmond Halley (1656–1742) applied Newton's method to a set of comets, and discovered what was later known as Halley's Comet, the first known periodical comet (Halleio, 1704), although the actual contribution of both Newton and Halley has been long disputed and it has been suggested that John Flamsteed (1646–1719), the then Astronomer Royal that made most observations of the Great Comet of 1680, should perhaps get a credit in this set of discoveries. Halley's Comet was recovered by German astronomer Johann Georg Palitzsch (1723–1788) in 1758, which proved the validity of Newton's law of gravity and Halley's prediction and laid the foundation of modern cometary science.

We now know that meteors are mostly directly associated with comets, but the true nature of meteors remained in a mystery until as late as the mid 19th century. The earliest known record of a meteor shower dates back to ca. 16–17th century B.C., recorded in the *Bamboo Annals* of China, simply described the event as "stars fell like rain". There exists several hundreds of such records in Chinese chronicles through the end of 19th century, most of which are unfortunately no more than simplified phrases such as "stars fell like rain". The *radiant*, a common point in the sky that all meteors seem to radiate from during a meteor shower, was not reported until the Leonid meteor storm in 1833, which was widely observed by American observers. By noticing the radiant as well as the fact that the storm was not visible in Europe, Denison Olmsted (1791–1859) correctly inferred that the meteor storm originated as a cloud of particles (meteoroids) traveling in space (Olmsted, 1834). Giovanni Virgínio Schiaparelli (1835–1910) calculated the orbits of the Leonid and Perseid meteor showers and noticed that they are similar to those of two comets, 55P/Tempel-Tuttle and 109P/Swift-Tuttle, leading him to propose that (some) meteoroids originated from comets (Schiaparelli, 1867). The theory was soon widely accepted, and people started to look into the reverse problem, i.e. predicting meteor showers produced by Earth-approaching comets, such as 21P/Giacobini-Zinner and the October Draconids (Ye et al., 2013a).

The idea that comets are releasing solid particles naturally led to the conclusion that cometary tails are composed of such particles. In advance of Schiaparelli's idea, Russian astronomer Fyodor Aleksandrovich Bredikhin (1831–1904) further quantified the cometary tail model with the consideration of the repulsive force from the Sun (Bredikhin & Jaegermann, 1903), followed by several others, including the gas dynamical model by Finson & Probstein (1968a,b) that remains widely used today.

The exploration of the true nature of cometary nuclei started in the 1930s, when Wurm (1939) and Swings (1943) attempted to explain spectroscopic observations of comets and suggested that the observed gaseous species were created by photochemistry of more stable species residing in cometary nuclei. These studies led to the "dirty snowball" model that Whipple (1950) proposed in his celebrated paper, a model that was eventually confirmed by the historic *in situ* investigation of Halley's Comet by a set of spacecraft during its apparition in 1986.

The investigation of the source region of comets started at the same period of the proposal of Whipple's dirty snowball model. Edgeworth (1949); Oort (1950) and Kuiper (1951) presented a series of dynamical studies and proposed the existence of a belt of cometary nuclei (now called the Kuiper belt) and a spherical cloud of cometary nuclei (now called the Oort cloud) beyond Neptune's orbit enriched in small, icy bodies, now thought of as reservoirs for short- and long-period comets (SPCs/LPCs; i.e. comets that orbit around the Sun with periods < 20 and > 200 years respectively). Interestingly, although the region would later bear his name, Kuiper argued that such a region had long been cleared by the gravitational influence of Pluto (of which the mass was significantly overestimated at that time). It was Fernandez (1980) who first predicted the existence of this region in a quantitative manner. The discovery of the first Kuiper-belt object (KBO) (15760) 1992 QB_1 by Jewitt & Luu (1993), as well as the several thousands of KBOs found ever since, confirmed the existence of the Kuiper belt. Oort cloud objects are thought to be too distant and too small to detect with current technology, but the clustering of the aphelion distances of LPCs has provided some evidence of the existence of the Oort cloud (Wiegert & Tremaine, 1999).

In situ exploration of cometary nuclei conducted over the recent decades revealed a massive amount of information about comets. To-date, there have been 9 successful missions to a total of 6 comets. The first-ever comet encounter was conducted by the International Cometary Explorer (ICE), originally known as the International Sun-Earth Explorer 3 (ISEE-3), in September 1985 on comet 21P/Giacobini-Zinner (von Rosenvinge et al., 1986). 1P/Halley was visited by the Soviet spacecraft Vega-1 and Vega 2, Japanese spacecraft Sakigake and Suisei, European Space Agency's (ESA) Giotto, and ICE in 1986. United States spacecraft Deep Space 1 visited 19P/Borrelly in 2001, Stardust visited 81P/Wild 2 in 2004 and gathered cometary dust particles that were delivered back to Earth in 2006. Stardust also visited 9P/Tempel 1 in 2011, a comet that were previously visited by the Deep Impact spacecraft in 2005 and was deliberately impacted upon in the hope of excavating material from the interior of the nucleus. ESA's Rosetta mission, which is now orbiting 67P/Chryumov-Gerasimenko has performed the first-ever landing onto a cometary nucleus.

The advancement of meteor science, on the other hand, has grown out of the hazard that meteoroids pose to human presence and activity in space. Since the late 19th century, researchers measured a large quantity of meteors in the hope to search for new meteor showers and map the meteoroid background in the near-Earth environment. The search was initially based on visual observations (e.g. Denning, 1899; McIntosh, 1935), extended to photographic and radar observations in the mid-twentieth century thanks to the advancement of technology (c.f. Brown et al., 2008, and references therein). Increasing amount of meteor data, as well as the occasional campaigns on meteor showers that harbor short and strong meteor "outbursts", has enhanced our understanding of the meteoroid background at the Earth's orbit. The meteor data allowed astronomers to gain knowledge about the past activity of comets, an information that is virtually impossible to retrieve otherwise. The recent and most spectacular example is the study of the Leonid meteor shower (Milon, 1967; Jenniskens, 1995; Yeomans et al., 1996; Jenniskens, 2006, and many others).
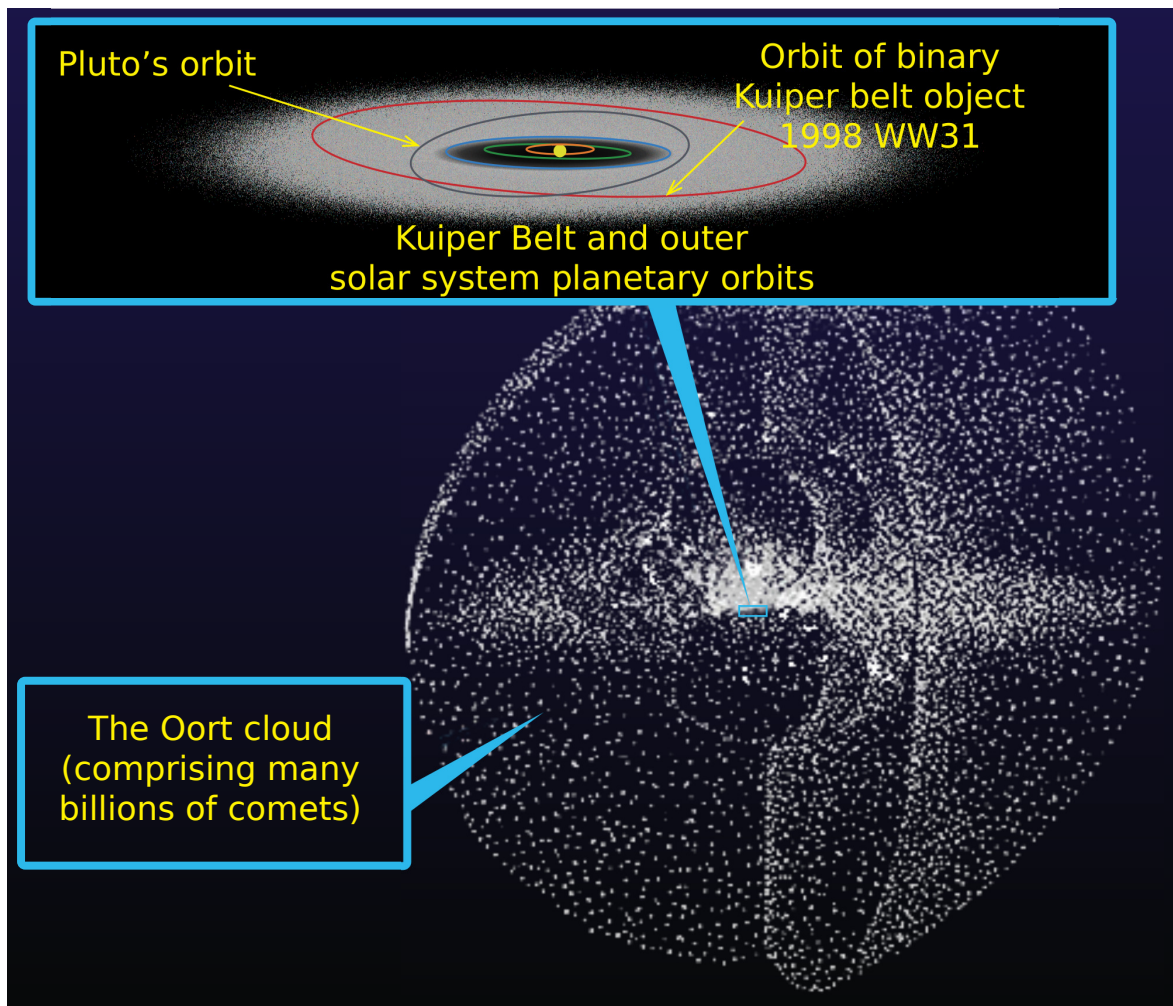
Figure 1.4 Depiction of the Kuiper belt (inset figure) and the Oort cloud in the Solar System. Rendered by William Crochot (JPL).

1.3 Evolution of Comets and Their Meteoroid Streams

1.3.1 Repositories of Comets

It is thought that comets originate from two regions in the solar system: the Oort cloud and the Kuiper belt.

The Oort cloud extends to $\sim 10^5$ AU from the Sun. It is thought that the Oort cloud is the repository of LPCs, as the aphelia of many LPCs cluster in this region (Oort, 1950). On rare occasions, LPCs are referred to as "non-periodic comets", but both terms are just conventional
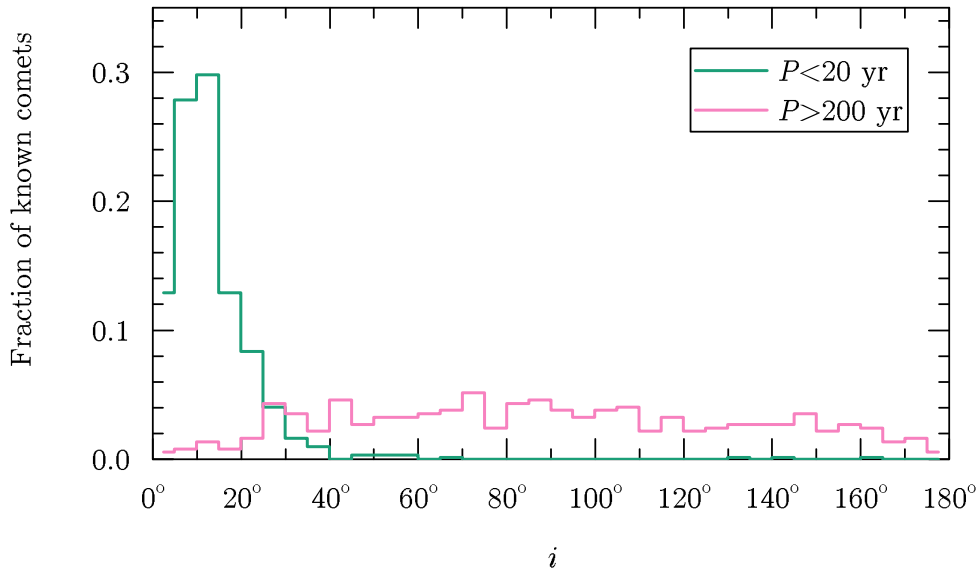
Figure 1.5 Distribution of orbit inclination of SPCs with $P < 20$ yr and LPCs with $P > 200$ yr, based on data extracted from the JPL Small-Body Database (retrieved 2016 June 16). It is clear that most SPCs stay close to the ecliptic plane while the distribution of LPCs orbits is largely isotropic.

and neither term can be associated with the true dynamical property of the comets, due to the difficulty to distinguish bound and unbound orbits for these comets. The definition of the dynamically new comet is a parallel definition that is also widely used. A dynamically new comet is, by definition, a comet that visits the inner Solar System for the first time, and has its $1/a < 10^{-4}$ AU^{-1} (Oort & Schmidt, 1951, where a is the semimajor axis of the orbit). This definition is based on the orbit at the moment it is first observed and does not consider its true dynamical history, it is therefore debatable whether the $1/a$ definition can be used as an authentic classification for LPCs.

As opposed to SPCs, whose orbits are close to the ecliptic plane, the distribution of LPC orbits is largely isotropic (Figure 1.5). This suggests that these cometary nuclei originated much nearer to the Sun in the proto-planetary disk and were ejected by the outer planets during planetary migration (Hahn & Malhotra, 1999), as they should otherwise stay close to the ecliptic plane. It is estimated that $\sim 10^{12}$ kilometer-sized cometary nuclei reside in the Oort

	Unstable orbit (T_J<2)	JFC-like orbit (2<T_J<3)	Stable orbit (T_J>3)
Coma	LPC or HTC	JFC	Active asteroids
No coma	Damocloids	Dormant JFC	Asteroids

Figure 1.6 Definition of LPCs, HTCs, Damocloids, JFCs, active and asteroids based on the Tisserand parameter (T_J). Definition adapted from Levison (1996) and Jewitt et al. (2015).

cloud (Dones et al., 2004). Halley-type Comets (HTCs) are of much shorter period than LPCs (between 20 to 200 years) but also with a wide range of inclinations, with 1P/Halley (Halley's Comet) as the most prominent example. It is thought that HTCs originated from the inner part of the Oort cloud by planetary perturbations (e.g. Levison et al., 2001).

The Kuiper belt, occasionally referred to as the Edgeworth-Kuiper belt in older literature, lies closer to the Sun than the Oort cloud. It is thought to be the primary source region for JFCs based on the fact that the inclination distributions of the two populations are similar (Fernandez, 1980; Duncan et al., 1988). It is estimated to contain $\sim 10^8$ kilometer-sized bodies (Bernstein et al., 2004). Under the gravitational perturbations of giant planets or passing stars, Kuiper belt objects (KBOs) may enter more elliptical orbits that may bring them farther or closer to the Sun. The population in the latter scenario is called Centaurs, which is thought to be an intermediate state between KBOs and JFCs. The first Centaur, (944) Hidalgo, was discovered in 1920, but the Centaurs were not recognized as a distinct population until the discovery of (2060) Chiron, which also held a cometary designation 95P/Chiron due to its cometary activity.

The Tisserand's parameter with respect to Jupiter is often used to distinguish between different cometary populations (Figure 1.6). It is defined as

$$T_J = \frac{a_J}{a} + 2 \left[(1 - e^2) \frac{a}{a_J} \right]^{\frac{1}{2}} \cos i \tag{1.1}$$

where a_J = 5.2 AU is the semimajor axis of the orbit of Jupiter. Dynamical JFCs T_J within

2–3, while dynamical asteroids have $T_J > 3$. Here we should note that T_J is derived assuming a restricted three-body problem, it is not precisely constant over time and could change by as much as 1–2% during a typical cometary lifetime (e.g. Murray & Dermott, 1999, § 3.4). Therefore, a more relaxed $T_J = 3.05$ is empirically chosen as a cut-off to distinguish between (most) asteroids and comets (c.f. Hsieh & Haghighipour, 2016).

Mathematically speaking, T_J is simply a measure of the relative velocity between the small body and Jupiter when the small body approaches Jupiter, as Jupiter itself has $T_J = 3$. However, observational studies by Fernández et al. (2005) did provide observational support for the $T_J \simeq 3$ threshold: objects with $T_J < 3$ are darker, or essentially "comet-like" than those with $T_J > 3$, which are brighter and "asteroid-like". This is in accordance with the fact that cometary nuclei usually possess very low albedo (e.g. Lamy et al., 2004, and references therein) due to organic-rich material (Keller et al., 2004) and hints at a possible cometary origin of $T_J < 3$ bodies.

1.3.2   End States of Comets

Comets lose a significant amount of mass due to sublimation during every perihelion passage. It is estimated that 1P/Halley loses $\sim 0.5\%$ of its total mass in every perihelion passage (Whipple, 1951), which implies a physical lifetime of a few hundred revolutions or a few dozen kyrs. The depletion of volatiles for JFCs occurs more rapidly due to their proximity to the Sun. Assuming a characteristic orbital period of 5 yrs, the physical lifetime of JFCs is at the order of 1 kyr.

De-volatilized comets continue to orbit the Sun until final disintegration, solar or planetary impact, or dynamical ejection from the Solar System. They may also be reactivated upon exposure of sub-surface volatiles (by impacts, for example). However, detection of cometary activity is limited by observation sensitivity. "Inactive" comets may, in fact, be weakly active at a level that may go undetected in regular observations, creating a gray zone for definition. For example, (3552) Don Quixote, the third largest NEO, is found to possess a coma and a tail after careful analysis of infrared observations obtained with the Spitzer Space Telescope (Mommert et al., 2014), after having escaped a number of ground-based searches for signs of

cometary activity. Comet 107P/Wilson-Harrington possessed a diffuse tail at its discovery in 1949, but appeared asteroidal in subsequent apparitions (Ishiguro et al., 2011).

Occasionally, comets split or disintegrate before depleting all volatiles. Splitting refers to the event that the comet splits into several smaller fragments, while disintegration refers to the event that the comet has been reduced into meteoric dust (Chen & Jewitt, 1994). The most famous examples include 3D/Biela (split into two before disintegration and is responsible for the Andromedid meteor shower), D/Shoemaker-Levy 9 (split into a few dozen pieces before Jovian impact) and the Kreutz sungrazing comet family. Some comets break up due to strong tidal force, such as the case of D/Shoemaker-Levy 9 (Asphaug & Benz, 1996) and the Kreutz comets (e.g. Sekanina & Chodas, 2002), but most splitting/disintegration events do not have an obvious cause (Boehnhardt, 2004).

1.3.3   Formation and Evolution of Meteoroid Streams

Sublimation of volatiles (such as water ice) is known as the primary driving force for the formation of meteoroid streams. Cometary dust particles or meteoroids are lifted from the nucleus surface by cometary outgassing due to sublimation. After release, different sizes of meteoroids follow different osculating Keplerian trajectories due to different amounts of radiation pressure (F_{rad}) and gravity (F_{grav}) from the Sun. The ratio of the latter two quantities is defined as β_{rp} (Burns et al., 1979; Williams & Fox, 1983; Fulle, 2004):

$$\beta_{\text{rp}} = \frac{F_{\text{rad}}}{F_{\text{grav}}} = \frac{5.74 \times 10^{-4}\ \text{kg} \cdot \text{m}^{-2}}{\rho_{\text{d}} a_{\text{d}}} \tag{1.2}$$

where ρ_{d} and a_{d} is respectively the bulk density and diameter of the meteoroid (in SI units). Here we see that β_{rp} corresponds to the magnitude of radiation pressure that offsets the gravitational force on the particle.

Under planetary perturbations, meteoroids in a meteoroid stream undergo a slightly different dynamical evolution than others, leading to the dispersion of the entire stream. Younger

ejections experience little evolutionary effects, and thus the meteoroids are concentrated in a narrow arc on the orbit; older ejections are more evolved such that they are stretched along the entire orbit. *Meteor outbursts* (sudden increase of meteor activity that does not occur every year) from young meteoroid trails provide clues to their ejection timing (e.g. the case of the Leonid meteor shower and comet 55P/Tempel-Tuttle, c.f. Yeomans et al., 1996), while *annual showers* from highly evolved streams are useful for the estimation of the age of the entire stream (e.g. the case of the Perseid meteor shower and comet 109P/Swift-Tuttle, c.f. Brown & Jones, 1998). It is estimated that meteoroid streams produced by JFCs will disperse into a diffuse, structure-less meteoroid cloud in $\sim 10^4$ yrs, forming most of the *zodiacal cloud*, which is a donut-shape structure of interplanetary dust on the ecliptic plane (Jenniskens, 2006).

1.4   Observations of Comets and Meteors

1.4.1   Observation of Comets

Observation of comets is similar to the observation of asteroids and interstellar clouds. The complexity is the challenge presented by a moving, sometimes transient, object that may be of complex and variable structure and of low surface brightness. It must be acknowledged that recent advancement of computational and detection technology has enabled many amateur astronomers to produce scientifically useful observations. Collaboration between these so-called "citizen astronomers" makes it possible to gather a large amount of high cadence data that could reveal the short-term (in the order of days and weeks) evolution of various of cometary phenomena. This greatly complements the effort from the professional astronomers and has shown its potential to enhance our understanding of comets as well as other astronomical phenomena. Interested readers can refer to Marshall et al. (2015) for a complete review.

The primary technique for comet observation is optical imaging at visible wavelengths. This technique can be used to study a variety of cometary phenomena, such as the morphology and evolution of comae and tails as well as cometary nuclei. The detected signal originates

from two sources: for observation of cometary nuclei and dust tails, the signal originates from the reflected sunlight by dust particles and the nucleus, while for ion tails, the signal originates from ionization emission produced by the cometary molecules when they interact with solar wind and interplanetary magnetic field or are ionized by ultraviolet sunlight. Cometary imaging can be conducted by either wide-field or narrow-field telescopes. While most comets are faint and are only accessible by professional facilities, bright comets appear every a few years and are able to attain great apparent size. The tail of comet C/1995 O1 (Hale-Bopp) – the last "Great Comet" as of the writing of this thesis – attained a length of $\sim 45°$ when at the perihelion.

One of the most useful quantities that is frequently used by citizen and professional astronomers is the $Af\rho$ parameter which broadly measures the dust production of a comet (A'Hearn et al., 1984):

$$Af\rho = \frac{4r_{\mathrm{h}}^2 \varDelta^2}{(1\ \mathrm{AU})\rho} \frac{\mathcal{F}_{\mathrm{C}}}{\mathcal{F}_{\odot}} \tag{1.3}$$

where r_{h} is the heliocentric distance of the comet in AU, $\varDelta$ is the geocentric distance of the comet (in the same unit of the linear radius of aperture at the comet, ρ, typically in km or cm), and $\mathcal{F}_{\mathrm{C}}$ and $\mathcal{F}_{\odot}$ are the fluxes of the comet within the field of view as observed by the observer and the Sun at a distance of 1 AU. The photometric aperture diameter, or $2\rho/\varDelta$, is determined by the threshold value that the flux reaches the asymptote. On the left-hand side, A is the albedo and f is the dimensionless filling factor defined by the total cross section of the dust within the field of view. The $Af\rho$ of typical comets vary from 1–100 m.

Cometas Obs has a collection of $Af\rho$ (along with some other quantities) reported by amateur astronomers (`http://www.astrosurf.com/cometas-obs/`).

The large amount of high cadence data also makes it possible to look at the morphological changes of cometary features (coma and tail) in small time steps. Pro-Am collaborations become more common in the recent years and provide insight into the origin of various cometary phenomena (e.g. Lang & Hogg, 2012; Samarasinha et al., 2015).

Another useful technique is to perform single or multi-band photometry on the nucleus

(Lamy et al., 2004). This allows us to derive the size and compositional properties of cometary nuclei. However, the observation can be challenging, as it needs to be conducted when the comet is sufficiently far from the Sun (and thus very faint) to reveal the "bare" nucleus. The assumption that cometary activity terminates at large heliocentric distance is also not very robust, as "aphelion activity" is not unheard of, and even a weak, unresolved coma can still contaminate the signal and thus alter the results.

For very active comets, emission lines can be present. Emission line observations are extremely useful on quantifying the gaseous species of the comet and provides clues on the composition of the cometary nucleus. Spectroscopic observations are frequently used for such studies (c.f. Feldman et al., 2004). Narrow-band observations are occasionally used to study the same topic, but relevant instruments are expensive to build (c.f. Schleicher & Farnham, 2004). Common optical cometary species include OH (309 nm), CN (387 nm), C_3 (406 nm), C_2 (513 nm) and NH_2 (663 nm).

Other less frequently-used techniques for cometary observations include polarimetry and thermal observations of cometary dust (c.f. Kolokolova et al., 2004).

1.4.2 Observation of Meteors

A typical meteor observation has four components: the radiant, a celestial point where the meteor radiates from (usually in equatorial coordinates or sun-centered ecliptical coordinates), the apparent speed of the meteoroid, and the time of the meteor event. Crudely speaking, this defines a vector along which the meteoroid travels in interplanetary space, and can be linked to a unique orbit. One of the main goals of meteor observation is to find out the orbit of the meteoroid.

Visual and photographic observations are the oldest methods in meteor observation but are now largely superseded by the video method. Since World War II, the radio technique has emerged as a useful technique to detect a large number of meteors. We will briefly introduce both video and radar techniques, but we should note that only data obtained with the backscatter

radar technique is used in this thesis.

Most video meteor observations are conducted using commercially available low light level video cameras to record meteors. Usually, multi-station observations are coordinated in the hope to constrain the meteor trajectory using the triangulation method, although it is also common for amateur astronomers to deploy cameras at only one site while still being scientifically valuable, such as the IMO Video Meteor Network project (Molau & Barentsen, 2014).

There are two types of video meteor observation, each having its own pros and cons. All-sky cameras cover larger areas (and in most cases, the entire meteor trajectory) but are less precise in terms of astrometric and photometric measurements and are only sensitive to brighter meteors. Examples include the All Sky and Guided Automatic Real-time Detection (ASGARD) operated by the Western Meteor Physics Group (WMPG) at the University of Western Ontario (Brown et al., 2010). Narrow-field cameras are sensitive to fainter meteors, but only cover a limited area and may not cover the entire meteor trajectory unless being specifically designed to do so. Examples include the Canadian Automated Meteor Observatory (CAMO) operated by the WMPG (Weryk et al., 2013).

Radar observation makes use of the ionization trail formed during the meteor event. When a meteoroid enters the Earth's atmosphere, the collisions between atmospheric atoms and vaporized atoms evaporated from the meteoroid surface form an ionization trail, which can reflect radio waves. Radar observation has unique advantages compared to visual and video observations, as it is insensitive to the change of weather and can be conducted during the day. It is also more sensitive to smaller meteoroids comparing to optical observations. However, radar observation does have its own caveats. Data reduction of radar observations are considerably more complicated than optical observations. Due to the inhomogeneity of radio wave power at different direction, one needs to be careful when trying to calculate meteoric flux from radar observations. Radar is also insensitive to slow meteors ($v \lesssim 15$ km/s) as the ionization efficiency of the meteor trail drops quickly at slow speed, making the trail deficient in electrons and thus only weakly reflect radar waves.
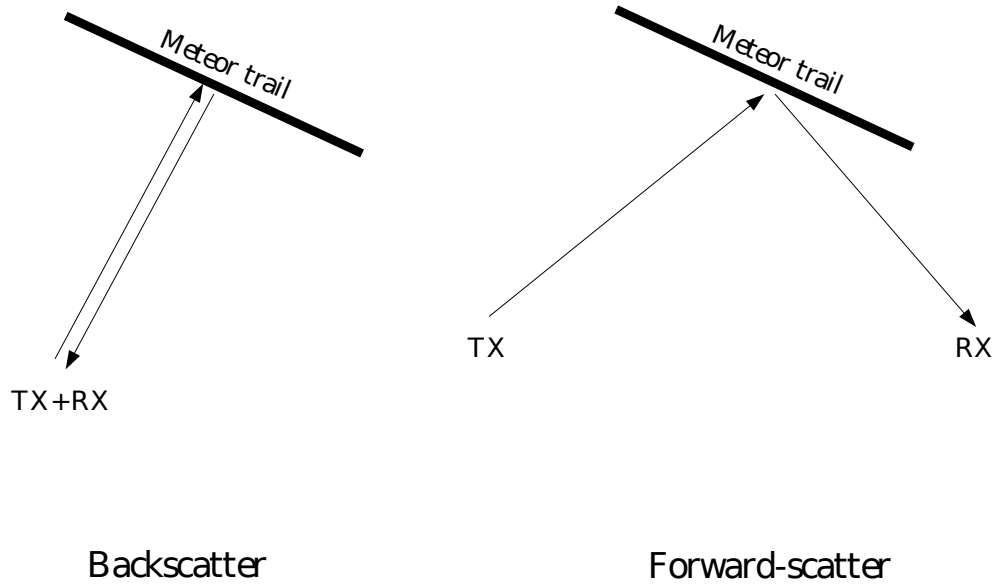
Figure 1.7 Observing geometry for backscatter (left) and forward-scatter systems. TX stands for transmitter and RX stands for receiver.

There are two main types of radar observations: backscatter observation and forward-scatter observation. A backscatter radar system detects the specular reflection of radar pulse from the meteor trail (i.e. the transmitter and the receiver is at the same place), while a forward-scatter system detects the radar pulse sent by a distant transmitter (usually 1000–2000 km away) that is reflected by the meteor trail. The Canadian Meteor Orbit Radar, the system that is used in this thesis, is a backscatter system (Appendix B).

1.4.3   Modeling of Cometary Dust and Meteoroids

Dust modeling is a useful technique to explore the properties and evolution of cometary and meteoric dust, which can in turn reveal the histories of parent bodies.
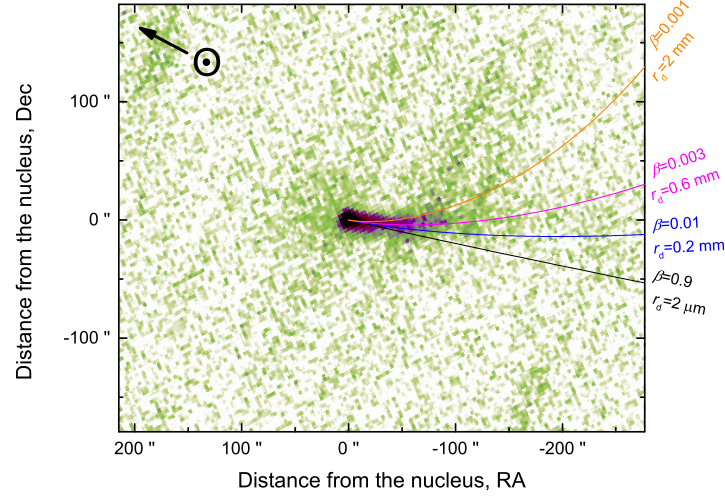
Figure 1.8 Syndyne diagram of a comet. Reproduced from Figure 1 of Ye & Wiegert (2014).

The simplest model is the syndyne-synchrone model. Assuming zero ejection speed ($v_{ej} = 0$), the set of meteoroids with the same β_{rp} and different ejection epoch is called *syndyne* curve, while that with different β_{rp} but same ejection epoch is called *synchrone* curve. The concept of syndyne and synchrone was first introduced by Fyodor Aleksandrovich Bredikhin (1831–1904) in 1877, and was derived in a more quantitative way by Finson & Probstein (1968a). This simple model is commonly used for zero-order analysis of cometary tail morphology, and it also shows how ejected meteoroids evolve in space. For typical sizes of meteoroids studied in meteor science ($a_d \gtrsim 1\,\mu$m), smaller particles are associated with larger β_{rp}, therefore experiencing stronger radiation pressure and more rapidly moving away from the Sun; larger particles are associated with smaller β_{rp}, therefore tend to stay closer to the nucleus. Therefore, depending on the mass, ejected particles may enter elliptic, parabolic or hyperbolic orbits.

In reality, v_{ej} is not zero. There exists a variety of ejection models, but all of them are the descendants of the classic Whipple (1950) model. To the zeroth order, Whipple's model states that

$$v_{ej} \propto \beta_{rp}^{1/2} \tag{1.4}$$

Once released, the motion of a meteoroid is mainly controlled by gravity and radiation forces from the Sun (c.f. Burns et al., 1979; Dermott et al., 2001). The radiation force breaks down to two components, the radial one being the radiation pressure from the Sun that pushes the meteoroid away from the Sun, and the tangential being the angular momentum lost due to the force applied to the meteoroid by radiation pressure tangential to the meteoroid's motion. The latter is also known as the Poynting-Robertson effect (Poynting, 1903; Robertson, 1937). The radiation-corrected gravitational equation hence becomes

$$F_{\mathrm{G}} = -(1 - \beta_{\mathrm{rp}})G\frac{M_{\odot}m_{\mathrm{d}}}{r_{\mathrm{H}}^{2}} \tag{1.5}$$

where F_{G} is the solar gravity applied on the meteoroid and m_{d} is the mass of the meteoroid. The Poynting-Robertson force is equal to

$$F_{\mathrm{PR}} = \frac{a_{\mathrm{d}}^{2}L_{\odot}}{4c^{2}}\left(\frac{GM_{\odot}}{r_{\mathrm{h}}^{5}}\right) \tag{1.6}$$

where $L_{\odot}$ is the solar luminosity, c is the speed of light, G is the gravitational constant and $M_{\odot}$ is the solar mass.

Meteoroids are also occasionally perturbed by major planets, making it difficult to solve their motion analytically. Instead, meteoroid motions are usually solved for by N-body integrators. Popular N-body integrators include SWIFT (Levison & Duncan, 1994), MERCURY (Chambers, 1999), HNBODY (Rauch & Hamilton, 2002) and many others. In this thesis MERCURY is used for all the numerical simulations.

1.4.4 Meteoroid Stream Identification and Stream-Parent Linkage

The problems of meteoroid stream identification and stream-parent linkage are essentially one problem: determining whether a set of orbits (should it be orbits of meteoroids, asteroids or comets) are similar enough such that they are likely to be genetically related. The most popular method for determination of the similarity between two orbits is the *D*-criterion method first

introduced by Southworth & Hawkins (1963). The basic idea of the D-criterion method is to generalize the distance of two orbits in a 5-dimensional space constructed by orbital parameters, q (perihelion distance), e (eccentricity), i (inclination), Ω (longitude of the ascending node) and ω (argument of perihelion):

$$D_{\text{SH}}^2 = (e_2 - e_1)^2 + (q_2 - q_1)^2 + \left(2 \sin \frac{I_{21}}{2}\right)^2 + \left[\left(\frac{e_2 + e_1}{2}\right)\left(2 \sin \frac{\pi_{21}}{2}\right)\right]^2 \qquad (1.7)$$

where

$$\left(2 \sin \frac{I_{21}}{2}\right)^2 = \left(2 \sin \frac{i_2 - i_1}{2}\right)^2 + \sin i_1 \sin i_2 \left(2 \sin \frac{\Omega_2 - \Omega_1}{2}\right)^2 \qquad (1.8)$$

and

$$\pi_{21} = \omega_2 - \omega_1 + 2 \arcsin\left(\cos \frac{i_1 + i_2}{2} \sin \frac{\Omega_2 - \Omega_1}{2} \sec \frac{I_{21}}{2}\right) \qquad (1.9)$$

and the subscripts 1 and 2 refer to the two orbits being compared. Note that the sign of the arcsin term needs to be reversed if $\Omega_2 - \Omega_1$ is over 180°. To check if orbit 1 and orbit 2 are similar orbits, one calculate the D_{SH} for the two orbits and see if it satisfies the condition

$$D_{\text{SH}} < D_{\text{threshold}} \qquad (1.10)$$

where $D_{\text{threshold}}$ is the threshold.

There are many variants of the D-criterion such as those by Drummond (1981), Jopek (1993), Asher et al. (1994), Steel (1995) and others, but they all based on the same philosophy. However, attention should be paid to the shortcomings of this method (and its variants), one of the most prominent issues being the problem of obtaining precise stream orbits. Determination of meteoroid orbits is subject to measurement uncertainties and systematic bias such as the atmospheric drag. This is especially true for weakly-active meteor showers (where the statistics are low) and streams rich in fragile meteoroids (e.g. Draconids, Ye et al., 2013b). There have

been attempts to (at least partially) overcome this issue by starting from the observed quantities rather than from derived orbits (Valsecchi et al., 1999), but this would restrict the usage to meteoroid-meteoroid associations.

Another issue is the determination of $D_{\mathrm{threshold}}$. Many earlier authors empirically define $D_{\mathrm{threshold}} = 0.1$ that is somewhat arbitrary. Of course, a smaller D may imply a higher chance that the two bodies are related, but how small is "small"? This creates a gray zone where the possibility of chance alignments is difficult to quantify. The first widely-accepted association between a meteor stream and a NEA is the Geminids-Phaethon pair (Whipple, 1983), while the issue of chance linkages between NEAs and meteor streams was first critically reviewed by Porubcan et al. (1992), who tested an updated list of NEAs against photographic meteoroid orbits. As noted by the authors, the orbit match does not guarantee a physical association, and the results can be misleading (as later shown in Steel, 1995).

1.5   Previous Studies

1.5.1   Studies of Weakly-Active and Dormant Comets

Early exploration by Öpik (1963) speculated that a significant fraction of NEAs are of cometary origin. In subsequent decades, it became more common for some asteroids to be found to exhibit cometary activity and be reclassified as comets. Although some of these reclassifications were due to cometary nuclei discovered initially beyond the typical water-ice sublimation line (~ 3 AU) and later becoming active as they approached the sun, most cases are associated with JFCs that are weakly active (and therefore the cometary features can be difficult to observe). Though one may speculate that the weak activity may simply due to the small sizes of the nuclei (e.g. sub-km nuclei), surprisingly, most measured weak-active cometary nuclei are comparable in sizes to their normally-active counterparts (Ye et al., 2016).

The earliest known weakly-active comet is 28P/Neujmin 1. It has been studied extensively partly due to its large size (10–15 km versus a few km for typical JFC nuclei, c.f. Lamy et al.,

2004) making it easier to observe. It is found that the fraction of active surface area is $\sim 0.1\%$ or 100 times lower than typical JFCs (Campins et al., 1987). Spectroscopic studies suggested that the nucleus of 28P/Neujmin 1 is highly evolved and is similar to the Trojan asteroids (Campins et al., 2007).

Another well-known object that is likely approaching its dormancy is 107P/(4015) Wilson-Harrington. Readers may immediately notice the dual comet-asteroid designation of this object. 107P/Wilson-Harrington displayed a diffuse tail when it was discovered in 1949 but has appeared asteroidal since its recovery in 1979 (Fernández et al., 1997). It may be a near-dead comet with intermittent activity, although this argument is weakened by the fact that the detection of cometary activity is old and unrepeated, as well as the fact that it has a $T_J = 3.08$ is slightly beyond the classical $T_J = 3$ boundary (Jewitt et al., 2015).

Since weakly-active comets are faint, diffuse and often require observations with either large telescopes, sensitive detectors or long integrations, it is unsurprising that the known population of weakly-active comets remained tiny until the 2000s, when a number of modern NEO surveys were put into operation (Figure 1.10). By creating a debiased near-Earth JFC model, Fernández & Morbidelli (2006) predicted that there are as much as 10^3 NEJFCs that are larger than ~ 100 m. For comparison, there are ~ 500 known JFCs at this size or larger as the time of writing (mid 2016), which implies a significant number of undetected comets. Since the coverage of NEO surveys are fairy frequent and complete now (one full-sky coverage every ~ 2 weeks), it is likely these comets are undetected primarily due to their faintness.

Dormant comets are even more difficult to directly study than weakly-active comets, as they do not display any cometary features. As such, dynamical methods of isolating potential dormant comets have proved to be very useful. Different authors (e.g. Levison & Duncan, 1997; Bottke et al., 2002; Fernández & Morbidelli, 2006) have arrived at two major conclusions: (1) there are at least as many dormant JFCs as active JFCs; and (2) there is a small but non-negligible chance for main-belt asteroids to achieve JFC-like orbits via certain mean-motion resonances, which presents extra challenges for observational studies. While observational
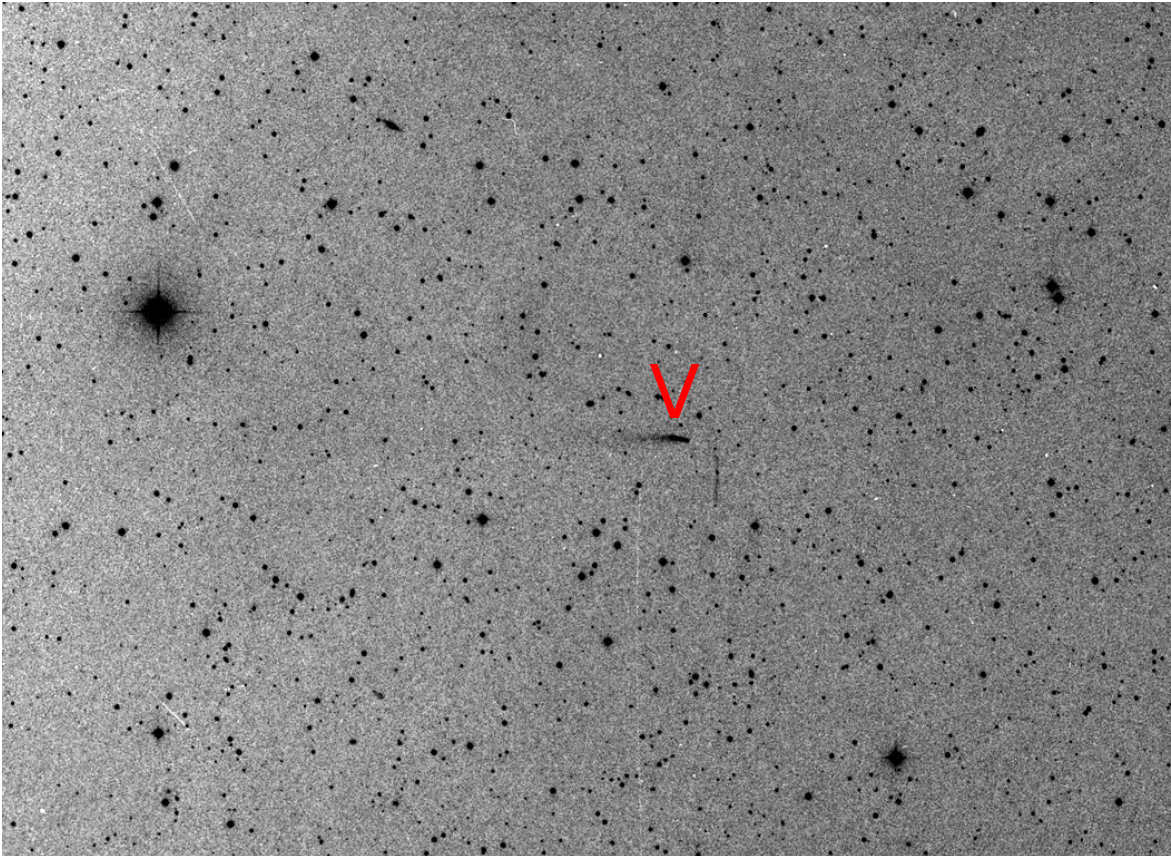
Figure 1.9 Comet 107P/(4015) Wilson-Harrington at discovery (1949 November 19). The comet is marked by an arrow. The plate was taken by the 48-inch Oschin Telescope at Palomar Observatory appropriated to *B*-band. The image has been enhanced by the European Southern Observatory (ESO) photographic laboratory at Garching.
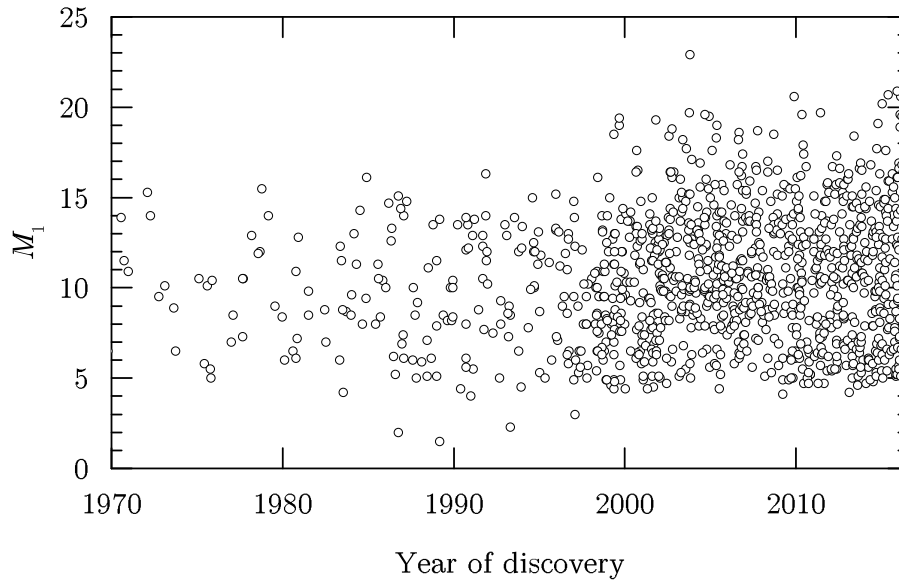
Figure 1.10 The distribution of total cometary absolute magnitudes (M_1) versus the year discovered. The magnitude data is retrieved from the JPL Small-Body Database on 2016 June 16. It can be seen that most comets with $M_1 > 15$ were found after about the year 2000.

method is difficult, there are signs that a large number of dormant comets exist. Fernández et al. (2002) showed that objects on comet-like orbits do, in general, possess comet-like (i.e. low) albedo, than those on asteroid-like orbits.

As individual objects (either weakly-active comets or dormant comet candidates) are usually difficult to observe, most studies to-date focus at the general characteristics of the population. However, our understanding of this topic would not advance without close examination of a sufficient number of specific objects.

1.5.2 Meteor Studies

Meteor observation provides a unique perspective to look into the properties of the dust that originated from the associated parent bodies. Drummond (1982) pioneered this topic by looking at theoretical meteor radiants from NEAs and comparing them against contemporary and medieval fireball observations. Drummond used Southworth & Hawkins (1963)'s D-criterion

(and its variant) to quantify orbital similarity between meteoroid stream and the parent, a technique that was followed by many later studies. A handful of associations were speculated upon; however, as the author pointed out, the lack of precise meteor orbits hampered the confidence of the proposed associations.

The recognition of asteroid (3200) Phaethon as the parent body of the annual Geminid meteor shower in 1983 sparked interest in searching for meteor showers that trace to dormant comet candidates and other ordinary asteroids. Systematic searches were conducted by several parties (see the reviews by Jenniskens, 2008a,b) of which a few dozen linkages were proposed. As meteor showers are produced by dust ejection, meteor observations can provide a strong constraint on previous dust production of the parent body. However, the lack of precise meteor orbits continued to be a limiting factor (e.g. Jopek et al., 2002) until very recently, when a number of extensive video networks are established and data interpretations just begun. The problem is further complicated by a variety of ejection mechanisms (sublimation, tidal or thermal disruption, collision, etc.) the details which are still not well understood. The secular evolution of meteoroid streams as well as the challenges in accurately measuring stream orbits (the latter of which is essential in comparing the similarities between the orbit of the stream and the parent) all make the problem difficult to solve. For example, questions still exist over the formation of the Geminid stream, some 30 years after Phaethon has been identified as the parent body of this stream.

Using meteor observation to study weakly-active comets is an exciting but largely uncharted territory. NEJFC 15P/Finlay has been suspected to be a near-death comet due to the absence of the Finlayid meteor shower (Beech et al., 1999), though this theory has been neither confirmed nor disproved. Jenniskens (2006) has noted a few predicted showers from several weakly-active or inactive bodies including JFC 209P/LINEAR, one of the most weakly-active comets found to-date.

1.6   Questions for This Thesis

The aging process of comets relates to some fundamental questions of planetary science such as the evolutionary process of the Earth and the Solar System as a whole. It is also a difficult question given the scarcity of observations and the difficulty for interpretation. In this thesis, we make an attempt to probe into this question by bringing the knowledge from two close but different fields – cometary studies (more on astrophysics and planetary astronomy) and meteor science (more on atmospheric science) – together.

The core question is, what happens when a comet gets old? Admittedly, this is a broad question and our attempt could not cover every aspect at one time. Here we look at three parts of the aging spectrum:

in Chapter 2 we study a moderately-active JFC, 15P/Finlay. The comet had been quiet for a century and was thought to be approaching its dormancy phase, before a significant recurring activity during its perihelion passage in 2015. Apart from characterizing the recurring activity of the comet and trying to understand the mechanism that drove the activity, we also revisit the "Finlayids puzzle", a puzzle that has been lingered around in the meteor community for several decades, regarding the non-detection of meteor showers from this comet.

in Chapter 3 we study a weakly-active JFC, 209P/LINEAR. This comet is among the most weakly-active comets currently known. Exploratory surveys by Fernández & Sosa (2015) suggests that 209P/LINEAR may reside in a very stable orbit for 10^4 yr, a long time scale that is rare for JFCs, underlying the possibility that this comet is very long-lived and is approaching dormancy. 209P/LINEAR passed extremely close to the Earth in May 2014, providing a rare opportunity for high-resolution cometary observations. Our earlier work (Ye & Wiegert, 2014) also confirmed the arrival of a previously unknown meteor shower, the Camelopardalids, that originates from 209P. We attempt to draw conclusions on the nature and evolution of 209P/LINEAR from dual comet-meteor observations.

in Chapter 4 we conduct a meteor-based survey looking for dormant comets in the NEO population. The dormant comet issue is recognized as a difficult issue in the field due to two reasons: observationally, these objects are indistinguishable from their asteroidal counterparts; dynamically, asteroidal contamination in the cometary population is known to be non-negligible. However, as we will show in that Chapter, meteor observation is a robust method to identify dormant comets, and we will attempt to constrain the fraction of dormant comets among NEOs.

We will conclude the thesis in Chapter 5 and list future works that we intend to accomplish.

Bibliography

A'Hearn, M. F., Schleicher, D. G., Millis, R. L., Feldman, P. D., & Thompson, D. T. 1984, AJ, 89, 579

Altwegg, K., Balsiger, H., Bar-Nun, A., et al. 2015, Science, 347, 1261952

Asher, D. J., Clube, S. V. M., Napier, W. M., & Steel, D. I. 1994, Vistas in Astronomy, 38, 1

Asphaug, E., & Benz, W. 1996, Icarus, 121, 225

Beech, M., Nikolova, S., & Jones, J. 1999, MNRAS, 310, 168

Bernstein, G. M., Trilling, D. E., Allen, R. L., et al. 2004, AJ, 128, 1364

Bockelée-Morvan, D., Biver, N., Swinyard, B., et al. 2012, A&A, 544, L15

Boehnhardt, H. 2004, Split comets, ed. G. W. Kronk, 301–316

Bottke, W. F., Morbidelli, A., Jedicke, R., et al. 2002, Icarus, 156, 399

Bredikhin, F., & Jaegermann, R. 1903, Prof. Dr. Th. Bredichin's Mechanische Untersuchungen über Cometenformen: in systematischer Darstellung (Voss)

Brown, P., & Jones, J. 1998, Icarus, 133, 36

Brown, P., Weryk, R. J., Kohut, S., Edwards, W. N., & Krzeminski, Z. 2010, WGN, Journal of the International Meteor Organization, 38, 25

Brown, P., Weryk, R. J., Wong, D. K., & Jones, J. 2008, Icarus, 195, 317

Burns, J. A., Lamy, P. L., & Soter, S. 1979, Icarus, 40, 1

Campins, H., A'Hearn, M. F., & McFadden, L.-A. 1987, ApJ, 316, 847

Campins, H., Licandro, J., Pinilla-Alonso, N., et al. 2007, AJ, 134, 1626

Ceplecha, Z., Borovička, J., Elford, W. G., et al. 1998, Space Sci. Rev., 84, 327

Chambers, J. E. 1999, MNRAS, 304, 793

Chen, J., & Jewitt, D. 1994, Icarus, 108, 265

Chyba, C., & Sagan, C. 1992, Nature, 355, 125

Delsemme, A. 1997, The Origin of the Atmosphere and of the Oceans, ed. P. J. Thomas, C. F. Chyba, & C. P. McKay (New York, NY: Springer New York), 29–67

Denning, W. F. 1899, MmRAS, 53, 203

Dermott, S. F., Grogan, K., Durda, D. D., et al. 2001, Orbital Evolution of Interplanetary Dust, ed. E. Grün, B. A. S. Gustafson, S. Dermott, & H. Fechtig, 569

Di Sisto, R. P., Fernández, J. A., & Brunini, A. 2009, Icarus, 203, 140

Dones, L., Weissman, P. R., Levison, H. F., & Duncan, M. J. 2004, Oort cloud formation and dynamics, ed. G. W. Kronk, 153–174

Drummond, J. D. 1981, Icarus, 45, 545

—. 1982, Icarus, 49, 143

Duncan, M., Quinn, T., & Tremaine, S. 1988, ApJ, 328, L69

Edgeworth, K. E. 1949, MNRAS, 109, 600

Emel'yanenko, V. V., Asher, D. J., & Bailey, M. E. 2013, Earth Moon and Planets, 110, 105

Feldman, P. D., Cochran, A. L., & Combi, M. R. 2004, Spectroscopic investigations of fragment species in the coma, ed. M. C. Festou, H. U. Keller, & H. A. Weaver, 425–447

Fernandez, J. A. 1980, MNRAS, 192, 481

Fernández, J. A., Gallardo, T., & Brunini, A. 2002, Icarus, 159, 358

Fernández, J. A., & Morbidelli, A. 2006, Icarus, 185, 211

Fernández, J. A., & Sosa, A. 2015, Planet. Space Sci., 118, 14

Fernández, Y. R., Jewitt, D. C., & Sheppard, S. S. 2005, AJ, 130, 308

Fernández, Y. R., McFadden, L. A., Lisse, C. M., Helin, E. F., & Chamberlin, A. B. 1997, Icarus, 128, 114

Festou, M. C., Keller, H. U., & Weaver, H. A. 2004, A brief conceptual history of cometary science, ed. M. C. Festou, H. U. Keller, & H. A. Weaver, 3–16

Finson, M. J., & Probstein, R. F. 1968a, ApJ, 154, 327

Finson, M. L., & Probstein, R. F. 1968b, ApJ, 154, 353

Fulle, M. 2004, Motion of cometary dust, ed. M. C. Festou, H. U. Keller, & H. A. Weaver, 565–575

Furukawa, Y., Sekine, T., Oba, M., Kakegawa, T., & Nakazawa, H. 2009, Nature Geoscience, 2, 62

Genda, H., & Ikoma, M. 2007, in Planetary Atmospheres, Vol. 1376, 43

Hahn, J. M., & Malhotra, R. 1999, AJ, 117, 3041

Halleio, E. 1704, Royal Society of London Philosophical Transactions Series I, 24, 1882

Hartogh, P., Lis, D. C., Bockelée-Morvan, D., et al. 2011, Nature, 478, 218

Hsieh, H. H., & Haghighipour, N. 2016, Icarus, 277, 19

Ishiguro, M., Ham, J.-B., Tholen, D. J., et al. 2011, ApJ, 726, 101

Jenniskens, P. 1995, A&A, 295, 206

—. 2006, Meteor Showers and their Parent Comets

—. 2008a, Icarus, 194, 13

—. 2008b, Earth Moon and Planets, 102, 505

Jewitt, D., Hsieh, H., & Agarwal, J. 2015, The Active Asteroids, ed. P. Michel, F. E. DeMeo, & W. F. Bottke, 221–241

Jewitt, D., & Luu, J. 1993, Nature, 362, 730

Jewitt, D. C. 2004, From cradle to grave: the rise and demise of the comets, ed. G. W. Kronk, 659–676

Jopek, T. J. 1993, Icarus, 106, 603

Jopek, T. J., Valsecchi, G. B., & Froeschlé, C. 2002, Asteroid Meteoroid Streams, ed. W. F. Bottke, Jr., A. Cellino, P. Paolicchi, & R. P. Binzel, 645–652

Keller, H. U., Britt, D., Buratti, B. J., & Thomas, N. 2004, In situ observations of cometary nuclei, ed. G. W. Kronk, 211–222

Kolokolova, L., Hanner, M. S., Levasseur-Regourd, A.-C., & Gustafson, B. Å. S. 2004, Physical properties of cometary dust from light scattering and thermal emission, ed. M. C. Festou, H. U. Keller, & H. A. Weaver, 577–604

Kuiper, G. P. 1951, Proceedings of the National Academy of Science, 37, 1

Lamy, P. L., Toth, I., Fernandez, Y. R., & Weaver, H. A. 2004, The sizes, shapes, albedos, and colors of cometary nuclei, ed. G. W. Kronk, 223–264

Lang, D., & Hogg, D. W. 2012, AJ, 144, 46

Levison, H. F. 1996, in Astronomical Society of the Pacific Conference Series, Vol. 107, Completing the Inventory of the Solar System, ed. T. Rettig & J. M. Hahn, 173–191

Levison, H. F., Dones, L., & Duncan, M. J. 2001, AJ, 121, 2253

Levison, H. F., & Duncan, M. J. 1994, Icarus, 108, 18

—. 1997, Icarus, 127, 13

Marshall, P. J., Lintott, C. J., & Fletcher, L. N. 2015, ARA&A, 53, 247

McIntosh, R. A. 1935, MNRAS, 95, 709

Milon, D. 1967, Journal of the British Astronomical Association, 77, 89

Molau, S., & Barentsen, G. 2014, in The Meteoroids 2013, Proceedings ot the Astronomical Conference held at A.M. University, Poznań, Poland, Aug. 26-30, 2013, Eds.: T.J. Jopek, F.J.M. Rietmeijer, J. Watanabe, I.P. Williams, A.M. University Press, 2014, p. 297-305, ed. T. J. Jopek, F. J. M. Rietmeijer, J. Watanabe, & I. P. Williams, 297–305

Mommert, M., Hora, J. L., Harris, A. W., et al. 2014, ApJ, 781, 25

Morbidelli, A., Chambers, J., Lunine, J. I., et al. 2000, Meteoritics and Planetary Science, 35, 1309

Murray, C. D., & Dermott, S. F. 1999, Solar system dynamics

Napier, W. M., Wickramasinghe, J. T., & Wickramasinghe, N. C. 2007, International Journal of Astrobiology, 6, 321

Newton, I. 1760, Philosophiae naturalis principia mathematica, vol. 1 - 4

Olmsted, D. 1834, American Journal of Science, 25, 354

Oort, J. H. 1950, Bull. Astron. Inst. Netherlands, 11, 91

Oort, J. H., & Schmidt, M. 1951, Bull. Astron. Inst. Netherlands, 11, 259

Öpik, E. J. 1963, Adv. Astron. Astrophys, 2, 219

Porubcan, V., Stohl, J., & Vana, R. 1992, in Asteroids, Comets, Meteors 1991, ed. A. W. Harris
    & E. Bowell, 473–476

Poynting, J. H. 1903, MNRAS, 64, 1

Rauch, K. P., & Hamilton, D. P. 2002, in Bulletin of the American Astronomical Society,
    Vol. 34, AAS/Division of Dynamical Astronomy Meeting #33, 938

Robertson, H. P. 1937, MNRAS, 97, 423

Samarasinha, N. H., Mueller, B. E. A., Knight, M. M., et al. 2015, Planet. Space Sci., 118, 127

Schiaparelli, G. V. 1867, MNRAS, 27, 246

Schleicher, D. G., & Farnham, T. L. 2004, Photometry and imaging of the coma with narrow-
    band filters, ed. M. C. Festou, H. U. Keller, & H. A. Weaver, 449–469

Sekanina, Z., & Chodas, P. W. 2002, ApJ, 581, 760

Southworth, R. B., & Hawkins, G. S. 1963, Smithsonian Contributions to Astrophysics, 7, 261

Steel, D. I. 1995, Earth Moon and Planets, 68, 13

Swings, P. 1943, MNRAS, 103, 86

Valsecchi, G. B., Jopek, T. J., & Froeschle, C. 1999, MNRAS, 304, 743

von Rosenvinge, T. T., Brandt, J. C., & Farquhar, R. W. 1986, Science, 232, 353

Weryk, R. J., Campbell-Brown, M. D., Wiegert, P. A., et al. 2013, Icarus, 225, 614

Whipple, F. L. 1950, ApJ, 111, 375

—. 1951, ApJ, 113, 464

—. 1983, IAU Circ., 3881, 1

Wiegert, P., & Tremaine, S. 1999, Icarus, 137, 84

Williams, I. P., & Fox, K. 1983, in Asteroids, Comets, and Meteors, ed. C.-I. Lagerkvist &
    H. Rickman, 399–409

Wurm, K. 1939, ApJ, 89, 312

Ye, Q., Brown, P. G., Campbell-Brown, M. D., & Weryk, R. J. 2013a, MNRAS, 436, 675

—. 2013b, MNRAS, 436, 675

Ye, Q., & Wiegert, P. A. 2014, MNRAS, 437, 3283

Ye, Q.-Z., & Hui, M.-T. 2014, ApJ, 787, 115

Ye, Q.-Z., Hui, M.-T., Brown, P. G., et al. 2016, Icarus, 264, 48

Yeomans, D. K., & Chamberlin, A. B. 2013, Acta Astronautica, 90, 3

Yeomans, D. K., Yau, K. K., & Weissman, P. R. 1996, Icarus, 124, 407

Chapter 2

Moderately active comet: the case of 15P/Finlay

A version of this chapter has been published as:

Ye, Quan-Zhi; Brown, Peter G.; Bell, Charles; Gao, Xing; Mašek, Martin; and Hui, Man-To (2015): Bangs and Meteors from the Quiet Comet 15P/Finlay. The Astrophysical Journal, Volume 814, Number 1.

2.1 Introduction

Small bodies in the inner solar system are historically classified based on their appearance. The term comet refers to an object in a heliocentric orbit with extended appearance and sometimes one or several tails; while asteroid refers to an object that is much smaller than the major planets and appears star-like. Classification by orbital dynamics of these bodies shows that the dynamical characteristics of the two groups of objects differ as well: comets usually possess highly elliptical, parabolic or hyperbolic orbits, while asteroids usually possess more circular orbits.

Bodies which deviate from these trends (i.e. comets in asteroidal orbits, or asteroids in

cometary orbits) are of significant interest, as their dynamical evolution and/or physical properties are apparently exceptional. Although the first such outlier was officially recognized no later than 1989 (e.g. the case of 95P/(2060) Chiron, c.f. Meech & Belton, 1989), most outliers were not found until recently with the commissioning of a number of near-Earth asteroid search/follow-up programs. Due to their distinct appearance, comet-like objects in asteroid-like orbits, or "active asteroids" (Jewitt, 2012), are more straightforward to recognize due to their significant morphological change during the transition to comet-like state, and so the recognition is usually robust. In contrast, their counterparts, asteroid-like objects in cometary orbits (ACOs), due to their nature, are considerably more difficult to identify. From an orbital perspective, ACOs are most easily interpreted to be comets that have exhausted their volatiles (or have their volatiles permanently buried below their crusts) so that they appear asteroidal, i.e. they become "dormant comets". However, dynamical studies have shown that a significant fraction of ACOs could be asteroids leaking out from the main-belt and temporarily residing in comet-like orbits (Tancredi, 2014; Fernández & Sosa, 2015), therefore complicating the effort to disentangle orbital properties from physical properties of these bodies.

One approach to identify dormant comets in the ACO population is to look at comets at an intermediate state between active comets and dormant comets, sometimes labeled as comet-asteroid transition objects (CATOs; e.g. Licandro et al., 2007). A handful of such objects have been suggested, such as 107P/(4015) Wilson-Harrington (Ishiguro et al., 2011), 209P/LINEAR (Ye & Wiegert, 2014) and (3552) Don Quixote (Mommert et al., 2014). However, these objects are usually faint and produce little dust, presenting a challenge for further investigation of their surface and dust properties.

15P/Finlay, a Jupiter-family comet (JFC), has been reportedly faint and tail-less since its discovery in 1886 (Kronk, 2004, 2008; Kronk & Meyer, 2010). The comet has a small Minimum Orbit Intersection Distance (MOID) of 0.0094 AU to the Earth's orbit, but has never been associated with any known meteor shower (Beech et al., 1999). Coupled with the fact that 15P/Finlay has shown a systematic decrease of maximum brightness at each perihelion pas-

sage in the past century it has been suggested that the comet is approaching a state of complete dormancy (Kresak & Kresakova, 1989).

However, during its current perihelion passage (2014–2015), 15P/Finlay exhibited two outbursts, each producing a parabolic "shell" around the original coma accompanied by a straight, freshly-formed "tail" in the anti-sunward direction. This resembles the historic outburst of 17P/Holmes in 2007 (Buzzi et al., 2007) albeit at a much smaller scale. However, it is notable that 17P/Holmes's outbursts took place at a larger heliocentric distance (2.4 AU) than those of 15P/Finlay ($\sim$ 1.0 AU), therefore the underlying mechanism may not be necessarily the same although the similarity of their overall appearances is striking.

The outbursts of 15P/Finlay are significant in another context: as an Earth-approaching comet, the outburst ejecta may find their way to the Earth, creating a meteor outburst. Previously, numerical simulations by Mikhail Maslov[1] have suggested that the material released in 2014 will have a direct encounter with the Earth in 2021, which may produce a meteor outburst with a Zenith Hourly Rate (ZHR) of up to 50. Recent calculations by Mikiya Sato[2] also arrived at similar results. An outburst from the parent comet may result in a stronger meteor event depending on the ejection velocity and planetary perturbations. Potential meteor observations allow us to directly sample materials from a dormant comet candidate without a dedicated space mission, which may help in understanding the comet itself as well as the dormant comets as a population. In particular, meteor activity from ACOs can help establish prior periods of activity and constrain the dust production history of ACOs.

In this work, we present an analysis of the observations of 15P/Finlay taken during the two 2014/2015 outbursts. The goal is to understand the underlying nature of the outburst as well as the evolutionary status of the comet. We also examine the yet-to-be-discovered Finlayid meteor shower and especially the potential 2021 meteor outburst. Non-detection of the shower places constraints on the past dust production history of 15P/Finlay.

---

[1] http://feraj.narod.ru/Radiants/Predictions/1901-2100eng/Finlayids1901-2100predeng.html, accessed 2015 Jan. 17.

[2] https://groups.yahoo.com/neo/groups/meteorobs/conversations/messages/44030, retrieved 2015 Mar. 4.
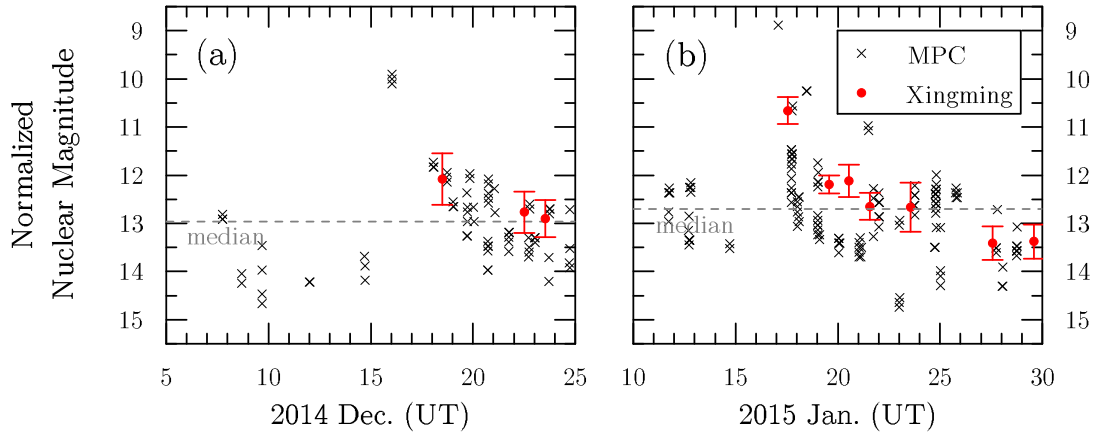
Figure 2.1 Nucleus magnitude of 15P/Finlay around the time of (a) the first outburst, and (b) the second outburst. The Minor Planet Center (MPC) magnitudes (plotted in crosses) are extracted from the Observations Database on the MPC website. The Xingming magnitudes (plotted in red dots) are derived from the monitoring observations by the Xingming 0.35-m telescope with aperture radius $\rho = 5000$ km. The magnitudes are normalized to $\Delta = r_{\rm h} = 1$ AU assuming a brightening rate $n = 4$ (Everhart, 1967).

2.2   Observations

2.2.1   Amalgamation of Outburst Reports

The first outburst of 15P/Finlay took place in the late hours of 2014 Dec. 15, the timing being constrained by reports from Christopher Wyatt (Walcha, Australia; Dec. 15.43 UT) and Slooh.com Chile Observatory (La Dehesa, Chile; Dec. 16.04 UT)[3]. During the outburst, the comet brightened by about 3 magnitudes and developed a spiky tail. The tail diluted into the background with the brightness returning to normal by Dec. 21–22 (Figure 2.1a, 2.2).

The second outburst took place around 2015 Jan. 16.0 UT as noted by Alan Hale (Cloudcroft, NM) at Jan. 16.07 who noted "very bright, almost star-like central condensation" that was absent in the earlier observations[4]. The last negative observation comes from the Solar

---

[3]Wyatt's observation is accessible through the Comet Observation Database (COBS), available at `http://www.cobs.si`; observation from Slooh.com Chile Observatory was published in the Minor Planet Circular No. 90932 (`http://www.minorplanetcenter.net/iau/ECS/MPCArchive/2015/MPC_20150105.pdf`). Both resources were accessed on 2015 Jan. 17.

[4]`https://groups.yahoo.com/neo/groups/comets-ml/conversations/messages/24322`, accessed on 2015 Jul. 17, as well as private communication with Alan Hale.
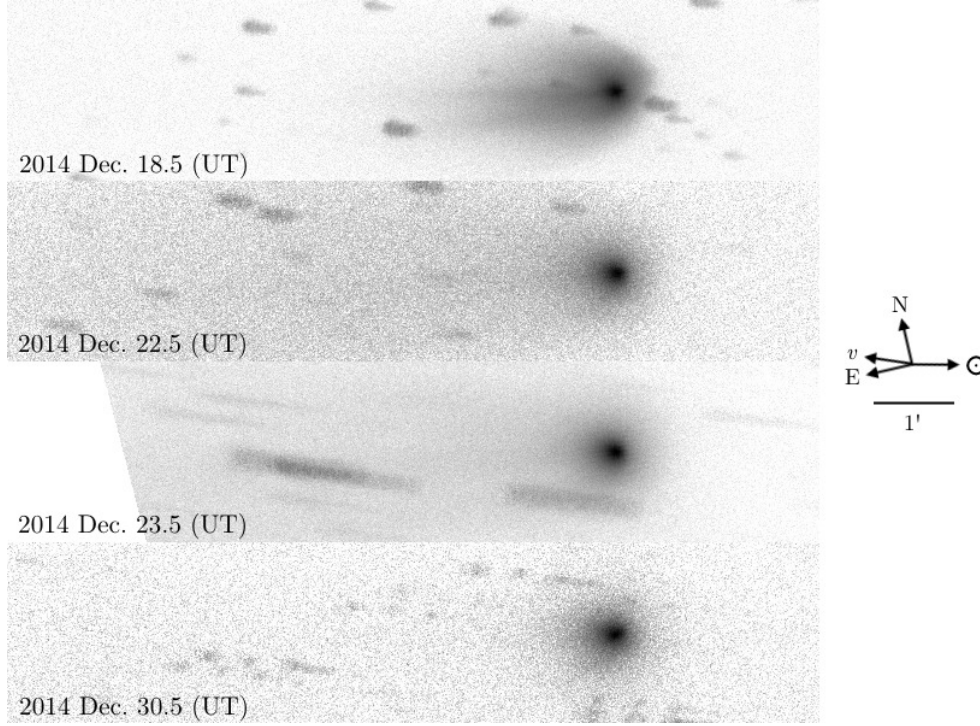
Figure 2.2 Composite images of 15P/Finlay for the first outburst as observed at Xingming Observatory. The images have been stretched in asinh scale. The scale bar shows the direction to the Sun, the comet's velocity vector and the directions of the plane of the sky.

Wind ANisotropies all-sky hydrogen Ly-α camera (SWAN) on-board the Solar and Heliospheric Observatory (SOHO) (Bertaux et al., 1995) around Jan. 15.5 UT[5]. The outburst was subsequently noted independently by Guo Zheng-Qiang (Shenyang, China; Jan. 16.43 UT) and Michael Mattiazzo (Swan Hill, Australia; Jan. 16.45 UT)[6], as well as on the SWAN image taken near Jan. 16.5 UT (next to the last non-detection image). The comet brightened by about 4–5 magnitudes during the second outburst, again with a freshly-formed tail. The brightness returned to the normal range around Jan. 20 (Figure 2.1b), but the tail lingered for a few more days until around Jan. 30 (Figure 2.3).

---

[5]`http://sohowww.nascom.nasa.gov/data/summary/swan/swan-images.html`), accessed on 2015 Feb. 9.

[6]Guo's observation was posted on `http://www.astronomy.com.cn/bbs/thread-305185-1-1.html` (in Chinese), Mattiazzo's report was posted on his Facebook page. Both resources were accessed on 2015 Jan. 17.
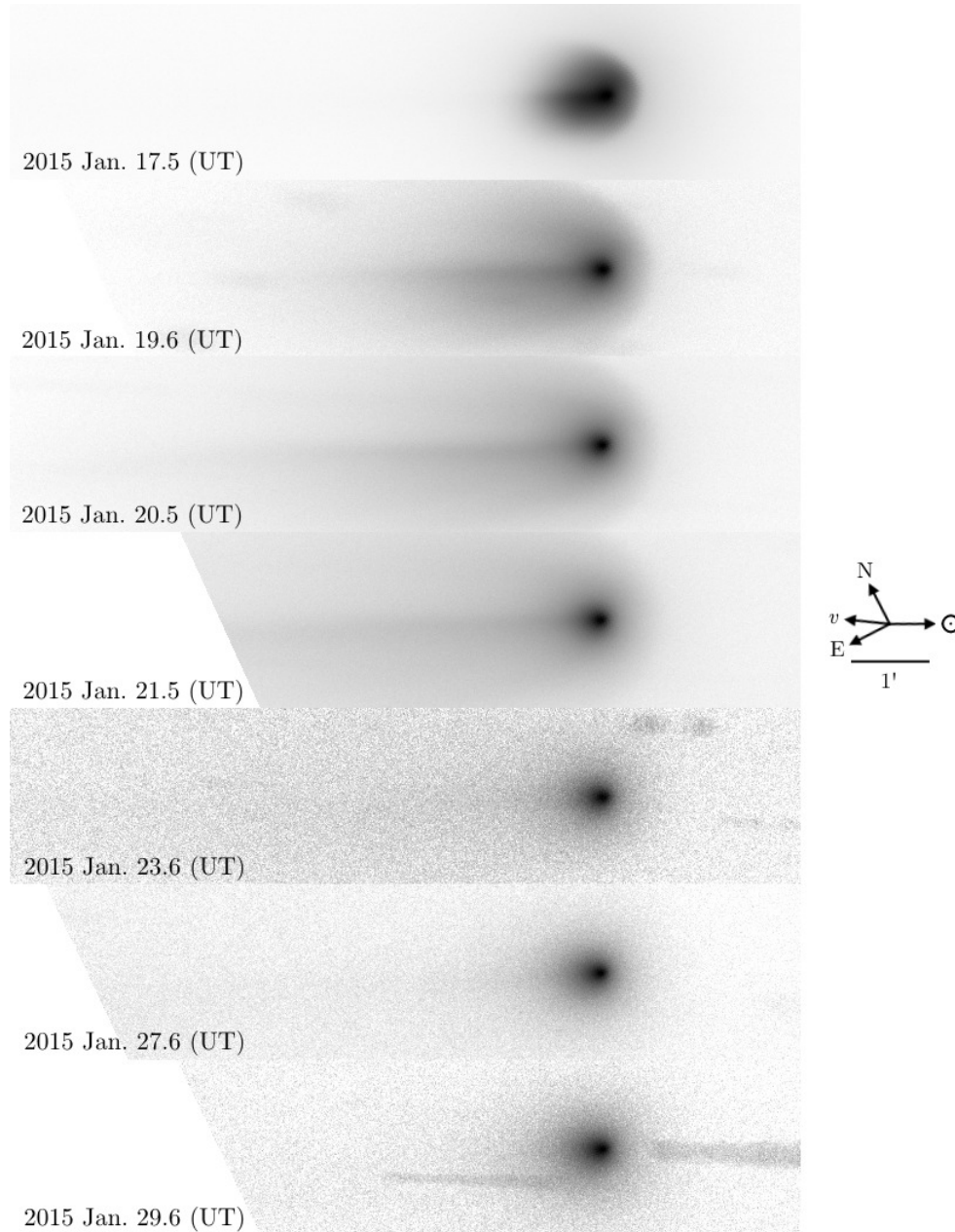
Figure 2.3 Composite images of 15P/Finlay images for the second outburst as observed at Xingming Observatory. The images have been stretched in asinh scale. The scale bar shows the direction to the Sun, the comet's velocity vector and the directions of the plane of the sky.

2.2.2 Observation and Image Processing

After receiving the reports of the outbursts, 15P/Finlay was monitored using the facilities at F(/Ph)otometric Robotic Atmospheric Monitor (FRAM) located at Pierre Auger Observatory (Argentina), Xingming Observatory (China) and Vicksburg (U.S.). The FRAM observations were conducted with a 0.3-m f/6.6 telescope equipped with a Kodak KAF-1603ME sensor, which gives a resolution of 0.93″; the Xingming observations were conducted with a 0.35-m f/6.9 telescope with a Kodak KAF-8300 sensor, images are binned by 2, which gives a resolution of 1.2″. The Vicksburg observations were conducted with a 0.3-m f/10 telescope equipped with Kodak KAF-1600 sensor which gives a resolution of 1.87″.

The observations at FRAM and Vicksburg are intended for dust modeling, as such they were conducted with a Cousins R filter that blocks flux from major cometary gaseous emissions (such as CN, C_2, C_3). The Xingming observations were conducted with wider temporal coverage but without a filter, intended as a continuous monitor of the development of the outburst. Details of the observations are summarized in Table A.1. The images are processed using standard procedures (bias subtraction, dark subtraction, flat division), with plate constants solved using the UCAC 4 catalog (Zacharias et al., 2013). The images are then median combined following the motion of the comet.

The composite images from FRAM and Vicksburg are collapsed into a 1-dimensional profile. This is necessary as the considerable irregularities of the near-nucleus dust (i.e. localized jets) complicate the modeling work. The orbital plane angle at the two outbursts were also shallow enough ($\sim 4°$) to minimize the information loss during the image collapse. The 1-dimensional profile is simply derived from averaging a 2′ wide strip along the Sun-comet axis, with the width of 2′ corresponding to the maximum width of the tail.

Date	Time[a] (UT)	Facility[b]	Total Exposure (min.)	Filter	r_h (AU)	Δ (AU)	Plane Angle
2014 Dec. 17	00:57	FRAM	8	R_C	0.987	1.472	4.3°
2014 Dec. 18	00:57	FRAM	8	R_C	0.985	1.467	4.3°
2014 Dec. 18	12:01	Xingming	10	Unfiltered	0.984	1.465	4.3°
2014 Dec. 22	12:10	Xingming	24	Unfiltered	0.978	1.446	4.5°
2014 Dec. 23	12:18	Xingming	51	Unfiltered	0.977	1.442	4.5°
2014 Dec. 30	12:20	Xingming	26	Unfiltered	0.977	1.416	4.7°
2015 Jan. 17	12:43	Xingming	83	Unfiltered	1.025	1.394	4.7°
2015 Jan. 18	00:30	Vicksburg	3	R_C	1.023	1.393	4.7°
2015 Jan. 19	00:18	Vicksburg	6	R_C	1.028	1.395	4.6°
2015 Jan. 19	13:41	Xingming	16	Unfiltered	1.035	1.396	4.6°
2015 Jan. 20	12:53	Xingming	91	Unfiltered	1.040	1.397	4.6°
2015 Jan. 21	00:44	Vicksburg	6	R_C	1.042	1.398	4.7°
2015 Jan. 21	13:13	Xingming	88	Unfiltered	1.045	1.399	4.6°
2015 Jan. 23	13:29	Xingming	17	Unfiltered	1.055	1.403	4.6°
2015 Jan. 27	13:19	Xingming	88	Unfiltered	1.078	1.415	4.3°
2015 Jan. 29	13:32	Xingming	68	Unfiltered	1.091	1.422	4.2°

Table 2.1: Summary of the imaging observations.

2.3 Analysis

2.3.1 General Morphology and Evolution of the Outbursts

The composite images from the monitoring observations at Xingming (Figure 2.2 and 2.3) show that the morphologies and evolution of both outbursts are comparable: both outbursts produced a newly-formed dust shell that is slightly asymmetric with respect to the comet-Sun axis; the dust shell expands as time goes by and fades into the background within ∼ 1 week.

We perform aperture photometry with the Xingming data. This is motivated by the considerable scatter shown on the magnitudes provided by the Minor Planet Center (MPC)[7], possibly due to different instrumental and measurement settings adopted by different observers. Data from FRAM and Vicksburg is not used at this stage to avoid the complication due to instrumental differences. We use an aperture of $\rho = 5000$ km as projected at the distance of the comet centered at the nucleus. Both 0.35-m and MPC magnitudes are reduced to "normalized"

---

[7]Available from the MPC Observations Database, `http://www.minorplanetcenter.net/db_search`, retrieved 2015 Feb. 3.

magnitudes at $r_h = \Delta = 1$ AU using $M_n = m_n - 5 \log \Delta - 2.5n \log r_h$, where M_n and m_n are normalized and observed nuclear magnitudes, r_h and Δ are heliocentric and geocentric distances in AU, and $n = 4$ is the canonical brightening rate exponent (Everhart, 1967). The photometric calibration is performed using the V-band data from the AAVSO All-Sky Photometric Survey (APASS) catalog (Henden et al., 2012) as the Xingming system is most sensitive at V-band. As shown in Figure 2.1, the characteristic outburst decay time (i.e. the time elapsed from the peak of the outburst to the point that the brightness reaches $1/e$ of the peak brightness) is estimated to be at the order of 1 d.

2.3.2 Dust Model and Kinematics of the Ejecta

To understand the dust produced by the outburst event, we model the observations using a Monte Carlo dust model developed in our earlier works (e.g. Ye & Hui, 2014; Ye et al., 2016).

The dynamical evolution of the cometary dust is controlled by the ratio between radiation pressure and solar gravity, $\beta_{rp} = 5.7 \times 10^{-4}/(\rho_d a_d)$, where ρ_d is the bulk density of the dust and a_d the diameter of the dust, both in SI units (Wyatt & Whipple, 1950), as well as the initial ejection velocity of the dust. The latter is defined as

$$v_{ej} = V_0 \beta_{rp}^{1/2} \cdot v \tag{2.1}$$

where V_0 is the mean ejection speed of a dust particle of $\beta_{rp} = 1$ and v follows a Gaussian probability density function:

$$P(v) = \mathcal{N}(1, \sigma_v^2) \tag{2.2}$$

where σ_v is the standard deviation of v, used to account for the physical spread v due to the shape of the dust particles. In this work we use $\sigma_v = 0.3$ following exploration by, e.g. Ishiguro et al. (2014); Jewitt et al. (2014) and Ye et al. (2016).

We assume the dust size follows a simple power-law with a differential size index of q, and

that observed flux is solely contributed by scattered light from the dust particles. Hence, the dust production rate is expressed as

$$N(r_{\mathrm{h}}, a_{\mathrm{d}}) \mathrm{d}a_{\mathrm{d}} = N_0 \left(\frac{a_{\mathrm{d}}}{1\ \mu\mathrm{m}} \right)^{-q} \mathrm{d}a_{\mathrm{d}} \tag{2.3}$$

where N_0 is the mean dust production rate of 1 μm particles.

Simulated particles are symmetrically released from the nucleus. For both outbursts, two possible outburst epochs are tested, each corresponding to either the epochs of the last negative (non-outburst) report or the first positive report. For the first outburst, outburst epochs of 2014 Dec. 15.4 UT (as indicated by Wyatt's negative report) and 16.0 UT (indicated by Slooh.com's positive report) are tested; for the second outburst, outburst epochs of 2015 Jan. 15.5 UT (indicated by SOHO/SWAN's negative report) and 16.0 UT (indicated by Hale's positive report) are tested. The production rate peaks at the outburst epoch and decays exponentially at a characteristic time of 1 d as discussed in § 2.3.1.

The size distribution is set to the interval of $\beta_{\mathrm{rp,max}} = 1$ to an upper size limit constrained by the escape speed $v_{\mathrm{esc}} = \sqrt{2GM_{\mathrm{n}}/R_{\mathrm{G}}}$ where $M_{\mathrm{n}} = \frac{4}{3}\pi R_{\mathrm{n}}^3 \rho_{\mathrm{N}}$ is the total mass of the nucleus, $\rho_{\mathrm{n}} = 500\ \mathrm{kg \cdot m^{-3}}$ the bulk density of the nucleus, $R_{\mathrm{n}} = 0.92$ km the effective nucleus radius (Fernández et al., 2013), and $R_{\mathrm{G}} = 10R_{\mathrm{n}}$ the characteristic distance where gas drag becomes negligible (Gombosi et al., 1986). We only consider $\beta_{\mathrm{rp,max}} = 1$ as (1) optical observations are most sensitive to $\beta_{\mathrm{rp}} \sim 1$ (micron-sized) particles; (2) larger particles stay closer to the nucleus (where the gravitational force dominates), models with $\beta_{\mathrm{rp,max}} \ll 1$ are incompatible with the observations as they are not able to reproduce the obscured extended dust tails; and (3) complications arise for the dynamics of $\beta_{\mathrm{rp,max}} \gg 1$ (submicron-sized) particles as these are also subjected to Lorentz forces.

We use the MERCURY6 package (Chambers, 1999) to integrate particles from the start epoch (i.e. the outburst epoch) to the observation epoch, using the 15th order RADAU integrator (Everhart, 1985). To accommodate the uncertainty in the exact epoch of the outburst, multiple outburst epochs, cued by the reports discussed in § 2.2.1, are tested in the simulation.

Parameter	Value
Semimajor axis a	3.48762 AU
Eccentricity e	0.72017
Inclination i	6.79902°
Longitude of the ascending node Ω	13.77506°
Argument of perihelion ω	347.55924°
Epoch of perihelion passage t_p	2014 Dec. 27.05599 UT
Total magnitude H	10.7
Non-grav. radial acceleration parameter A_1	4.075×10^{-9} AU/d^2
Non-grav. transverse acceleration parameter A_2	5.744×10^{-11} AU/d^2
Nucleus radius R_n	0.9 km
Nucleus bulk density ρ_n	500 kg $\cdot$ m^{-3} (assumed)
Dust bulk density ρ_d	1000 kg $\cdot$ m^{-3} (assumed)
Minimum dust size $\beta_{rp,max}$	1.0

Table 2.2: General parameters for the dust model. The orbital elements are quoted from the JPL elements K085/15. The nucleus radius is reported by Fernández et al. (2013).

The production of simulated particles peaks at the assumed outburst epoch and decays exponentially afterwards, with a characteristic decay time of 1 d as found earlier in § 2.3.1. Gravitational perturbations from the eight major planets (the Earth-Moon system is represented by a single mass at the barycenter of the two bodies), radiation pressure and Poynting-Robertson effect are included in the integration. 15P/Finlay's orbital elements are extracted from the JPL small body database elements K085/15 (`http://ssd.jpl.nasa.gov/sbdb.cgi`) as listed in Table 3.3.

The resulting modeled image is convolved with a 2-dimensional Gaussian function (with FWHM equal to the FWHM of the actual images) to mimic observational effects such as the instrumental point spread function effect and atmospheric seeing. The modeled image is then collapsed into a 1-dimensional profile as done with the observations (§ 2.2.2). Observed and modeled surface brightness profiles are normalized to 3 FWHMs beyond the nucleus along the Sun-comet axis. We mask out the region within 1 FWHM from the nucleus to avoid contamination of the signal from the nucleus. The region that is dominated by submicron-sized dust (i.e. the tailward region that is too far from the nucleus for > 1 μm dust to reach) is also masked, as we focus on μm to mm-sized dust. To evaluate the degree of similarity between

	Outburst Epoch (UT)	Observation Epoch (UT)	V_0 $\mathrm{m \cdot s^{-1}}$	q
Test grids	-	-	100 to 1200 in steps of 20	-5.4 to -2.0 in steps of 0.1
1$^{\mathrm{st}}$ Outburst	2014 Dec. 15, 10 h	2014 Dec. 17	320 ± 10	-3.7 ± 0.2
	..	2014 Dec. 18	320 ± 20	-3.0 ± 0.3
	2014 Dec. 16, 0 h	2014 Dec. 17	640 ± 30	-4.0 ± 0.6
	..	2014 Dec. 18	670 ± 90	-3.7 ± 0.5
2$^{\mathrm{nd}}$ Outburst	2015 Jan. 15, 12 h	2015 Jan. 18	540 ± 40	-3.6 ± 0.6
	..	2015 Jan. 19	590 ± 120	-3.4 ± 0.5
	..	2015 Jan. 21	570 ± 30	-3.6 ± 0.6
	2015 Jan. 16, 0 h	2015 Jan. 18	780 ± 30	-3.8 ± 0.5
	..	2015 Jan. 19	670 ± 100	-3.6 ± 0.5
	..	2015 Jan. 21	750 ± 40	-3.4 ± 0.4

Table 2.3: Best-fit dust models for the FRAM and Vicksburg observations.

the observed and the modeled profiles, we calculate the normalized error variance (NEV) as defined by

$$\mathrm{NEV} = \frac{1}{n} \sum_{i=1}^{n} \frac{\sqrt{(\mathbf{M}_i - \mathbf{O}_i)^2}}{\mathbf{O}_i} \qquad (2.4)$$

where n is the number of pixels, $\mathbf{M}_i$ and $\mathbf{O}_i$ are the pixel brightness from the modeled and observed brightness profile respectively. We set the tolerance level of NEV to 10%. The input parameters, test grids and best-fit results are tabulated in Table 3.3, 2.3 and Figure 2.4.

It is encouraging that the best-fit models under the respective outburst epochs are largely consistent. We conclude that the characteristic ejection speed V_0 = 300 to 650 $\mathrm{m \cdot s^{-1}}$ for the ejecta of the first outburst, while V_0 = 550 to 750 $\mathrm{m \cdot s^{-1}}$ for the ejecta of the second outburst. The dust size index is at the range of $q \approx 3.5$. The ejection speed is comparable or is slightly larger than the one derived from the classic Whipple (1950) model (which gives $V_0 \sim 400 \mathrm{m \cdot s^{-1}}$ in our model), while the size index is comparable to the classic value, $q = 3.6$ (Fulle, 2004). It also appears that the characteristic ejection speed of the second outburst is higher than that of the first outburst, which seemingly supports the idea that the second outburst was a more energetic event than the first one.
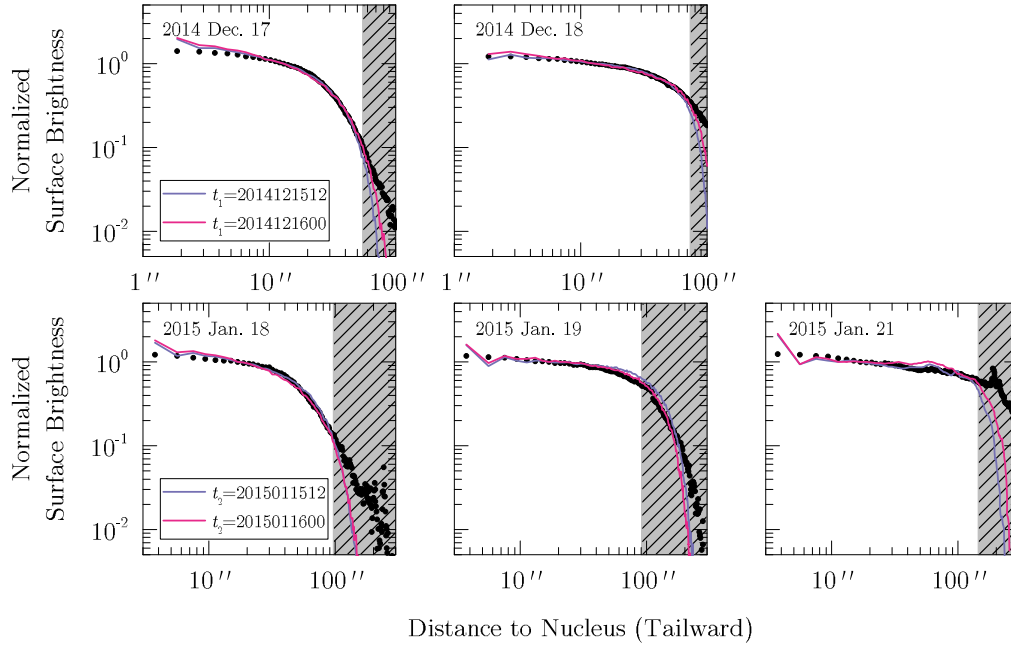
Figure 2.4 Observed surface brightness profiles (scatter dots) and the best-fit dust models (color lines) for FRAM and Vicksburg observations. The assumed outburst epochs (see main text) are denoted as t_1 for the first outburst and t_2 for the second outburst. The regions that are dominated by submicron-sized particles are masked away from the modeling as described in the main text. For the profile on 2015 Jan. 19 an additional region is masked due to contamination from a background star.

2.4 Discussion

2.4.1 Nature of the Outburst

The total mass of the dust emitted in the two outbursts are related to the effective scattering cross-section of the materials, C_e, that can be calculated by

$$C_e = \left(\frac{r_h}{1 \text{ AU}}\right)^2 \frac{\pi \Delta^2}{A_\lambda(\alpha)} 10^{0.4(m_{\odot,\lambda} - m_\lambda)} \tag{2.5}$$

where $A_\lambda(\alpha)$, the phase angle corrected geometric albedo, is calculated using the compound Henyey-Greenstein model by Marcus (2007), assuming $A_\lambda(0°) = 0.05$, and $m_{\odot,\lambda}$, m_λ are the apparent magnitudes of the Sun and the comet. This yields $C_e = 7 \times 10^3$ km^2 for the first outburst and $C_e = 2 \times 10^4$ km^2 for the second outburst, using the photometric measurements in Figure 2.1. The total mass of the ejecta can then be calculated via $M_d = \frac{4}{3}\rho_d \bar{a}_d C_e$, where the mean dust size $\bar{a}_d$ can be derived from the dust model discussed in § 2.3.2. Considering the variances among the best-fit models, we derive $M_d = 2$ to 3×10^5 kg for the first outburst and $M_d = 4$ to 5×10^5 kg for the second outburst (depending on the exact timing of the individual outburst), corresponding to less than 10^{-7} of the nucleus mass assuming a spherical nucleus.

With this mass, the specific energy of the two outbursts is calculated to be 0.3 to 2×10^5 J · kg^{-1} using the speed component derived from the dust model. This value is comparable to the value derived for 17P/Holmes's 2007 outburst ($\sim 10^5$ J · kg^{-1}, c.f. Reach et al., 2010; Li et al., 2011). For the case of 17P/Holmes, the large distance to the Sun at the time of its outburst, as well as the closeness of the derived specific energy to the specific energy of the amorphous ice to crystalline, are compatible with the idea that the comet's mega-outburst was triggered by the energy released by the crystallization of amorphous ice. However, 15P/Finlay was much closer to the Sun at its two outbursts than 17P/Holmes at its 2007 outburst (1.0 AU versus 2.5 AU) such that solar heat may be sufficient to drive the outburst to some degree, hence we consider it difficult to assess the role of crystallization for 15P/Finlay's outburst at this stage.

2.4.2   The Finlayid Puzzle Revisited

15P/Finlay is puzzling in the sense that despite its occasional proximity to the Earth's orbit, the hypothetical Finlayid meteor shower has never been observed. This matter has been discussed in depth by Beech et al. (1999), who concluded that the perturbation of Jupiter has effectively dispersed the meteoroid stream, such that $\gtrsim$ 99% of the meteoroids released $\sim$ 20 orbits ago would end up with distant *nodal* passages (> 0.01 AU) from the Earth's orbit. However, we think that this conclusion is unconvincing as the nodal plane approximation for Earth impact may not be valid for 15P/Finlay due to its shallow orbital plane ($i = 6.8°$). Additionally, new astrometric observations of 15P/Finlay in the last decade have reduced the uncertainty of the orbital elements by an order of magnitude; hence the issue of the long term evolution of the Finlayid meteoroid stream is worth revisiting.

We first investigate the orbital stability of 15P/Finlay. This is done by generating 100 clones of 15P/Finlay using the orbital covariance matrix provided in JPL K085/15, and integrating all of them 10^3 yr backwards. The integration is performed with MERCURY6 using the Bulirsch-Stoer integrator. The evolution of the perihelion distance of all clones is shown in Figure 2.5. It can be seen that the perihelion distance of the clones are highly compact until 1613 A.D., when a close encounter (miss distance of the order of 0.1 AU) between 15P/Finlay and Jupiter occurred. This implies that any backward meteoroid stream simulation will be physically meaningful only as long as the starting date is after 1613 AD.

Next, we simulate a total of 39,000 (a randomly chosen number) hypothetical particles released by 15P/Finlay during its 1886, 1909 and 1960 perihelion passage and examine their distribution in 2001, to directly compare to Beech et al. (1999)'s simulations. The simulation is performed using the same collection of subroutines described in § 2.3.2 except that the ejection model by Crifo & Rodionov (1997) is used and only $\beta_{\mathrm{rp}} = 0.001$ (millimeter-sized) particles are simulated. The Minimum Orbit Intersection Distance vector $\overrightarrow{MOID}$ between the Earth and each meteoroid is calculated using the subroutine developed by Gronchi (2005) to assess the likelihood of an Earth encounter. The original MOID is defined as a scalar; here I define the
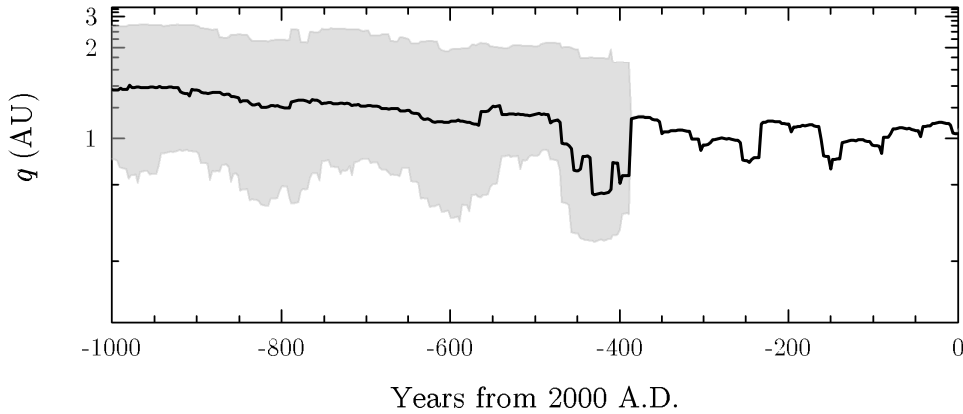
Figure 2.5 Dynamical evolution of the perihelion distance of 100 clones of 15P/Finlay in the interval of 1000–2000 A.D.

direction of $\overrightarrow{MOID}$ to be the same as $r_{\mathrm{D}} - r_{\mathrm{E}}$, where r_{D}, r_{E} are the heliocentric distance of the meteoroid and the Earth at the MOID point. We find as much as $\sim 15\%$ of the particles stay within 0.01 AU from the Earth's orbit as of 2001, different from Beech et al. (1999)'s finding. In addition, the dust trail is able to overlap with the Earth's orbit (Figure 2.6), further supporting the idea that a significant number of particles released by 15P/Finlay 10–20 orbits ago may still have direct encounters with the Earth.

The background meteoroid flux originating from 15P/Finlay may be estimated in an order-of-magnitude manner. The absolute magnitude of 15P/Finlay is ~ 100 times brighter than low-activity comet 209P/LINEAR for which the meteoroid production capacity has been measured to be 10^{14} meteoroids per orbit (Ye et al., 2016). Hence, in 10 orbits, 15P/Finlay would generate 10^{17} meteoroids. Assuming the meteoroids distribute uniformly along the orbit with an orbital period of 5 yr, as well as a delivery efficiency of 10% to the region ± 0.01 AU from the Earth's orbit and a characteristic duration of meteor activity of 1 week, the flux can be calculated by $10^{17} \times 10\% \times 7\,\mathrm{d}/5\,\mathrm{yr} \approx 0.1\ \mathrm{km}^{-2} \cdot \mathrm{hr}^{-1}$, which should be detectable by modern meteor survey systems.

To look for any undetected Finlayid activity, we conduct a "cued" search in the Canadian Meteor Orbit Radar (CMOR) database. CMOR is an interferometric radar array located near
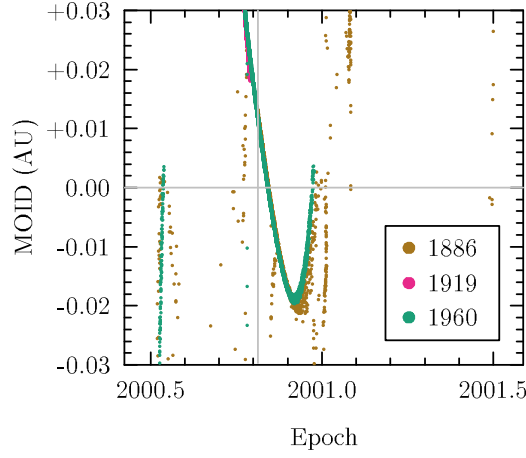
Figure 2.6 The distribution of the dust trails released by 15P/Finlay during its 1886, 1909 and 1960 perihelion passages in 2001. Vertical gray line marks the time that the Earth passes the trails. It can be seen that the trails cross the Earth's orbit, suggestive of the possibility of a direct encounter with the Earth.

London, Canada operating at 29.85 MHz with a pulse repetition frequency of 532 Hz (c.f. Jones et al., 2005; Brown et al., 2008; Ye et al., 2013). Since its commissioning in 2002, CMOR has measured 12 million meteoroid orbits, making it suitable for the search for weak meteor showers such as the Finlayids. We first calculate the characteristics of the hypothetical Finlayid radiant using the simulation results above, which yields $\lambda - \lambda_\odot = 66° \pm 11°, \beta = -18° \pm 9°$ at Sun-centered ecliptic coordinates, and a geocentric speed of 13 ± 3 km $\cdot$ s^{-1}. We then combine 14 years of CMOR data into a stacked "virtual" year and look for any enhanced activity at the location of the theoretical radiant, using a wavelet-based search algorithm (Brown et al., 2008, 2010) with probe sizes tuned to the expected radiant characteristics (radiant probe size $\sigma_{\rm rad} = 10°$, velocity probe size $\sigma_{\rm v} = 3$ km $\cdot$ s^{-1}).

As shown in Figure 2.7, no significant enhancement can be found at the expected period of activity (solar longitude $\lambda_\odot \sim 210°$). Ye et al. (2016) has calculated that the detection limit for the wavelet algorithm applied on CMOR is at the order of 0.01 km$^{-2} \cdot$ hr^{-1}; however, CMOR sensitivity is also an order of magnitude less at a southerly radiant at $\delta = -40°$ compared to northerly radiants, so the shower flux limit is probably closer to 0.1 km$^{-2} \cdot$ hr^{-1}. Hence, the
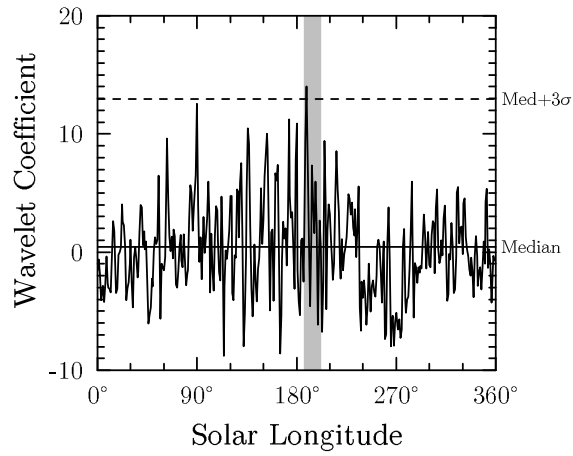
Figure 2.7 The variation of the wavelet coefficient at the calculated Finlayid radiant $\lambda - \lambda_\odot = 66°, \beta = -25°, v_G = 13 \text{ km} \cdot \text{s}^{-1}$ using the stacked "virtual year" CMOR data. The shaded area is the expected time window for Finlayid activity (solar longitude $\lambda_\odot \sim 193°$).

existence and intensity (or derived upper-limit) of the Finlayid meteor shower is not definitive,

but favors southern hemisphere meteor surveys (e.g. Younger et al., 2012; Janches et al., 2013).

2.4.3   The 2021 Earth Encounter of the 2014/2015 Outburst Ejecta

The potential 2021 encounter with the 2014 trail from 15P/Finlay is of particular interest given

the additional dust released from the two outbursts, as it offers an excellent opportunity to

examine 15P/Finlay's ejecta. The encounter is studied by simply extending the numerical

integration described in § 2.3.2 to the year 2021. Similar to the meteoroid trail model presented

in Ye et al. (2016), we assigned a *space criterion* to select Earth-approaching meteoroids,

defined by

$$\Delta X = v_{\text{rel}} \times \Delta T \tag{2.6}$$

where v_{rel} is the relative velocity between the meteoroid and the Earth and ΔT is called the

time criterion that is the characteristic duration of the event, typically $\Delta T = 1$ d. Similar to the

dust model discussed in § 2.3.2, we test two sets of outburst epochs that correspond to either

	Peak Time (UT)	Radiant α_g, δ_g	v_g km·s^{-1}	Note hr^{-1}
Maslov[a]	2021 Oct. 7, 1:19	255.8°, −48.3°	10.7	ZHR 5–50
Sato[b]	2021 Oct. 7, 1:10	255.7°, −48.4°	10.7	-
Vaubaillon[c]	-	-	-	No encounter
This work	2021 Oct. 7, 0:34–1:09[d]	255.6°, −48.4°	10.7	Ejecta from the first outburst
	2021 Oct. 6, 21:59–22:33[e]	256.3°, −48.5°	10.7	Ejecta from the second outburst

Table 2.4: Predictions of the 2021 encounter of 15P/Finlay's 2014 meteoroid trails.
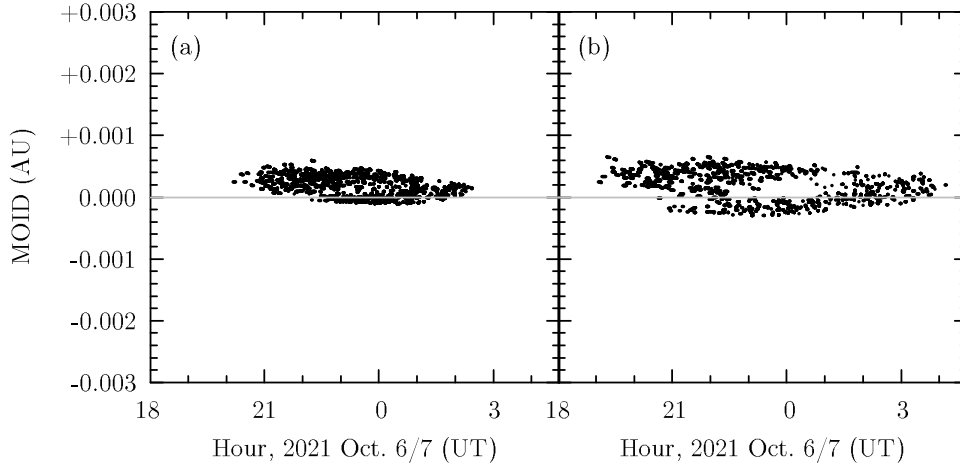
Figure 2.8 Encounter of 15P/Finlay's 2014/2015 outburst ejecta in 2021 Oct. 6/7. Subfigure (a) corresponds to the simulation results assuming the earliest possible outburst epoch (2014 Dec. 15.4 UT for the first outburst, 2015 Jan. 15.5 UT for the second outburst), while (b) corresponds to the results assuming the latest possible outburst epoch (2014 Dec. 16.0 UT for the first outburst, 2015 Jan. 16.0 UT for the second outburst).

the epochs of the last non-outburst report or the first positive report.

The simulation result confirms the general findings by Maslov and Sato, that a direct encounter of the 2014/2015 meteoroid trail will occur on 2021 Oct. 6/7 (Table 2.4, Figure 2.8) with a full-width-half-maximum (FWHM) of about 1 hour. The uncertainty in outburst epochs results in about 0.5 hour uncertainty in the peak time in 2021. The ejecta from the second outburst are calculated to arrive around 2021 Oct. 6 at 22 h UT, followed by those from the first outburst which are expected to arrive around 2021 Oct. 7 at 1 h UT. The radiant is at geocentric equatorial coordinates of $\alpha_g = 257°$, $\delta_g = −48°$ or in the constellation of Ara, favoring the observers in the southern tip of Africa. As 15P/Finlay was ∼ 20 times more active during the two outbursts compared to its normal dust production level as indicated by Figure 2.1, the meteor

activity may also be significantly stronger than previously expected. However, we also note that the range of the meteoroid sizes delivered to the Earth's vicinity seems to be concentrated at the order of $\beta_{rp} \sim 0.001$, which translates to a visual magnitude of +8 (Campbell-Brown & Koschny, 2004) considering the very low encounter speed. This indicates that the meteor activity in 2021 may only be visible to meteor radars and low-light video cameras.

2.5　Summary

We present an analysis of the two outbursts of the potentially comet-asteroid transition object, 15P/Finlay, at its 2014/2015 perihelion passage. These outbursts took place between 2014 Dec. 15.4–16.0 UT and 2015 Jan. 15.5–16.0 UT as constrained by ground-based and spacecraft observations. As seen in monitoring images, both outbursts produced a newly-formed dust shell that expands and fades in ~ 1 week.

The images from five observing nights (two for the first outburst, three for the second outburst) were studied using a Monte Carlo dust model, and yield a characteristic ejection speed of $V_0 = 300$ to $650 \, \mathrm{m \cdot s^{-1}}$ for the ejecta of the first outburst and $V_0 = 550$ to $750 \, \mathrm{m \cdot s^{-1}}$ for that of the second outburst, taking into account the uncertainty in the determination of outburst epoch. The dust size index is in the range of $q \approx -3.5$. We derive the mass of the ejecta to be $M_d = 2$ to 3×10^5 kg for the first outburst and $M_d = 4$ to 5×10^5 kg for the second outburst, corresponding to less than 10^{-7} of the nucleus mass. The specific energy of the two outbursts is calculated to be 0.3 to $2 \times 10^5 \, \mathrm{J \cdot kg^{-1}}$, comparable to the specific energy produced by the crystallization of amorphous ice, but does not prove the latter as the driving force for 15P/Finlay's outbursts.

We also revisited the long-standing puzzle of the non-detection of the Finlayids, the hypothetical meteor shower generated by 15P/Finlay, as well as the future possibility for meteor activity generated by the 2014/2015 outbursts. We find the efficiency of meteoroid delivery to the Earth's orbit is ~ 10 times higher than previously reported by Beech et al. (1999). As-

suming 15P/Finlay's recent (last ~ 20 orbits) activity is comparable to its contemporary level, the meteoroid flux of the Finlayids should be high enough to be detected by modern meteor surveys. However, a cued search with the 12 million meteor orbits gathered by the Canadian Meteor Orbit Radar over the past 13 years does not reveal any positive detection. The encounter with the 2014/2015 outburst ejecta may provide an answer to the Finlayid puzzle, as the Earth is expected to pass though the ejecta trails directly around 2021 Oct. 6 at 22 h UT to Oct. 7 at 1 h UT, with a chance for some significant meteor activity in the video or radio range. The timing and the southerly radiant in the constellation of Ara will favor observers in the southern tip of Africa.

The recent outburst episode of 15P/Finlay seems to suggest that the comet, originally thought to be quiet and largely inactive, does possess the ability for significant activity. Whether the recent outbursts are the overtures of a resurrection of the comet or a finale of its career remains to be seen. Cometary observations in the forthcoming perihelion passage in July 2021, as well as observations during the potential meteor outburst, will likely provide more information.

Acknowledgements

Bibliography

Beech, M., Nikolova, S., & Jones, J. 1999, MNRAS, 310, 168

Bertaux, J. L., Kyrölä, E., Quémerais, E., et al. 1995, Sol. Phys., 162, 403

Brown, P., Weryk, R. J., Wong, D. K., & Jones, J. 2008, Icarus, 195, 317

Brown, P., Wong, D. K., Weryk, R. J., & Wiegert, P. 2010, Icarus, 207, 66

Buzzi, L., Muler, G., Kidger, M., et al. 2007, IAU Circ., 8886, 1

Campbell-Brown, M. D., & Koschny, D. 2004, A&A, 418, 751

Chambers, J. E. 1999, MNRAS, 304, 793

Crifo, J. F., & Rodionov, A. V. 1997, Icarus, 127, 319

Everhart, E. 1967, AJ, 72, 716

Everhart, E. 1985, in Dynamics of Comets: Their Origin and Evolution, Proceedings of IAU
    Colloq. 83, held in Rome, Italy, June 11-15, 1984. Edited by Andrea Carusi and Giovanni B.
    Valsecchi. Dordrecht: Reidel, Astrophysics and Space Science Library. Volume 115, 1985,
    p.185, ed. A. Carusi & G. B. Valsecchi, 185

Fernández, J. A., & Sosa, A. 2015, IAU General Assembly, 22, 44024

Fernández, Y. R., Kelley, M. S., Lamy, P. L., et al. 2013, Icarus, 226, 1138

Fulle, M. 2004, Motion of cometary dust, ed. M. C. Festou, H. U. Keller, & H. A. Weaver,
    565–575

Gombosi, T. I., Nagy, A. F., & Cravens, T. E. 1986, Reviews of Geophysics, 24, 667

Gronchi, G. F. 2005, Celestial Mechanics and Dynamical Astronomy, 93, 295

Henden, A. A., Levine, S. E., Terrell, D., Smith, T. C., & Welch, D. 2012, Journal of the American Association of Variable Star Observers (JAAVSO), 40, 430

Ishiguro, M., Ham, J.-B., Tholen, D. J., et al. 2011, ApJ, 726, 101

Ishiguro, M., Jewitt, D., Hanayama, H., et al. 2014, ApJ, 787, 55

Janches, D., Hormaechea, J. L., Brunini, C., Hocking, W., & Fritts, D. C. 2013, Icarus, 223, 677

Jewitt, D. 2012, AJ, 143, 66

Jewitt, D., Ishiguro, M., Weaver, H., et al. 2014, AJ, 147, 117

Jones, J., Brown, P., Ellis, K. J., et al. 2005, Planet. Space Sci., 53, 413

Kresak, L., & Kresakova, M. 1989, Bulletin of the Astronomical Institutes of Czechoslovakia, 40, 269

Kronk, G. W. 2004, Cometography

—. 2008, Cometography

Kronk, G. W., & Meyer, M. 2010, Cometography . Volume 5, 1960-1982: A Catalog of Comets

Li, J., Jewitt, D., Clover, J. M., & Jackson, B. V. 2011, ApJ, 728, 31

Licandro, J., Campins, H., Mothé-Diniz, T., Pinilla-Alonso, N., & de León, J. 2007, A&A, 461, 751

Marcus, J. N. 2007, International Comet Quarterly, 29, 39

Meech, K. J., & Belton, M. J. S. 1989, IAU Circ., 4770, 1

Mommert, M., Hora, J. L., Harris, A. W., et al. 2014, ApJ, 781, 25

Reach, W. T., Vaubaillon, J., Lisse, C. M., Holloway, M., & Rho, J. 2010, Icarus, 208, 276

Tancredi, G. 2014, Icarus, 234, 66

Whipple, F. L. 1950, ApJ, 111, 375

Wyatt, S. P., & Whipple, F. L. 1950, ApJ, 111, 134

Ye, Q., Brown, P. G., Campbell-Brown, M. D., & Weryk, R. J. 2013, MNRAS, 436, 675

Ye, Q., & Wiegert, P. A. 2014, MNRAS, 437, 3283

Ye, Q.-Z., & Hui, M.-T. 2014, ApJ, 787, 115

Ye, Q.-Z., Hui, M.-T., Brown, P. G., et al. 2016, Icarus, 264, 48

Younger, J. P., Reid, I. M., Vincent, R. A., & Murphy, D. J. 2012, MNRAS, 425, 1473

Zacharias, N., Finch, C. T., Girard, T. M., et al. 2013, AJ, 145, 44

Chapter 3

Weakly active comet: the case of 209P/LINEAR

A version of this chapter has been published as:

3.1   Introduction

Dormant comets are comets that have depleted their volatiles in the near surface layers but may still possess an ice-rich interior. It is not easy to study these objects directly, as their optical properties are indistinguishable from those of some of their asteroidal counterparts. Dormant comets among the population of near-Earth objects (NEOs) are particularly interesting, as they may have a significant contribution to Earth's history. It has been suggested that $\sim 10\%$ of NEOs had their origins as Jupiter-family Comets or JFCs (e.g. Fernández et al., 2002; DeMeo & Binzel, 2008).

The dynamical lifetime of common JFCs is about 10^5 yr (Levison & Duncan, 1994). The physical lifetime of kilometer-sized JFCs, however, is estimated to be only a few 10^3 yr (e.g. Di Sisto et al., 2009). It is therefore evident that a typical JFC, presuming it does not fragment or split, would spend most of its time as a dormant comet. The details of the active-dormancy transition remain nebulous, but classical understanding of cometary evolution argues that the transition might include a period of low or intermittent cometary activity, possibly due to the buildup of dust mantles on the surface (c.f. Jewitt, 2004). Hence, it is natural to speculate that some weakly active comets may be active-dormancy transitional objects. From an observer's perspective, these objects are at a unique stage of the evolution of cometary nuclei, as they are still observationally identifiable as physical comets, as opposed to completely dormant comets that are indistinguishable from low albedo asteroids.

We define a low activity comet as a comet where the absolute total magnitude, M_1, is higher (fainter) than the absolute magnitude of a dark asteroid (defined by V-band geometric albedo $p_v = 0.1$) of equivalent effective body (nucleus) size. The physical implication of this definition is that the cometary activity is so low, that the comet would be recognized as a dark asteroid ($p_v < 0.1$) if extended cometary features are unresolvable to an observer. Mathematically, the definition can be expressed as

$$M_1 > 16.6 - 5\log\left(\frac{R_n}{1\text{ km}}\right) \tag{3.1}$$

where R_n is the effective nucleus radius. Among the 121 comets with constrained nucleus sizes[1], we find 9 comets meeting our definition of low activity comets (Table 3.1) of which 8 are near-Earth JFCs.

What are the nature and the origins of these comets? To answer this question, we need to look at their physical and dynamical properties. In particular, we note four of these comets – namely 209P/LINEAR, 252P/LINEAR, 289P/2003 WY25 (Blanpain) and 300P/2005 JQ5

---

[1]The nucleus sizes of these 121 comets are extracted from the JPL Small-Body Database (`http://ssd.jpl.nasa.gov/sbdb_query.cgi`) on 2015 June 3.

Comet	M_1	R_n (km)	Assoc. meteor shower
10P/Tempel 2	13.2	10.6[a]	-
28P/Neujmin 1	11.5	21.4[a]	-
102P/Shoemaker 1	15.7	1.6[b]	-
184P/Lovas 2	14.4	6.2[b]	-
209P/LINEAR	16.9	2.7[c]	Camelopardalids
252P/LINEAR	18.6	0.5[d]	Predicted, not yet observed[g]
289P/Blanpain	22.9	0.32[e]	Phoenicids
300P/Catalina	18.3	1.4[f]	June ϵ-Ophiuchids (?)
C/2001 OG108 (LONEOS)	13.1	13.6[a]	-

Table 3.1: A list of low activity comets according to the definition given in §1.

(Catalina) – can produce meteor showers currently observable at Earth. Meteor showers are caused by cometary dust ejected in past orbits of the parent, therefore meteor observations have the potential of enhancing our understanding of the physical history of the parent, as demonstrated in the investigation of the present and past activity of 55P/Tempel-Tuttle (e.g. Yeomans, 1981; Brown, 1999) and a couple of potential dormant comets (e.g. Babadzhanov et al., 2012; Kokhirova & Babadzhanov, 2015).

In this paper, we focus on one particular comet in our list, 209P/LINEAR. 209P/LINEAR is among the most weakly active comets ever recorded (e.g. Schleicher, 2014; Ishiguro et al., 2015) and is associated with a new meteor shower, the Camelopardalids (e.g. Jenniskens, 2014; Madiedo et al., 2014). What makes 209P/LINEAR ideal in studying cometary dormancy transition is (1) the close approach to the Earth of the comet during its 2014 perihelion passage, reaching ~ 0.05 AU from the Earth where it had brightened to $V \sim 11$ magnitude; and (2) the simultaneous encounter of a series of dust trails produced by the comet in its past orbits. These two events provide a rare opportunity to look at a potential comet-asteroid transitional object from two complementary approaches. Therefore, we observe 209P/LINEAR itself (§2) as well as the associated meteor activity (§3) to characterize the current state and recent history of the comet's activity. The observations are coupled with the results from numerical simulations to understand the nature and origin of 209P/LINEAR (§4). We also discuss the implication of our results to the state of other low activity comets through the examination of 209P/LINEAR.

3.2   The Comet

3.2.1   Observation

Imaging observations were conducted with three facilities at three different epochs. The observations and reduction procedures are summarized below and tabulated in Table 3.2.

1. Gemini North + Gemini Multi-Object Spectrographs (GMOS) camera at 2014 April 9.25 UT. This is a single frame taken as a snapshot observation. The observation was conducted relatively early in the active phase of 209P, making it suitable for examining the initial activation of the comet.

2. The 0.35-m telescope + QHY-9 camera at Xingming Observatory on 2014 May 18.75 UT. Around this date, the viewing geometry was favorable for separating dust of different sizes and emission epochs. The observation was conducted without filters and was processed using standard procedures (bias and dark frame subtraction, flat frame division).

3. Gemini South + Flamingo-2 (F-2) camera on 2014 May 25.94 UT. Around this date, the Earth was close to the comet and near the orbital plane of the comet. The observation was conducted in the K_s band, with 15 s of exposure of each frame. The telescope was nodded in the direction perpendicular to the tail axis, to avoid contamination from the tail signal at the sky subtraction stage. As the comet was moving at a fast rate of $\sim 18''$/min (or 25 pix per frame), we opted for the non-guided non-sidereal tracking mode to avoid frequent changes of guide stars. Because of this, a small fraction ($< 5\%$) of frames suffer from poor tracking and are discarded. At the end, a total of 41 frames were useful for later analysis. The data reduction is performed with the Image Reduction and Analysis Facility (IRAF) supplied by Gemini.

Time (UT)	Facility	Res.	Exposure	Airmass	FWHM	r_h	Δ	Plane Angle
		km/pix	min.		arcsec	AU	AU	
2014 Apr 9.25	GMOS-N	23	0.2	1.7	0.4	1.043	0.441	$-34.7°$
2014 May 18.75	XM 0.35-m	77	84	1.3	4.4	0.986	0.117	$-16.9°$
2014 May 25.94	F-2	8	10	1.7	0.8	1.009	0.064	$+9.3°$

Table 3.2: Summary of the imaging observations of 209P/LINEAR.
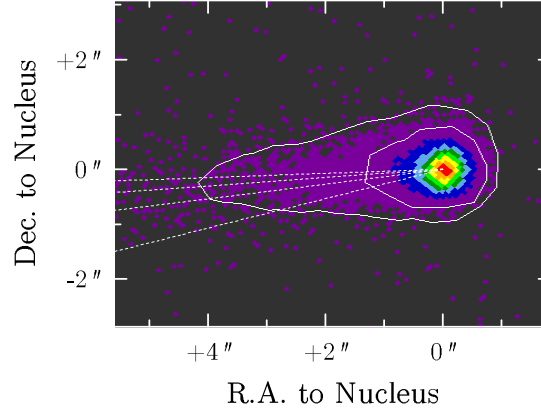
Figure 3.1 The 2014 Apr. 9 GMOS-N image (stretched in logarithmic scale) superimposed with the synchrone model. The ages of the synchrone lines (dashed lines) are (in counterclockwise order) 10, 25, 50 and 100 d respectively. The oldest visible dust was released at $\tau \sim 50$ d, appropriate to late Feb. 2014.

3.2.2 Results and Analysis

Start of Cometary Activity and General Morphology

Previous research (Hergenrother, 2014; Ishiguro et al., 2015) found that the activity of 209P/LINEAR started at a small activation distance of $r_h = 1.4$ AU. With the GMOS image, we conduct an independent check of the start time of activity of 209P/LINEAR. This is done by comparing the surface brightness profile to a synchrone model (Finson & Probstein, 1968). We estimate the start of activity occurred no later than late February 2014 or a lead time of $\tau \sim 50$ d, where 209P/LINEAR was at $r_h = 1.4$ AU (Figure 3.1). This is in agreement with previous results.

Composite images taken by Xingming 0.35-m telescope and Gemini F-2 on May 18 and 25 are shown as Figure 3.2. In the optical image from Xingming, 209P/LINEAR showed a symmetric coma measuring $6 - 7''$ (or about 50% larger than mean Full-Width-Half-Maximum
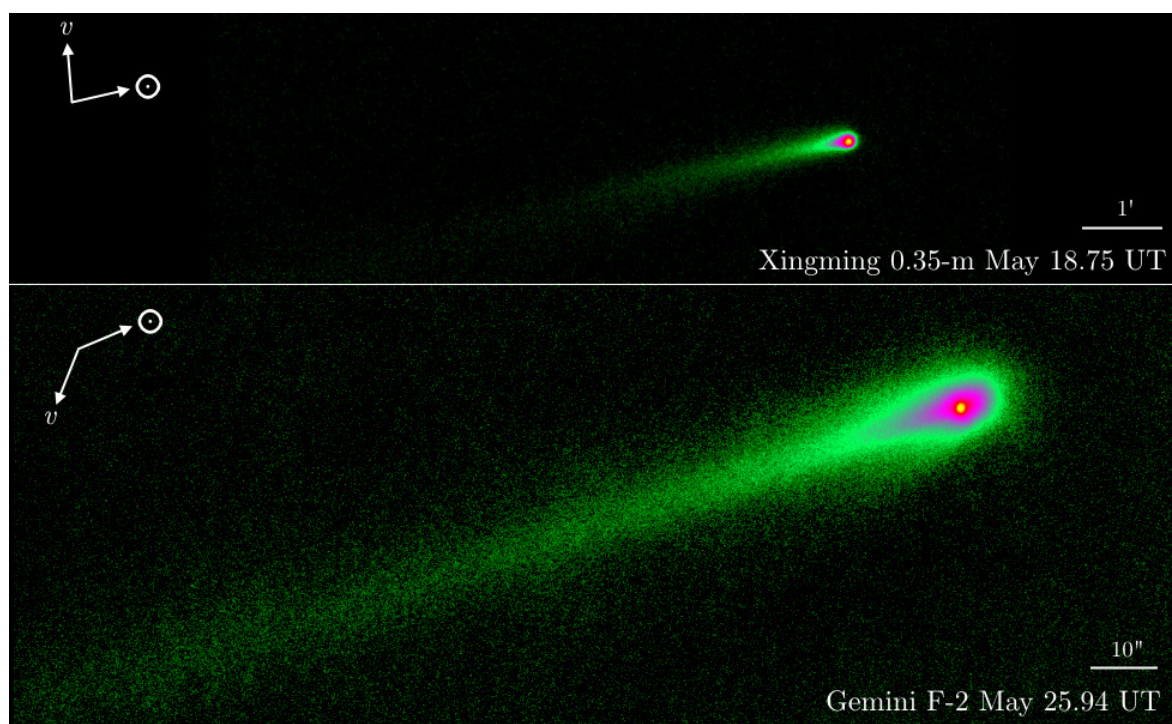
Figure 3.2 Composite images of 209P/LINEAR taken by Xingming 0.35-m telescope and Gemini Flamingo-2 on 2014 May 18 and 25. The images are stretched in asinh scale and are rotated to have north-up east-left.

or FWHM of background stars) in size and a mostly straight dust tail extended beyond the field of view. In the near infrared image from F-2, the nucleus, with the same FWHM compared to background stars, is clearly separated from the coma. The coma is significantly elongated along the Sun-comet axis, with the sunward side extending $\sim 5''$ or ~ 230 km towards the solar direction.

Modeling the Dust

To understand the dust properties, we model the observations using a Monte Carlo dust model evolved from the one used in Ye & Hui (2014). The dynamics of the cometary dust are determined by two parameters: the ratio between radiation pressure and solar gravity, $\beta_{rp} = 5.7 \times 10^{-4}/(\rho_d a_d)$, where ρ_d the bulk density of the dust and a_d the diameter of the dust, both in SI units (Wyatt & Whipple, 1950; Burns et al., 1979); and the initial ejection velocity of the dust. The latter is found following the philosophy of the physical model proposed by Crifo & Rodionov (1997), defined as

$$v_{ej} = V_0 \beta_{rp}^{1/2} \cos z \cdot v \tag{3.2}$$

where V_0 is the mean ejection speed of a dust particle of $\beta_{rp} = 1$, z is the local solar zenith angle, and v follows a Gaussian probability density function:

$$P(v) = \mathcal{N}(1, \sigma_v^2) \tag{3.3}$$

where σ_v is the standard deviation of v. The $P(v)$ function heuristically accounts for the variable shape and cross-section of the cometary dust particles that affects the radiation force impulse experienced by the dust.

We assume the dust size follows a simple power-law with a differential size index of q. Therefore, the dust production rate is expressed as

Parameter	Value
Semimajor axis a	2.93102 AU
Eccentricity e	0.69237
Inclination i	19.44783°
Longitude of the ascending node Ω	65.46431°
Argument of perihelion ω	150.46931°
Epoch of perihelion passage t_p	2009 Apr 17.43973 UT
Nucleus radius R_n	1.35 km
Nucleus bulk density ρ_n	500 kg·m^{-3}
Dust bulk density ρ_d	1000 kg·m^{-3}
Dust albedo A_d	0.05

Table 3.3: Input parameters for the Monte Carlo dust model. The orbital elements are extracted from the JPL elements 130, epoch 2011 Jun 8.0 UT.

$$N(r_h, a_d)\mathrm{d}a_d = N_0 \left(\frac{r_h}{1\ \text{AU}}\right)^{-n} \left(\frac{a_d}{1\ \mu m}\right)^{-q} \mathrm{d}a_d \tag{3.4}$$

where N_0 is the mean dust production rate of 1 μm particles and r_h is the heliocentric distance at which the dust is released. We use $n = 4$ following the canonical comet brightening rate (c.f. Everhart, 1967).

We assume the observed flux is solely contributed by scattered light from the dust particles released in the current perihelion passage, and set the start epoch of dust emission to 2014 Feb. 18 ($\tau = 50$ d) as found in § 3.2.2. Simulated particles are symmetrically released around the comet-Sun axis line at the sunlit side. The size distribution is set to the interval of the free parameter $\beta_{\text{rp,max}}$ (i.e. the lower limit of dust size) to an upper size limit constrained by the escape speed $v_{\text{esc}} = \sqrt{2GM_n/R_G}$, where $M_n = \frac{4}{3}\pi R_n^3 \rho_N$ is the total mass of the nucleus, $\rho_N = 500$ kg·m^{-3} the bulk density of the nucleus, $R_n = 1.35$ km the effective nucleus radius (Howell et al., 2014), and $R_G = 10R_n$ the characteristic distance that gas drag become negligible (Gombosi et al., 1986). A modified MERCURY6 package (Chambers, 1999) is used to integrate particles from the start epoch to the observation epoch using the 15th order RADAU integrator (Everhart, 1985). Gravitational perturbations from the eight major planets (the Earth-Moon system is represented by a single mass at the barycenter of the two bodies), radiation pressure and the Poynting-Robertson effect are included in the integration. The

orbital elements of 209P/LINEAR are extracted from the JPL small body database elements 130 (`http://ssd.jpl.nasa.gov/sbdb.cgi`) and are listed in Table 3.3 together with other parameters used for the model. The resulting image is convolved with a 2-dimensional Gaussian function (with FWHM equals to the FWHM of the actual images) to mimic observational effects such as the instrumental point spread effect and atmospheric seeing.

We first model the May 18 Xingming image with the following procedure. First, we select the pixels $> 3\sigma$ from the background with σ the standard deviation of all the pixels in the image. Observed and modeled surface brightness profiles are then normalized to 3 FWHMs beyond the nucleus along the Sun-comet axis, with the region within 1 FWHM from the nucleus being masked out, as the signal from the nucleus may contaminate the central condensation. The degree of similarity of the two profiles is then evaluated using the normalized error variance (NEV), under a polar coordinate system centered at the nucleus with angular resolution of $1°$:

$$\text{NEV} = \frac{1}{n} \sum_{i=1}^{n} \frac{\sqrt{(\mathbf{M}_i - \mathbf{O}_i)^2}}{\mathbf{O}_i} \tag{3.5}$$

where n is the number of pixels above 3σ from the background, $\mathbf{M}_i$ and $\mathbf{O}_i$ are the pixel brightness from the modeled and observed brightness profile respectively. We set the tolerance level of NEV to 5% in order to derive uncertainties of the model parameters. We then test a range of parameters as tabulated in Table 3.4, which yields $\beta_{\text{rp,max}} = 0.005$, $V_0 = 40 \pm 10 \text{ m} \cdot \text{s}^{-1}$, $q = 3.8 \pm 0.4$ and $\sigma_v = 0.3 \pm 0.1$, shown as Figure 3.3). We find the dominance of larger dust in general agreement with previous results (e.g. Ye & Wiegert, 2014; Younger et al., 2015), except for a steeper size distribution ($q = 3.8$ vs. $q = 3.25$) and a slightly lower ejection velocity ($v_{\text{ej}} = 1.5 \text{ m} \cdot \text{s}^{-1}$ vs. $v_{\text{ej}} = 2.5$ to $4.4 \text{ m} \cdot \text{s}^{-1}$ for millimeter-sized dust) compared to the results from Ishiguro et al. (2015). The ejection speed is about an order of magnitude lower than the one given by some classic ejection models (e.g. Jones, 1995; Crifo & Rodionov, 1997; Williams, 2001) and is not much higher than the escape velocity ($v_{\text{esc}} = 0.2 \text{ m} \cdot \text{s}^{-1}$).

We then model the May 25 Gemini image. As the image was taken almost edge-on to the comet's orbital plane, dust particles at different sizes collapse onto the viewing plane, making

Parameter	Tested Values	Best-fit Values
Dust size lower limit, $\beta_{rp,max}$	0.001–0.1 in steps of	XM: 0.005
	1/40 of full range in log space	F-2: 0.004
Mean speed of $\beta_{rp} = 1$ dust at 1 AU, V_0	10–400 in steps of 10	XM & F-2: 40 ± 10 m $\cdot$ s^{-1}
Lagging parameter, σ_v	0.0–0.5 in steps of 0.1	XM & F-2: 0.3 ± 0.1
Size index, q	2.6 to 4.4 with steps of 0.1	XM & F-2: 3.8 ± 0.4

Table 3.4: Dust model parameters derived from observations of Xingming 0.35-m (XM) and Gemini F-2 (F-2).
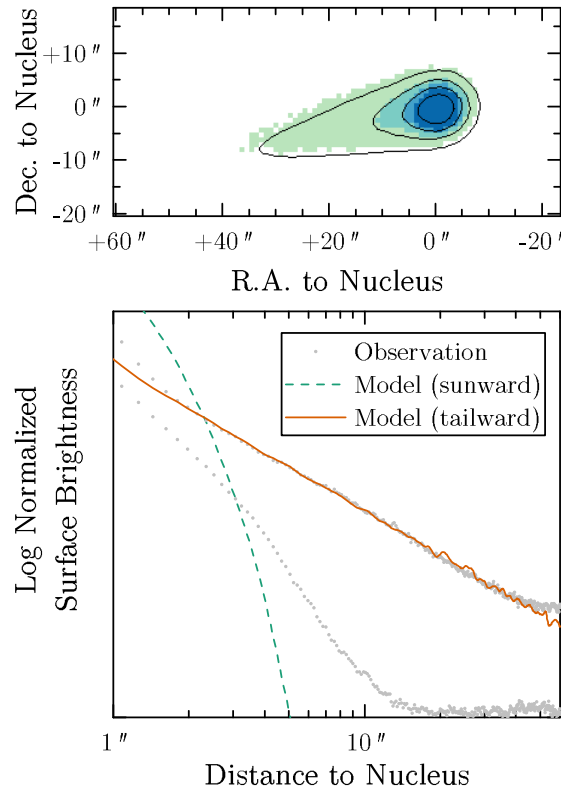
Figure 3.3 Observed (colored pixels) and modeled (contours) surface brightness profiles for the Xingming image (upper figure) and the Gemini F-2 image (lower figure; the sunward data is shifted downwards for clarity). The surface brightness profiles are normalized to the pixel intensity 3 FWHMs behind the nucleus along the Sun-comet axis to avoid contamination from the nucleus signal. The mean best model for both the Xingming and the Gemini F-2 images has $\beta_{rp,max} = 0.004$ to 0.005, $V_0 = 40$ m $\cdot$ s^{-1}, $q = 3.8$ and $\sigma_v = 0.3$.
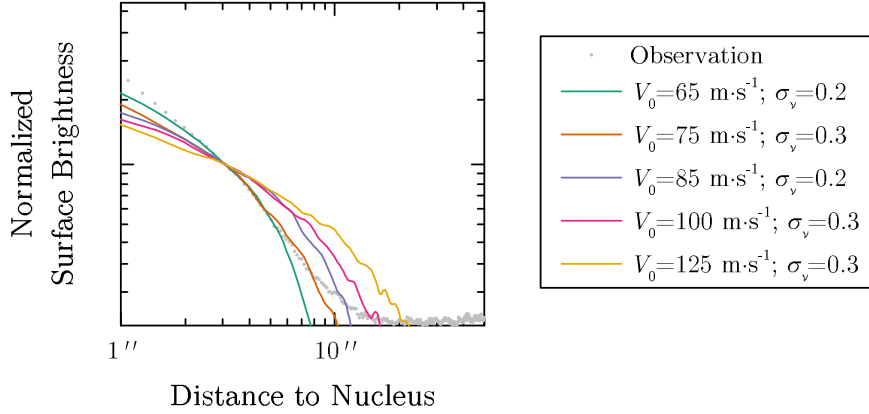
Figure 3.4 Representative attempts to fit the sunward section of the coma in the Gemini F-2 image. The observed and modeled profiles are all normalized to 3 FWHMs away from the nucleus along the comet-Sun axis. These models have $q = -3.8$ and $\beta_{\mathrm{rp,max}} = 0.004$.

it possible to collapse the image into a 1-dimensional profile without losing too much information. This comes with the benefit of simplifying subsequent analysis. Here we recognize that the orbital plane angle at the time of the observation ($+9.3°$) was not really as small as those used in other studies (generally $< 5°$), therefore collapsing the image may result in a loss in the resolution of the data, which should be reflected as an elevation in the uncertainties of the modeled parameters. However, we later see that the uncertainties of the best models of the May 25 Gemini image are comparable to that of the May 18 Xingming image (which was not collapsed). Hence, we conclude that the collapse of the image does not have a significant impact to our result.

We test the same range of parameters as listed in Table 3.4 to model the May 25 Gemini image. The observed and modeled surface brightness profiles are then integrated along the direction perpendicular to the orbital plane, and normalized to 3 FWHMs behind the nucleus along the Sun-comet axis. The goodness of the model is determined using Eq. 3.5. We find $\beta_{\mathrm{rp,max}} = 0.004$, $V_0 = 40 \pm 10 \mathrm{~m \cdot s^{-1}}, q = 3.8 \pm 0.4$ and $\sigma_v = 0.3 \pm 0.1$, which is in good agreement with the parameters found from the May 18 Xingming image. However, we note that despite the fact that the fit at the tailward direction is good, the discrepancy between the modeled and the observed profile at the sunward direction is striking (Figure 3.3). Additional

testing at the sunward-only section with the same test grid as Table 3.4 reveals no compatible dust model (Figure 3.4), which suggest a violation of the steady flow assumption we used for the model.

Near Nucleus Environment

To understand the physical properties of the non-steady coma, we separate the steady (i.e. the dust tail) and the non-steady component (i.e. the coma) in the surface brightness profile and calculate the flux for each of them. We first perform an internal absolute photometric calibration using the 2MASS stars in the image (Skrutskie et al., 2006). The selected calibration stars are at least $0.5'$ away from the tail axis to avoid contamination from the comet. We then correlate the observed profile to the modeled profile on the absolute scale. We subtract the modeled tail component (from § 3.2.2), and interpolate the linear portion of the coma to further isolate the nucleus signal (Figure 3.5). This leaves the profiles of the steady tail and the non-steady coma calibrated to an absolute scale. By integrating these profiles, we derive the flux for the tail and the coma to be $\mathcal{F}_{\text{tail}} = 0.40$ Jy and $\mathcal{F}_{\text{coma}} = 0.04$ Jy respectively. The effective cross-section area for each component can be calculated by

$$C_{\text{e}} = \left(\frac{r_{\text{h}}}{1\ \text{AU}} \right)^2 \frac{\pi \Delta^2}{A_\lambda(\alpha)} \frac{F_\lambda}{F_{\odot,\lambda}} \tag{3.6}$$

where Δ is the geocentric distance, F_λ and $F_{\odot,\lambda}$ is the flux of the component of interest and the Sun at the desired wavelength λ, which $F_{\odot,\lambda} = 1.4 \times 10^{14}$ Jy for K_{s} band, and $A_\lambda(\alpha)$ the phase angle corrected geometric albedo.

For the tail component, the dust model gives a mean dust size $\bar{a}_{\text{d}} = 2 \times 10^{-4}$ m. By using $A_\lambda(0°) = 0.05$ and calculating the phase angle correction following the compound Henyey-Greenstein function (Marcus, 2007a,b), we derive $C_{\text{e}} = 5$ km^2 and the corresponding dust mass $M_{\text{d}} = \frac{4}{3}\rho_{\text{d}}\bar{a}_{\text{d}}C_{\text{e}} = 1 \times 10^6$ kg. Considering the r_{h} dependency, the dust production rate at the observation epoch is calculated to be $\dot{M}_{\text{d}} = 0.4$ kg $\cdot$ s^{-1}, yielding a dust-water mass ratio of $\sim 1 : 2$ using the water production rate derived from narrow band observations (Schleicher,
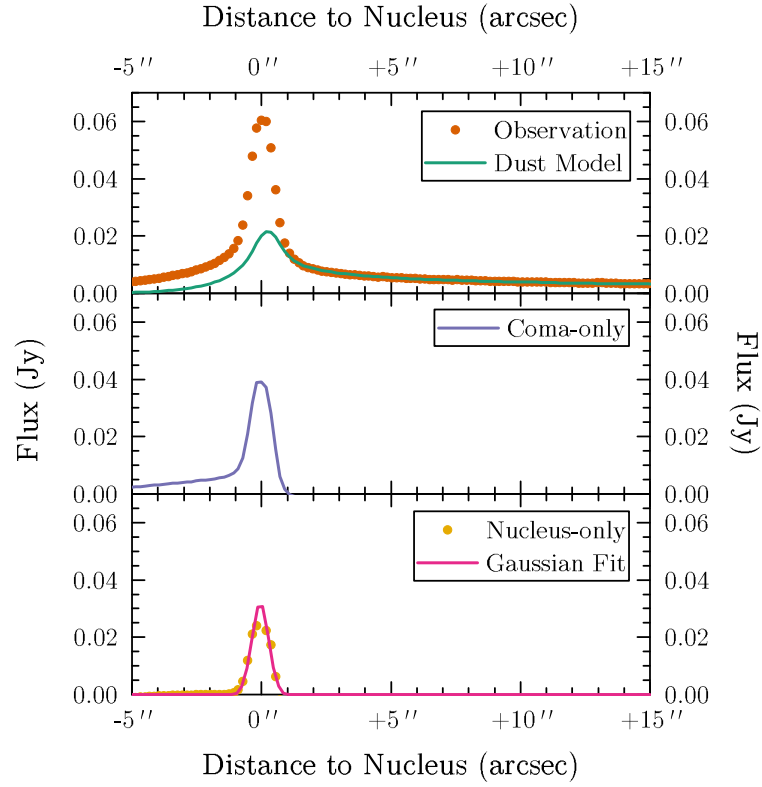
Figure 3.5 Separation of the coma and nucleus signal based on the Gemini F-2 image. Upper figure: observed profile and modeled profile from the dust model. Middle figure: derived coma+nucleus profile by subtracting the modeled profile from the observed profile. Lower figure: nucleus-only profile, derived from subtracting the linear portion of the coma profile. The X-axis corresponds to the Sun-comet axis.

2014). This is lower than other measurements (e.g. Küppers et al., 2005; Rotundi et al., 2015) but is perhaps not unexpected, given the large scatter (within a factor of 10–100) of the dust-gas ratio among comets (A'Hearn et al., 1995). We also note the derived dust production is about an order of magnitude lower than the value derived by Ishiguro et al. (2015), likely due to different model parameters (such as $\bar{a}$) used for the calculation.

On the other hand, the non-steady region extends no more than $\sim 2''$ behind the nucleus, corresponding to a mean lifetime of ~ 1 d appropriate to 10–100 μm particles. Interestingly, this is comparable to the mean lifetime of icy grains (purity $X_1 \gtrsim 0.9999$) of comparable sizes at $r_h = 1$ AU (Hanner, 1981; Beer et al., 2006, e.g.), seemingly supporting the presence of an icy grain halo as a self-consistent explanation to the observations. However, we note that this hypothesis is not without problems: for dirtier icy grains such as $X_1 = 0.9$, centimeter-sized grains would be required to survive to 1 d; we also note that icy grain halos are known to exist only on long period comets and hyperactive JFCs (c.f. Combi et al., 2013). Therefore, more direct evidence is needed to prove/disprove the icy grain halo hypothesis for the case of 209P/LINEAR.

Nucleus Properties

As the nucleus is effectively a point source in our data, we reconstruct the nucleus signal by fitting the isolated nucleus signal in Figure 3.5 with a Gaussian function. This yields the nucleus flux $\mathcal{F}_{nucleus} = 0.02$ Jy. As the nucleus size has been reliably measured by radar, we derive the corresponding geometric albedo of the nucleus by

$$A_\lambda(0°) = \left(\frac{r_h}{1\,\text{AU}}\right)^2 \frac{\Delta^2}{R_n^2 \Phi(\alpha)} \frac{F_\lambda}{F_{\odot,\lambda}} \tag{3.7}$$

where $\Phi(\alpha) = 10^{-0.4\beta\alpha}$ is the phase angle function, with α the phase angle and $\beta = 0.035$ mag $\cdot$ deg^{-1} the phase slope (e.g. Gehrels & Tedesco, 1979). We yield $A_\lambda(0°) = 0.12$ in the K_s band. This implies a steep spectral slope considering the R_C-band albedo constrained by Ishiguro et al. (2015) that is at the order of 0.05, making the nucleus of 209P/LINEAR

similar to D-type asteroids and most Trojan asteroids (Dumas et al., 1998).

3.3 The Meteors

3.3.1 Instrument and Data Acquisition

The Camelopardalid meteor shower was observed using the Canadian Meteor Orbit Radar (CMOR). CMOR is an interferometric radar array located near London, Canada. The main component of CMOR consists of six stations operated at 29.85 MHz with a pulse repetition frequency of 532 Hz. Meteors are detected along a great circle on the sky plane perpendicular to the radiant vector, when their ionized trails reflect the radar waves sent by the transmitter. Observations are routinely processed by an automatic pipeline to eliminate false detections and calculate trajectory solutions. The details of the CMOR operation can be found in Jones et al. (2005); Brown et al. (2008) and Weryk & Brown (2012).

In this study, we focus on multi-station data as it allows for reliable determination of many meteoroid properties. Single-station data (from the main site) is only used for flux calculation. We first prepare our *initial* dataset by extracting Camelopardalid meteors from the processed daily multi-station data, following the procedure described in Ye et al. (2014). The aperture (both spatial and velocity) are initially set to the predicted value by Ye & Wiegert (2014) and iterated several times until the optimal values (i.e. includes a maximum number of meteors) are found. A Monte Carlo procedure (Weryk & Brown, 2012) is then used to determine the weighted mean radiant and meteor velocity, which are found to be $\lambda - \lambda_\odot = 38°, \beta = +57°$ in the sun-centered coordinate system and with an in-atmosphere velocity $v_m = 18.8$ km $\cdot$ s^{-1}. The sizes of the spatial and velocity apertures are then found by comparing to the radiant/velocity density profile between the outburst date and the background as determined from ambient meteor activity ±2 days away from the outburst date. As shown in Figure 3.6, spatial and velocity aperture sizes are determined to be 10° and 11% of v_m. A total of 99 Camelopardalid meteors are selected in such manner.
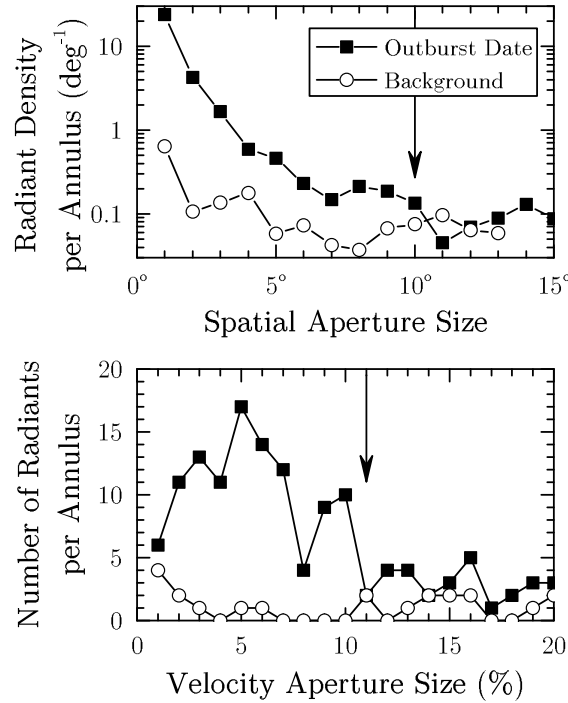
Figure 3.6 Determination of the optimal radiant and velocity apertures. Radiant aperture is centered at $\lambda - \lambda_\odot = 38°, \beta = +57°$ in the Sun-centered ecliptic coordinate system, (in-atmosphere) velocity aperture is centered at $v_m = 18.8$ km · s^{-1}. Background values are extracted from non-outburst dates ±2 days from the outburst date (i.e. 2014 May 22 and 26). The optimal radiant and speed apertures are determined to be 10° and 11% respectively (marked by arrows). The velocity aperture is determined for the spatial aperture of 10°.

Label	*N*	Description
Initial	99	Extracted from processed daily data, includes 85 underdense meteors and 14 overdense meteors.
Underdense	85	Subset of *initial* dataset, contains only underdense meteors.
Overdense	63	Manually extracted from raw data, includes 14 meteors from *initial* dataset.

Table 3.5: Summary of the CMOR datasets used for analyzing the 2014 Camelopardalid outburst.

The meteor population studied by CMOR can be broadly classified into *overdense* and *underdense* meteors (e.g. McKinley, 1961). For meteors with similar compositions and properties, overdense meteors are typically associated with larger meteoroids and vice versa. For the case of the Camelopardalid meteor shower, the size cutoff between underdense and overdense meteors is approximately $\beta_{\rm rp} = 0.0003$ (equivalent to $a_{\rm d} = 2$ mm assuming $\rho_{\rm d} = 1000$ kg $\cdot$ m^{-3}). Compared to the underdense meteors, whose appearance is usually simple, overdense meteors tend to exhibit a complicated and variable appearance, making them sometimes difficult to be identified automatically. Therefore, we retrieved and inspected the raw data ±6 hr from the predicted peak of the meteor outburst for overdense meteors. A total of 63 Camelopardalid overdense meteors are manually identified in this manner, labeled as the *overdense* dataset. Out of these 63 meteors, 14 of them are also found in the *initial* dataset. We remove these 14 meteors from the *initial* dataset, leaving the other 85 underdense meteors, and label them as the *underdense* dataset. The three datasets are summarized in Table 3.5.

3.3.2 Results and Analysis of the 2014 Outburst

General Characteristics

We derive a weighted mean geocentric radiant of $\alpha_{\rm g} = 124.9° \pm 1.0°$, $\delta_{\rm g} = 79.2° \pm 0.2°$ (J2000 epoch) and in-atmosphere velocity $v_{\rm m} = 18.8 \pm 0.1$ km $\cdot$ s^{-1}, using the 99 Camelopardalid meteors in the *initial* dataset. This is consistent with the values derived by other studies (Jenniskens, 2014; Madiedo et al., 2014; Younger et al., 2015). We also note a change in the percentage of overdense and underdense meteors around the peak hour (Figure 3.7), which may reflect the arrival of meteoroids at different sizes to the Earth's orbit.

We then derive the mass distribution index s (defined as d$N \propto m^{-s}$dm where m is the mass) for the underdense and overdense population respectively. For underdense meteors, the cumulative amplitude-number relation is typically used to derive the shower mass index (e.g. Blaauw et al., 2011); for overdense meteors, the cumulative duration-number relation is sometimes used (e.g. McIntosh, 1968; Ye et al., 2014). For our underdense sample, we
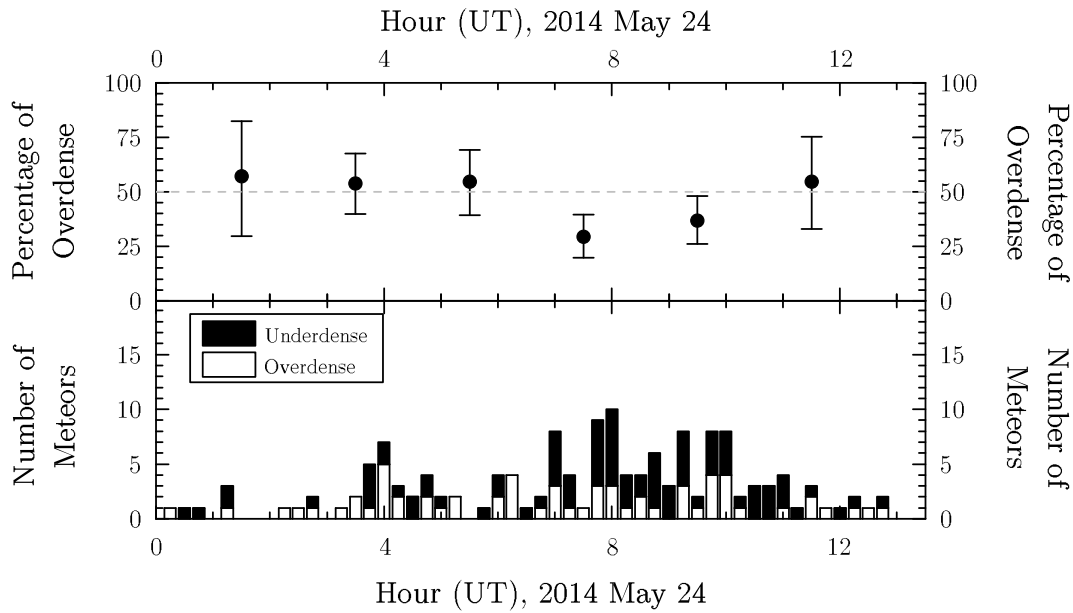
Figure 3.7 Top: Variations of the overdense meteor fraction with Poisson errors, binned in 2 h intervals. A dip (i.e. larger proportion of small meteoroids) is apparent around the peak hour (7–8h UT). Bottom: Raw numbers of overdense and underdense Camelopardalid meteors detected by CMOR, binned in 15 min intervals.

select 50 underdense meteors with echo range within 110–130 km; the range filter is applied to avoid contamination from overdense transition echoes (Blaauw et al., 2011). For the overdense sample, all 63 meteors in the *overdense* dataset are used. The data and the uncertainty are fitted using the MultiNest algorithm (Feroz et al., 2013), taking into account the number statistics of the data. The technique will be described in a separate paper in more detail (Pokorný & Brown, in prep). We find $s_{ud} = 1.84 \pm 0.07$ and $s_{od} = 2.02 \pm 0.19$ for underdense and overdense meteors respectively (Figure 3.8). This can be related to the size index q by

$$q = 3s - 2 \tag{3.8}$$

which, for our range of observed s, corresponds to $q = 3.5$ to 4.1. This agrees with the number derived from cometary observations in § 3.2.2.

The flux is calculated from the number of meteors detected per unit time divided by the effective collecting area of the radar system, following the procedure described in Brown &
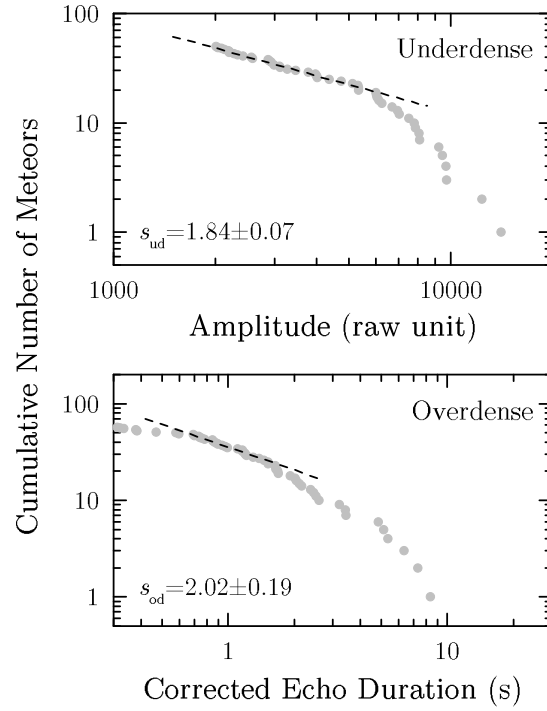
Figure 3.8 Determination of mass indices for the underdense (upper figure) and overdense (lower figure) populations. The mass indices are determined to be 1.84 ± 0.07 for underdense and 2.02 ± 0.19 for overdense meteors. The dashed lines show the best fit as determined by the technique developed by (Pokorný & Brown 2015, in prep). The uncertainties are based on the distributions of the posterior probabilities obtained by the MultiNest algorithm (Feroz et al., 2013). The correction of echo duration is described in Ye et al. (2013).
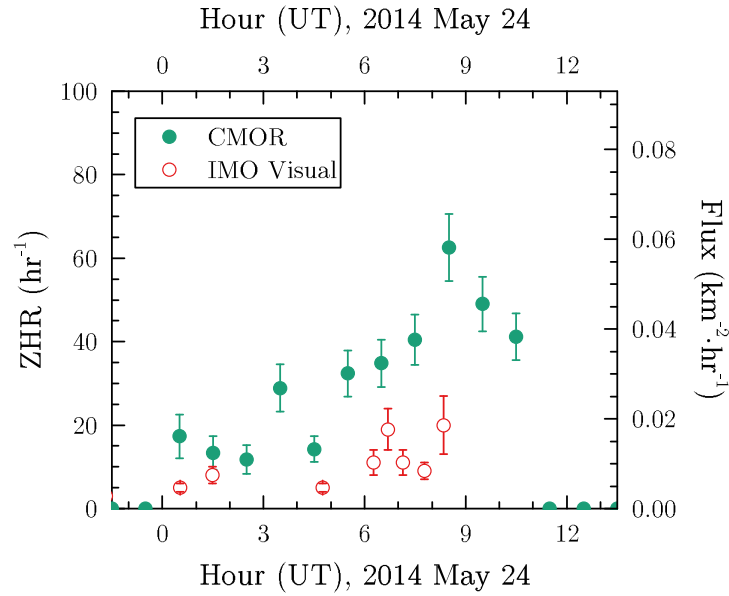
Figure 3.9 The variation of the flux (corrected to a limiting magnitude of +6.5) of the 2014 Camelopardalid meteor outburst as observed by CMOR and IMO visual observers. The CMOR observations are binned in 1 hr intervals. Error bars denote Poisson errors.

Jones (1995). The calculation of flux does not require a multi-station setup; single-station data is usually sufficient with proper background subtraction. In fact, by using the main-station detections, the statistics can be raised by a factor of ∼ 5. To derive the Camelopardalid-only flux, we subtract the raw meteor flux from the background flux following the procedure described in Ye et al. (2013) and Campbell-Brown & Brown (2015). The flux is converted to a Zenith Hourly Rate (ZHR) assuming a single power law size distribution applies to the observed size range (Koschack & Rendtel, 1990). The derived CMOR flux is shown in Figure 3.9 along with the flux derived from visual observations[2]. Overall, radar and visual observations show agreement in terms of activity timing, with a moderate rise and a steep decline in rates, as well as a main peak around 8h UT, 2014 May 24. We note that the visual profile suffers from small number statistics (only ∼ 15 meteors per bin during the peak, compared to ∼ 60 meteors for the radar), and so the two "peak-lets" at 6:30 and 8:30 UT are likely artifacts. In both techniques, further refinement of the exact peak time is perhaps not meaningful due to the relatively small

---

[2]Available at `http://www.imo.net/live/cameleopardalids2014/`, retrieved on 2015 April 2.

number statistics of the data. The CMOR flux (corrected to a limiting magnitude of +6.5) is about half an order of magnitude higher than the visual flux, seemingly indicating an over-abundance of faint meteors and a break in the power law somewhere beyond the naked-eye limit.

Meteoroid Properties

The Camelopardalids have almost identical entry speeds and geometry (with respect to CMOR) as another JFC shower, the October Draconids, which was observed by CMOR during its 2011 and 2012 outbursts (Ye et al., 2013, 2014). This coincidence allows us to directly compare the main characteristics of these two showers independent of instrumental effects or entry speed corrections. A distinct difference between the two showers is in the specular height distribution of the meteors: the Draconids appear 5–10 km higher than the Camelopardalids as observed by CMOR (Figure 3.10). It has long been thought that the exceptional ablation height of the Draconids is the direct consequence of their extreme fragility (e.g. Borovička et al., 2007). Hence, a simple interpretation of the observed height distribution of the two showers is that the Camelopardalid meteoroids are less fragile relative to the Draconids. As the outbursts from the two showers originated from cometary ejecta with young ejection ages (less than a few hundred years), the difference in space weathering is not significant; the observations seem to suggest that the surface material properties of the two parent comets are different.

We compare our result to the results derived from other Camelopardalid studies. Younger et al. (2015), who also observed the 2014 Camelopardalid outburst with a meteor radar, reported that the Camelopardalid meteoroids were less fragile than sporadic meteoroids, a finding that is not apparent in our Figure 3.10 due to our aggressive binning to enhance the statistics; but Younger et al.'s finding is at least qualitatively consistent with our finding that the Camelopardalid meteoroids being less fragile relative to the Draconids. Conversely, optical observations by Jenniskens (2014) and Madiedo et al. (2014) show that the Camelopardalid meteoroids are very fragile and are consistent with fluffy aggregates like the Draconids. How-
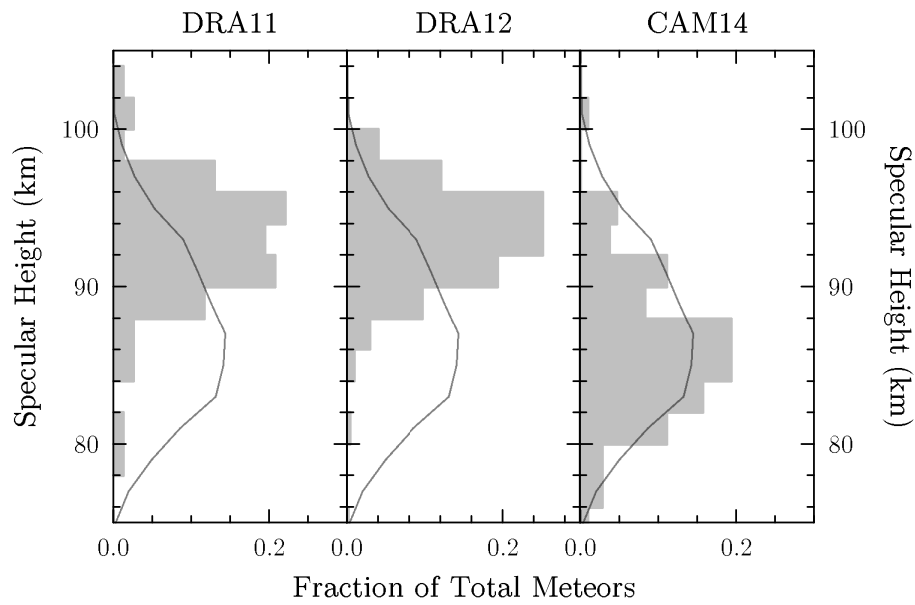
Figure 3.10 Specular height distribution of the underdense meteor echoes observed by CMOR for the 2011/12 Draconid outbursts (denoted as DRA11 and DRA12) and 2014 Camelopardalid outburst (denoted as CAM14), plotted as shaded bars. Specular height distribution of sporadic meteors (generated using all meteors detected by CMOR with v_m within 5% from 20 km · s^{-1}) is shown as a line.

ever, we note that (1) optical observations are sampling meteoroids of a larger size range (close to centimeter-sized, while radar observations are sampling millimeter-sized meteoroids); and (2) Jenniskens (2014) and Madiedo et al. (2014)'s observed meteors were recorded in a wider time span than the radar (on the order of 1 d vs. a few hours). Meteors detected away from the predicted peak mainly consist of background meteoroids that are part of older, disrupted trails. Hence, the optical meteors, whose properties seem very different than the radar meteors, may represent Camelopardalid meteoroids at different sizes and ages.

3.3.3 Camelopardalid Activity in Other Years

We conduct a search in the CMOR database for any undetected Camelopardalid activity in previous years, using the 3-dimensional wavelet analysis technique (e.g. Brown et al., 2010; Bruzzone et al., 2015) to compute the wavelet coefficient at the location of the Camelopardalid radiant. The time window is restricted to one week around the nodal passage of 209P, namely in the solar longitude range $\lambda_\odot = 60° - 66°$. CMOR has been fully operational since 2002, but data in 2002, 2006, 2009 and 2010 are severely (off-line periods more than 24 hours) interrupted by instrumental issues; hence we only inspect years with complete data for possible Camelopardalid activity.

We find distinct activity in 2011, while the activity in other years, if any, was too weak to be reliably separated from the background (Figure 3.11). The 2011 outburst is even noticeable on the raw, unprocessed radiant map (Figure 3.12), albeit much weaker than the 2014 outburst. We were able to extract 15 meteors for the 2011 outburst, which yields a weighted radiant of $\alpha_g = 119.5° \pm 2.1°$, $\delta_g = 77.2° \pm 0.3°$ (J2000 epoch) and in-atmosphere velocity $v_m = 19.3 \pm 0.3$ km$\cdot$s^{-1}. We find no obvious peak of activity, but the core of the activity falls between 2011 May 25 at 6–11 h UT ($\lambda_\odot = 63.6°$). The 2011 activity was not high enough to derive a statistically meaningful flux, but we estimate the 2011 flux to be about an order of magnitude lower than the 2014 flux, since the number of raw echoes is roughly 1/10 of that of
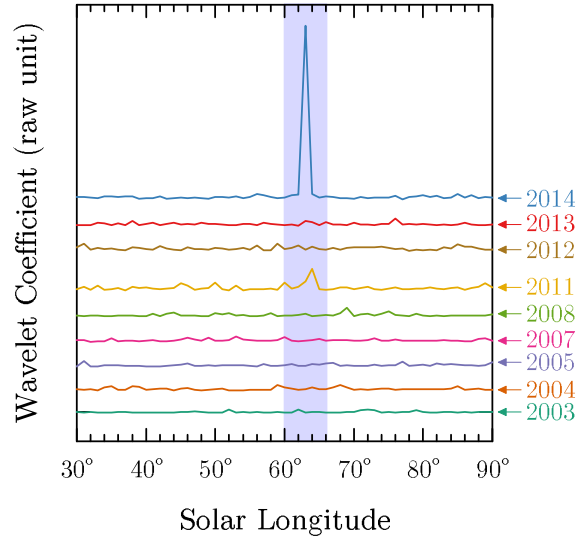
Figure 3.11 Variation of the relative wavelet coefficient at $\lambda - \lambda_\odot = 38°$, $\beta = +57°$ and $v = 20\,\text{km}\cdot\text{s}^{-1}$ within $\lambda_\odot = 30° - 90°$ in 2003–2014 (except 2006, 2009 and 2010). The expected Camelopardalid activity period is shaded. Activity is noticeable only in 2011 and 2014.

2014[3]. By following the same technique described in § 3.3.2, we derive a 1σ upper limit of the flux to be $\lesssim 0.01\,\text{km}^{-2}\cdot\text{hr}^{-1}$ for other years.

3.3.4   Modeling the Dust (II)

The dust model derived from cometary observations has placed some useful constraints on the physical properties of the Camelopardalid meteoroids. In this section, we explore the contribution of young meteoroid trails (defined as trails formed within ~ 50 orbital revolutions) to the observed meteor activity using numerical techniques. Older dust trails have experienced more perturbations from the major planets and are too disrupted to model. The simulation procedure is essentially the same as that in § 3.2.2, apart from extending the integration time several hundred years backward. To address possible meteor activity, we select a subset of Earth-approaching meteoroids following the method discussed by Brown & Jones (1998) and Vaubaillon et al. (2005):

---

[3]The change of radar collecting area in different years is negligible thanks to the high declination of the Camelopardalid radiant.
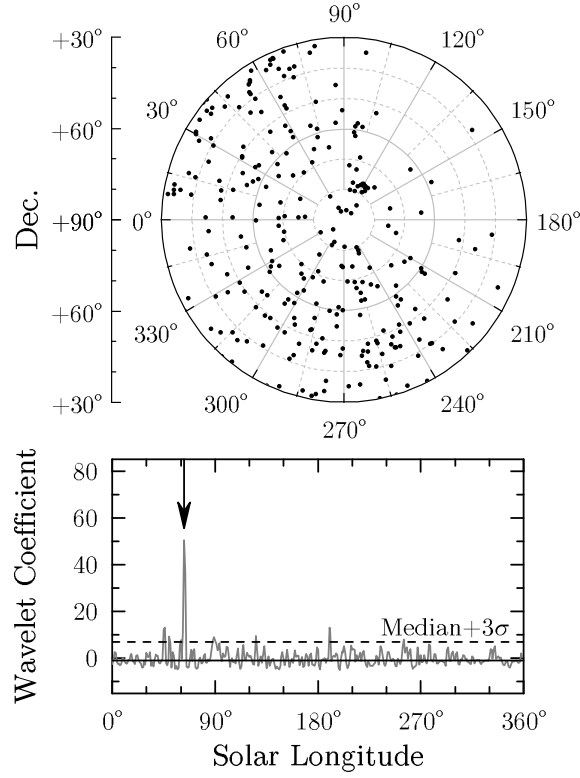
Figure 3.12 Upper figure: the raw radiant map of all meteor echoes detected by CMOR on 2011 May 25, corresponding to solar longitude $\lambda_\odot = 63°$. Angular axis represents R.A. and the radial axis represents Declination, both in geocentric coordinates in J2000 coordinates. Radiants are plotted as black dots. The Camelopardalid activity is clearly visible near $\alpha_g = 120°, \delta_g = +80°$. Lower figure: variation of the relative wavelet coefficient at $\lambda - \lambda_\odot = 38°$, $\beta = +57°$ and $v = 20$ km·s^{-1} in 2011, with the Camelopardalid activity marked by an arrow. Solid and dashed lines are median and 3σ above median, respectively.

$$\Delta X = v_{\text{rel}} \times \Delta T \tag{3.9}$$

where $v_{\text{rel}} \approx 17 \text{ km} \cdot \text{s}^{-1}$ is the relative velocity between the meteoroid and the Earth, ΔT is the characteristic duration of the meteor shower which we take as $\Delta T = 1$ d. These yield $\Delta X = 0.01$ AU. The simulated meteoroid is included in the subset when its Minimum Orbit Intersection Distance (MOID) to the Earth's orbit, calculated with the subroutine developed by Gronchi (2005), is smaller than ΔX.

We use the dust model derived from our cometary observations for the ejection of meteoroids. For comparison, the traditional Crifo & Rodionov (1997) model (denoted as the C&R model hereafter) is also used in a parallel simulation. The start of the integration is set to 50 orbits ago (or about 1750 A.D.). We first integrate 209P/LINEAR back to the year of 1750, and then integrate it forward with meteoroids released at each perihelion passage when the parent has $r_{\text{h}} < 1.4$ AU, the heliocentric limit of cometary activity as indicated by cometary observations. When the simulation is finished, we examine the encounters of all meteoroid trails in the years that CMOR was operational.

The results from both ejection models are largely identical, making it difficult to distinguish the better ejection model using observations. This emphasizes that the evolution of older trails is predominantly controlled by planetary perturbations rather than ejection speed. The 2014 encounter is easily identifiable thanks to the high density of the corresponding trail (Figure 3.13), with the simulation agreeing with the observations. We also note that our simulation predicts the Earth would first encounter larger meteoroids (Figure 3.16), a result consistent with CMOR observation of early overdense meteors noted in § 3.3.2.

The flux of meteoroids can be estimated by relating the number of meteoroids in Earth's vicinity to the dust production rate of the comet. From the analysis in § 3.2.2, we estimate the current dust production rate of 209P/LINEAR is of the order of 10^6 kg, or $N \sim 10^{14}$ meteoroids per orbit (taking $\bar{a} \sim 10^{-4}$ m as found previously). From the meteoroid stream simulation, we find $\sim 1\%$ of the meteoroids released between 1750–2014 are delivered to the Earth's
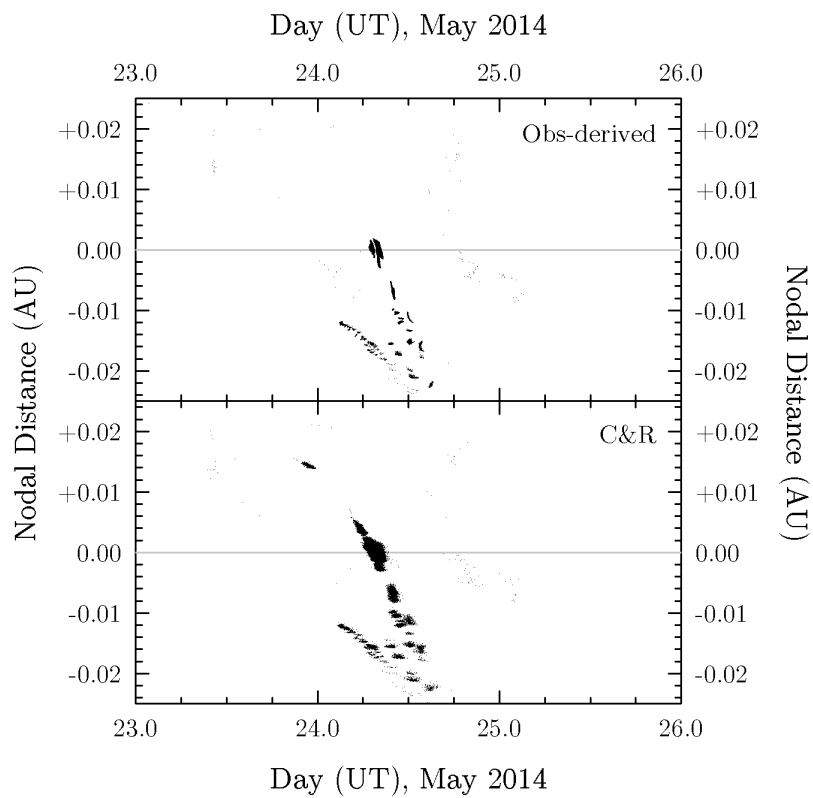
Figure 3.13 Nodal footprint of the 1750–2000 trails around 2014 May 24, using the ejection model derived from comet observations (upper figure) and the Crifo & Rodionov (1997) ejection model (lower figure).
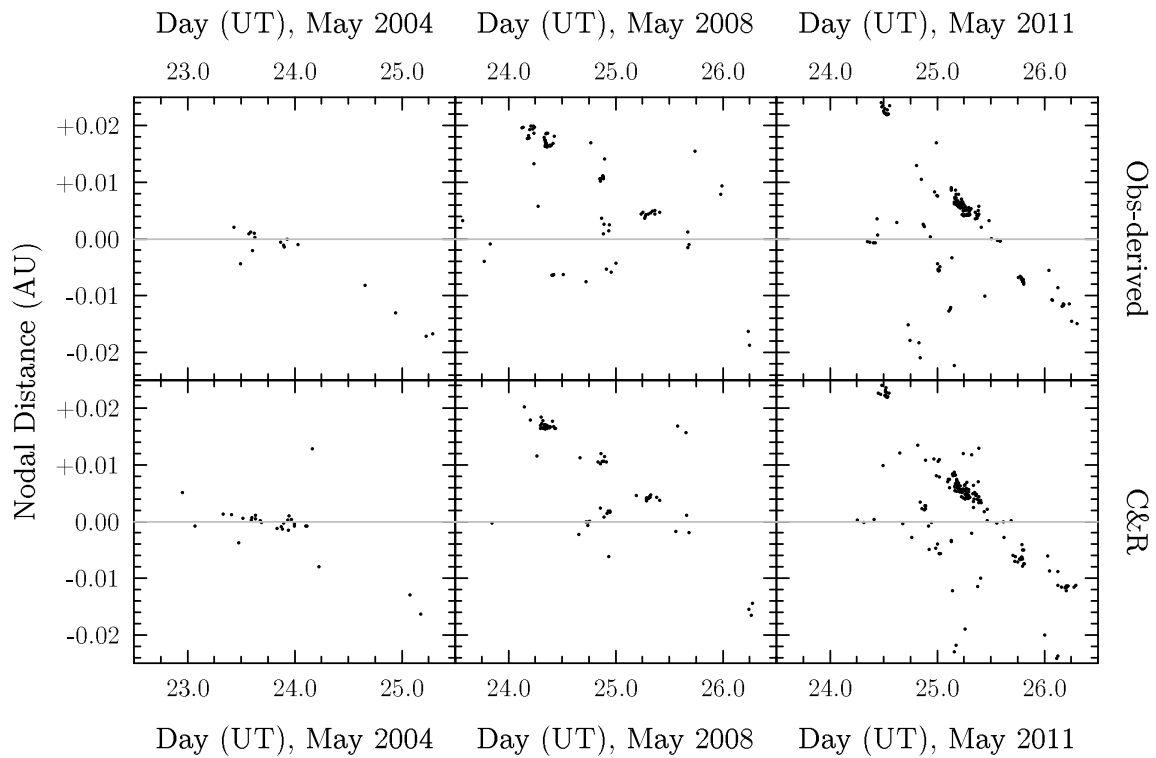
Figure 3.14 Nodal footprint of the 1750–2000 trails around 2004 May 24, 2008 May 25 and 2011 May 25, using the ejection model derived from comet observations (upper row) and the Crifo & Rodionov (1997) ejection model (lower row). The scale of meteoroid number is identical to that of Figure 3.13, but for clarity the meteoroids in this figure are marked with larger symbols.

vicinity during the 2014 encounter, corresponding to a flux of $\mathcal{F} \sim 1\% \times N \times \Delta X^{-2} \times \Delta T^{-1} =$ $0.01 \times 10^{14} \times (0.01 \text{ AU})^{-2} \times (1 \text{ d})^{-1} = 0.02 \text{ km}^{-2} \cdot \text{hr}^{-1}$, comparable to the flux determined from visual and radar meteor observations. This implies that 209P/LINEAR was not substantially much more active in the past several centuries, an idea also supported by the apparent lack of annual activity of the Camelopardalid meteor shower.

Additionally, we find predicted encounters in 2004, 2008 and 2011 from our simulations (Figure 3.14). The 2004 and 2008 encounters are predicted to be about an order of magnitude weaker than the 2011 encounter, thus we expect this activity to be buried in the sporadic background. The 2011 case is interesting as the parent was near aphelion at the time of the meteor outburst. Both the C&R model and our ejection model derived from the cometary observations only indicate encounters with a few extremely weak trails formed between 1763–1768 in 2011. The calculated peak time and width (both ejection models suggest peak times of 2011 May 25 ~5:40 and 9:00 UT for the 1763- and 1768-trail, with full-width-half-maximum of $\sim$ 8 hr) is consistent with CMOR observations. However, the flux predicted by the model is by a factor of 100 lower than what was observed, potentially hinting at a significant but transient increase of activity of 209P/LINEAR around those epochs. The same 1763- and 1768-trail also contribute to the 2014 meteor event; however, the overlapping peak time between trails (mostly < 1 hr apart) makes it difficult to distinguish activity from individual trails in the observations.

3.4 Discussion

3.4.1 The Dynamical Evolution of 209P/LINEAR

Recent work by Fernández & Sosa (2014) revealed a set of unique members among the JFCs that reside in highly stable ($> 10^4$ yr) orbits, including 209P/LINEAR. We extend their work for the case of 209P/LINEAR by generating 1000 clones of 209P/LINEAR using the orbital covariance matrix provided in JPL 130, and integrate all of them 10^5 yr backwards. The integration is performed with MERCURY6 using the Bulirsch-Stoer integrator (Bulirsch, 1972;

Stoer, 1972).

As shown in Figure 3.15, the core of the clones remain in Earth's vicinity for $\sim 10^4$ years, much longer than the typical physical lifetime for similar-sized JFCs in the near-Earth region (e.g. Di Sisto et al., 2009). In addition, we note the core of the clones is extremely compact for more than 100 orbits (1σ width in semimajor axis ~ 0.0002 AU), until an extreme close approach to the Earth ($d_{\min} \approx 0.006^{+0.010}_{-0.005}$ AU) around 1400 Mar 12 (on Julian calendar) scatters the clones. The miss distance of this approach to the Earth is smaller than the recorded close approach by Lexell's Comet in 1770 (0.015 AU; Kronk, 2008) and prompted us to look at medieval astronomical records for possible sightings, without success. If the activity level of 209P/LINEAR in the 15th century is comparable to what it is now, the comet would have been +7 mag during its approach in 1400, below the naked-eye limit of medieval astronomers; however, any significant (by several magnitudes) increase in activity could have been noticeable. The lack of possible sightings for 209P/LINEAR's close approach in 1400 suggests that the comet was not substantially more active ~ 100 orbits ago.

Since 209P/LINEAR is in a stable orbit, the associated meteoroid stream may also possess a set of orbits that are more stable than other JFC streams. To quantify the dispersion process of the Camelopardalid meteoroid stream, we adopt the same integration procedure as described in § 3.3.4 and examine the evolution of meteoroid trails released between 1-revolution (5 yr) and 1000-revolution (5000 yr), shown as Figure 3.17. It can be seen that the narrow stream structure is maintained for trails that formed as far as ~ 1000 to 2000 yr ago, which is a few times longer than other JFC streams such as the π-Puppid meteoroid stream (e.g. Cremonese et al., 1997). We also note that the meteoroid stream evolves differently than the parent. The degree of the difference increases as the age of the stream increases. For example, the current radiant of the core of 200-rev meteoroids (i.e. meteoroids released at about 1000 A.D.) would be at $\alpha_g = 120°$, $\delta_g = +60°$, encountered at $\lambda_\odot = 70°$ (approximately June 1). There is no established meteor activity related to this hypothetical radiant, although a few other possible annual showers have been associated with 209P/LINEAR (e.g. Rudawska & Jenniskens, 2014;
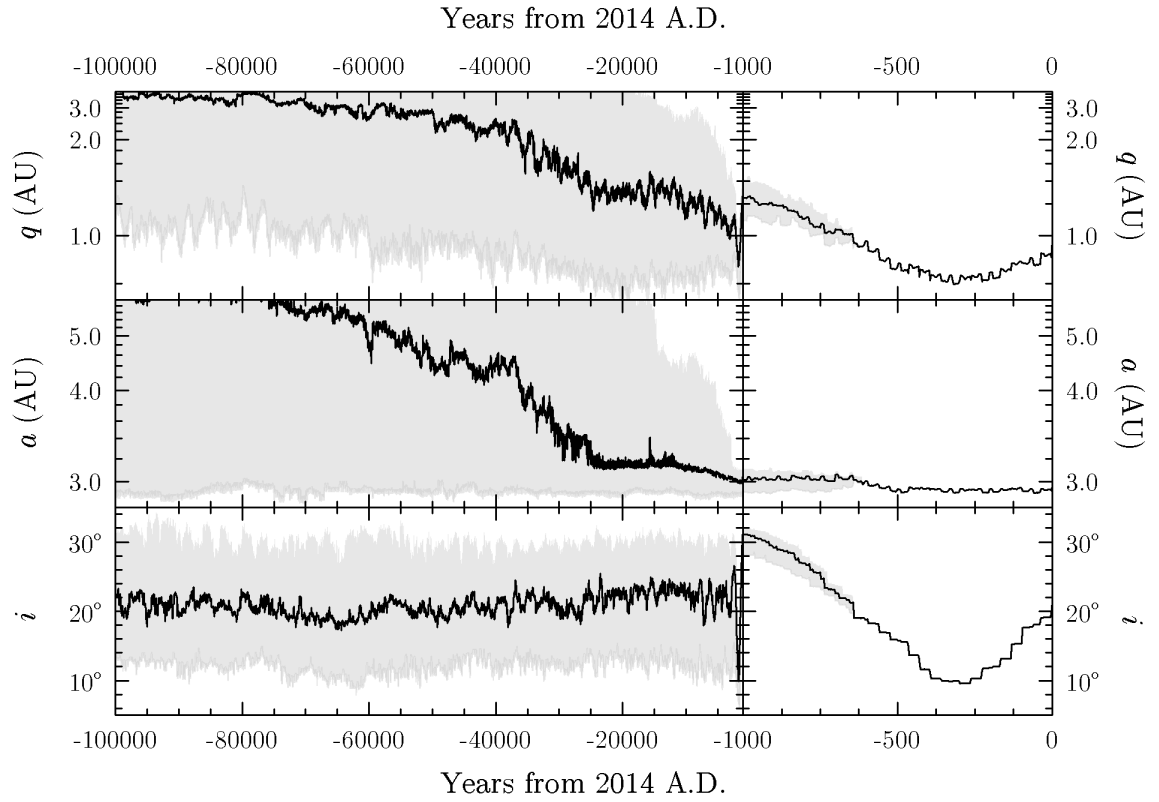
Figure 3.15 Dynamical evolution of 1000 clones of 209P/LINEAR in a time interval of 10^5 yr with a zoomed section for within the last 1000 yr. The median (black line) and $\pm 1\sigma$ region (shaded area) is shown. A highly stable section is seen up to 3×10^4 years, during which the core of the clones remains in near-Earth region and 95% of the clones remain in bounded orbits.
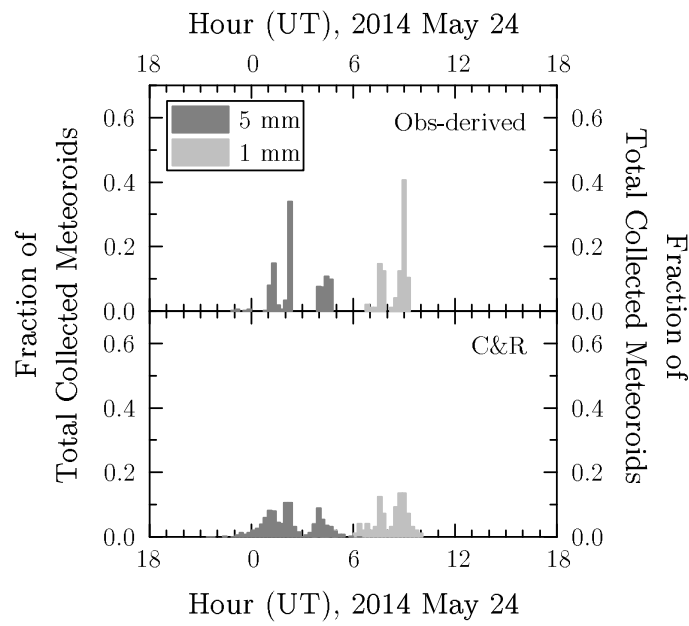
Figure 3.16 The arrival distribution of large, overdense-like (a_d = 5 mm or β_rp = 0.0001) and small, underdense-like (a_d = 1 mm or β_rp = 0.0005) meteoroids from observation-derived (upper figure) and the Crifo & Rodionov (1997) ejection models (lower figure) for the 2014 Camelopardalid meteor outburst. It is apparent that larger meteoroids arrived earlier than smaller meteoroids, consistent with CMOR observations.
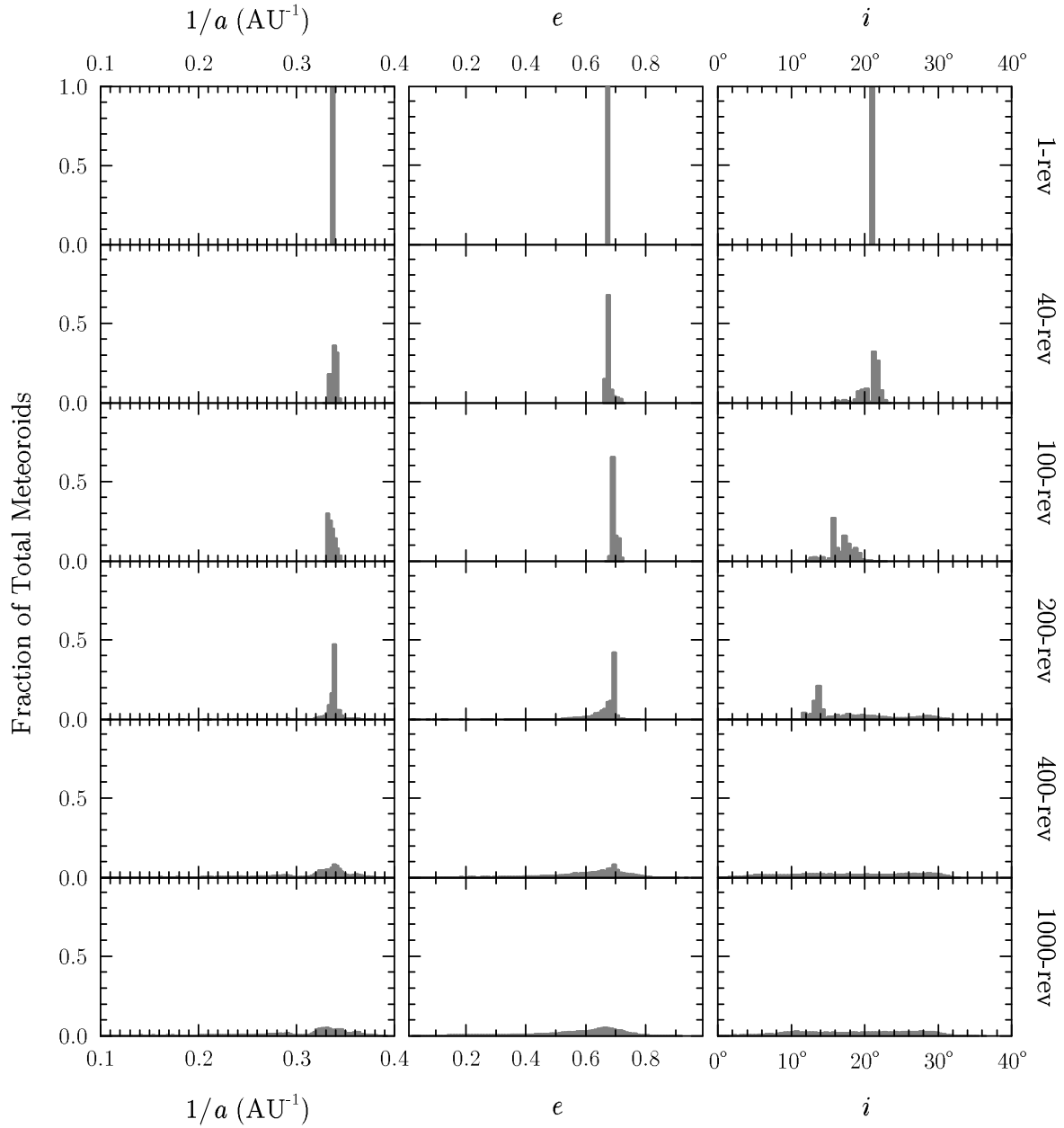
Figure 3.17 Secular evolution of orbital elements of meteoroids of different ages: 1-rev (meteoroids released 5 yr ago), 40-rev (released 200 yr ago), 100-rev (released 500 yr ago), 200-rev (released 1000 yr ago), 400-rev (released 2000 yr ago) and 1000-rev (released 5000 yr ago). The meteoroid ejection model is based on comet observations, but the result is insensitive to the choice of ejection model, as the evolution of meteoroid stream is predominantly controlled by planetary perturbations over the investigated time scale. It can be seen that the dispersion time scale of the Camelopardalid meteoroid stream is at the order of 1000 yr (200-rev).

Šegon et al., 2014).

3.4.2   Nature of 209P/LINEAR and Comparison with Other Low Activity Comets

Following our analysis, it seems evident that 209P/LINEAR has been mostly weakly active for the last few hundred orbits, while it might have been in a near-Earth JFC orbit on the time scale of $\sim 10^4$ yr. This is compatible with the idea of 209P/LINEAR as an aging comet exhausting its remaining near surface volatiles as derived from the classical interpretation of cometary evolution. It is perhaps not possible to know how long the comet has stayed in the inner solar system; however, we note that the gradual decrease of the perihelion over the course of few thousand years (as indicated in Figure 3.15) may provide a prolonged favorable environment for weak cometary activity, as the sub-surface volatiles underneath the dust mantles can be (re-)activated by the gentle decrease of the perihelion distance (Rickman et al., 1990).

What does 209P/LINEAR tell us about other low activity comets? In the following we briefly discuss three other Earth-approaching comets (i.e. those that may generate meteor showers) listed in Table 3.1 and compare them to 209P/LINEAR. The other five comets in the list do not generate meteor showers, making it difficult to address their physical history in a manner similar to 209P/LINEAR.

252P/LINEAR Little is known about this newly discovered comet at the moment, except that numerical simulations indicate a recent (< 100 orbits) entry to the inner solar system (Tancredi, 2014, see also `http://www.astronomia.edu.uy/Criterion/Comets/Dynamics/table_num.html`, retrieved 2015 May 17), implying a different origin and evolution compared to 209P/LINEAR. Considering its young dynamical age in the inner solar system, the low activity of 252P/LINEAR may reflect a relative lack of volatiles at the time of formation of the nucleus.

289P/Blanpain   289P/Blanpain is the only low activity comet in the list that is associated unambiguously with annual meteor activity (Jenniskens, 2008). The comet itself was lost for some 200 yr after its initial discovery in 1819 (when it was assigned the designation D/1819 W1), until being re-discovered as the faint asteroidal body 2003 WY25 in 2005 (Foglia et al., 2005). Multiple clues suggest 2003 WY25 is the remnant of the original 289P/Blanpain following a catastrophic fragmentation event (e.g. Jenniskens & Lyytinen, 2005; Jewitt, 2006). Hence, the low activity nature of 289P/Blanpain may have a completely different origin than that of 209P/LINEAR.

300P/Catalina   300P/Catalina (known as 2005 JQ5 in some early literature) is interesting, as it is the only other comet in our list that is concurrently classified as a stable JFC by Fernández & Sosa (2014). It has not been associated with any established annual meteor shower, although a few possible linkages have been suggested (e.g. Rudawska & Jenniskens, 2014). Radar observations by Harmon et al. (2006) revealed a rough surface similar to 209P/LINEAR; however, the presence of cm-sized dust around the nucleus of 300P/Catalina, which is absent for 209P/LINEAR (Howell et al., 2014), seems to indicate stronger outgassing activity of 300P/Catalina compared to 209P/LINEAR at the present time. It may be possible that 300P/Catalina is at an earlier stage of dormancy compared to 209P/LINEAR.

3.5   Conclusions and Summary

The low activity comet, 209P/LINEAR, may indeed be an aging comet that is quietly exhausting its last bit of near surface volatiles. This idea is supported by the convergence of several different lines of evidence: dust modeling of cometary images that revealed a presently weakly active comet, analysis and modeling of meteor observations that revealed a low dust production over the past few hundred orbits, numerical analysis of the dynamical evolution of the comet that suggested a stable orbit in the inner solar system over a time scale of 10^4 yr.

The main findings of this paper are:

1. The best-fit dust model to the cometary images involves a low ejection speed (1/10 of moderately active comets) and large dust grains ($\bar{a}_d = 10^{-4}$ m). The dust production rate of the comet at 19 d after perihelion is 0.4 kg $\cdot$ s^{-1}, a remarkably small number.

2. The coma region appears to be inconsistent with the steady-flow model. The general characteristics of this region is compatible with the icy grain halo theory, a theory that is known to be only applicable to active long period comets and hyperactive Jupiter-family comets. More conclusive evidence is needed to establish or disprove this hypothesis.

3. By applying a coma subtraction technique, the nucleus signal is separated from the coma, yielding a geometric albedo $A_\lambda(0°) = 0.12$ appropriated to K_s band. Coupling with optical measurements at visible band, this indicates a reddish spectrum of the nucleus of 209P/LINEAR similar to that of D-type asteroids and most Trojans.

4. Radar observations by CMOR show the peak of 2014 Camelopardalid meteor outburst around 2014 May 24 at 8 h UT. From CMOR observations, we derive a mean radiant of $\alpha_g = 124.9° \pm 1.0°$, $\delta_g = 79.2° \pm 0.2°$ (J2000 epoch), mean in-atmosphere velocity $v_m = 18.8 \pm 0.1$ km $\cdot$ s^{-1}, and a peak flux of 0.06 km^{-2} $\cdot$ hr^{-1}, consistent with visual, optical and other radar observations. Numerical simulations confirm that the outburst originated from the dust trails formed in the 18–20th century, a time that the parent was perhaps not much more active. The mass distribution index of the meteors, $s = 1.8$ to 2.0, agrees with the size index $q = 3.8$ derived from modeling of the cometary images.

5. A direct comparison to the Draconids, a meteor shower with almost identical entry speed that was also observed with CMOR, shows a distinctly different height distribution between the Camelopardalids and Draconids: the Camelopardalids tend to appear $\sim 10\%$ lower than the Draconids. This is likely due to the Camelopardalids being less fragile relative to the Draconids, the latter of which have long been known to be extremely fragile meteoroids. This agrees with other radar measurements but differs from optical measurements, which support highly fragile meteoroids. As optical observations are

sampling meteoroids at larger sizes and a wider range of arrival times, the difference in meteoroid properties derived from different techniques may be due to sampled meteoroids of different sizes and ages.

6. We examine CMOR data from 2003 onwards (except 2006, 2009 and 2010) and find a previously unnoticed Camelopardalid outburst in 2011. The activity peaks around 2011 May 25 between 6–11 h UT, with a peak flux of the order of 0.005 km$^{-2} \cdot$ hr^{-1}. Numerical simulations suggest the dust trail encountered in 2011 was formed in 1763–1768, however the predicted flux seems to be a factor of 100 smaller than what was observed. This may indicate some temporary increase in activity of 209P/LINEAR around those times.

7. Numerical integrations indicate that 209P/LINEAR may have resided in a stable near-Earth JFC orbit for $\sim 10^4$ yr. The dispersion time scale for the Camelopardalid stream is about 1000–2000 yr, which is a few times longer than JFC streams such as the π-Puppids. The lack of significant annual activity of the Camelopardalid shower may serve as a strong evidence of the low activity of 209P/LINEAR over the past several hundred orbits.

8. We compare 209P/LINEAR to three other low activity comets that are associated with known or hypothetical meteor showers: 252P/LINEAR (associated with a hypothetical meteor shower in the constellation of Lepus), 289P/Blanpain (associated with the Phoenicid meteor shower), and 300P/Catalina (associated with a few possible meteor showers, such as the June ϵ-Ophiuchids). A diversity is seen: the low activity of 252P/LINEAR may be congenital; that of 289P/Blanpain may be due to catastrophic fragmentation. 300P/Catalina shares many similar physical and dynamical characteristics with 209P/LINEAR; but the presence of cm-sized meteoroids around the nucleus may indicate a stronger outgassing activity of 300P/Catalina compared to 209P/LINEAR at the moment.

Acknowledgements

Bibliography

A'Hearn, M. F., Millis, R. C., Schleicher, D. O., Osip, D. J., & Birch, P. V. 1995, Icarus, 118, 223

Babadzhanov, P. B., Williams, I. P., & Kokhirova, G. I. 2012, MNRAS, 420, 2546

Beer, E. H., Podolak, M., & Prialnik, D. 2006, Icarus, 180, 473

Blaauw, R. C., Campbell-Brown, M. D., & Weryk, R. J. 2011, MNRAS, 414, 3322

Borovička, J., Spurný, P., & Koten, P. 2007, A&A, 473, 661

Brown, P. 1999, Icarus, 138, 287

Brown, P., & Jones, J. 1995, Earth Moon and Planets, 68, 223

—. 1998, Icarus, 133, 36

Brown, P., Weryk, R. J., Wong, D. K., & Jones, J. 2008, Icarus, 195, 317

Brown, P., Wong, D. K., Weryk, R. J., & Wiegert, P. 2010, Icarus, 207, 66

Bruzzone, J. S., Brown, P., Weryk, R. J., & Campbell-Brown, M. D. 2015, MNRAS, 446, 1625

Bulirsch, R. 1972, in Bulletin of the American Astronomical Society, Vol. 4, Bulletin of the American Astronomical Society, 418

Burns, J. A., Lamy, P. L., & Soter, S. 1979, Icarus, 40, 1

Campbell-Brown, M., & Brown, P. G. 2015, MNRAS, 446, 3669

Chambers, J. E. 1999, MNRAS, 304, 793

Combi, M. R., Mäkinen, J. T. T., Bertaux, J.-L., et al. 2013, Icarus, 225, 740

Cremonese, G., Fulle, M., Marzari, F., & Vanzani, V. 1997, A&A, 324, 770

Crifo, J. F., & Rodionov, A. V. 1997, Icarus, 127, 319

DeMeo, F., & Binzel, R. P. 2008, Icarus, 194, 436

Di Sisto, R. P., Fernández, J. A., & Brunini, A. 2009, Icarus, 203, 140

Dumas, C., Owen, T., & Barucci, M. A. 1998, Icarus, 133, 221

Everhart, E. 1967, AJ, 72, 716

Everhart, E. 1985, in Dynamics of Comets: Their Origin and Evolution, Proceedings of IAU
    Colloq. 83, held in Rome, Italy, June 11-15, 1984. Edited by Andrea Carusi and Giovanni B.
    Valsecchi. Dordrecht: Reidel, Astrophysics and Space Science Library. Volume 115, 1985,
    p.185, ed. A. Carusi & G. B. Valsecchi, 185

Fernández, J., & Sosa, A. 2014, in Asteroids, Comets, Meteors 2014. Proceedings of the con-
    ference held 30 June - 4 July, 2014 in Helsinki, Finland. Edited by K. Muinonen et al., ed.
    K. Muinonen, A. Penttilä, M. Granvik, A. Virkki, G. Fedorets, O. Wilkman, & T. Kohout,
    161

Fernández, J. A., Gallardo, T., & Brunini, A. 2002, Icarus, 159, 358

Feroz, F., Hobson, M. P., Cameron, E., & Pettitt, A. N. 2013, ArXiv e-prints, arXiv:1306.2144

Finson, M. J., & Probstein, R. F. 1968, ApJ, 154, 327

Foglia, S., Micheli, M., Ridley, H. B., Jenniskens, P., & Marsden, B. G. 2005, IAU Circ., 8485,
    1

Gehrels, T., & Tedesco, E. F. 1979, AJ, 84, 1079

Gombosi, T. I., Nagy, A. F., & Cravens, T. E. 1986, Reviews of Geophysics, 24, 667

Gronchi, G. F. 2005, Celestial Mechanics and Dynamical Astronomy, 93, 295

Hanner, M. S. 1981, Icarus, 47, 342

Harmon, J. K., Nolan, M. C., Margot, J.-L., et al. 2006, Icarus, 184, 285

Hergenrother, C. 2014, Central Bureau Electronic Telegrams, 3870, 1

Howell, E. S., Nolan, M. C., Taylor, P. A., et al. 2014, in AAS/Division for Planetary Sciences
    Meeting Abstracts, Vol. 46, AAS/Division for Planetary Sciences Meeting Abstracts, 209.24

Ishiguro, M., Kuroda, D., Hanayama, H., et al. 2015, ApJ, 798, L34

Jenniskens, P. 2008, Earth Moon and Planets, 102, 505

—. 2014, WGN, Journal of the International Meteor Organization, 42, 98

Jenniskens, P., & Lyytinen, E. 2005, AJ, 130, 1286

Jewitt, D. 2006, AJ, 131, 2327

Jewitt, D. C. 2004, From cradle to grave: the rise and demise of the comets, ed. M. C. Festou,
    H. U. Keller, & H. A. Weaver, 659–676

Jones, J. 1995, MNRAS, 275, 773

Jones, J., Brown, P., Ellis, K. J., et al. 2005, Planet. Space Sci., 53, 413

Kokhirova, G. I., & Babadzhanov, P. B. 2015, Meteoritics and Planetary Science, 50, 461

Koschack, R., & Rendtel, J. 1990, WGN, Journal of the International Meteor Organization, 18,
    44

Kronk, G. W. 2008, Cometography

Küppers, M., Bertini, I., Fornasier, S., et al. 2005, Nature, 437, 987

Lamy, P. L., Toth, I., Fernandez, Y. R., & Weaver, H. A. 2004, The sizes, shapes, albedos, and
    colors of cometary nuclei, ed. M. C. Festou, H. U. Keller, & H. A. Weaver, 223–264

Levison, H. F., & Duncan, M. J. 1994, Icarus, 108, 18

Madiedo, J. M., Trigo-Rodríguez, J. M., Zamorano, J., et al. 2014, MNRAS, 445, 3309

Marcus, J. N. 2007a, International Comet Quarterly, 29, 39

—. 2007b, International Comet Quarterly, 29, 119

McIntosh, B. A. 1968, in IAU Symposium, Vol. 33, Physics and Dynamics of Meteors, ed. L. Kresak & P. M. Millman, 343

McKinley, D. W. R. 1961, Meteor science and engineering.

Rickman, H., Fernandez, J. A., & Gustafson, B. A. S. 1990, A&A, 237, 524

Rotundi, A., Sierks, H., Della Corte, V., et al. 2015, Science, 347, 3905

Rudawska, R., & Jenniskens, P. 2014, Meteoroids 2013, 217

Schleicher, D. 2014, Central Bureau Electronic Telegrams, 3881, 2

Scotti, J. V. 1994, in Bulletin of the American Astronomical Society, Vol. 26, American Astronomical Society Meeting Abstracts, 1375

Skrutskie, M. F., Cutri, R. M., Stiening, R., et al. 2006, AJ, 131, 1163

Stoer, J. 1972, in Bulletin of the American Astronomical Society, Vol. 4, Bulletin of the American Astronomical Society, 422–423

Tancredi, G. 2014, Icarus, 234, 66

Šegon, D., Gural, P., Andreić, Ž., et al. 2014, WGN, Journal of the International Meteor Organization, 42, 57

Vaubaillon, J., Colas, F., & Jorda, L. 2005, A&A, 439, 751

Weryk, R. J., & Brown, P. G. 2012, Planet. Space Sci., 62, 132

Williams, I. P. 2001, in ESA Special Publication, Vol. 495, Meteoroids 2001 Conference, ed.
    B. Warmbein, 33–42

Wyatt, S. P., & Whipple, F. L. 1950, ApJ, 111, 134

Ye, Q., Brown, P. G., Campbell-Brown, M. D., & Weryk, R. J. 2013, MNRAS, 436, 675

Ye, Q., & Wiegert, P. A. 2014, MNRAS, 437, 3283

Ye, Q., Wiegert, P. A., Brown, P. G., Campbell-Brown, M. D., & Weryk, R. J. 2014, MNRAS,
    437, 3812

Ye, Q.-Z., & Hui, M.-T. 2014, ApJ, 787, 115

Yeomans, D. K. 1981, Icarus, 47, 492

Younger, J., Reid, I., Li, G., Ning, B., & Hu, L. 2015, Icarus

Chapter 4

Dormant comets: a meteor-based survey

A version of this chapter has been accepted by the Monthly Notices of Royal Astronomical Society as:

4.1   Introduction

Dormant comets are comets that have depleted their volatiles and are no longer ejecting dust[1]. Due to their inactive nature, dormant comets cannot be easily distinguished from their asteroidal counterparts by current observing techniques (e.g. Luu & Jewitt, 1990). As the physical lifetime of a comet is typically shorter than its dynamical lifetime, it is logical that a large number of defunct or dormant comets exist (Wiegert & Tremaine, 1999; Di Sisto et al., 2009). Dormant comets in the near-Earth object (NEO) population are of particular interest, as they

---

[1] We note that the term "extinct comet" is also frequently used in the literature. Strictly speaking, "dormant comet" is usually associated with comets that only temporarily lose the ability to actively sublimate, while the term "extinct comet" usually refers to the cometary nuclei that have permanently lost the ability to sublimate (c.f. Weissman et al., 2002, for a more comprehensive discussion). However, in practice, it is difficult to judge whether the comet is temporarily or permanently inactive. In this work we use the general term "dormant comet" which can mean either scenario.

can impact the Earth and contribute to the terrestrial accretion of water and organic materials as normal comets (e.g. Hartogh et al., 2011, and the references therein).

It has long been known that the dust produced by Earth-approaching comets can be detected as meteor showers at the Earth (e.g. Schiaparelli, 1866, 1867). Dormant comets, though no longer being currently active, may have produced dust during their final active phases, which are potentially still detectable as weak meteor showers. This has a significant implication for the investigation of dormant comets, as any cometary features of these objects are otherwise no longer telescopically observable. Past asteroid-stream searches have revealed some possible linkages, the most notable being (3200) Phaethon and the Geminids (e.g. Williams & Wu, 1993; de León et al., 2010; Jewitt et al., 2013, and many others) as well as (196256) 2003 EH$_1$ and the Quadrantids (Jenniskens, 2004; Abedin et al., 2015), both involving meteor showers that are exceptional in terms of activity. However, most showers are weak in activity, making parent identification difficult.

Radar was introduced into meteor astronomy in the 1940s and has developed into a powerful meteor observing technique (c.f. Ceplecha et al., 1998). Radar detects meteors through the reflection of transmitted radio pulses from the ionized meteor trail formed during meteor ablation. Radar observations are not limited by weather and/or sunlit conditions and are able to detect very faint meteors. The Canadian Meteor Orbit Radar (CMOR), for example, has recorded about 14 million meteor orbits as of May 2016, which is currently the largest dataset for meteor orbits and hence a powerful tool to investigate weak meteor showers.

Efforts have been made to the search for dormant comets for several decades. Among the early attempts, Kresak (1979) discussed the use of the Tisserand parameter (Tisserand, 1891) as a simple dynamical indicator for the identification of dormant comets. Assuming Jupiter as the perturbing planet, the Tisserand parameter is defined as

$$T_{\mathrm{J}} = \frac{a_{\mathrm{J}}}{a} + 2 \sqrt{\frac{a(1 - e^2)}{a_{\mathrm{J}}}} \cos i \qquad (4.1)$$

where a_{J} is the semi-major axis of Jupiter, and a, e, and i are the semi-major axis, eccentricity,

and inclination of orbital plane of the small body. A small body is considered dynamically comet-like if $T_J \lesssim 3$. An asteroid with $T_J \lesssim 3$ is classified as an asteroid in cometary orbit (ACO). Note that dormant comets and ACOs are not all physical comets as a fraction of ACOs might originate from the main asteroid belt (e.g. Binzel et al., 2004). Separation of main belt interlopers is difficult, but attempts have been made both dynamically (e.g. Fernández et al., 2002; Tancredi, 2014) and spectroscopically to separate possible cometary nuclei from asteroidal bodies (e.g. Fernández et al., 2005; DeMeo & Binzel, 2008; Licandro et al., 2016). However, few attempts have been made to link ACOs with meteor showers. Jenniskens (2008) provides a comprehensive review of meteoroid streams possibility associated with dormant comets based on the similarity between their orbits, but a comprehensive contemporary "cued" survey to look for all possible weak streams from the large number of recently discovered ACOs/NEOs that may have had weak past activity, including formation of early meteoroid trails, is yet to be performed.

In this work, we present a survey for dormant comets in the ACO component in the NEO population through the meteoroid streams they might have produced during their active phase, using the most complete CMOR dataset available to date. The survey is performed in a "cued search" manner rather than a commonly-used blind search: we first identify eligible ACOs (i.e. with well-determined orbits suitable for longterm integration) in the NEO population (§ 2), then simulate the formation and evolution of the meteoroid trails produced by such ACOs assuming they have recently been active (§ 3), and then search the CMOR data using the virtual shower characteristics to identify "real" streams now visible at the Earth (§ 4). Our survey thus simulates *all* near-Earth ACOs (NEACOs) which are now known and which would have produced meteor showers at the Earth if they were recently active. This approach accounts for orbital evolution of the parent *and* the subsequent evolution of the virtual meteoroid stream.

4.2 Identification of Potential Shower-Producing Objects

4.2.1 Dormant Comets in the NEO Population

To establish the starting conditions for the survey, we first identify possible dormant comets in the NEO population. By definition, NEOs have perihelion distance $q < 1.3$ AU. In this work we focus our sampling among the orbit range of Jupiter-family comets or JFCs which overlaps the NEO population (near-Earth JFCs or NEJFCs as used by other authors). We use a slightly more relaxed constraint than the original Tisserand's derivation, namely $1.95 < T_J < 3.05$, to account for the fact that Tisserand's parameter was derived assuming restricted three-body problem. We consider the precision of the perturbed orbit solution, which is parameterized though the Uncertainty Parameter, U (see Marsden et al., 1978). We only consider objects with $U \leq 2$, as objects falling into this category are considered "secure" and will be permanently numbered[2]. With these criteria, we identify a total of 407 objects from 13 763 known NEOs as of 2016 February 9. These 407 ACOs in the NEO population represent possible dormant comets which may have produced meteoroid streams in the recent past.

4.2.2 Objects with Detectable Meteor Showers

The next step is to simulate the "virtual" meteoroid stream of each object to see if a meteor shower is currently detectable by CMOR. Following the discussion in Ye et al. (2016a), the meteoroid flux $\mathcal{F}$ at Earth can be calculated by

$$\mathcal{F} = \frac{\eta N_m \tau_{\mathrm{stream}}}{P^2 \Delta t_{\mathrm{shower}}^2 V_\oplus^2} \tag{4.2}$$

where η is the fraction of *potentially visible meteoroids*, a subset of the Earth-bound meteoroids that may be visible as meteors, defined as meteoroids with Minimum Orbital Intersection Distance (MOID) < 0.01 AU with respect to the Earth's orbit (typical cross-section of meteoroid

---

[2]See http://www.minorplanetcenter.org/iau/info/UValue.html, retrieved 2016 February 10.
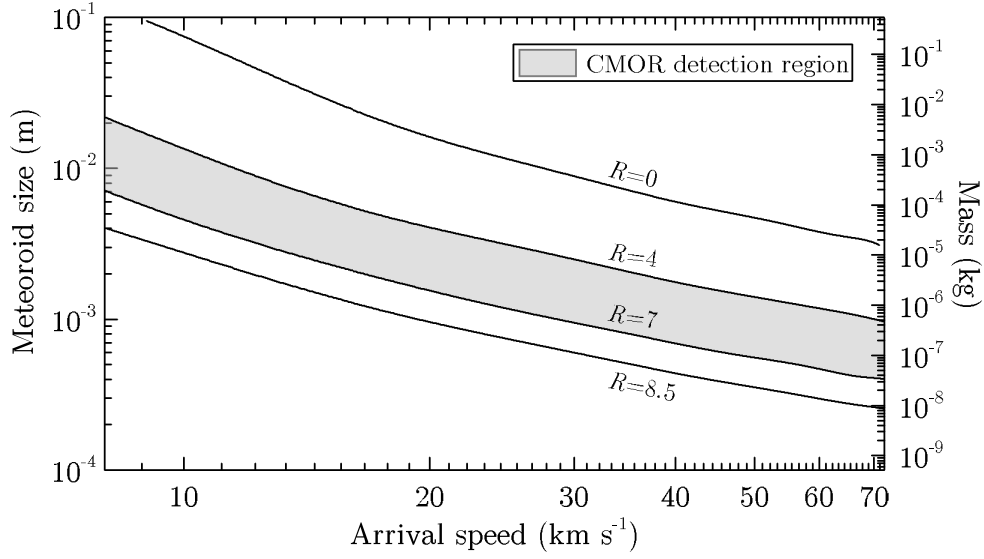
Figure 4.1 Size-speed relation of meteors as a function of absolute magnitude in the general R bandpass of $R = 0$ (typical detection limit of all-sky video networks), $R = 4$ (typical detection limit of narrow field video networks, as well as the upper limit of automated radar detection as meteor echo scattering changes from the underdense to the overdense regime, c.f. Ye et al., 2014), $R = 7$ (CMOR median for meteor orbits) and $R = 8.5$ (CMOR detection limit) assuming bulk density of 1000 kg m^{-3}. Calculated using the meteoroid ablation model developed by Campbell-Brown & Koschny (2004), where the luminous efficiency is constant at 0.7% and the ionization coefficient is from Bronshten (1981). Note that other authors (Jones, 1997; Weryk & Brown, 2013) have argued that these coefficients may be off by up to a factor of ~ 10 at extreme speeds ($v_\mathrm{g} \lesssim 15$ km s^{-1} or $v_\mathrm{g} \gtrsim 70$ km s^{-1}), but most of the showers we examined in this work have moderate v_g, hence this issue does not impact our final results. The CMOR detection range is appropriated to an ionization coefficient I of 5–100 in Wiegert et al. (2009)'s model.

stream, see Brown & Jones, 1998; Göckel & Jehn, 2000); N_m is the meteoroid/dust production of the parent, which we take $N_\mathrm{m} \sim 10^{15}$ per orbit as a median case for near-Earth JFCs (elaborated in Appendix 4.6); τ_stream is the age of the meteoroid stream; P is orbital period of the parent; Δt_shower is the duration of the meteor shower (defined by half-width-half-maximum of the shower), and $V_\oplus = 30$ kms^{-1} is the orbital speed of the Earth.

The CMOR-observed flux will be different from $\mathcal{F}$ as the detection efficiency of CMOR is a function of the meteoroid arrival speed (Figure 4.1) and meteoroid stream size distribution (Figure 4.2). For each virtual stream, we assign η_CMOR being the CMOR detection efficiency,
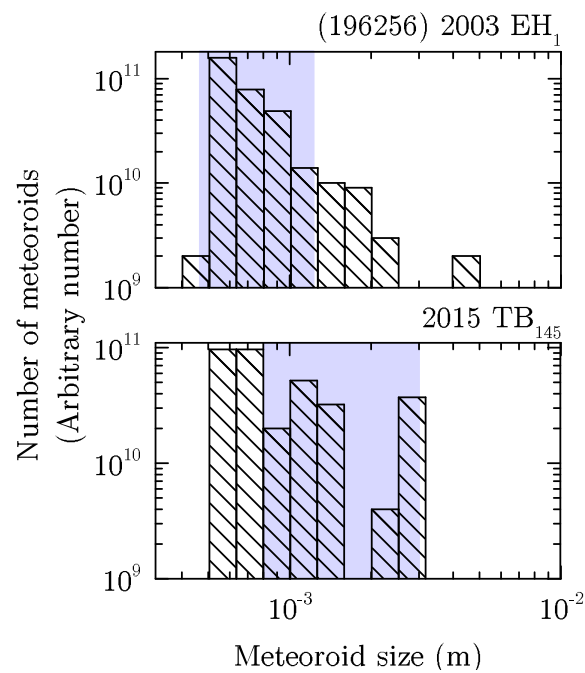
Figure 4.2 Examples of altered arrival size distribution due to different delivery efficiency at different sizes. The meteoroids from (196256) 2003 EH$_1$ (top figure) is more similar to the original size distribution at the parent, while for the case of 2015 TB$_{145}$ (lower figure), larger meteoroids are more efficiently delivered than smaller meteoroids. Shaded areas are the CMOR-detection size range.

as

$$\mathcal{F}_{\text{CMOR}} = \eta_{\text{CMOR}} \cdot \mathcal{F} \qquad\qquad (4.3)$$

There remain four unknown variables: η, τ_{stream}, Δt_{shower} and η_{CMOR}. Typical numbers for the first three variables are $\eta \sim 0.1$ (i.e. 1 out of every 10 simulated meteoroids will reach the Earth), $\tau_{\text{stream}} \sim$ a few 10^2 yr and $\Delta t_{\text{shower}} \sim$ a few days, but all of these quantities are highly variable (McIntosh & Hajduk, 1983; Cremonese et al., 1997; Jenniskens, 2006). For our survey we compute all of these quantities per object (and the fourth variable, η_{CMOR}) numerically using the following procedure.

We define τ_{stream} first as the other three variables depend on it. Simulations are performed using the MERCURY6-based (c.f. Chambers, 1999) meteoroid model developed in our earlier works (e.g. Ye & Hui, 2014; Ye et al., 2015). We employ the ejection model described by Jones (1995) for meteoroids with sizes between 0.5 and 50 mm, a size envelop appropriated to the detection range of CMOR as given by the meteoroid ablation model (Figure 4.1, c.f. Campbell-Brown & Koschny, 2004), assuming a bulk density of 1 000 kg · m^{-3} and a size distribution of dN/d$a \propto a^{-q}$ where $q = 3.6$ (Fulle, 2004, § 5). Meteoroids are released in a time step of 10 d when the parent is within the sublimation line ($r_{\text{h}} < 2.3$ AU). The system of planets, parent bodies and meteoroids are then integrated with a RADAU integrator (Everhart, 1985) with an initial time step of 7 d. Time step is reduced upon close encounters as explained in Chambers & Migliorini (1997). Gravitational perturbations from the eight major planets (with the Earth-Moon system represented by a single mass at the barycenter of the two bodies), radiation pressure, and Poynting-Robertson effect are considered in the integration.

We operationally define τ_{stream} as the time taken for the median D-parameter of any two test meteoroids to grow beyond a given threshold. The D-parameter was originally introduced by Southworth & Hawkins (1963) for meteor shower identification; it is essentially a measure of the similarity between a pair of orbits denoted as A and B:

$$D_{A,B}^2 = (q_B - q_A)^2 + (e_B - e_A)^2 + \left(2 \sin \frac{I}{2}\right)^2 + \left[(e_A + e_B) \sin \frac{\Pi}{2}\right]^2 \tag{4.4}$$

where

$$I = \arccos\left[\cos i_A \cos i_B + \sin i_A \sin i_B \cos (\Omega_A - \Omega_B)\right] \tag{4.5}$$

$$\Pi = \omega_A - \omega_B + 2 \arcsin\left(\cos \frac{i_A + i_B}{2} \sin \frac{\Omega_A - \Omega_B}{2} \sec \frac{I}{2}\right) \tag{4.6}$$

and the subscripts A and B refer to the two orbits being compared. Here q is the perihelion distance in AU, e is the eccentricity, i is the inclination, Ω is the longitude of ascending node, and ω is the argument of perihelion. The sign of the arcsin term in the equation for Π switches if $|\Omega_A - \Omega_B| > 180°$.

The quantity of τ_{stream} can be physically interpreted as a measure of the dispersion timescale of the meteoroid stream, equivalent to the age of the stream.

For each object, the simulation starts with $\tau_{\text{stream}} = 100$ yr. This value is incremented in steps of 100 yr, until the median D-parameter among all test particles that composed the virtual stream reaches $D = 0.1$, an empirical cutoff that was found by Southworth & Hawkins (1963) and was later revisited by many (e.g. Sekanina, 1976; Drummond, 1981; Ceplecha et al., 1998); or $\tau_{\text{stream}} = 10^4$ yr which we adopt as an operational upper limit for the simulation, as this is comparable to the oldest estimated stream ages based on de-coherence timescales (Pauls & Gladman, 2005).

Once τ_{stream} is determined, we calculate the MOID of each test meteoroid with respect to the Earth's orbit at the epoch of 2012 Jan. 1 Terrestrial Time and collect those with MOID< 0.01 AU (i.e. potentially visible meteoroids). The values of η, η_{CMOR} (the number of meteoroids detectable by CMOR size bins divided by the total number of potentially visible meteoroids) and Δt_{shower} (defined as the standard deviation of the solar longitudes of the MOID points) are readily available at this stage. The number of test meteoroids making the CMOR-detectable

virtual meteor shower (not the total simulated test meteoroids which is $\sim 10^5$) at this stage is typically $\sim 10^3$ and at least 100. The virtual meteoroid shower flux for each parent is then calculated using Eq. 4.2 and 4.3. The detection limit for multi-year CMOR data is of the order of 10^{-3} km^{-2} hr^{-1} (Bruzzone et al., 2015). Hence, we only consider virtual showers with $\mathcal{F}_{\mathrm{CMOR}} \gtrsim 10^{-3}$ km^{-2} hr^{-1} as CMOR-detectable showers.

Readers may immediately notice that, for a significant fraction of the objects, the calculated values of τ_{stream} are beyond the typical chaotic timescale of JFCs (~ 1000 yrs, e.g. Tancredi, 1995). Here it is important to note that our approach focuses at the *mean orbit* rather than the exact position of the parent; therefore we are to examine the chaotic timescale of the orbit instead of the parent's location along the orbit. For each object, we generate 100 clones from the covariance matrix of the orbital elements[3] and integrate them backward in time. Similar to the definition of τ_{stream}, we define the parental orbital chaotic timescale τ_{parent} as the time taken for the median D-parameter of any two clones to grow beyond 0.1. Thus, τ_{parent} corresponds to the time that the parent orbit is well constrained and the associated meteoroid stream can therefore be simulated with confidence. The value of τ_{stream} should be viewed cautiously if $\tau_{\mathrm{parent}} \ll \tau_{\mathrm{stream}}$.

Following this procedure, we identify 44 objects that meet both our visibility and detection criteria, and that the stream formation process have the potential of producing CMOR-detectable meteor activity between 2002 and 2015. Note that no geographic constraint is considered at this stage; i.e. southerly virtual radiants are still included. Detailed results are tabulated in Table 4.1 and in Appendix 4.6. The values of τ_{parent} and τ_{stream} for each object are also listed. Several known asteroid-stream linkages are among the list, such as (196256) 2003 EH$_1$ – Quadrantids (Jenniskens, 2004; Abedin et al., 2015) and 2004 TG$_{10}$ – Taurid complex (Jenniskens, 2006; Porubčan et al., 2006). For these established linkages, the calculated radiants and arrival speeds agree with observations within uncertainties, providing some basic validation of the meteoroid modeling approach. In particular, we note that the calculated

---

[3]Available from the JPL Small-Body Database, retrieved on 2016 February 15.

stream ages (τ_{stream}) are 300 yr for Quadrantids and 6100 yr for the 2004 TG$_{10}$ component in the Taurid complex, consistent with previous findings (200 yr for Quadrantids and $\sim 10^4$ yr for Taurids, e.g. Steel et al., 1991; Abedin et al., 2015). Additionally, our model predicts a flux of 0.012 km^{-2} hr^{-1} for the Quadrantids to CMOR's limiting sensitivity, broadly consistent with daily average fluxes of a few 0.01 km^{-2} hr^{-1} (e.g. Brown et al., 1998). The modeled flux for the Taurids, however, is about 100 times higher than observations, likely related to the formation mechanism of the Taurids not being purely sublimation-driven (c.f. Jenniskens, 2006, § 25, and the references therein) which differs from our modeling assumption.

4.3   Prediction of Virtual Meteor Showers

Meteor activity is classified into two categories: annual showers, which are visible every year at more or less the same time and rate; and outbursts, which are enhancements visible in some years but not others. This divide plainly reflects the evolution of the meteoroid cloud: recently-formed meteoroid *trails* experience little differential effects due to radiation pressure and planetary perturbations, and thus tend to remain concentrated in a narrow arc along the orbit and only become visible as meteor outbursts when this "arc" of denser material impacts the Earth. After some time, differential effects gradually stretch the trail along the entire orbit into a meteoroid *stream*, visible as an annual meteor shower every time the Earth arrives at the stream intersection point. Outbursts from young trails provide clues to the ejection state (epoch, particle ejection speed, etc.) of the trails, such as the case of 55P/Tempel-Tuttle and the Leonids (e.g. Yeomans et al., 1996). In contrast, more highly evolved streams are useful for the estimation of the age of the entire stream, such as the case of 109P/Swift-Tuttle and the Perseids (e.g. Brown & Jones, 1998).

For the prediction of annual showers, we use the simulation result obtained in § 4.2.2 and calculate the radiants and timing of the potentially visible meteoroids at the Earth. Results are tabulated in Table 4.1. The values of τ_{parent} and τ_{stream} are also listed in the same table. We find

Parent	H	MOID (AU)	T_J	τ_{parent} (yr)	τ_{stream} (yr)	τ_{enc} (yr)	Node	$\lambda_\odot$	$\lambda - \lambda_\odot$	β	σ_{rad}	v_g (km s^{-1})	$\mathcal{F}_{CMOR}$ (km^{-2} hr^{-1})
(3360) Syrinx	15.9	0.108	2.965	5400	4650	500	☋	212°±2°	357°	+23°	±1°	24.9±0.3	0.001
(16960) 1998 QS$_{52}$	14.3	0.015	3.000	>10000	10000	100	Ω	83°±1°	344°	−13°	±1°	30.8±0.1	2.651
(137427) 1999 TF$_{211}$	15.2	0.020	2.968	5300	550	200	☋	348°±1°	345°	+81°	±1°	24.2±0.2	0.002
(139359) 2001 ME$_1$	16.6	0.012	2.674	4900	700	200	☋	92°±2°	191°	+4°	±1°	29.9±0.3	0.021
(192642) 1999 RD$_{32}$	16.3	0.050	2.872	2500	800	100	Ω	155°±3°	2°	−9°	±1°	22.8±0.6	0.001
(196256) 2003 EH$_1$	16.2	0.212	2.065	1300	300	200	☋	283°±1°	275°	+63°	±1°	41.6±0.2	0.012
(247360) 2001 XU	19.2	0.005	2.749	>10000	6700	100	☋	262°±1°	191°	+17°	±1°	29.1±0.2	0.773
(248590) 2006 CS	16.5	0.105	2.441	2000	1800	200	Ω	352°±1°	305°	−77°	±1°	30.6±0.4	0.419
(297274) 1996 SK	16.8	0.004	2.968	2200	1250	200	☋	204°±3°	184°	+2°	±1°	24.4±0.6	0.009
(307005) 2001 XP$_1$	18.0	0.016	2.560	>10000	10000	200	☋	268°±1°	191°	+50°	±1°	28.5±0.0	0.781
(399457) 2002 PD$_{43}$	19.1	0.029	2.439	>10000	300	300	Ω	130°±3°	334°	−8°	±1°	39.1±0.6	0.002
(401857) 2000 PG$_3$	16.1	0.210	2.550	3200	2150	100	Ω	176°±2°	192°	−12°	±1°	30.2±0.3	0.006
(436329) 2010 GX$_{62}$	20.1	0.014	2.756	>10000	600	200	Ω	25°±2°	19°	−50°	±2°	18.7±0.3	0.003
(442037) 2010 PR$_{66}$	19.3	0.002	2.818	2800	1200	200	Ω	114°±2°	25°	−40°	±4°	16.4±0.2	0.001
(451124) 2009 KC$_3$	18.0	0.006	2.728	4300	900	700	Ω	162°±2°	46°	−31°	±2°	12.6±0.3	0.001
1999 LT$_1$	17.6	0.095	2.586	2100	1800	200	☋	67°±1°	343°	+78°	±1°	25.9±0.5	0.544
2001 HA$_4$	17.7	0.018	2.772	>10000	4250	200	Ω	179°±2°	184°	−20°	±1°	25.0±0.2	0.122
..	..	..	..	..	..	..	☋	360°±2°	357°	+21°	±1°	24.8±0.3	0.028
2002 EV$_{11}$	20.0	0.047	3.046	>10000	6600	150	Ω	355°±3°	339°	−6°	±1°	33.5±0.6	0.013
2003 BK$_{47}$	17.8	0.026	2.857	8500	4750	200	☋	133°±3°	169°	+36°	±2	19.5±0.2	0.006
2003 CG$_{11}$	20.5	0.018	2.900	>10000	7200	200	☋	134°±2°	1°	+30°	±1°	22.9±0.2	0.057
2003 OV	18.3	0.082	2.987	>10000	6300	100	Ω	108°±4°	194°	−5°	±1°	30.0±0.8	0.015
..	..	..	..	..	..	..	☋	346°±4°	346°	+5°	±1°	29.5±0.9	0.008
2004 BZ$_{74}$	18.1	0.032	2.369	7900	3750	100	Ω	60°±1°	192°	−11°	±1°	32.0±0.2	0.044
2004 CK$_{39}$	19.2	0.068	2.991	>10000	9350	150	Ω	197°±3°	348°	−11°	±1°	29.1±0.4	0.002
..	..	..	..	..	..	..	☋	334°±2°	191°	+11°	±1°	29.1±0.4	0.010
2004 TG$_{10}$	19.4	0.022	2.992	6600	6100	400	Ω	102°±2°	346°	−3°	±1°	30.1±0.6	0.094
..	..	..	..	..	..	..	☋	223°±3°	194°	+3°	±1°	30.0±0.5	0.065
2005 FH	17.7	0.038	2.821	6200	8100	150	Ω	328°±2°	3°	−58°	±2°	22.5±0.2	0.012
2005 UN$_{157}$	18.2	0.420	2.581	6000	3750	200	Ω	175°±2°	339°	−13°	±1°	36.4±0.4	0.008
..	..	..	..	..	..	..	☋	261°±3°	203°	+13°	±1°	36.9±0.5	0.003
2005 WY$_{55}$	20.7	0.004	3.042	4700	2500	1200	Ω	70°±3°	7°	−12°	±1°	19.6±0.6	0.012
2006 AL$_8$	18.4	0.056	2.159	2900	7300	100	☋	312°±2°	339°	+24°	±1°	36.0±0.4	0.013
2006 KK$_{21}$	20.4	0.033	2.605	5000	4000	100	Ω	51°±2°	347°	−11°	±1°	30.5±0.4	0.022
..	..	..	..	..	..	..	☋	180°±2°	192°	+10°	±1°	30.2±0.3	0.031
2007 CA$_{19}$	17.6	0.019	2.679	4300	300	100	Ω	354°±1°	185°	−10°	±1°	27.1±0.2	0.018
..	..	..	..	..	..	..	☋	190°±1°	355°	+10°	±1°	27.0±0.1	0.010
2008 SV$_{11}$	18.4	0.018	2.957	8400	3300	200	☋	8°±4°	10°	+15°	±3	18.6±0.5	0.005
2008 YZ$_{28}$	20.0	0.094	2.969	3300	4000	200	☋	270°±6°	358°	+54°	±5	23.8±0.4	0.001
2009 HD$_{21}$	18.2	0.015	2.881	6900	1400	100	☋	180°±3°	20°	+41°	±3	17.7±0.2	0.005
2009 SG$_{18}$	17.8	0.025	2.313	8500	9250	200	☋	177°±1°	237°	+70°	±1°	34.1±0.3	0.172
2009 WN$_{25}$	18.4	0.114	1.959	2700	100	400	☋	232°±1°	271°	+63°	±1°	41.7±0.1	1.034
2010 JL$_{33}$	17.7	0.033	2.910	4100	4000	100	Ω	250°±5°	10°	−8°	±2°	19.0±1.1	0.001
2010 XC$_{11}$	18.7	0.030	2.792	6400	850	700	Ω	282°±2°	192°	−7°	±1°	29.9±0.4	0.002
2011 GH$_3$	18.5	0.149	3.020	8600	6850	200	Ω	237°±1°	357°	−9°	±1°	24.6±0.2	0.011
..	..	..	..	..	..	..	☋	49°±1°	183°	+9°	±1°	24.7±0.2	0.013
2011 GN$_{44}$	18.3	0.009	2.922	>10000	10000	200	Ω	196°±1°	318°	−65°	±1°	32.6±0.1	5.829
2012 BU$_{61}$	21.3	0.027	2.933	8400	1700	1100	Ω	101°±4°	180°	−6°	±1°	23.1±0.9	0.002
..	..	..	..	..	..	..	☋	280°±4°	359°	+6°	±1°	23.5±1.0	0.001
2012 FZ$_{23}$	18.2	0.020	2.367	4400	1250	200	☋	359°±1°	269°	−61°	±1°	41.7±0.2	0.369
2012 HG$_8$	19.7	0.004	2.967	4000	2800	100	☋	215°±4°	182°	+36°	±3	23.7±0.3	0.013
2012 TO$_{139}$	19.7	0.001	2.759	4800	300	100	Ω	290°±4°	196°	−4°	±1°	33.1±0.8	0.001
..	..	..	..	..	..	..	☋	179°±1°	345°	+3°	±1°	32.6±0.1	0.196
2015 TB$_{145}$	19.9	0.002	2.964	>10000	10000	100	Ω	217°±1°	204°	−24°	±1°	34.9±0.2	1.738

Table 4.1: Objects that are capable of producing CMOR-detectable annual meteor activity. Listed are the properties of the parent (absolute magnitude H, Tisserand parameter with respect to Jupiter, T_J, Minimum Orbit Intersection Distance (MOID) with respect to the Earth, orbital chaotic timescale τ_{parent}), dynamical properties of the hypothetical meteoroid stream (stream age τ_{stream}, encircling time τ_{enc}), and calculated meteor activity at ascending node Ω and/or descending node ☋ (including the time of activity in solar longitude $\lambda_\odot$, radiant in J2000 sun-centered ecliptic coordinates, $\lambda - \lambda_\odot$ and β, radiant size σ_{rad}, geocentric speed v_g, and meteoroid flux $\mathcal{F}$ derived from the median JFC model.

the median τ_{parent} to be 4300 yr, comparable to the typical timescale of 100% growth in the positional uncertainty of a JFC (Tancredi, 1995). For individual bodies, τ_{parent} depends on the dynamical characteristics of the body as well as the precision of the observations. Objects with extremely long τ_{parent} are usually found in/near mean-motion resonances, and/or observed by high-precision techniques (e.g. radar observations). The median τ_{stream} is found to be ~ 1800 yr, which is also consistent with other studies (e.g. Babadzhanov & Obrubov, 1992; Jenniskens, 2006, §26.1).

For the prediction of meteor outbursts, we first probe the transition timescale from trail to stream, or simply the *encircling time* of the meteoroid cloud, τ_{enc}. In another sense, τ_{enc} corresponds to the time that the ejection state of a meteoroid trail is preserved. We define τ_{enc} as the time taken for the standard deviation of the mean anomalies of the meteoroids to reach $60°$ (The mathematical consideration is that 99.7% or 3σ of the meteoroids spread along half the orbit or $180°$ in mean anomaly assuming a Gaussian distribution). The simulation is conducted in the same manner as the simulation in § 4.2.2. We then follow the evolution of the meteoroid trail formed by each parent up to τ_{enc} years preceding 2012 AD and search for encounters between the trails and the Earth in CMOR-operational years (2002–2015). For each encounter, we estimate the meteoroid flux following the method described in Ye et al. (2016b) taking the median JFC model for dust production of the parent. We only consider encounters with the Earth's orbit of less than ~ 0.002 AU (c.f. the discussion regarding the "second space criterion" in Vaubaillon et al., 2005) and predicted meteoroid flux $\mathcal{F}_{\text{CMOR}} > 10^{-2}$ km^{-2} hr^{-1}, the detection limit of single year CMOR data (Ye et al., 2016b). Our model predicts 25 outburst events from a total of 11 objects that are potentially detectable by CMOR. These are tabulated in Table 4.4.

4.4   Observational Survey of Virtual Meteor Activity

The observational data for our survey is gathered by CMOR, an interferometric backscatter radar system located near London, Canada (e.g. Jones et al., 2005; Brown et al., 2008; Weryk & Brown, 2012). CMOR consists of one main site equipped with an interferometer as well as five remote receivers, all of which operate at 29.85 MHz (Ye et al., 2013). Orbits of the meteoroids can be derived from the interferometry and the time delay for common radar echoes between various stations. Routine and continuous observation commenced in early 2002. As of early 2016, CMOR has measured $\sim$ 13 million meteor orbits with a corresponding representative meteor magnitude of $\sim$ +7.

Meteor showers (outbursts) are defined as an enhancement in meteor rates from a certain celestial point (the *radiant*) at a certain speed over a short period of time. The wavelet transform method has been demonstrated as a robust method for shower identification in radar data (Galligan, 2000). Here we perform the survey search using a quasi 4-dimensional Mexican hat wavelet, with the wavelet coefficient $\psi(x_0, y_0, v_{g,0})$ at celestial coordinate (x_0, y_0) and speed $(v_{g,0})$ defined as:

$$
\begin{aligned}
\psi(x_0, y_0, v_{g,0}) = {} & \frac{1}{(2\pi)^{3/2} \sigma_v^{1/2}} \int_{v_{g,\min}}^{v_{g,\max}} \int_{-\infty}^{\infty} \int_{-\infty}^{\infty} f\left(x, y, v_g\right) \\
& \times \left[3 - g\left(x, y, \sigma_{\mathrm{rad}}\right) - h\left(v_g, \sigma_v\right) \right] \\
& \times \exp\left\{ -\frac{1}{2} \left[g\left(x, y, \sigma_{\mathrm{rad}}\right) - h\left(v_g, \sigma_v\right) \right] \right\} \mathrm{d}x\mathrm{d}y\mathrm{d}v_g
\end{aligned}
\tag{4.7}
$$

and

$$
g(x, y, \sigma) = \frac{(x - x_0)^2 + (y - y_0)^2}{\sigma^2}
\tag{4.8}
$$

$$
h(v_g, \sigma_v) = \frac{(v_g - v_{g,0})^2}{\sigma_v^2}
\tag{4.9}
$$

where $f(x, y, v_g)$ is the distribution of radiants, σ_{rad} and σ_v are the spatial and speed probe sizes, x, y and v_g are spatial coordinates and speed in the geocentric space of observed radiants.

To enhance the signal from annual weak showers, we follow the procedure described in Bruzzone et al. (2015) and combine the entire CMOR dataset into a stacked virtual year. The data in both calendar year and stacked virtual year are divided into $1°$ solar longitude bins, producing a quasi 4-dimensional data-set that is then analyzed using the wavelet technique. The wavelet transform detects only radiants within roughly one spatial/speed probe size, as these contribute significantly to the wavelet coefficient. As such, radiant distributions that match the specified spatial/speed probe sizes will show enhanced wavelet coefficient. For most showers, the simulated radiants are very compact such that the spatial/speed spreads are comparable to or smaller than CMOR's measurement uncertainty. For these cases we use the empirical probe sizes of $4°$ and 10% adopted by Brown et al. (2008) for shower detection.

For each shower/outburst, we inspect the variation of $\psi(x_0, y_0, v_{g,0})$ as a function of time within the virtual/natural year to search for enhancements. Positive detections behave as a rise in $\psi(x_0, y_0, v_{g,0})$ that is well above the background noise (e.g. Brown et al., 2010, Fig. 1).

4.5 Results and Discussion

4.5.1 Annual Showers from Old Streams

Among the 44 virtual streams predicted to be detectable by CMOR, we identify four probable positive detections in the stacked CMOR data that can be associated with (196256) 2003 EH_1, 2004 TG_{10}, 2009 WN_{25}, and 2012 BU_{61}, as shown in Figure 4.3. Among these associations, two are considered established: (196256) 2003 EH_1 and the Quadrantids (e.g. Jenniskens, 2004; Abedin et al., 2015) and 2004 TG_{10} as part of the Taurids complex (e.g. Jenniskens, 2006; Porubčan et al., 2006); one is recently proposed: 2009 WN_{25} annd the November i Draconids (Micheli et al., 2016). For all these three cases, the predicted shower characteristics are consistent with the observations, except for the activity duration of the November i Draconids

– 2009 WN$_{25}$ pair. The predicted duration is about 1 day while the observed activity lasted for ∼ 20 days (Brown et al., 2010). This simply reflects the fact that we assume the operational stream age τ_{stream} = 100 yr while the actual stream might be much older (and thus more dispersed). One node of the detection associated with 2012 BU$_{61}$ is identified with the Daytime ξ Sagittariids (descending node), which in turn has been previously associated with 2002 AU$_5$ (Brown et al., 2010) though the linkage is not considered well established. The ascending nodal intersection for 2012 BU$_{61}$ can not be identified with any known showers, but does show detectable enhancement as shown in Figure 4.3.

A complicating issue in the parent-shower linkage is the likelihood of chance alignment. This is especially true as there are over 14 000 known NEOs and ∼ 700 identified/proposed meteor showers as of May 2016[4]. Therefore, **it is not sufficient to propose a linkage by simply noting the similarity of the respective orbits**. Instead, following the exploration by Wiegert & Brown (2004), we evaluate the following question to establish orbital similarity significance: consider the D_{SH} parameter between the proposed parent-shower pair to be D'_0, what is the expected number of parent bodies $\langle X \rangle$ that have orbits such that $D' < D'_0$ (where D' is the D_{SH} parameter between the "new" parent and the shower)?

This question can be answered using a NEO population model providing the orbits of the possible parent and the meteoroid stream are well known. We employ the de-biased NEO model developed by Greenstreet et al. (2012) and generate two large samples of NEOs down to absolute magnitude H = 18 and H = 22 following α = 0.35 for H < 18 and α = 0.26 for 18 < H < 22 (where α is the size distribution index of the NEO population; see Jedicke et al., 2015). Orbits of the meteoroid streams of interest are calculated from the respective wavelet maxima as found in the CMOR data. The ascending node activity for 2012 BU$_{61}$ is heavily contaminated by sporadic activity later in the year ($\lambda_\odot$ ∼ 240°) which prevents useful orbits to be obtained. This procedure is repeated for the proposed linkages of November i Draconids – 2009 WN$_{25}$ and Daytime ξ Sagittariid – 2002 AU$_5$ and 2012 BU$_{61}$. The results are summarized

---

[4]http://www.minorplanetcenter.net/mpc/summary and http://www.astro.amu.edu.pl/~jopek/ MDC2007/Roje/roje_lista.php?corobic_roje=0&sort_roje=0, retrieved 2016 May 7.
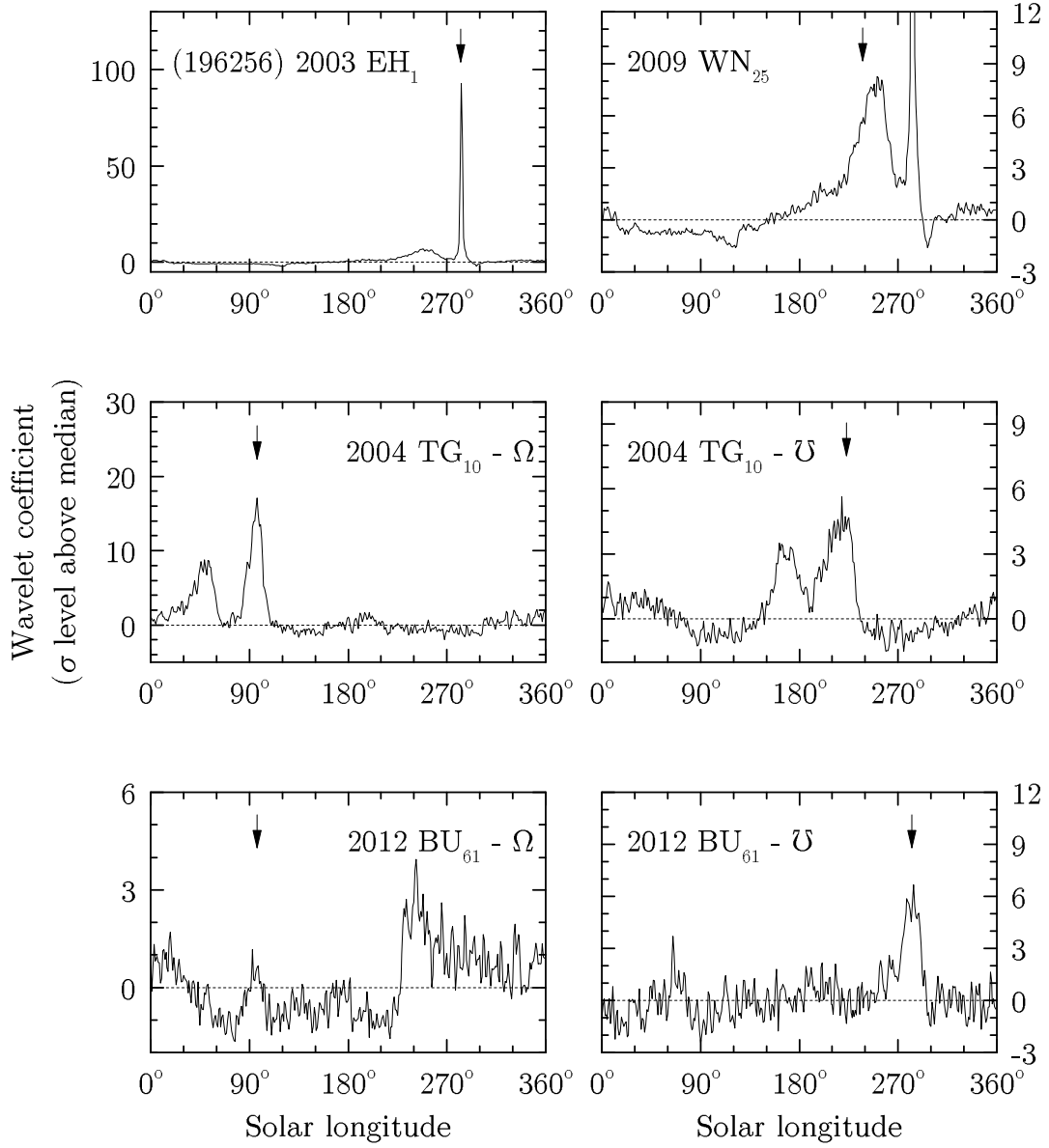
Figure 4.3 Detection of annual meteor activity that may be associated with (196256) 2003 EH$_1$, 2004 TG$_{10}$ (both ascending node Ω and descending node $\mho$), 2009 WN$_{25}$, 2011 BE$_{38}$ and 2012 BU$_{61}$ (both ascending node Ω and descending node $\mho$). Activity peaks are highlighted by arrows. The figures show the relative wavelet coefficients at radiants given in each graph in units of the numbers of standard deviations above the annual median.

	Orbital elements (J2000)					Geocentric radiant (J2000)			$\langle X \rangle$	
	q (AU)	e	i	Ω	ω	$\lambda - \lambda_\odot$	β	v_g (km s^{-1})	$H < 18$	$H < 22$
2009 WN$_{25}$ ($H = 18.4$) – November i Draconids										
2009 WN$_{25}$	1.10238	0.66278	71.986°	232.086°	180.910°	271°	+63°	41.7		
						±1°	±1°	±0.1		
Shower prediction – this work	0.987	0.619	73.6°	238.0°	184.6°	267.6°	+62.0°	41.4	0.001–0.05	0.02–0.6
	±0.002	±0.133	7 ± 2.3°	±0.5°	±2.9°	±0.1°	±0.1°	±0.1		
Observed shower – Brown et al. (2010)	0.9874	0.737	74.9°	241.0°	181.09°	270.1°	+62.5°	43	0.003	0.04
Observed shower – Jenniskens et al. (2016)	0.973	0.734	72.9°	254.4°	194.7°	260.9°	+63.2°	41.9	0.4	6
2002 AU$_5$ ($H = 17.8$) & 2012 BU$_{61}$ ($H = 21.5$) – Daytime ξ Sagittariids (XSA) & Daytime Scutids (JSC)[b]										
2002 AU$_5$	0.40301	0.75531	9.256°	354.989°	21.261°	359°	+6°	23.5		
						±1°	±1°	±1.0		
2012 BU$_{61}$	0.55333	0.78023	5.277°	297.700°	72.461°	359°	+6°	23.5		
						±1°	±1°	±1.0		
XSA prediction – this work	0.46	0.77	5.9°	291.0°	76.6°	352.6°	+6.4°	25.2	AU$_5$: 0.8–1.2	AU$_5$: 10–15
	±0.02	±0.04	±1.0°	±0.5°	±2.1°	±0.1°	±0.1°	±0.1	BU$_{61}$: 0.05–0.2	BU$_{61}$: 0.6–2
XSA observation – Sekanina (1976)	0.29	0.74	1.1°	304.9°	46.9°	338.0°	+0.9°	24.4	AU$_5$: 12–13	AU$_5$: 156–164
	±0.01	±0.02	±0.7°	±1.4°	±1.8°	±1.0°	±0.6°		BU$_{61}$: 8–10	BU$_{61}$: 101–126
XSA observation – Brown et al. (2010)	0.4708	0.784	6.0°	288.0°	79.31°	353.9°	+6.6°	25.3	AU$_5$: 1.0	AU$_5$: 13
									BU$_{61}$: 0.04	BU$_{61}$: 0.6
JSC observation – Sekanina (1973)	0.55	0.77	12.4°	280.4°	89.4°	358.5°	+15.4°	24.1	AU$_5$: 1.8–2.3	AU$_5$: 23–29
	±0.01	±0.02	±1.4°	±0.5°	±1.1°	±0.4°	±1.8°		BU$_{61}$: 0.05–0.3	BU$_{61}$: 0.3–4

Table 4.2: Orbits and radiant characteristics of possible meteor activity associated with 2009 WN$_{25}$ and 2012 BU$_{61}$. Listed are perihelion distance q, eccentricity e, inclination i, longitude of ascending node Ω and argument of perihelion ω for the parent (taken from JPL 31, 28 and 15 for the respective parent) and the meteor shower from the given reference. The uncertainties in the orbital elements for the parents are typically in the order of 10^{-5} to 10^{-8} in their respective units and are not shown. Epochs are in J2000. Shown are the absolute magnitude of the parent as well as the expected number of NEOs with $H < 18$ and $H < 22$ that have $D' < D'_0$ relative to that of the proposed parent. Values of $\langle X \rangle$ near or larger than 1 suggest that the association is not statistically significant.

in Table 4.2.

We observe the following:

1. The statistical model supports 2009 WN$_{25}$ as the likely parent for the November i Draconids.

2. The case of 2012 BU$_{61}$ and the Daytime ξ Sagittariids is complicated. The orbits derived from this work and Brown et al. (2010) are notably different from the one initially proposed in the Harvard Radio Meteor Project (Sekanina, 1976, listed as ξ Sagittariids, though the IAU catalog has identified it as the same shower) which has $D_{SH} = 0.28$, though this work and Brown et al. (2010) use virtually the same data. The Daytime ξ Sagittariids has not been reported by a third observing system. However, we note that the Daytime Scutids, another unestablished shower reported by the Harvard survey, resembles the orbit of the Daytime ξ Sagittariids observed by CMOR (see Sekanina, 1973, the orbit of Daytime Scutids is appended in Table 4.2), with $D_{SH} = 0.15$. We suspect

that these two different showers have been accidentally assigned the same name. The association to 2012 BU$_{61}$ would be statistically significant, either using the CMOR orbit or the Harvard orbit for the Daytime Scutids.

3. The linkage between 2002 AU$_5$ and Daytime ξ Sagittariids or Daytime Scutids is not statistically significant.

We note that among the four parent-shower associations found by our survey, three parents, namely 2004 TG$_{10}$, 2009 WN$_{25}$ and 2012 BU$_{61}$, are sub-kilometer bodies. They are likely larger fragments of break-ups, as rotational disruption is considered as an effective mechanism in eliminating sub-kilometer bodies (Rubincam, 2000; Taylor et al., 2007; Jewitt et al., 2010). In fact, 2004 TG$_{10}$ is generally recognized as being part of the Taurid complex (Porubčan et al., 2006), while the November i Draconid streams (which 2009 WN$_{25}$ is linked to) has been considered to be associated with the Quadrantid stream (Brown et al., 2010).

In addition to the positive detections, we have not reproduced a number of previously proposed associations. Our initial shortlist included most of the objects in earlier proposed associations except objects with short orbital arc (i.e. low orbit quality). The calculation of $\langle X \rangle$ is repeated for every proposed association. As shown in Table 4.3, only 8 out of 32 previously proposed associations have $\langle X \rangle \ll 1$:

1. Corvids – (374038) 2004 HW. Linkage first proposed by Jenniskens (2006). The Corvid meteor shower is one of the slowest known meteor showers, with $v_\mathrm{g} = 9$ km s^{-1}. It was only observed in 1937 (Hoffmeister, 1948) until being recently recovered by Jenniskens et al. (2016) and has not been detected by many radar and photographic surveys. The Corvids are undetected by CMOR, which is unsurprising as back-scatter radars are insensitive to very slow meteors.

2. ψ Cassiopeiids – (5496) 1973 NA. Linkage first proposed by Porubcan et al. (1992). The object is not included in Table 4.1 due to low expected flux being below the CMOR

Shower	Proposed parent	H	Reference	$\langle X \rangle_{H<18}$	$\langle X \rangle_{H<22}$
Established showers:					
Corvids	(14827) Hypnos	18.3	O87, J16, JPL 49	1.4	18
..	(374038) 2004 HW	17.0	Je06, J16, JPL 60	0.1	1.4
Daytime April Piscids	2003 MT$_9$	18.6	B09, B10, JPL 37	0.9	11
..	(401857) 2000 PG$_3$[a]	16.1	B09, B10, JPL 43	34	432
..	2002 JC$_9$[a]	18.5	B09, B10, JPL 26	10	121
κ Cygnids	(153311) 2001 MG$_1$	17.2	Jo06, J16, JPL 63	0.8	10
..	(361861) 2008 ED$_{69}$	17.0	J08, J16, JPL 36	1.7	21
Northern ι Aquariids	2003 MT$_9$	18.6	B09, J16, JPL 37	9	114
ψ Cassiopeiids	(5496) 1973 NA	16.0	P92, J16, JPL 51	0.2	1.9
Unestablished showers:					
66 Draconids	2001 XQ	19.2	S14a, JPL 14	0.003	0.04
August θ Aquillids	2004 MB$_6$	19.5	K14, K15, JPL 17	16	203
Daytime April Cetids	2003 MT$_9$	18.6	K67, B09, JPL 37	0.6	8
Daytime c Aquariids	(206910) 2004 NL$_8$	17.1	G75, Je06, JPL 108	7	89
Daytime δ Scorpiids	2003 HP$_{32}$[b]	19.6	N64, B15, JPL 17	0.6	8
..	2007 WY$_3$[b]	18.2	N64, B15, JPL 18	6	75
δ Mensids	(248590) 2006 CS	16.5	Je06, JPL 48	0.001	0.02
η Virginids	2007 CA$_{19}$	17.6	B15, J16, JPL 56	3.3	42
γ Piscids	6344 P-L	20.4	T89, Je06, JPL 16	51	648
γ Triangulids	2002 GZ$_8$	18.2	P94, Je06, JPL 33	3.1	39
ι Cygnids	2001 SS$_{287}$	18.3	A13, JPL 21	0.1	1.2
κ Cepheids	2009 SG$_{18}$	17.8	S15, JPL 22	0.0004	0.006
λ Cygnids	(189263) 2005 CA	15.6	T89, Je06, JPL 51	15	185
Northern δ Leonids	(192642) 1999 RD$_{32}$	16.3	L71, Je06, JPL 125	0.7	9
Northern δ Piscids	(401857) 2000 PG$_3$[a]	16.1	B09, J16, JPL 43	24	302
..	2002 JC$_9$[a]	18.5	B09, J16, JPL 26	8	107
Northern γ Virginids	2002 FC	18.9	T89, Je06, JPL 52	0.2	2.2
Northern σ Sagittariids[c]	(139359) 2001 ME$_1$	16.6	S76, Je06, JPL 71	2.3	29
Southern α Leonids	(172678) 2003 YM$_{137}$	18.7	Je06, JPL 51	13	166
Southern δ Piscids	(401857) 2000 PG$_3$[a]	16.1	B09, J16, JPL 43	15	195
..	2002 JC$_9$[a]	18.5	B09, J16, JPL 26	20	251
Southern ι Aquariids	2003 MT$_9$	18.6	B08, B09, JPL 37	0.6	7
ζ^1 Cancrids	2012 TO$_{139}$	19.7	S14b, JPL 13	0.08	1.0

Table 4.3: Previously proposed associations that are not reproduced in this work. Only objects that are in our initial 407-object list are included. "Established showers" means confirmed meteor showers in the IAU catalog, not established parent-shower linkages (likewise for unestablished showers). Listed are the absolute magnitude of the parent H, sources where the linkage was proposed, orbital elements, and $\langle X \rangle$ for the NEO population of $H < 18$ and $H < 22$.

detection limit. Our test simulation shows that only a small fraction ($< 0.1\%$) of sub-millimeter-sized meteoroids (~ 0.1 mm) released in the past 1000 yr would be arriving at the Earth's orbit. The fact that the meteor shower is detectable by video techniques (which only detect larger, millimeter-sized meteoroids) is incompatible with the modeling result.

3. 66 Draconids – 2001 XQ. The unconfirmed shower has only been reported by Šegon et al. (2014b) who also propose the linkage. Our survey wavelet analysis at the reported radiant of the 66 Draconids did not detect any enhancement.

4. δ Mensids – (248590) 2006 CS. Linkage first proposed by Jenniskens (2006). The unconfirmed shower is only accessible by observers in the southern hemisphere.

5. ι Cygnids – 2001 SS$_{287}$. Linkage first proposed by Andreić et al. (2013) who remains the only observer of this unconfirmed shower at the time of writing. No enhancement is seen in the CMOR wavelet analysis at the reported radiant.

6. κ Cepheids – 2009 SG$_{18}$. Shower discovered by Šegon et al. (2015) who also propose the linkage. The predicted radiant is consistent with the reported radiant of κ Cepheids. The meteoroid speed is favorable for radar detection ($v_g = 34$ km s^{-1}) and a relatively strong flux is predicted ($\mathcal{F} = 0.22$ km^{-2} hr^{-1}), however no enhancement is seen in the wavelet analysis at either the predicted or the reported radiant.

7. Northern γ Virginids – 2002 FC. Linkage proposed by Jenniskens (2006). This unestablished shower has only been reported by Terentjeva (1989) who analyzed photographic fireball observations from 1963 to 1984. No enhancement is seen in wavelet analysis of the CMOR data at the reported radiant.

8. ζ^1 Cancrids – 2012 TO$_{139}$. Shower detection as well as potential linkage are both identified by Šegon et al. (2014a). No enhancement is seen in the CMOR wavelet analysis

at the predicted radiant. Also, the model predicts a stronger descending nodal shower which is also not seen in CMOR data.

It should be emphasized that the statistical test only addresses the likelihood of finding a better parent body match for a given stream orbit; it does not take into account the false positives in shower identification, a complicated issue heavily investigated for half a century (e.g. Southworth & Hawkins, 1963; Drummond, 1981; Galligan, 2001; Brown et al., 2008; Moorhead, 2016, and many others). There exists a danger of assigning a small body as the "parent" of some random fluctuation in the meteoroid background. This is especially true for unestablished showers, as most of them have been observed by only one observer.

4.5.2   Outbursts from Young Trails

Among the predictions given in Table 4.4, only one prediction is associated with a distinct detection: the event from (139359) 2001 ME_1 in 2006 (Figure 4.4, 4.5 and Table 4.5). The association is of high statistical significance, as $\langle X \rangle_{H<18} \sim 0.01$. From the wavelet profile, we estimate that the observed flux is close to the detection threshold or $\sim 10^{-2}$ km^{-2} hr^{-1}, as the signal is not very significantly higher than the background fluctuation. The event, if indeed associated with (139359) 2001 ME_1, should have originated from a relatively recent (< 100 yr) ejection event. Since the observed flux is about the same order as the model prediction, it can be estimated that the dust production associated to the ejection is comparable to the average dust production of known near-Earth JFCs. Curiously, the annual shower associated with (139359) 2001 ME_1, though with a moderate expected flux, is not detected. This may suggest that the ejection was a transient event rather than a prolonged one, possibly similar to the activity of 107P/(4015) Wilson-Harrington upon its discovery in 1949 (c.f. Fernández et al., 1997).

Another interesting aspect of our survey is the negative detection of several strong predicted events (with $\mathcal{F}_{CMOR} \gtrsim 1$ km^{-2} hr^{-1}). These can be used to place a tight constraint on the past dust production of the parent. It can be concluded that the dust production of 2001 HA$_4$, 2012
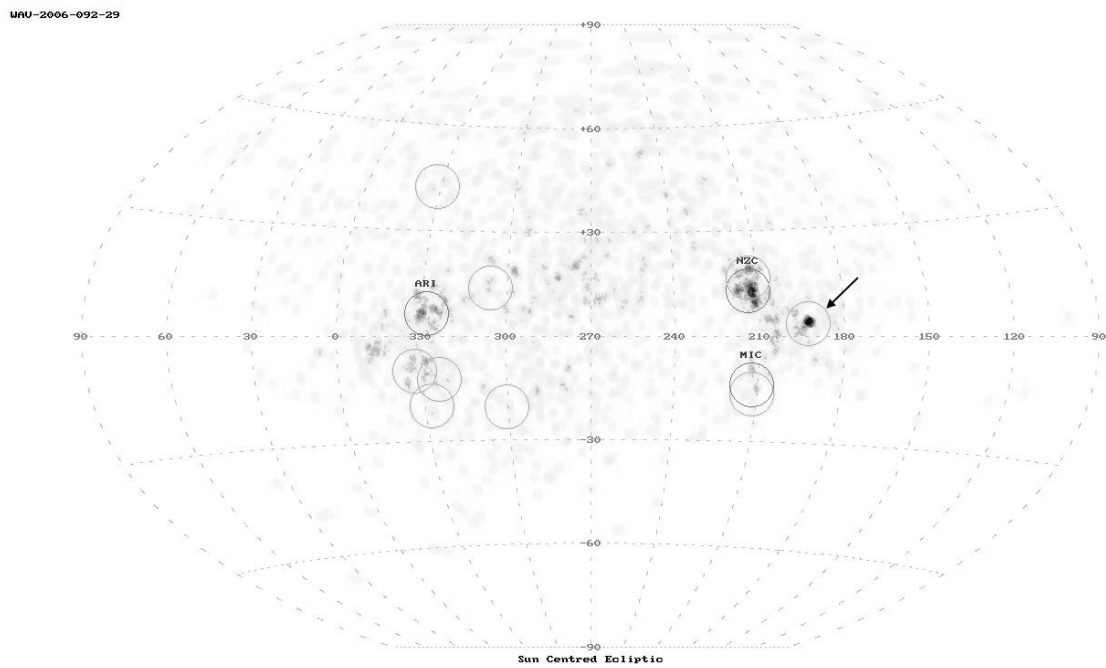
Figure 4.4 Possible activity from (139359) 2001 ME$_1$ on 2006 Jun. 24 in sun-centered ecliptic sphere. Darker contour corresponds to areas in the sky with denser radiants. Known showers are marked by dark circles and the International Astronomical Union (IAU) shower designation (ARI = Arietids, NZC = Northern June Aquilids, MIC = Microscopiids). Unknown enhancements are marked by gray circles. Note that most enhancements are random fluctuations. The possible activity associated with (139359) 2001 ME$_1$ is the strong enhancement near $\lambda - \lambda_\odot = 190°, \beta = +5°$.
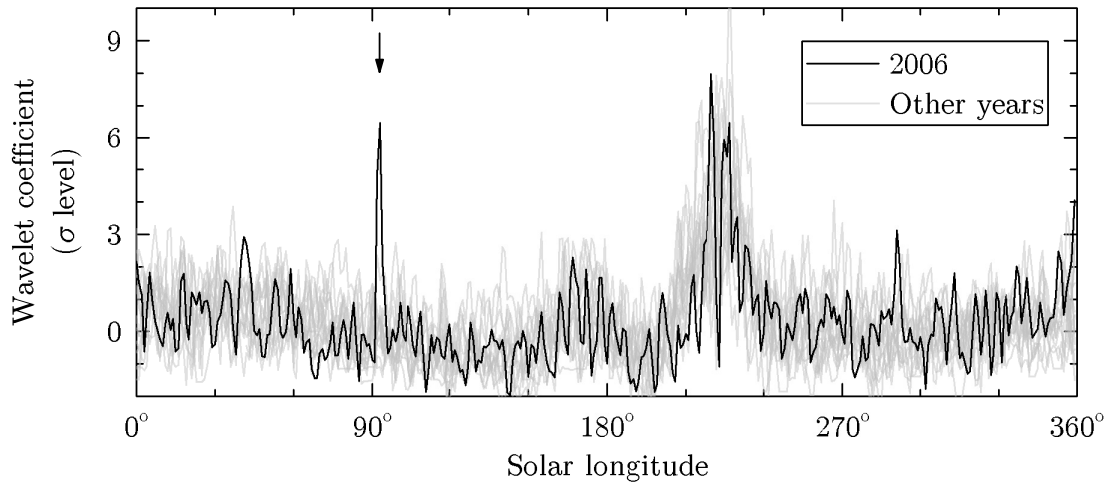
Figure 4.5 Variation of the wavelet coefficient at $\lambda - \lambda_\odot = 191°, \beta = +4°$ and $v_g = 30.0$ km s^{-1} in 2002–2015 (gray lines except for 2006). Possible activity from (139359) 2001 ME$_1$ in 2006 is marked by an arrow. Recurring activity around $\lambda_\odot = 220°$ is from the Taurids complex in November.

Parent	τ_{enc} (yr)	Date (UT)	Ejection	$\lambda_\odot$	$\lambda - \lambda_\odot$	β	v_g (km·s^{-1})	$\mathcal{F}_{CMOR}$ (hr^{-1}·km^{-2})
(139359) 2001 ME$_1$	200	2006 Jun. 24	1924–1967	93°	191°	+4°	30.0	0.01
(247360) 2001 XU	100	2014 Dec. 14	1903–1993	263°	190°	+17°	29.1	0.02
(297274) 1996 SK	200	2007 Apr. 17	1870–1903	27°	2°	−3°	21.5	0.01
(435159) 2007 LQ$_{19}$	200	2002 Jul. 13	1801–1978	111°	139°	+50°	14.1	0.01
..	..	2006 Jul. 13	1801–2003	111°	139°	+50°	14.1	0.03
..	..	2007 Jul. 13	1805–2003	111°	139°	+50°	14.1	0.04
2001 HA$_4$	200	2005 Sep. 21	1807–1974	179°	184°	−20°	24.5	2.71
2005 WY$_{55}$	1200	2002 May 31†	994–1765	70°	8°	−12°	19.3	0.16
..	..	2006 May 31‡	990–1753	70°	7°	−12°	19.5	0.14
..	..	2010 May 31	875–1761	70°	8°	−12°	19.4	0.06
..	..	2014 May 31	951–1725	70°	7°	−12°	19.5	0.05
2007 CA$_{19}$	100	2012 Mar. 14	1965–1993	354°	185°	−10°	27.1	0.42
2009 SG$_{18}$	200	2006 Sep. 20	1831–1852	178°	238°	+70°	34.1	0.01
..	..	2015 Sep. 21	1920–1931	178°	239°	+70°	34.3	0.01
2012 BU$_{61}$	1100	2007 Jun. 29	1500–1788	97°	181°	−6°	23.9	0.05
2012 TO$_{139}$	100	2012 Sep. 21	1954–2008	179°	345°	+4°	32.6	16.62
2015 TB$_{145}$	100	2003 Oct. 31	1902–1997	218°	204°	−24°	34.9	12.62
..	..	2004 Oct. 31	1908–1979	218°	204°	−24°	35.0	0.01
..	..	2006 Oct. 31	1902–2000	218°	204°	−24°	34.9	23.54
..	..	2009 Oct. 31	1902–2006	218°	204°	−24°	34.9	42.86
..	..	2010 Oct. 31‡	1905–1991	218°	204°	−24°	34.9	0.14
..	..	2012 Oct. 31	1930–2009	218°	204°	−24°	34.8	10.95
..	..	2013 Oct. 31	1902–1982	218°	204°	−24°	34.9	0.10
..	..	2014 Oct. 31	1911–1960	218°	204°	−24°	35.0	0.01
..	..	2015 Oct. 31	1905–2015	218°	204°	−24°	34.9	9.42

Table 4.4: Predicted meteor outbursts from virtual young meteoroid trails from the shower parents. Shown are the age of the trail, period of expected activity (in date and solar longitude, $\lambda_\odot$, rounded to the nearest 1° solar longitude), radiant (in J2000 sun-centered ecliptic coordinates, $\lambda - \lambda_\odot$ and β), geocentric speed (v_g), and estimated meteoroid flux derived from median JFC model.

	Orbital elements (J2000)				Geocentric radiant (J2000)			$\langle X \rangle$	
	q (AU)	e	i	Ω	ω	$\lambda - \lambda_\odot$	β	v_g (km s^{-1})	$H < 18$	$H < 22$
(139359) 2001 ME$_1$	0.35512	0.86598	5.796°	86.506°	300.254°	191° ±1°	+4° ±1°	30.0 ±0.1		
2006 outburst	0.32 ±0.02	0.87 ±0.03	4.7° ±1.4°	93.0° ±0.5°	298.8° ±2.2°	193.0° ±0.5°	+3.5° ±0.5°	30.5 ±0.5	0.01–0.02	0.1–0.3

Table 4.5: Orbits and radiant characteristics of the possible meteor activity associated to (139359) 2001 ME$_1$. Listed are perihelion distance q, eccentricity e, inclination i, longitude of ascending node Ω and argument of perihelion ω for the parent (taken from JPL 71) and the meteor outburst in 2006 (derived from the corresponding wavelet maximum). The uncertainties in the orbital elements for the parents are typically in the order of 10^{-5} to 10^{-8} in their respective units and are not shown. Epochs are in J2000.

TO$_{139}$ and 2015 TB$_{145}$ are either at least 2 magnitudes lower than the median near-Earth JFC model or have a much steeper dust size distribution than we assume.

4.5.3 Discussion

With the results discussed above, we now revisit the population statistics of the dormant comets. We first consider the number of streams detectable by CMOR, $\mathcal{N}_{CMOR}$, to be expressed as

$$\mathcal{N}_{CMOR} = \mathcal{N}_{dc} \cdot \eta_{NEACO} \cdot \eta_{shr} \cdot \eta_{CMOR} \qquad (4.10)$$

where $\mathcal{N}_{dc}$ is the true (de-biased) number of dormant comets in the NEACO population, η_{NEACO} is the detection efficiency of the NEACOs (i.e. the number of known NEACOs divided by the number of total NEACOs predicted by NEO population model), η_{shr} is the selection efficiency of NEACOs that produce visible meteor showers (i.e. the number of shower-producing NEACOs divided by the total number of NEACOs), and η_{CMOR} is the detection efficiency of CMOR (i.e. the number of total virtual showers observable by CMOR divided by the total number of virtual showers visible at the Earth). Rearranging the terms, we have

$$\mathcal{N}_{dc} = \mathcal{N}_{CMOR} \cdot (\eta_{NEACO} \cdot \eta_{shr} \cdot \eta_{CMOR})^{-1} \qquad (4.11)$$

We focus on annual shower detection in the following as the statistics for outburst detection (only 1) are too low. As presented above, we have $\mathcal{N}_{\mathrm{CMOR}} = 2$ for $H < 18$ population and $\mathcal{N}_{\mathrm{CMOR}} = 4$ for $H < 22$ population. For the remaining three coefficients:

1. For η_{NEACO}, we obtain the true (de-biased) number of NEACOs by using Greenstreet et al. (2012)'s NEO population model and incorporate the population statistics from Stuart (2001), Mainzer et al. (2011) and Jedicke et al. (2015). We derive $\mathcal{N}_{\mathrm{NEACO}} = 200 \pm 30$ for $H < 18$ and 2100 ± 300 for $H < 22$. Considering that we have selected 407 NEACOs in our initial sample, of which 199 are bodies with $H < 18$, we obtain $\eta_{\mathrm{NEACO}} = 1^{+0.00}_{-0.13}$ for $H < 18$ and $\eta_{\mathrm{NEACO}} = 0.19^{+0.03}_{-0.02}$ for $H < 22$.

2. For η_{shr}, we have 44 hypothetical showers as listed in Table 4.1, among which 15 are from $H < 18$ bodies. This yields $\eta_{\mathrm{shr}} \sim 0.1$.

3. For η_{CMOR}, we exclude the meteoroid streams whose are either too slow for reliable radar detection ($v_{\mathrm{g}} < 15$ km s^{-1} Weryk & Brown, 2013) or have radiants too far south for CMOR to detect ($\beta < -30°$). This leaves 36 streams in Table 4.1, including 14 originating from $H < 18$ bodies. This translates to $\eta_{\mathrm{CMOR}} \sim 0.8$.

With all these numbers, we obtain $\mathcal{N}_{\mathrm{dc}} = 25 \pm 21$ for $H < 18$ population and $\mathcal{N}_{\mathrm{dc}} = 263 \pm 173$ for $H < 22$ population, with uncertainties derived by error propagation. This translates to a fraction of $\sim 10\%$ of dormant comets in the NEACO population independent of the sizes. Assuming dormant comets in asteroidal orbits (i.e. $T_{\mathrm{J}} > 3$ bodies) are negligible, we further derive a dormant comet fraction of $2.0 \pm 1.7\%$ for the entire NEO population, which should be considered as a lower limit. This number is at the low end of previous estimates by Bottke et al. (2002), Fernández et al. (2005) and Mommert et al. (2015) who give ranges of 2–14%. It should be noted that all these authors also assume that dormant comets in asteroidal orbits are negligible during the derivation of the dormant comet fraction.

There are two caveats in our work that may lead to an underestimation of the dormant comet fraction. Since we used the median of the dust production of *known* JFCs to feed the

meteoroid flux model, if the actual JFC dust production is in fact lower, our treatment will lead to an overestimation of the number of visible showers, which will in turn reduce the derived dormant comet fraction. For a dormant comet fraction of $\sim 8\%$, we need to reduce η_{shr} by a factor of $8\%/2\% = 4$, equivalent to using a dust production rate that is 10 times lower than the median model. This is qualitatively consistent with the recently observed trend that more weakly-active comets are being discovered as more sensitive NEO surveys become operational. Another caveat is that the actual dust size distribution q may be different than what is used in the dust model. A steeper size distribution will result in a proportionally larger number of smaller meteoroids, making the stream more dispersed and hence more difficult to be detected. This hypothesis is not supported by reported cometary observations which are found to have $q \sim 3.6$ at micron-range sizes (e.g. Fulle, 2004), but a discrepancy between millimeter to sub-millimeter-sized meteoroids is possible, such as the case of 21P/Giacobini-Zinner and the Draconids (Ye et al., 2014).

Another fundamental question is, are dormant comets in asteroidal orbits really negligible? There is at least one prominent counter-example: (3200) Phaethon ($T_J = 4.508$). Phaethon is associated with the Geminid meteor shower and still possesses some outgassing activity at perihelion (e.g. Jewitt & Li, 2010). Nevertheless, the fact that we do not see a lot of active NEAs suggests that such objects are not very common.

Taking the median dynamical lifetime of near-Earth JFCs to be a few 10^3 yr, the derived dormancy rate translates to a dormancy probability of $\sim 10^{-5}$ yr^{-1} per comet independent of sizes. This is consistent with previous model predictions, and about 5–40 times lower than the disruption probability (Fernández et al., 2002; Belton, 2014). This result echoes earlier suggestions that near-Earth JFCs are more likely to be disrupted rather than achieving dormancy (Belton, 2014). Since the typical timescale for JFC disruption, a JFC's dynamical lifetime in the NEO region, and dispersion lifetime for a resulting meteoroid stream are all at the same order (a few 10^3 yr), there should exist a significant number of meteoroid streams with parents that are either disrupted or have been dynamically removed such that no parent can be found,

supporting the speculation of Jenniskens & Vaubaillon (2010) that many meteoroid streams
are produced from disrupted comets. Since disruption and dynamical removal are compet-
ing mechanisms to eliminate JFCs from the NEO region, it may be difficult to investigate the
formation of these "orphan" streams in the absence of an observable parent.

Finally, we compare our list against the dormant comet candidates proposed in previous
works. The largest list of dormant candidates to-date is published by Tancredi (2014) and
includes 203 objects in JFC-like orbits that meet a set of restrictive criteria. According to our
simulations, only 3 of these 203 objects have the potential of producing CMOR-detectable
activity [(196256) 2003 EH_1, 1999 LT_1, and 2004 BZ_{74}; note that not all of the objects are in
our initial shortlist, as Tancredi's list has a more relaxed constraint on orbital precision], and
only 1 out of the 7 objects has a detectable shower [(196256) 2003 EH_1]. Kim et al. (2014)
compiled a list of 123 NEACOs that have thermal observations, 29 of which overlap with
Tancredi's list. Among these, 3 have the potential of producing CMOR-detectable activity
[(307005) 2001 XP_1, 2001 HA_4, and 2010 JL_{33}] but none of them has a detectable shower.
DeMeo & Binzel (2008) analyzed spectra of 49 NEOs in cometary orbits (excluding 6 objects
that have been later identified as comets), 6 of which may produce CMOR-detectable activity
[(3360) Syrinx, (16960) 1998 QS_{52}, (137427) 1999 TF_{211}, (139359) 2001 ME_1, (401857) 2000
PG_3, and 1999 LT_1], only one of them produces a detectable shower, (139359) 2001 ME_1, for
which they reported an albedo of 0.04 and classified as a P-type asteroid. Other works (see
Mommert et al., 2015; Licandro et al., 2016, and the references therein) have reported smaller
samples consisting of the same objects already discussed that may produce showers from our
simulations. Each author has selected a somewhat different set of candidates, but there are
several objects that are selected by more than one author, including (248590) 2006 CS (which
is the possible parent of δ Mensid meteor shower), (394130) 2006 HY_{51}, (436329) 2010 GX_{62},
(451124) 2009 KC_3, 1999 LT_1, 2001 HA_4 and 2010 JL_{33}, none of which [except for (248590)
2006 CS, (436329) 2010 GX_{62}, (451124) 2009 KC_3 which produce southerly radiants that are
difficult to detect for CMOR] has detectable meteor activity. On the other hand, the remaining

three objects with detected showers (2004 TG_{10}, 2009 WN_{25} and 2012 BU_{61}) are not selected by any of the surveys largely due to the lack of astrometric/physical observations, though the most recent NEOWISE catalog release includes the measurements for 2004 TG_{10} (Nugent et al., 2015).

4.6   Conclusion

We conducted a direct survey for dormant comets in the ACO component in the NEO population. This was done by looking for meteor activity originated from each of 407 NEOs as predicted by a meteoroid stream model. This sample represents $\sim 80\%$ and $\sim 46\%$ of known NEOs in JFC-like orbits in the $H < 18$ and $H < 22$ population respectively.

To look for the virtual meteoroid streams predicted by the model, we analyzed 13 567 542 meteoroid orbits measured by the Canadian Meteor Orbit Radar (CMOR) in the interval of 2002–2016 using the wavelet technique developed by Galligan (2000) and Brown et al. (2008) and test the statistical significance of any detected association using a a Monte Carlo subroutine. Among the 407 starting parent bodies, we found 36 virtual showers that are detectable by CMOR. Of these, we identify 5 positive detections that are statistically unlikely to be chance association. These include 3 previously known asteroid-stream associations [(196256) 2003 EH_1 – Quadrantids, 2004 TG_{10} – Taurids, and 2009 WN_{25} – November i Draconids], 1 new association (2012 BU_{61} – Daytime ξ Sagittariids) and 1 new outburst detection [(139359) 2001 ME_1]. Except for the case of (139359) 2001 ME_1, which displayed only a single outburst in 2006, all other shower detections are in form of annual activity.

We also examined 32 previously proposed asteroid-shower associations. These associations were first checked with a Monte Carlo subroutine, from which we find only 8 associations are statistically significant. Excluding 3 associations that involve observational circumstances unfavorable for CMOR detection (e.g. southerly radiant or low arrival speed), 4 out of the remaining 5 associations involve showers that have only been reported by one study, while the

last association [ψ Cassiopeiids – (5496) 1973 NA] involves some observation–model discrepancy. We leave these questions for future studies.

Based on the results above, we derive a lower limit to the dormant comet fraction of 2.0 ± 1.7% among all NEOs, slightly lower than previous numbers derived based on dynamical and physical considerations of the parent. This number must be taken with caution as we assume a median dust production from *known* JFC comets. The typical dust production of already-dead comets, however, is not truly known. A dormant comet fraction of $\sim 8\%$ as concluded by other studies would require a characteristic dust production about 10% of the median model. Another caveat is the possibility of overestimating the number of visible showers (hence, reducing the derived dormant comet fraction) due to very steep dust size distribution ($q \gg 3.6$), but this is not supported by cometary observations.

We also derive a dormancy rate of $\sim 10^{-5}$ yr^{-1} per comet, consistent with previous model predictions and significantly lower than the observed and predicted disruption probability. This confirms disruption and dynamical removal as the dominant end state for near-Earth JFCs, while dormancy is relatively uncommon. We predict the existence of a significant number of "orphan" meteoroid streams where parents have been disrupted or dynamically removed. While it is challenging to investigate the formation of these streams in the absence of an observable parent, it might be possible to retrieve some knowledge of the parent based on meteor data alone.

Acknowledgements

Appendix A: Median Dust Production Model for Typical Jupiter-family Comets

To estimate the dust production of a typical Jupiter-family Comet (JFC), we compile the $Af\rho$ of 35 near-Earth JFCs from the Cometas-Obs database, using the measurements provided by various observers in the duration of 2009–2015. $Af\rho$ is an indicator of the dust production of a comet (c.f. A'Hearn et al., 1984, 1995) and is defined as

$$Af\rho = \frac{4r_{\mathrm{h}}^2 \Delta^2}{\rho} \frac{\mathcal{F}_C}{\mathcal{F}_\odot} \tag{4.12}$$

where r_{h} is the heliocentric distance of the comet in AU, Δ is the geocentric distance of the comet (in the same units as ρ, typically in km or cm), and $\mathcal{F}_C$ and $\mathcal{F}_\odot$ are the fluxes of the comet within the field of view as viewed by the observer and the Sun at a distance of 1 AU. The photometric aperture size, or $2\rho/\Delta$, is usually determined by the threshold value where the flux reaches an asymptote.

Since $Af\rho$ measurements are conducted at various r_{h}, we scale each $Af\rho$ measurement to $r_{\mathrm{h}} = 1$ AU by

$$Af\rho_0 = Af\rho \cdot r_{\mathrm{h}}^{4/3} \tag{4.13}$$

The $Af\rho_0$ number can be converted to the dust production rate at 1 AU following the derivation of Ye & Wiegert (2014):

$$N_{\mathrm{d}}(a_1, a_2) = \frac{655 A_1(a_1, a_2) Af\rho_0}{8\pi A_{\mathrm{B}} \phi(\alpha)[A_3(a_1, a_2) + 1000 A_{3.5}(a_1, a_2)]} \tag{4.14}$$

where $[a_1, a_2]$ is the size range of the meteoroids responsible for the detected flux where we use $a_1 = 10^{-5}$ m, $a_2 = 10^{-2}$ m, $A_x = (a_2^{x-s} - a_1^{x-s})/(x - s)$ for $x \neq s$ and $A_x = \ln a_2/a_1$ for $x = s$, with $s = 3.6$ being the size population index of the meteoroids (Fulle, 2004), $A_{\mathrm{B}} = 0.05$ is the Bond albedo and $\phi(\alpha)$ is the normalized phase function, which $\phi(\alpha) = 1$ for isotropic
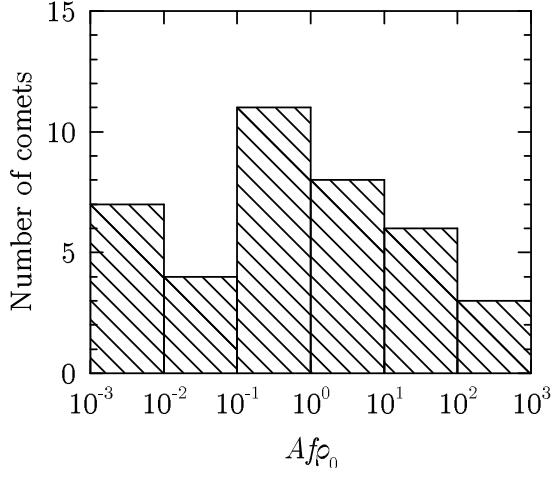
Figure 4.6 Distribution of $Af\rho_0$ of a number of near-Earth JFCs. The median $Af\rho_0$ is 0.2 m, corresponding to a dust production rate of 7×10^{14} meteoroids (appropriated within the size range of 0.5–50 mm) per orbit.

scattering. From Figure 4.6, we derive a median $Af\rho_0$ to be 0.2 m, corresponding to a dust production rate of 7×10^{14} particles per orbit assuming an active time per orbit of ~ 1 yr.

Appendix B: Radiants, Activity Profiles and Dust Size Distributions of Predicted Virtual Showers
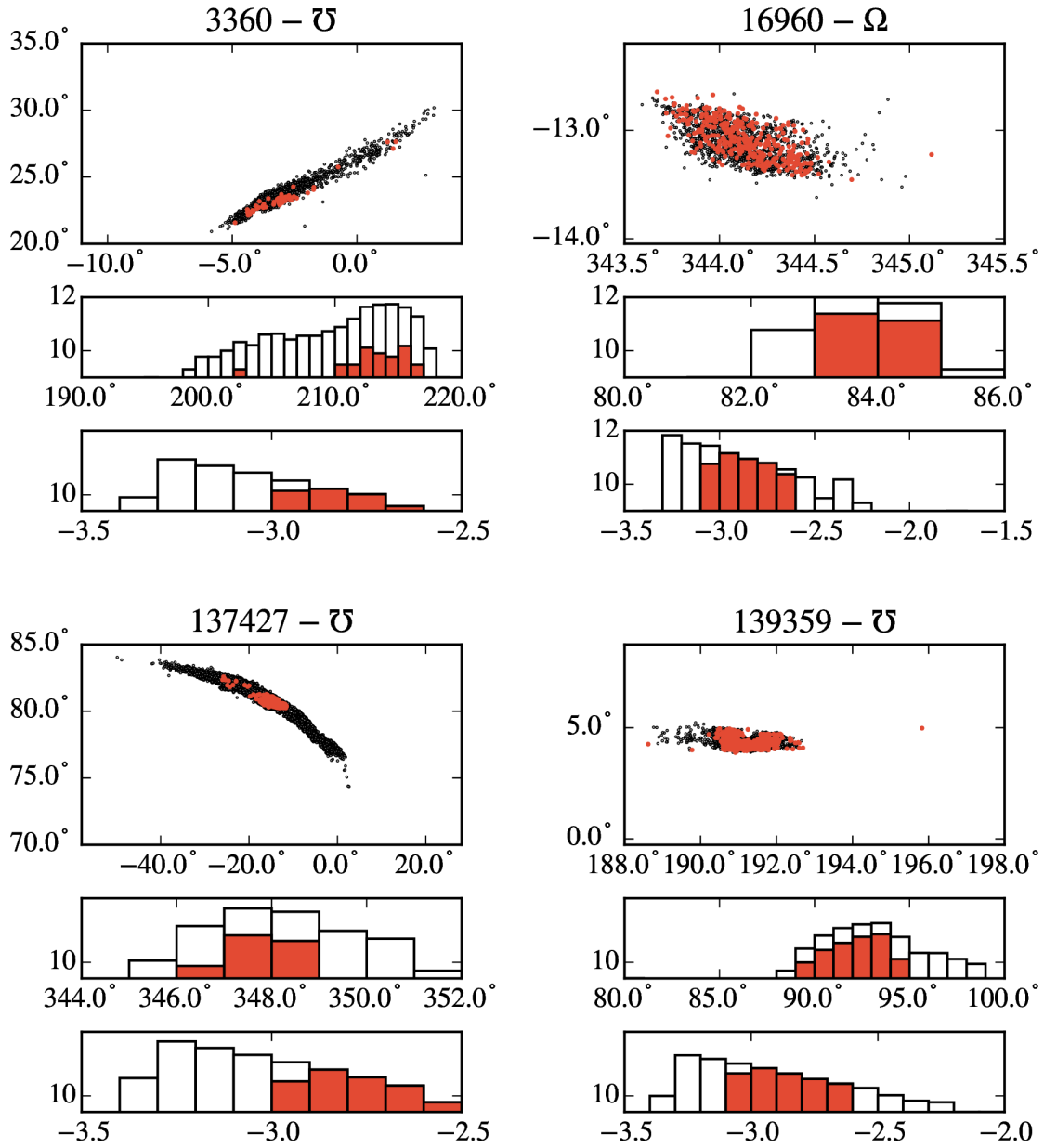
Figure 4.7 Radiants (in J2000 geocentric sun-centered ecliptic coordinates), activity profiles (arbitrary number vs. solar longitudes), and dust size distribution (arbitrary number vs. dust size [m] in logarithm scale) of the predicted virtual meteor showers of the listed bodies. Colored dots/filled bars represent CMOR-detectable meteoroids, while the rest represent all meteoroids in the size ranges of $[10^{-4}, 10^{-1}]$ m following a single power law of $s = 3.6$.
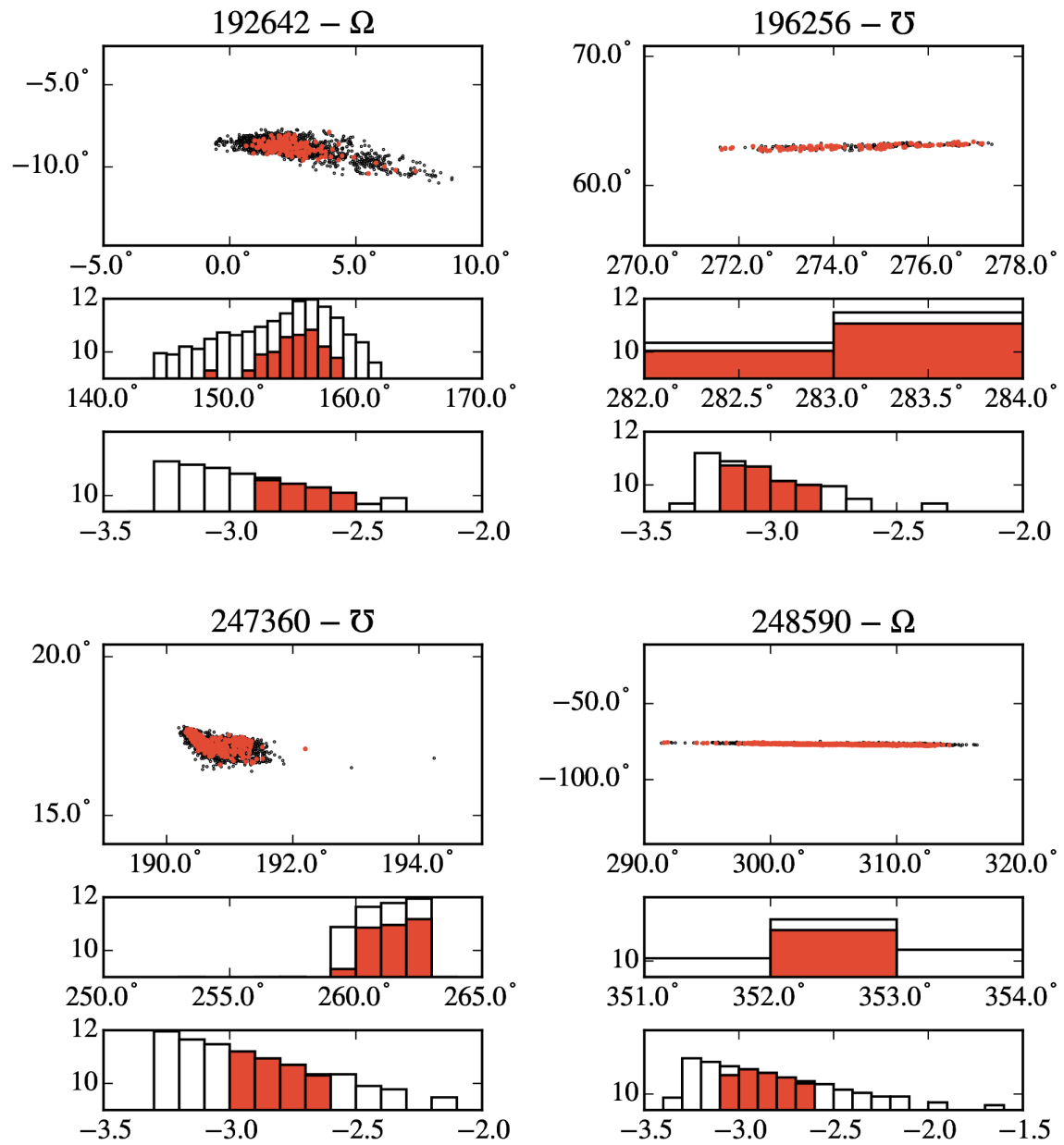
Figure 4.8 Same as Figure 4.7.
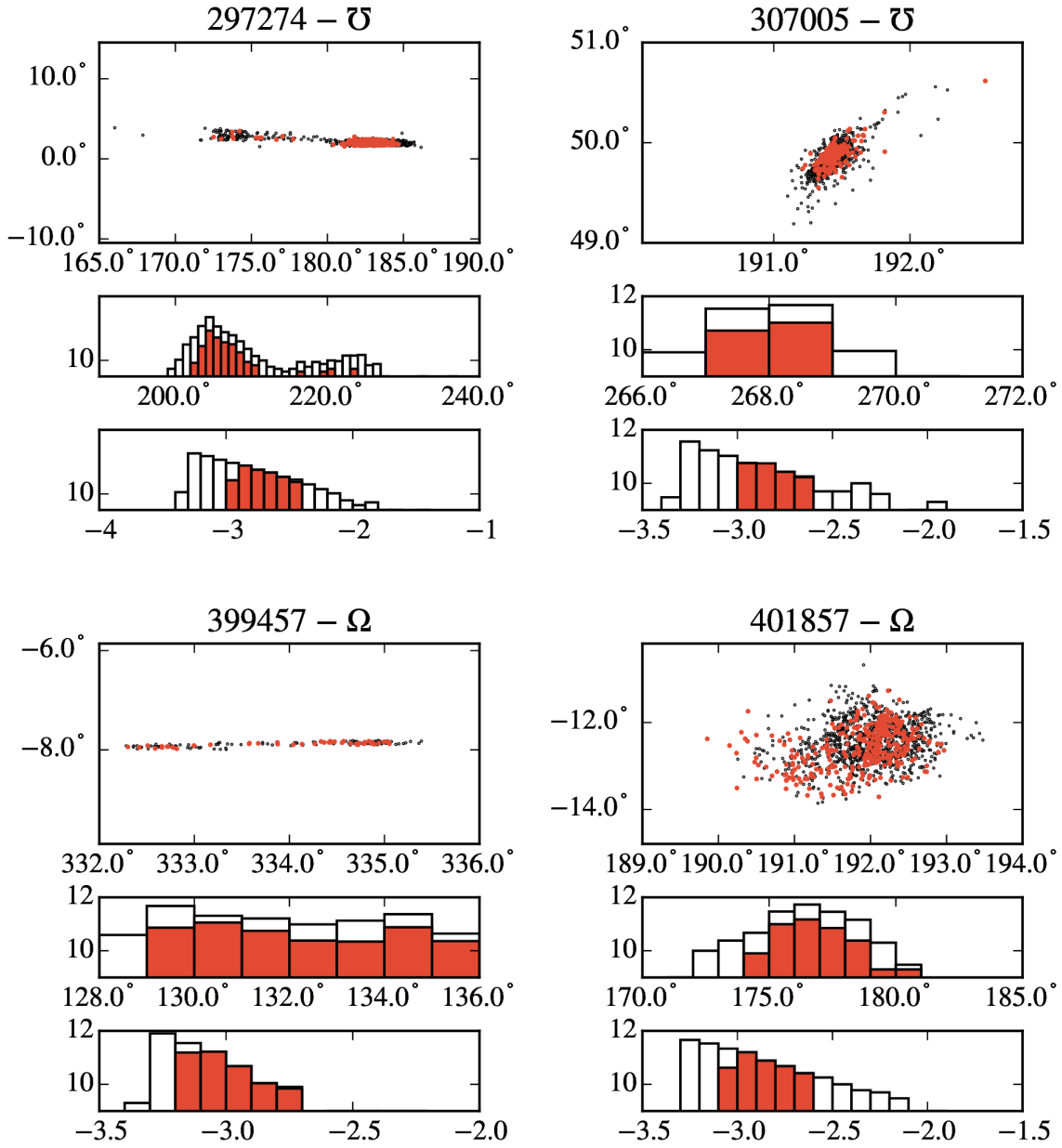
Figure 4.9 Same as Figure 4.7.
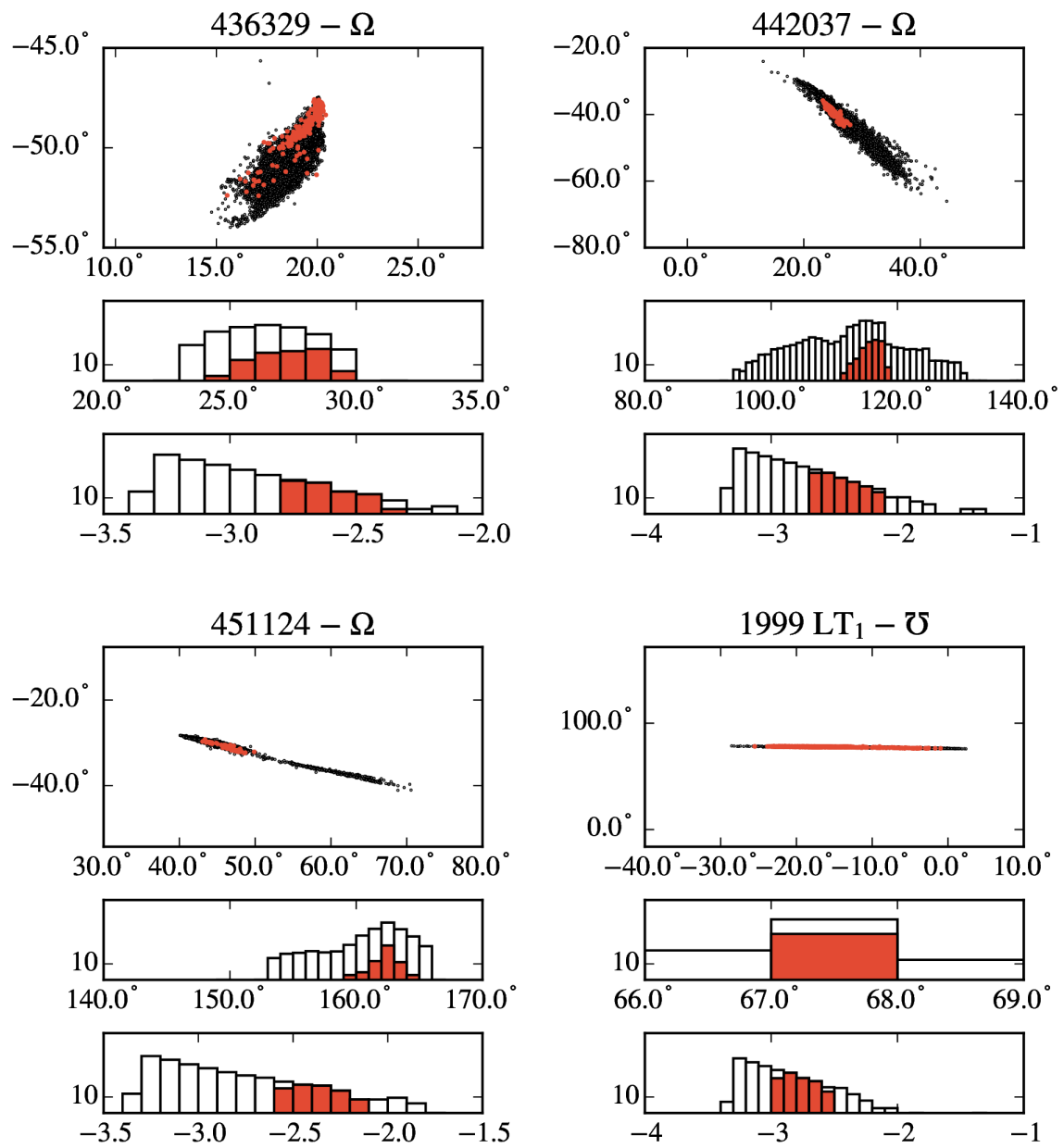
Figure 4.10 Same as Figure 4.7.
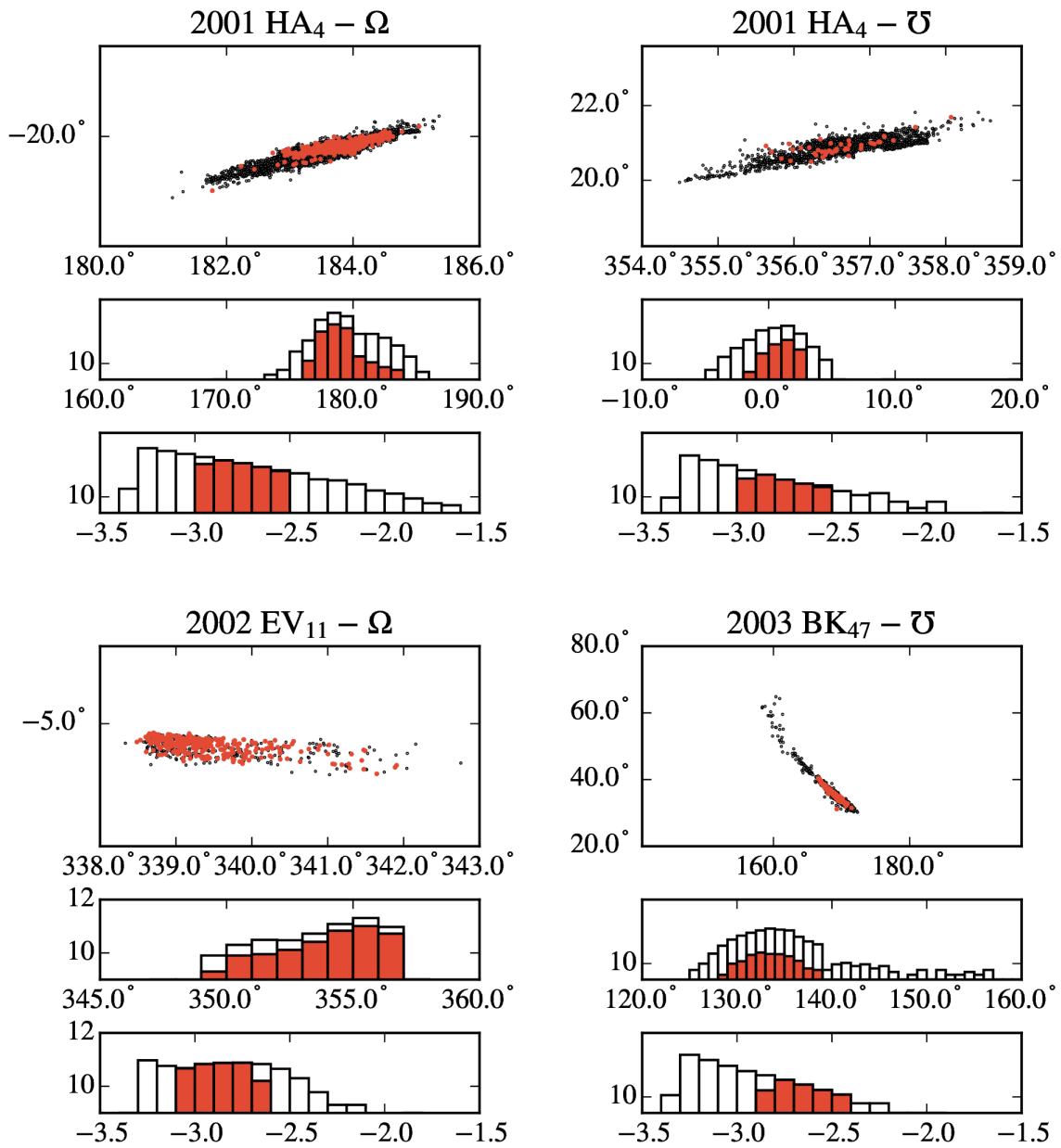
Figure 4.11 Same as Figure 4.7.
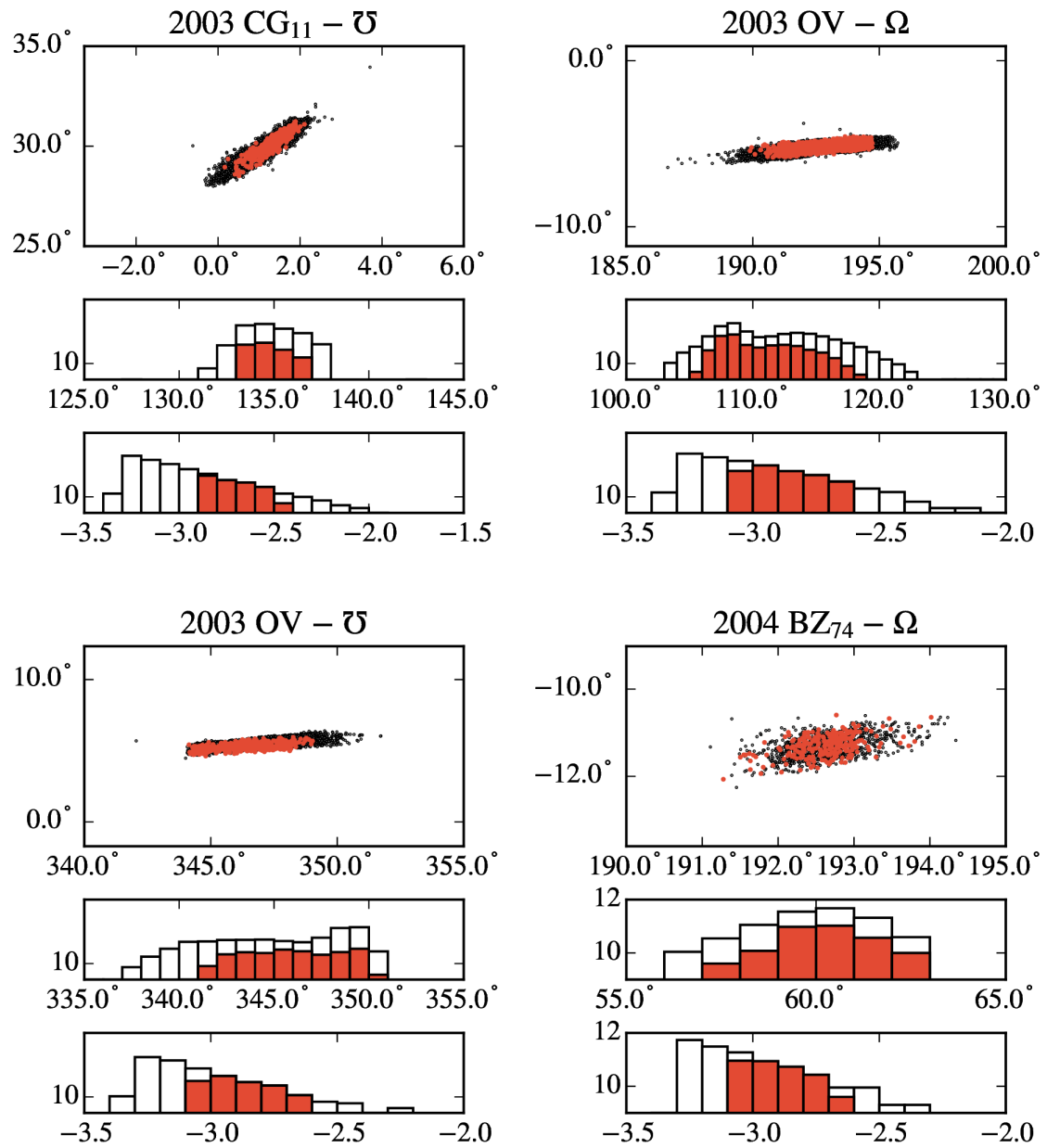
Figure 4.12 Same as Figure 4.7.
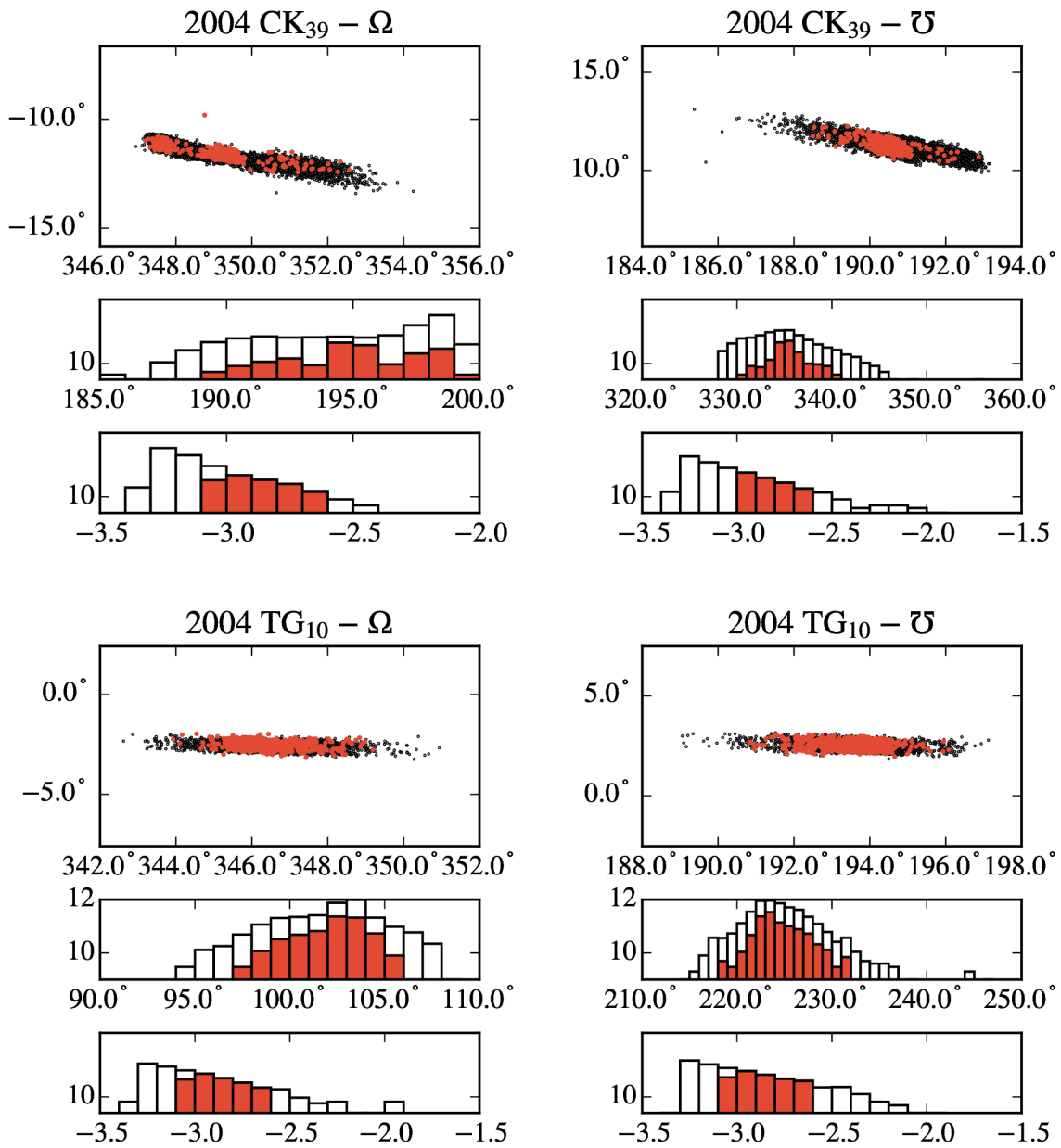
Figure 4.13 Same as Figure 4.7.
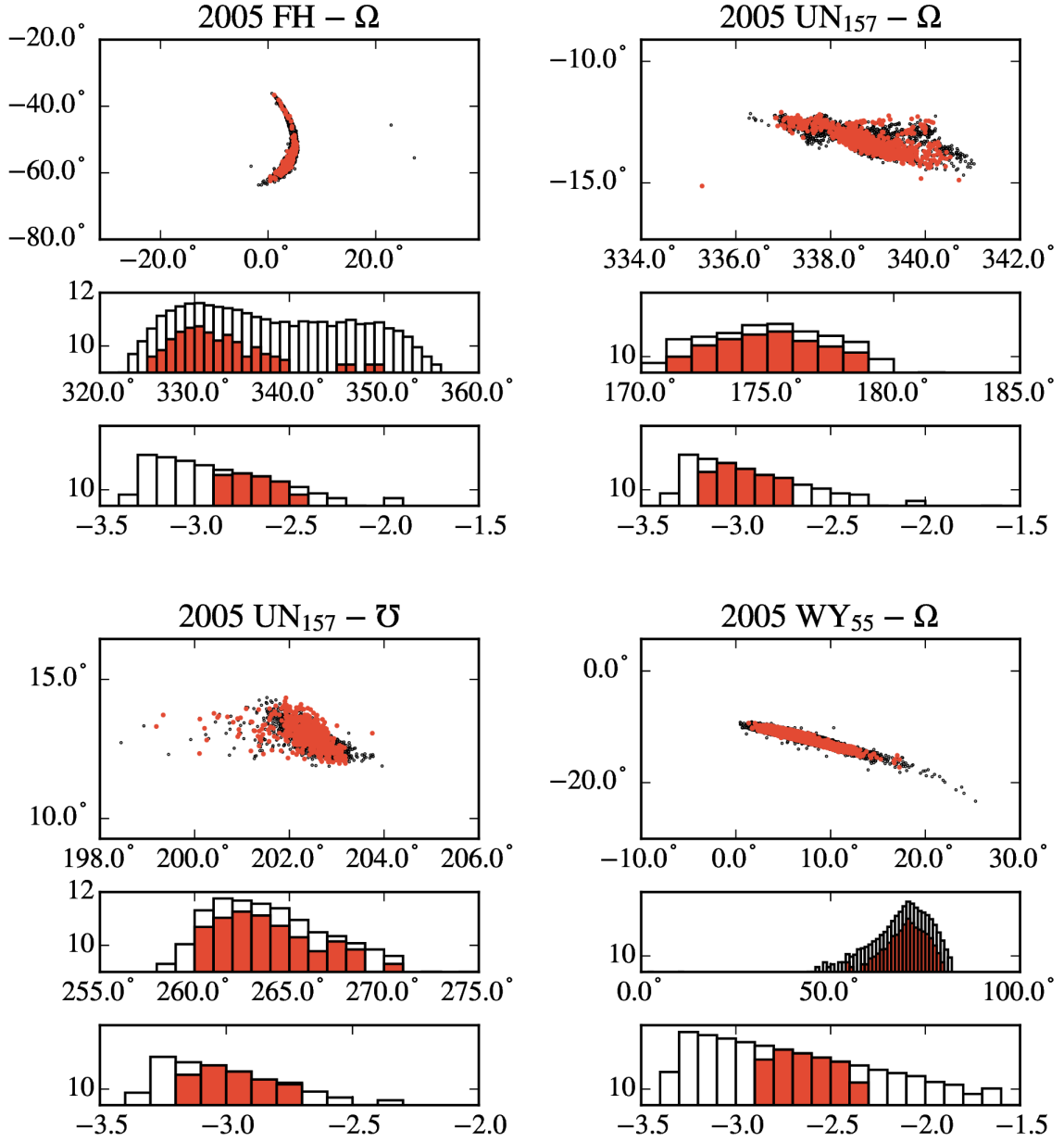
Figure 4.14 Same as Figure 4.7.
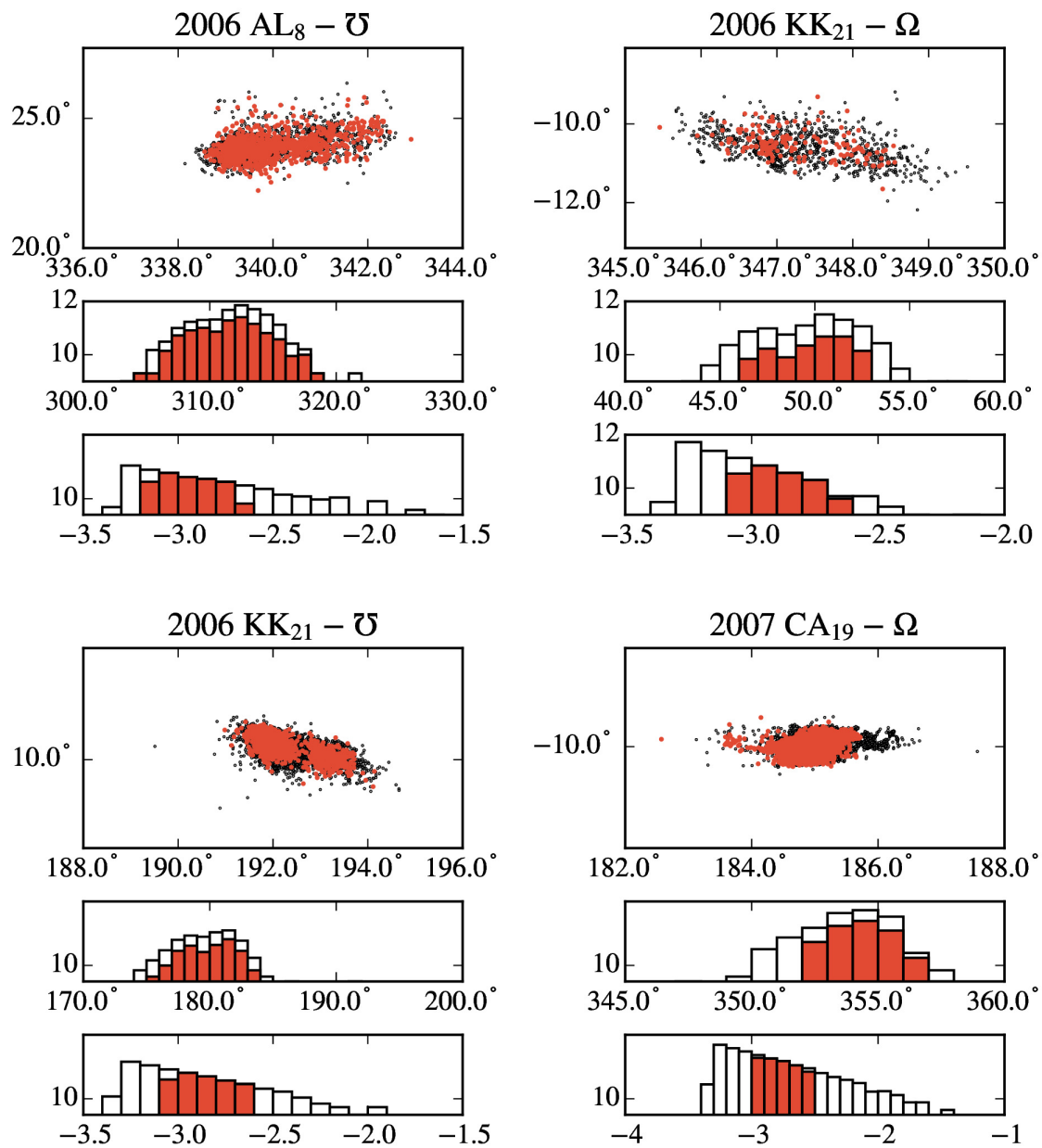
Figure 4.15 Same as Figure 4.7.
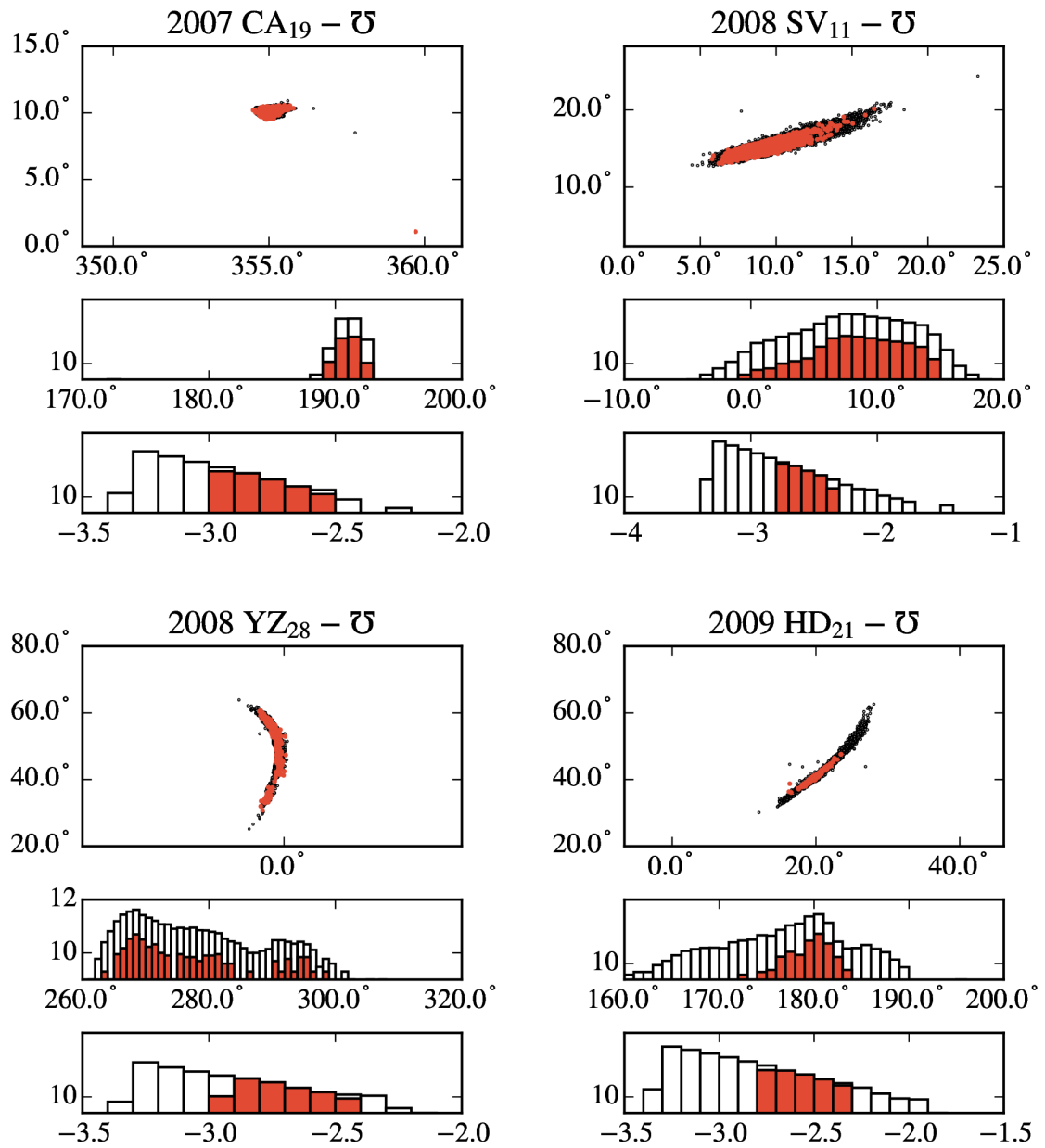
Figure 4.16 Same as Figure 4.7.
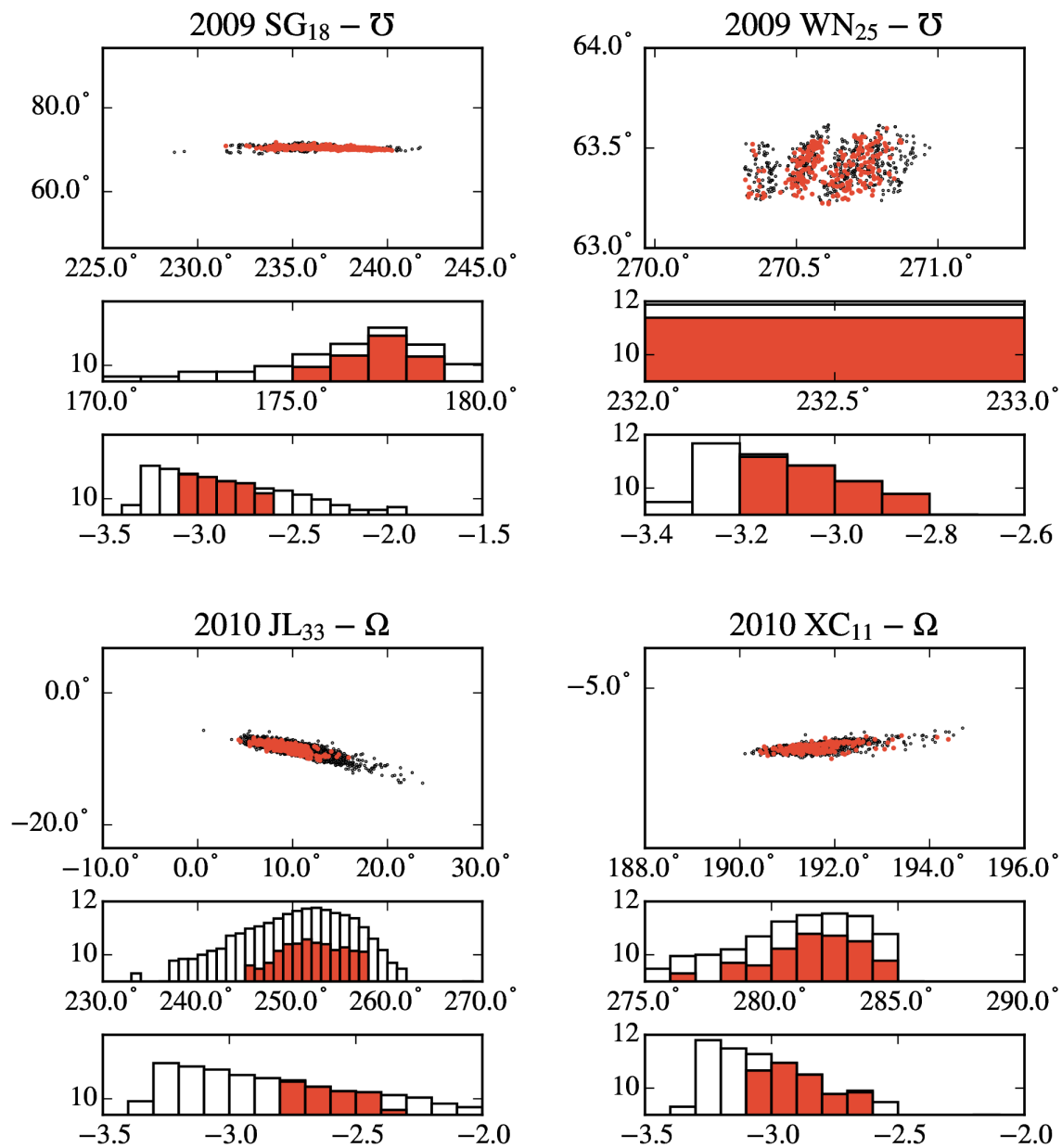
Figure 4.17 Same as Figure 4.7.
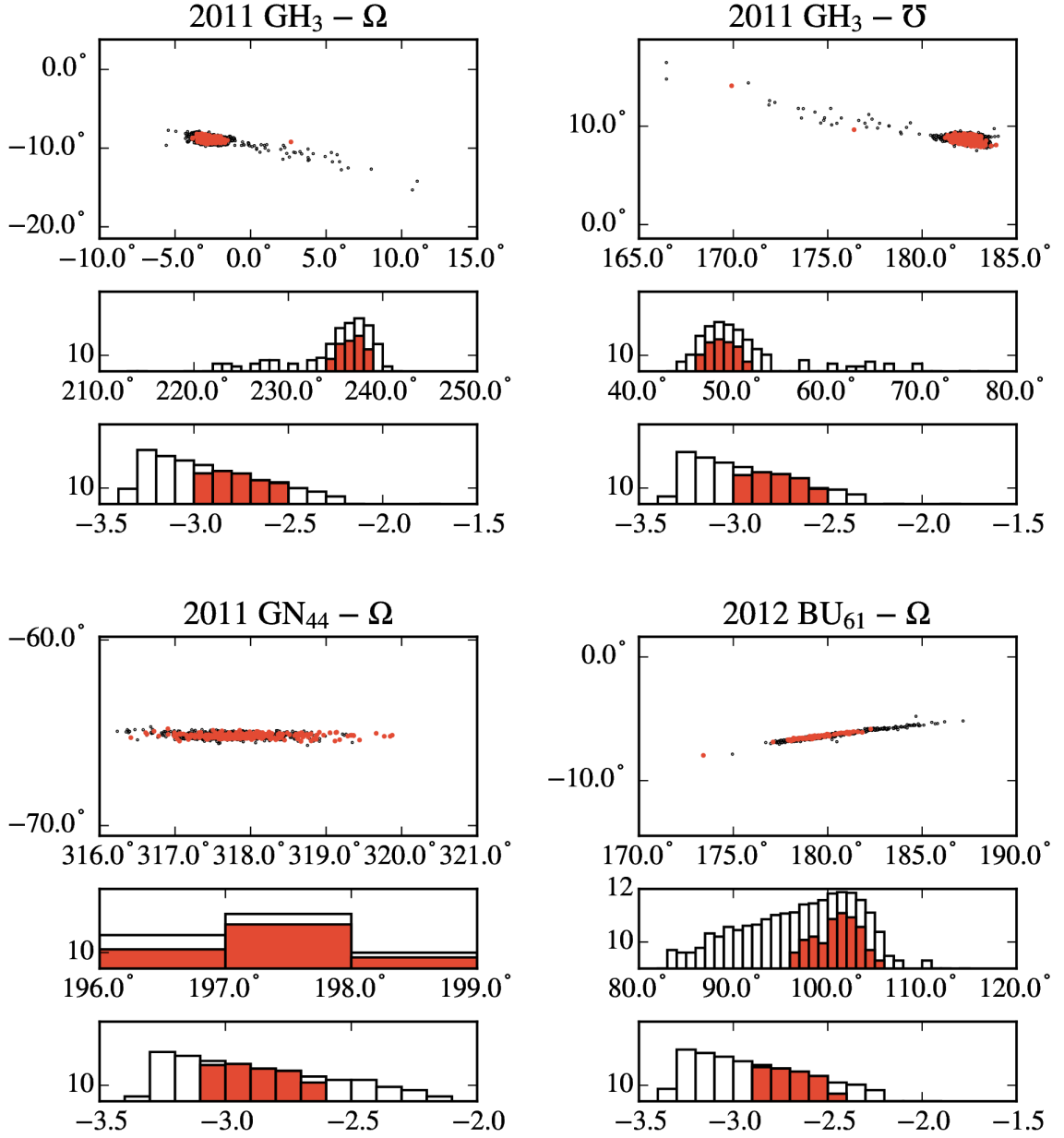
Figure 4.18 Same as Figure 4.7.
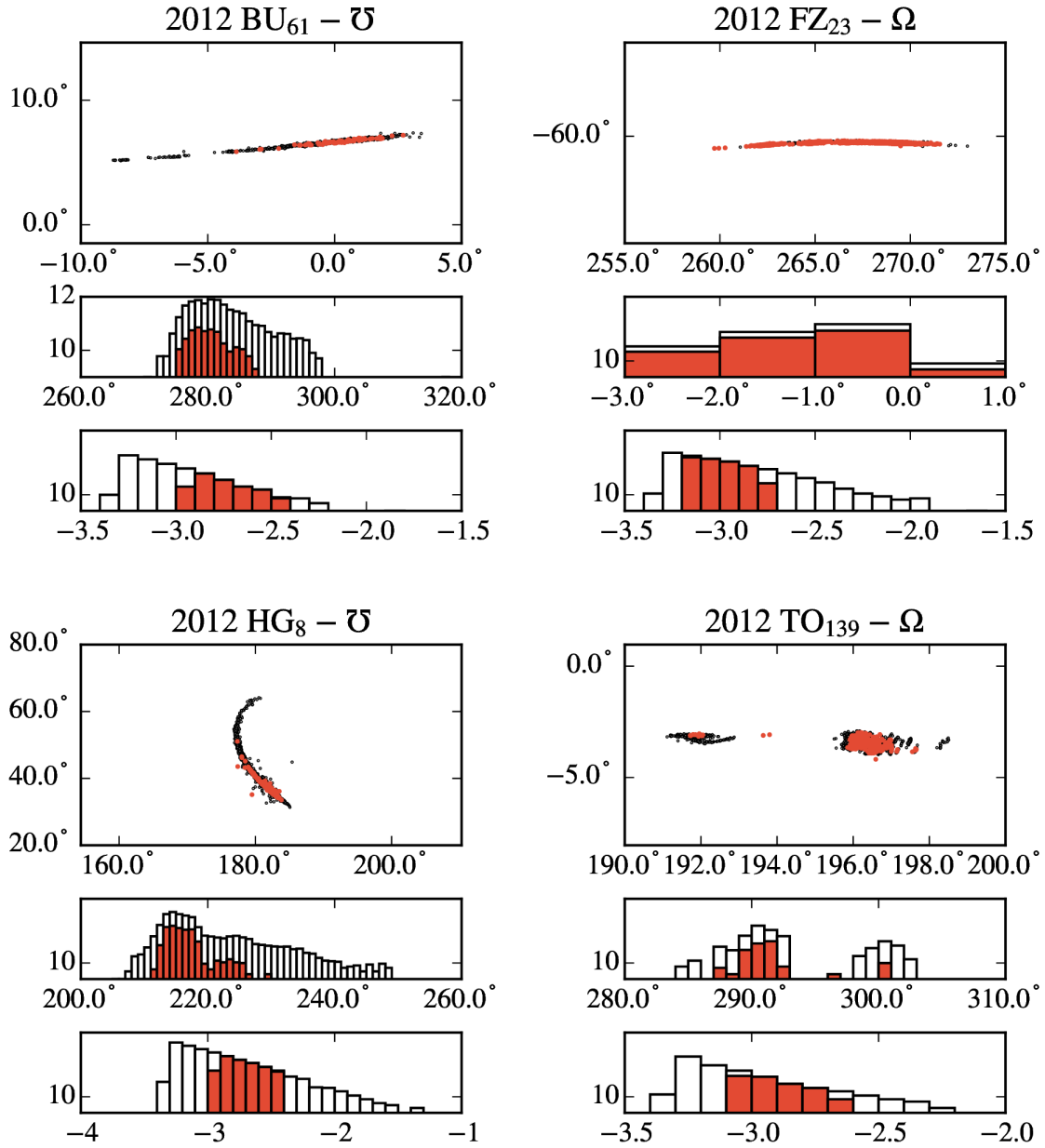
Figure 4.19 Same as Figure 4.7.
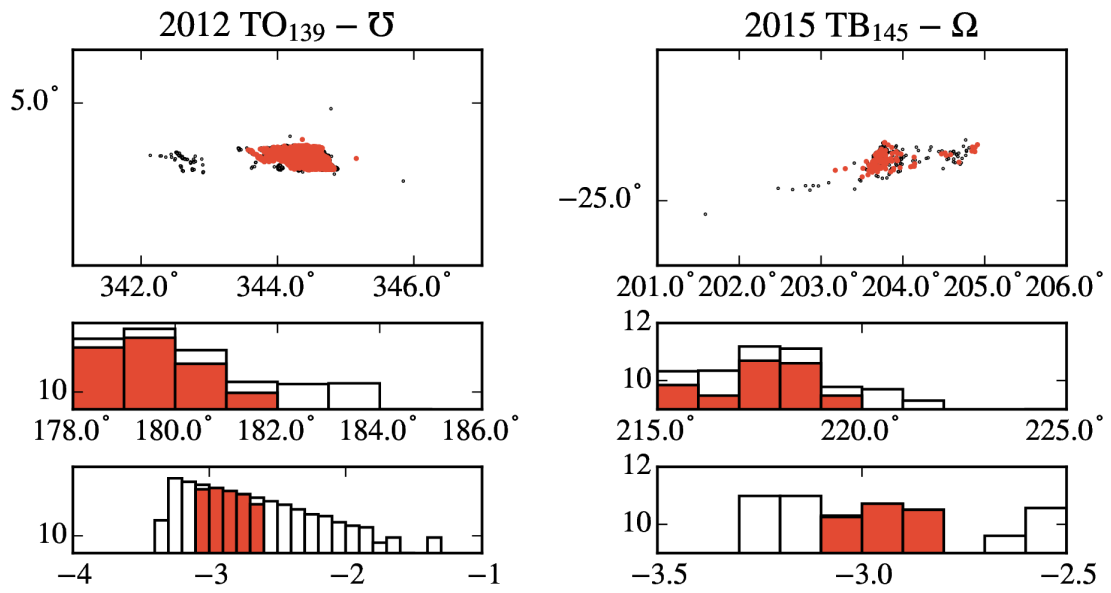
Figure 4.20 Same as Figure 4.7.

Bibliography

Abedin, A., Spurný, P., Wiegert, P., et al. 2015, Icarus, 261, 100

A'Hearn, M. F., Millis, R. C., Schleicher, D. O., Osip, D. J., & Birch, P. V. 1995, Icarus, 118, 223

A'Hearn, M. F., Schleicher, D. G., Millis, R. L., Feldman, P. D., & Thompson, D. T. 1984, AJ, 89, 579

Andreić, Ž., Šegon, D., Korlević, K., et al. 2013, WGN, Journal of the International Meteor Organization, 41, 103

Babadzhanov, P. B., Kokhirova, G. I., & Obrubov, Y. V. 2015, Solar System Research, 49, 165

Babadzhanov, P. B., & Obrubov, I. V. 1992, Celestial Mechanics and Dynamical Astronomy, 54, 111

Babadzhanov, P. B., Williams, I. P., & Kokhirova, G. I. 2009, A&A, 507, 1067

Belton, M. J. S. 2014, Icarus, 231, 168

Binzel, R. P., Rivkin, A. S., Stuart, J. S., et al. 2004, Icarus, 170, 259

Bottke, W. F., Morbidelli, A., Jedicke, R., et al. 2002, Icarus, 156, 399

Bronshten, V. A. 1981, Astronomicheskii Vestnik, 15, 44

Brown, P., Hocking, W. K., Jones, J., & Rendtel, J. 1998, MNRAS, 295, 847

Brown, P., & Jones, J. 1998, Icarus, 133, 36

Brown, P., Weryk, R. J., Wong, D. K., & Jones, J. 2008, Icarus, 195, 317

Brown, P., Wong, D. K., Weryk, R. J., & Wiegert, P. 2010, Icarus, 207, 66

Bruzzone, J. S., Brown, P., Weryk, R. J., & Campbell-Brown, M. D. 2015, MNRAS, 446, 1625

Campbell-Brown, M. D., & Koschny, D. 2004, A&A, 418, 751

Ceplecha, Z., Borovička, J., Elford, W. G., et al. 1998, Space Sci. Rev., 84, 327

Chambers, J. E. 1999, MNRAS, 304, 793

Chambers, J. E., & Migliorini, F. 1997, in Bulletin of the American Astronomical Society,
    Vol. 29, AAS/Division for Planetary Sciences Meeting Abstracts #29, 1024

Cremonese, G., Fulle, M., Marzari, F., & Vanzani, V. 1997, A&A, 324, 770

de León, J., Campins, H., Tsiganis, K., Morbidelli, A., & Licandro, J. 2010, A&A, 513, A26

DeMeo, F., & Binzel, R. P. 2008, Icarus, 194, 436

Di Sisto, R. P., Fernández, J. A., & Brunini, A. 2009, Icarus, 203, 140

Drummond, J. D. 1981, Icarus, 45, 545

Everhart, E. 1985, in Dynamics of Comets: Their Origin and Evolution, Proceedings of IAU
    Colloq. 83, held in Rome, Italy, June 11-15, 1984. Edited by Andrea Carusi and Giovanni B.
    Valsecchi. Dordrecht: Reidel, Astrophysics and Space Science Library. Volume 115, 1985,
    p.185, ed. A. Carusi & G. B. Valsecchi, 185

Fernández, J. A., Gallardo, T., & Brunini, A. 2002, Icarus, 159, 358

Fernández, Y. R., Jewitt, D. C., & Sheppard, S. S. 2005, AJ, 130, 308

Fernández, Y. R., McFadden, L. A., Lisse, C. M., Helin, E. F., & Chamberlin, A. B. 1997,
    Icarus, 128, 114

Fulle, M. 2004, Motion of cometary dust, ed. G. W. Kronk, 565–575

Galligan, D. P. 2000, PhD thesis, University of Canterbury

—. 2001, MNRAS, 327, 623

Gartrell, G., & Elford, W. G. 1975, Australian Journal of Physics, 28, 591

Göckel, C., & Jehn, R. 2000, MNRAS, 317, L1

Greenstreet, S., Ngo, H., & Gladman, B. 2012, Icarus, 217, 355

Hartogh, P., Lis, D. C., Bockelée-Morvan, D., et al. 2011, Nature, 478, 218

Hoffmeister, C. 1948, Meteorstrome. Meteoric currents.

Jedicke, R., Granvik, M., Micheli, M., et al. 2015, ArXiv e-prints, arXiv:1503.04272

Jenniskens, P. 2004, AJ, 127, 3018

—. 2006, Meteor Showers and their Parent Comets

—. 2008, Earth Moon and Planets, 102, 505

Jenniskens, P., & Vaubaillon, J. 2010, AJ, 139, 1822

Jenniskens, P., N'non, Q., Albers, J., et al. 2016, Icarus, 266, 331

Jewitt, D., & Li, J. 2010, AJ, 140, 1519

Jewitt, D., Li, J., & Agarwal, J. 2013, ApJ, 771, L36

Jewitt, D., Weaver, H., Agarwal, J., Mutchler, M., & Drahus, M. 2010, Nature, 467, 817

Jones, D. C., Williams, I. P., & Porubčan, V. 2006, MNRAS, 371, 684

Jones, J. 1995, MNRAS, 275, 773

Jones, J., Brown, P., Ellis, K. J., et al. 2005, Planet. Space Sci., 53, 413

Jones, W. 1997, MNRAS, 288, 995

Kashcheyev, B. L., & Lebedinets, V. N. 1967, Smithsonian Contributions to Astrophysics, 11, 183

Kim, Y., Ishiguro, M., & Usui, F. 2014, ApJ, 789, 151

Kokhirova, G. I., & Babadzhanov, P. B. 2015, Meteoritics and Planetary Science, 50, 461

Kornoš, L., Matlovič, P., Rudawska, R., et al. 2014, Meteoroids 2013, 225

Kresak, L. 1979, Dynamical interrelations among comets and asteroids, ed. T. Gehrels, 289–309

Licandro, J., Alí-Lagoa, V., Tancredi, G., & Fernández, Y. 2016, A&A, 585, A9

Lindblad, B. A. 1971, Smithsonian Contributions to Astrophysics, 12, 14

Luu, J., & Jewitt, D. 1990, Icarus, 86, 69

Mainzer, A., Grav, T., Bauer, J., et al. 2011, ApJ, 743, 156

Marsden, B. G., Sekanina, Z., & Everhart, E. 1978, AJ, 83, 64

McIntosh, B. A., & Hajduk, A. 1983, MNRAS, 205, 931

Micheli, M., Tholen, D. J., & Jenniskens, P. 2016, Icarus, 267, 64

Mommert, M., Harris, A. W., Mueller, M., et al. 2015, AJ, 150, 106

Moorhead, A. V. 2016, MNRAS, 455, 4329

Nilsson, C. S. 1964, Australian Journal of Physics, 17, 205

Nugent, C. R., Mainzer, A., Masiero, J., et al. 2015, ApJ, 814, 117

Olsson-Steel, D. 1987, Australian Journal of Astronomy, 2, 21

Pauls, A., & Gladman, B. 2005, Meteoritics and Planetary Science, 40, 1241

Porubcan, V., & Gavajdova, M. 1994, Planet. Space Sci., 42, 151

Porubcan, V., Stohl, J., & Vana, R. 1992, in Asteroids, Comets, Meteors 1991, ed. A. W. Harris
    & E. Bowell

Porubčan, V., Kornoš, L., & Williams, I. P. 2006, Contributions of the Astronomical Observa-
    tory Skalnate Pleso, 36, 103

Rubincam, D. P. 2000, Icarus, 148, 2

Schiaparelli, G. V. 1866, Intorno AL corso ed all' origine probabile delle stelle meteoriche

—. 1867, Note E riflessioni intorno alla teoria astronomica delle stelle cadenti

Sekanina, Z. 1973, Icarus, 18, 253

—. 1976, Icarus, 27, 265

Southworth, R. B., & Hawkins, G. S. 1963, Smithsonian Contributions to Astrophysics, 7, 261

Steel, D. I., Asher, D. J., & Clube, S. V. M. 1991, MNRAS, 251, 632

Stuart, J. S. 2001, Science, 294, 1691

Tancredi, G. 1995, A&A, 299, 288

—. 2014, Icarus, 234, 66

Taylor, P. A., Margot, J.-L., Vokrouhlický, D., et al. 2007, Science, 316, 274

Terentjeva, A. K. 1989, WGN, Journal of the International Meteor Organization, 17, 242

Tisserand, F. 1891, Traité de mécanique céleste (Gauthier-Villars)

Šegon, D., Andreić, Ž., Gural, P., et al. 2014a, WGN, Journal of the International Meteor
    Organization, 42, 227

Šegon, D., Andreić, Ž., Korlević, K., & Vida, D. 2015, in Proceedings of the International Meteor Conference Mistelbach, Austria, 27-30 August 2015, ed. J.-L. Rault & P. Roggemans, 51–57

Šegon, D., Gural, P., Andreić, Ž., et al. 2014b, WGN, Journal of the International Meteor Organization, 42, 57

Vaubaillon, J., Colas, F., & Jorda, L. 2005, A&A, 439, 761

Weissman, P. R., Bottke, Jr., W. F., & Levison, H. F. 2002, Asteroids III, 669

Weryk, R. J., & Brown, P. G. 2012, Planet. Space Sci., 62, 132

—. 2013, Planet. Space Sci., 81, 32

Wiegert, P., & Brown, P. 2004, Earth Moon and Planets, 95, 19

Wiegert, P., & Tremaine, S. 1999, Icarus, 137, 84

Wiegert, P., Vaubaillon, J., & Campbell-Brown, M. 2009, Icarus, 201, 295

Williams, I. P., & Wu, Z. 1993, MNRAS, 262, 231

Ye, Q., Brown, P. G., Campbell-Brown, M. D., & Weryk, R. J. 2013, MNRAS, 436, 675

Ye, Q., & Wiegert, P. A. 2014, MNRAS, 437, 3283

Ye, Q., Wiegert, P. A., Brown, P. G., Campbell-Brown, M. D., & Weryk, R. J. 2014, MNRAS, 437, 3812

Ye, Q.-Z., Brown, P. G., Bell, C., et al. 2015, ApJ, 814, 79

Ye, Q.-Z., Brown, P. G., & Wiegert, P. A. 2016a, ApJ, 818, L29

Ye, Q.-Z., & Hui, M.-T. 2014, ApJ, 787, 115

Ye, Q.-Z., Hui, M.-T., Brown, P. G., et al. 2016b, Icarus, 264, 48

Yeomans, D. K., Yau, K. K., & Weissman, P. R. 1996, Icarus, 124, 407

Chapter 5

Conclusions

As discussed in Chapter 1, the evolution of comets is one of the most critical yet poorly understood problems in planetary astronomy. The main goal of this thesis was to provide a new perspective into this problem by bridging observational and modeling aspects of both comet and meteor studies. The thesis focuses on the population of Jupiter-family comets (JFCs) and comprises three related papers examining a different part of the cometary aging "spectrum".

The core of the thesis is built upon a Monte Carlo cometary dust model that the author independently developed over the course of his doctoral research. The purpose of the model is to:

1. Characterize dust properties from cometary images, such as ejection timing and speed, as well as dust size distribution;

2. Simulate the evolution of the dust (meteoroid) trails from a defined parent and investigate their visibility as meteor activity at the Earth.

In Chapter 2, a moderately active JFC, 15P/Finlay, was examined. 15P/Finlay has a moderate but declining activity compared to other known member of the JFC population, which leads to speculation that the comet is approaching a state of dormancy. However, 15P/Finlay has unexpectedly produced two outbursts during its 2014/2015 perihelion passage. The purpose of

this Chapter is 2-fold: (1) to characterize and investigate the nature of these two outbursts; and (2) to revisit the long-standing problem of the absence of Finlayid meteor shower to improve understanding of the aging of the comet. It was found that the ejection speed of the ejecta was at the order of 500 m/s for both outbursts and the mass of the ejecta were at the order of 10^5 kg, corresponding to the specific energy of $\sim 10^5$ J/kg. This number is comparable to the specific energy produced by the crystallization of amorphous ice, a mechanism that has been suggested as one of the common driving forces for many cometary outburst events, but 15P/Finlay was too close to the Sun for amorphous ice to be present, hence the conclusion regarding the nature of the outburst is not definitive. The Finlayids puzzle was revisited on both modeling and observational front. It was confirmed that the activity of 15P/Finlay has been no higher than its contemporary level in the past several centuries. Although not arriving at a definitive conclusion, it was shown that "dying" comets such as 15P/Finlay do possess some ability for significant activity. It is yet to be seen whether these outbursts are a resurrection or final blows of the comet.

In Chapter 3, a weakly active JFC, 209P/LINEAR, was examined. The earlier work of the author (Ye & Wiegert, 2014) revealed 209P/LINEAR as one of the most weakly-active comets ever known, suggesting the comet was at an intermediate stage between an active comet and a dormant comet. The purpose of this Chapter was to comprehensively verify this speculation. This objective was attacked from three fronts: characterization of dust properties from optical and infrared imaging; analysis of meteor observations; and numerical investigation of the dynamical evolution of the comet. It was found that 209P/LINEAR not only has a remarkably low dust production but also a very low ejection speed for the dust. The ejection speed was a factor of 10 lower than moderately active comets as predicted by classic cometary models of cometary activity for an as-yet unclear reason. Observations also showed a coma that was inconsistent with the classic steady-flow model which might imply the existence of a large number of fresh icy grains, a phenomenon that had only been detected so far on hyperactive comets. Meteor observations and meteoroid stream modeling established that the activity level

of 209P/LINEAR was largely unchanged in the past several hundred orbits, although there were signs that the comet experienced some transient activity increase in the 18th century. Numerical integrations revealed that 209P/LINEAR had resided in a stable near-Earth JFC orbit for 10^4 years, significantly longer than typical JFCs. All these lines of evidences suggested that 209P/LINEAR is indeed a comet that is at the late stage of comet-asteroid transition.

In Chapter 4, the population of dormant near-Earth comets was examined. A comprehensive meteor-based survey was conducted to identify the dormant comets in the near-Earth object (NEO) population that had recently release dust. The NEO sample included 407 objects that resided in Jupiter-family comet (JFC) like orbits and represented $\sim 80\%$ and $\sim 46\%$ of known NEOs in JFC-like orbits in the $H < 18$ and $H < 22$ population respectively. The CMOR database was subsequently examined for predicted observable showers. Among 45 predicted showers for CMOR, a total of 4 showers were actually detected, including 3 known showers [(196256) 2003 EH_1 – Quadrantids, 2004 TG_{10} – Taurids, and 2009 WN_{25} – November i Draconids]. A total of 32 previously-proposed asteroid-shower associations were also critically examined, of which it was concluded that only 1/4 of them were statistically significant. Based on the detection rate, a lower limit of the dormant comet fraction of $2.0 \pm 1.7\%$ among the entire NEO population was found. This is at the lower end of previous determination based on dynamical and compositional properties of the objects. Such difference may imply the typical dust production of these dormant comets may be lower than the observed JFC population. A dormancy rate of $\sim 10^{-5}$ yr^{-1} was calculated from the dormant comet fraction. Coupled with previous observations and model predictions, it was concluded that comet dormancy is a relatively uncommon end state for JFCs.

This thesis has revealed an interesting diversity in comets low in activity that are possibly approaching their end stage: 15P/Finlay has sudden recurring activity for unclear reasons; 209P/LINEAR has had marginal activity for several hundreds of orbits; a wide range of already-dead comets may once had weaker activity than currently known JFC population. A logical next step in the understanding of cometary aging is to examine a large number of

near-death or dead comets. The author has already led or participated in several other investigations that focused on such objects: broad-band photometric survey on possible bare nuclei (Ye, 2011); highly-evolved cometary fragments (Ye et al., 2014); thermal destruction of dynamically new comets (Bodewits et al., 2013; Hui et al., 2015; Samarasinha et al., 2015); as well as several weakly active or reactivated bodies (Kleyna et al., 2016; Ye et al., 2016; Ye, 2016). At the end of Chapter 2, a short discussion was also given regarding several other notable weakly active comets that can be studied with the dual comet-meteor method, including 252P/LINEAR, 289P/Blanpain, and 300P/Catalina. All these comets seem to be weakly active for a different reason. This needs to be investigated.

On the long term, comprehensive investigation of cometary aging may provide further clues on fundamental questions such as the delivery of water and other life-essential material in the Solar System. In the recent decade, we have already seen the operation of a number of optical, radio and infrasound meteor surveys that have fueled exponential increase in meteor data. Service of future next-generation sky surveys such as the Large Synoptic Survey Telescope (LSST) and the proposed NEO Camera (NEOCam) will likely improve our understanding of the dark body population in near-Earth space. Last but not least, aging and dormant comets are among potential targets for unmanned and manned space missions; detailed in-situ data on these objects will certainly provided solid backbone for planning and operation of these missions.

Bibliography

Bodewits, D., Farnham, T., A'Hearn, M. F., et al. 2013, Central Bureau Electronic Telegrams, 3718

Hui, M.-T., Ye, Q.-Z., Knight, M., Battams, K., & Clark, D. 2015, ApJ, 813, 73

Kleyna, J. T., Ye, Q.-Z., Hui, M.-T., et al. 2016, ArXiv e-prints, arXiv:1602.07569

Samarasinha, N. H., Mueller, B. E. A., Knight, M. M., et al. 2015, Planet. Space Sci., 118, 127

Ye, Q. 2016, Central Bureau Electronic Telegrams, 4259

Ye, Q., & Wiegert, P. A. 2014, MNRAS, 437, 3283

Ye, Q.-z. 2011, AJ, 141, 32

Ye, Q.-Z., Brown, P. G., & Wiegert, P. A. 2016, ApJ, 818, L29

Ye, Q.-Z., Hui, M.-T., Kracht, R., & Wiegert, P. A. 2014, ApJ, 796, 83

Appendix A

Details of the Cometary Dust and Meteoroid Stream Model

The core purpose of the model is to simulate the motion of cometary dust (meteoroids). The goal is 2-fold: (1) understand dust properties as revealed by cometary images, and (2) study the evolution of meteoroid streams. The model is inspired by the dust tail model devised in Ye & Hui (2014), however it shall be noted that the purpose and structure of this model is different and the codes are completely redeveloped.

To begin a simulation, a parent body and an ejection model needs to be defined. The parent body is defined by its orbital elements, namely a (semimajor axis), q (perihelion distance), e (eccentricity), i (inclination), Ω (longitude of the ascending node), ω (argument of perihelion), M (mean anomaly), epoch of which the elements are applicable, and for the cases of comets, and the non-gravitational parameters (A_1, A_2, A_3). We note that the non-gravitational parameters can be variable over the timescale of a few decades (c.f. Yeomans et al., 2004). Unfortunately it is not possible to retrieve the non-gravitational parameters of comets before they have been discovered, hence we introduce an uncertainty in the backward integrations by sticking to the current values of non-gravitational parameters. However, from the comets with detectable changes in non-gravitational effects, such changes are generally well within an

order of magnitude and are not significant for statistical investigations (since the uncertainties in orbital determination are usually much larger).

There are different "flavors" of the ejection model but all of them are descendants of the classic Whipple (1950) model. For the purpose of cometary image analysis, a semi-analytic model is usually chosen, because the observations allow constraining additional free parameters. The semi-analytic ejection model can be written as

$$v_{\text{ej}} = V_0 \beta_{\text{rp}}^{1/2} \cos z \cdot \nu \tag{A.1}$$

where V_0 is a free parameter accounts for the mean ejection speed of a dust particle of $\beta_{\text{rp}} = 1$, z is the local solar zenith angle, and ν follows a Gaussian probability density function:

$$P(\nu) = \mathcal{N}(1, \sigma_\nu^2) \tag{A.2}$$

where σ_ν is the standard deviation of ν and is a free parameter.

For meteoroid stream modeling, the result is relatively insensitive to the ejection model. Two widely used models are those by Jones (1995) and Crifo & Rodionov (1997). We will not go into the details here, but results-wise these models are equivalent to our semi-analytic model (neglecting the z and ν dependence) to the lowest order when $V_0 \simeq 400$ m/s.

The dust size a_{d} follows a single power-law with a differential size index of q, i.e. $N(a_{\text{d}}) \propto a_{\text{d}}^{-q}$. The total dust production rate is therefore

$$N(r_{\text{H}}, a_{\text{d}}) \mathrm{d}a_{\text{d}} = N_0 \left(\frac{r_{\text{H}}}{1 \text{ AU}} \right)^{-k} \left(\frac{a_{\text{d}}}{1 \ \mu m} \right)^{-q} \mathrm{d}a_{\text{d}} \tag{A.3}$$

where N_0 is the mean dust production rate of 1 μm particles at 1 AU and r_{H} is the heliocentric distance at which the dust is released. There are three parameters to be determined: N_0, k and q. N_0 is typically derived from near-nucleus photometry (i.e. $Af\rho$ or coma measurements); a typical number for k is $k = 4$ as determined by Everhart (1967) using a collection of cometary brightening rate measurements; a typical number for q is $q \simeq 3.5$ as suggested by various

ground and spacecraft measurements, however it is known that q can vary between 3 and 4 and, because of the power-law nature, such a range can make a significant impact to the result. Hence it is recommended to treat q as a free parameter as long as the observation and computational capacity allows. It is possible to account for the variability of q by introducing statistical weighting in *a posteriori* manner (e.g. Vaubaillon et al., 2005a), however it is not currently implemented in our model.

A successful simulation requires a large number of particles (usually at the order of 10^6 or more) being generated and simulated in order to gather enough statistics. The parent body is first integrated backward, then integrated forward again with dust particles being released. A typical simulation takes a few CPU months to a few CPU years depends on the details of the parent bodies and the simulation setup. For the interest of cometary image modeling, where free parameters need to be determined, the free parameters are explored in a Monte Carlo manner to identify the best set of parameters. The particles are integrated using the MERCURY package version 6.2 (Chambers & Migliorini, 1997). MERCURY is bundled together with several integrators, but we typically use the 15th order RADAU integrator for the model, as it is fast and relatively accurate in most cases. The original MERCURY 6.2 does not include post Newtonian effects such as radiation pressure and Poynting-Robertson effects. We have modified the code accordingly to include such effects. Following the work of Burns et al. (1979), the motion of a dust particle can be written as

$$\vec{a} = -\frac{GM_\odot}{r_\mathrm{h}^2}\vec{r_\mathrm{h}}\beta_\mathrm{rp}\left[\frac{\vec{r_\mathrm{h}}}{\hat{r}_\mathrm{h}} - \frac{(\vec{r_\mathrm{h}}\cdot\vec{v})\,\vec{r_\mathrm{h}}}{r_\mathrm{h}^2 c} - \frac{\vec{v}}{c}\right] - \Sigma_{n=1}^{n=8}\frac{GM_n}{r_n^3}\vec{r_n} \qquad (A.4)$$

where G is the universal gravitational constant, $M_\odot$ is solar mass, $\vec{r_\mathrm{h}}$, $\vec{v}$, $\vec{a}$ is the position, velocity and acceleration vectors of the particle, $\hat{r}_\mathrm{h}$ is the unit position vector of the particle, β_rp is the ratio between radiation pressure and solar gravity, c is the speed of light, and M_n and r_n is the mass and particle-centric distance of the nth planet. The modified MERCURY6 package can be obtained from `https://github.com/Yeqzids/mercury`.

For cometary image modeling, we compute the spatial intensity on the sky plane con-

tributed by the dust particles. Since the light from the comet is dominated by the scattering of sunlight, we consider the light contribution from each particle as

$$I(a_{\rm d}, r_{\rm h}) = r_{\rm h}^{-2} a_{\rm d}^2 A_{\rm p} \qquad (A.5)$$

where $A_{\rm p}$ is the geometric albedo. The intensity at a given sky plane coordinate (α, δ) would simply be the integration of intensities from all particles within an infinitely small region around this point. By repeating this operation across the region around the comet, we are essentially modeling the surface brightness profile of the coma and tail structure. By looking at the profiles generated by different sets of parameters, we can determine which parameter sets can better reproduce the observed profile. Although the solution is rarely distinct and unique, the model is useful in the sense of excluding unlikely scenarios and constraining the general properties of the dust.

For meteoroid stream simulation, we examine the subset of Earth-approaching meteoroids (EAMs). The definition of EAMs depends on the purpose of the simulation: for investigation of highly evolved streams (which meteoroids are largely uniformly distributed along the orbit), EAMs are defined by their Minimum Orbit Intersection Distance (MOID) with respect to the Earth's orbit < 0.01 AU; for investigation of young meteoroid trails (which meteoroids are concentrated at a narrow section along the orbit), EAMs are defined by their minimal approaching distance to the Earth to be < 0.01 AU within the period of interest. In both cases we record the time and distance the particles pass their respective MOID points, which allow us to construct the demographics of the EAMs in $\overrightarrow{MOID}$ space. The threshold of 0.01 AU corresponds to the characteristic width of meteoroid streams projected on the MOID plane. Here we use the concept of MOID, rather than the traditional nodal approximation, because the nodal approximation is only valid when the inclination is sufficiently large.

For any meteor activity, prediction of meteoroid flux is of great interest, as it not only predicts the likelihood of detectability, but also allows us to understand the past activity of the parent which cannot be otherwise studied. However, the flux prediction is known to be

Year	Rev	Observation		This work		McNaught & Asher (1999)		Vaubaillon et al. (2005b)	
		Time (UT)	ZHR	Time (UT)	ZHR	Time (UT)	ZHR	Time (UT)	ZHR
1999	1932	Nov 18 1:43	2400	Nov 18 1:19	300	Nov 18 1:44	0	Nov 18 1:49	3000
	1899	Nov 18 2:02	3700	Nov 18 2:56	1000	Nov 18 2:08	1500	Nov 18 2:13	3000
2000	1932	Nov 17 8:07	130	Nov 17 8:53	0	Nov 17 7:53	0	Nov 17 7:55	400
	1733	Nov 18 3:24	290	Nov 18 3:22	1000	Nov 18 3:44	100–5000	Nov 18 3:48	700
	1866	Nov 18 7:12	480	Nov 18 7:30	200	Nov 18 7:51	100–5000	Nov 18 7:57	900
2001	1767	Nov 18 10:39	1600	Nov 18 10:21	300	Nov 18 10:01	2500	Nov 18 10:06	1400
	1699	Nov 18 18:02	2800	Nov 18 17:51	3200	-	-	Nov 18 17:59	4100
	1866	Nov 18 18:30	3400	Nov 18 18:18	2100	Nov 18 18:19	10000–35000	Nov 18 18:25	4100
2002	1767	Nov 19 4:10	2500	Nov 19 4:15	200	-	-	Nov 19 4:02	1500
	1866	Nov 19 10:47	2900	Nov 19 10:49	400	Nov 19 10:36	25000	Nov 19 10:48	1900

Table A.1: Re-predictions of the Leonid meteor storms in 1999–2002 using the model presented in this thesis. The model is appropriate for visual meteors (mag $\lesssim$ 6) and include meteoroid trails formed after 1699 AD. The predictions are compared to the observations and other predictions.

a difficult issue, both because of the complexity and poor knowledge of cometary activity and because of the limitation of computational resource. Here we consider the approach of Vaubaillon et al. (2005a). We only consider EAMs with MOID< 0.001 AU for flux calculation, with the threshold of 0.001 AU appropriate to the characteristic width of meteoroid trails. The volume density ρ_v, i.e. particles in unit volume, can be derived from the simulation and is related to the flux $\mathcal{F}$ by

$$\mathcal{F} = \rho_v \bar{v}_g \tag{A.6}$$

where $\bar{v}_g$ is the mean geocentric speed of the meteoroid trail. The flux can be converted to the Zenith Hourly Rate (ZHR), a more popular indicator used by visual meteor observers to quantify the activity level of meteor activity, using the empirical relation given by Koschack & Rendtel (1990):

$$\text{ZHR} = \frac{37200 \text{ km}^2 \mathcal{F}}{(13.1r - 16.5)(r - 1.3)^{0.748}} \tag{A.7}$$

where r is the population index that can be related to q by $q = 7.5 \log r + 1$. For $q = 3.5$, we have $r \simeq 2.2$. We define the median point in the $\overrightarrow{MOID}$ space as the center of the stream/trail. This allows us to calculate the time of the maximum of the meteor activity.

To verify our model, we reproduce the prediction of the historic Leonid meteor storms in

1999–2002. This set of events has been studied by a number of authors (e.g. McNaught & Asher, 1999; Lyytinen et al., 2001; Vaubaillon et al., 2005a; Maslov, 2007) and the timing and strength of the outbursts are well known. The results are tabulated in Table A.1 alongside with the observation (Arlt et al., 1999; Arlt & Gyssens, 2000; Arlt et al., 2001, 2002) and prediction from two representative models, McNaught & Asher (1999) and Vaubaillon et al. (2005b) (other authors gave similar predictions). It can be seen that the prediction agrees with the observation quite well and is comparable to other models. The timing is within an hour, and the ZHR prediction is within an order of magnitude.

Bibliography

Arlt, R., Bellot Rubio, L., Brown, P., & Gyssens, M. 1999, WGN, Journal of the International Meteor Organization, 27, 286

Arlt, R., & Gyssens, M. 2000, WGN, Journal of the International Meteor Organization, 28, 195

Arlt, R., Kac, J., Krumov, V., Buchmann, A., & Verbert, J. 2001, WGN, Journal of the International Meteor Organization, 29, 187

Arlt, R., Krumov, V., Buchmann, A., Kac, J., & Verbert, J. 2002, WGN, Journal of the International Meteor Organization, 30, 205

Burns, J. A., Lamy, P. L., & Soter, S. 1979, Icarus, 40, 1

Chambers, J. E., & Migliorini, F. 1997, in Bulletin of the American Astronomical Society, Vol. 29, AAS/Division for Planetary Sciences Meeting Abstracts #29, 1024

Crifo, J. F., & Rodionov, A. V. 1997, Icarus, 127, 319

Everhart, E. 1967, AJ, 72, 1002

Jones, J. 1995, MNRAS, 275, 773

Koschack, R., & Rendtel, J. 1990, WGN, Journal of the International Meteor Organization, 18, 44

Lyytinen, E., Nissinen, M., & van Flandern, T. 2001, WGN, Journal of the International Meteor Organization, 29, 110

Maslov, M. 2007, WGN, Journal of the International Meteor Organization, 35, 5

McNaught, R. H., & Asher, D. J. 1999, WGN, Journal of the International Meteor Organization, 27, 85

Vaubaillon, J., Colas, F., & Jorda, L. 2005a, A&A, 439, 751

—. 2005b, A&A, 439, 761

Whipple, F. L. 1950, ApJ, 111, 375

Ye, Q.-Z., & Hui, M.-T. 2014, ApJ, 787, 115

Yeomans, D. K., Chodas, P. W., Sitarski, G., Szutowicz, S., & Królikowska, M. 2004, Cometary orbit determination and nongravitational forces, ed. M. C. Festou, H. U. Keller, & H. A. Weaver, 137–151

Appendix B

CMOR Basics

A version of this appendix has been published as part of:

B.1 The CMOR System

The Canadian Meteor Orbit Radar (CMOR) is an interferometric backscatter meteor radar located near London, Ontario, Canada that is designed to observe meteor echoes and perform basic analysis continuously and automatically. It is based on the commercially available SKiYMET system (e.g. Hocking et al., 2001) with some modifications to optimize for astronomical meteor echo detection (e.g. Jones et al., 2005; Weryk & Brown, 2012). Currently it consists of six sites (Figure B.1) and operates at 29.85 MHz at 12 kW peak power[1]. The radar detects meteors through reflection of a transmitted pulse from the ionization trail left behind during meteor ablation and subsequently received after specular reflection by receivers. Meteors observed by the radar from the main station (Zehr) are always 90° from the apparent

---

[1]The system also operates in 17.45 and 38.15 MHz, but only data at 29.85 MHz is used in this study.
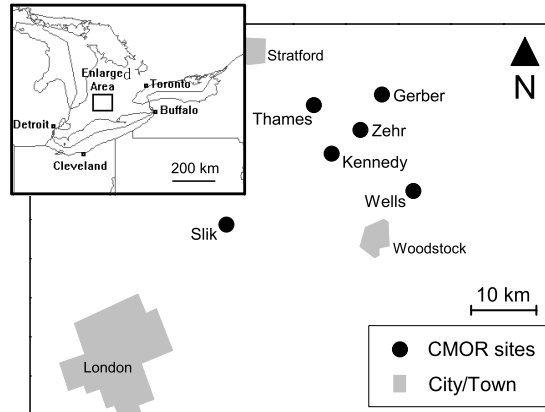
Figure B.1 Location and geographic distribution of the main CMOR station (Zehr) and other remote sites as of October 2011.

Parameter	Value
Frequency	29.85 MHz
Range interval	15–255 km
Range resolution	3 km
Pulse frequency	532 Hz
Peak power	12 kW
Noise floor	-107 dBm
Dynamic range	33 dB
Beam size	55° at -3 dB point

Table B.1: Basic specification of the 29.85 MHz CMOR system, adapted from Weryk & Brown (2012).

radiant. Because of this geometry, the underdense echo rate for radar observations has a secondary minimum when the radiant has a zenith angle $<\sim 20°$ due to lower elevations and larger ranges to the echo, as opposed to visual, photographic and video meteor observation, where the minimum in apparent rates typically occurs when the radiant is near the horizon.

If the echo from a meteor is detected at N sites ($N \geq 3$), we can record N specular scattering positions along the meteor trail, allowing us to measure the trajectory of the meteor using a time-of-flight (`tof`) algorithm (Figure B.2; see also Jones et al., 2005; Weryk & Brown, 2012). However, the uncertainty in such a trajectory largely depends on echo strength and geometry.
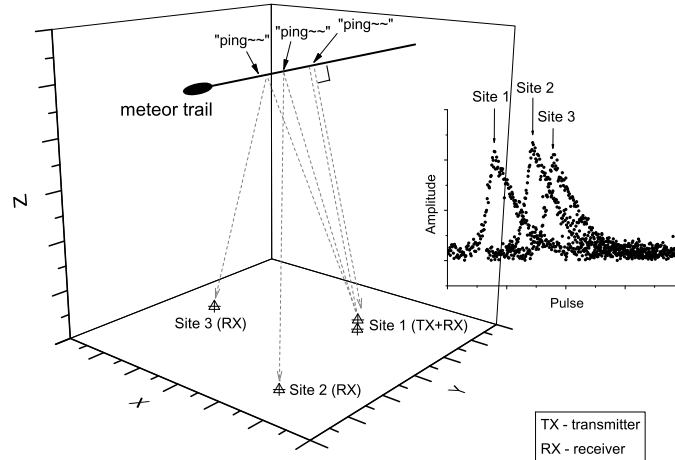
Figure B.2 Simplified example of how CMOR measures meteor trajectories. In this example, three radar sites detect signals reflected from the meteor trail at different points as the meteoroid moves in the atmosphere. The time differences between the three observations, together with the interferometric direction measured from the main site, can be used to construct the trajectory of the meteor.

If the echo is weak, determination of the time of occurrence (or "time pick") will be difficult. Since the specular locations along a trail may coincide from different sites depending on the geometry of the meteor trajectory, the time difference between these sites may be small, and small uncertainties of the time pick may result in significant errors to the trajectory.

Meteor echoes detected by CMOR are automatically processed to remove bad detections and to correlate common events across the sites. The selection algorithms are derived from manual examination of thousands of echoes. Generally, echoes that last $<\sim 4$ s, feature a clear, sharp rise and a gradual decline, and a single maximum will be considered as a "good" echo, while bumpy and/or noisy echoes, such as the lower one shown in Figure B.3, will be considered as a "bad" echo and may be rejected by the algorithm. Details of this process can be found in Jones et al. (2005); Brown et al. (2008, 2010) and Weryk & Brown (2012).

B.2   Echo Types

CMOR is composed by a series of Yagi 2-element receivers and 3-element transmitters (Brown et al., 2008), allowing the radar to detect meteors appearing almost anywhere in the sky. The gain distribution resembles a bubble rather than a uniform distribution. This not only affects the number of meteors detected with respect to different ranges, but also affects the determination of the physical properties of individual meteoroids. One of the most significant properties of any specular radar echoes is the trail type of the meteor, namely underdense or overdense.

An underdense trail occurs when radio waves scatter from all the individual the electrons in the trail. In contrast, an overdense echo occurs when the radio wave cannot completely penetrate the meteor trail due to the trail plasma frequency being higher than the radar wave frequency. Strictly speaking, the boundary between underdense and overdense echoes is a continuum; in between is transition echoes, which can exhibit characteristics from the other two types, but for simplicity we also consider them as overdense echoes in this study.

Visually, the amplitude-time series of an overdense echo will appear as "flat" (i.e. does not decay) for some time until ambipolar diffusion makes the trail underdense. Since overdense echoes have higher electron line density than underdense echoes, for a fixed velocity, overdense echoes tend to be generated by a larger meteoroid. They represent a higher fraction of echoes in regions where the radar gain is low, since fainter echoes will not be observed in these regions.

Examples of underdense and overdense echoes are shown in Figure B.3. Detailed theory of these two echo types is beyond the scope of this paper, but interested readers may refer to McKinley (1961, §8) or Ceplecha et al. (1998, §4) for details. The CMOR automatic detection algorithms are tuned to accept underdense echoes but generally suppress overdense-type echoes.
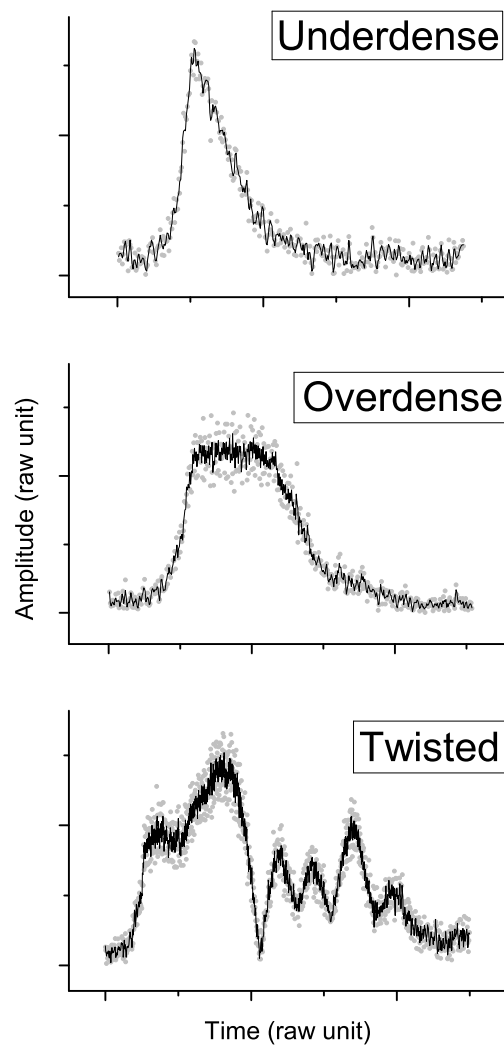
Figure B.3 A typical underdense echo (above), overdense echo (middle) and wind twisted overdense echo (below). We define these by the shape of their amplitude–time series.

B.3   Orbit Determination

A typical observation of a meteor consists of two elements: observed velocity vector of the meteor $\vec{V}_o$, and the time of the meteor event, usually expressed in solar longitude $\lambda_\odot$. The velocity vector comprises three elements that are more commonly used by astronomers: the right ascension (R.A.) and declination (Dec.) of the celestial point where the meteor radiates from (the *radiant*), as well as the observed linear speed (i.e. apparent speed) of the meteoroid v_a. $\lambda_\odot$ measures the ecliptic longitudinal distance between the Sun and the equinox at the time of the meteor event.

To determine the true orbit of the meteoroid, one needs to correct for the deceleration of the meteoroid due to atmospheric friction, as well as the rotation and gravitational attraction of the Earth, the latter two known as the *zenith attraction* and *diurnal aberration*. Correction for atmospheric deceleration is challenging as it depends on the physical properties of the meteoroid which is known to be variable. In CMOR operation, the algorithm developed by Brown et al. (2004) is being used, but it may not work as accurate as one would wish for hyper-solid or fragile meteoroid streams such as the Draconids (Ye et al., 2013, 2014). The deceleration-corrected meteoroid speed is usually called infinity speed, v_∞. The zenith attraction can then be corrected by

$$v_g = \left(v_\infty^2 - \frac{2GM_\oplus}{R_\oplus} \right)^{1/2} = \left(v_\infty^2 - 125 \right)^{1/2} \tag{B.1}$$

for the speed component, and

$$\tan \frac{\Delta Z}{2} = \frac{v_\infty - v_g}{v_\infty + v_g} \tan \frac{Z}{2} \tag{B.2}$$

for the directional component, where v_g is the geocentric speed of the meteoroid, $M_\oplus$ and $R_\oplus$ is the mass and radius of the Earth, respectively, Z is the observed zenith angle of the meteor, and ΔZ is the zenith angle reduction due to zenith attraction. The true zenith angle should therefore be $Z + \Delta Z$. The correction of diurnal aberration goes as $0.646 \cos \phi$ where ϕ is the latitude of

the observer and may be neglected.

It is apparent that the geocentric velocity vector $\vec{V}_g$ can be converted to the heliocentric velocity vector $\vec{V}$ by

$$\vec{V} = \vec{V}_g - \vec{V}_\oplus \tag{B.3}$$

which is essentially the state vector (i.e. equivalent to the orbital elements) of the meteoroid.

B.4   Wavelet Analysis

Wavelet transform is a useful technique in mining a large amount of data. It was first applied to radar meteor data by Galligan & Baggaley (2001) and has been used in probing video meteor data (e.g. Zhu et al., 2006; Molau & Rendtel, 2009).

The procedure of performing wavelet analysis on CMOR data was established in Brown et al. (2008) and Brown et al. (2010) and is constantly being updated (Bruzzone et al., 2015). Currently it makes use of a quasi 4-dimensional Mexican hat wavelet with the wavelet coefficient $\psi(x_0, y_0, v_{g,0})$ at celestial coordinate (x_0, y_0) and speed $(v_{g,0})$ defined as:

$$
\begin{aligned}
\psi(x_0, y_0, v_{g,0}) = {} & \frac{1}{(2\pi)^{3/2}\sigma_v^{1/2}} \int_{v_{g,\min}}^{v_{g,\max}} \int_{-\infty}^{\infty} \int_{-\infty}^{\infty} f\left(x, y, v_g\right) \\
& \times \left[3 - g\left(x, y, \sigma\right) - h\left(v_g, \sigma_v\right)\right] \\
& \times \exp\left\{-\frac{1}{2}\left[g\left(x, y, \sigma\right) - h\left(v_g, \sigma_v\right)\right]\right\} \mathrm{d}x\mathrm{d}y\mathrm{d}v_g
\end{aligned}
\tag{B.4}
$$

and

$$
g(x, y, \sigma) = \frac{(x - x_0)^2 + (y - y_0)^2}{\sigma^2}
\tag{B.5}
$$

$$h(v_{\mathrm{g}}, \sigma_v) = \frac{(v_{\mathrm{g}} - v_{\mathrm{g},0})^2}{\sigma_v^2} \tag{B.6}$$

where $f(x, y, v_{\mathrm{g}})$ is the distribution of radiants, σ and σ_v are the spatial and speed probe sizes, x, y and v_{g} are spatial coordinates and speed in the geocentric space of observed radiants which form three full dimensions for wavelet analysis. Furthermore, the data is divided into $1°$ solar longitude bins, forming an additional dimension. The wavelet transform works in such a way that only radiants within roughly one spatial/speed probe size will contribute significantly to the resulting wavelet coefficient $\psi(x_0, y_0, v_{\mathrm{g},0})$. Hence, potential enhancements in the meteor background behave as a rise in $\psi(x_0, y_0, v_{\mathrm{g},0})$ space.

Bibliography

Brown, P., Jones, J., Weryk, R. J., & Campbell-Brown, M. D. 2004, Earth Moon and Planets, 95, 617

Brown, P., Weryk, R. J., Wong, D. K., & Jones, J. 2008, Icarus, 195, 317

Brown, P., Wong, D. K., Weryk, R. J., & Wiegert, P. 2010, Icarus, 207, 66

Bruzzone, J. S., Brown, P., Weryk, R. J., & Campbell-Brown, M. D. 2015, MNRAS, 446, 1625

Ceplecha, Z., Borovička, J., Elford, W. G., et al. 1998, Space Sci. Rev., 84, 327

Galligan, D. P., & Baggaley, W. J. 2001, in ESA Special Publication, Vol. 495, Meteoroids 2001 Conference, ed. B. Warmbein, 569–574

Hocking, W. K., Fuller, B., & Vandepeer, B. 2001, Journal of Atmospheric and Solar-Terrestrial Physics, 63, 155

Jones, J., Brown, P., Ellis, K. J., et al. 2005, Planet. Space Sci., 53, 413

McKinley, D. W. R. 1961, Meteor science and engineering.

Molau, S., & Rendtel, J. 2009, WGN, Journal of the International Meteor Organization, 37, 98

Weryk, R. J., & Brown, P. G. 2012, Planet. Space Sci., 62, 132

Ye, Q., Brown, P. G., Campbell-Brown, M. D., & Weryk, R. J. 2013, MNRAS, 436, 675

Ye, Q., Wiegert, P. A., Brown, P. G., Campbell-Brown, M. D., & Weryk, R. J. 2014, MNRAS, 437, 3812

Zhu, J., Meng, H., & Li, J. 2006, in COSPAR Meeting, Vol. 36, 36th COSPAR Scientific Assembly

Appendix C

Copyright Permissions

This is a License Agreement between Quanzhi Ye ("You") and Elsevier ("Elsevier") provided by Copyright Clearance Center ("CCC"). The license consists of your order details, the terms and conditions provided by Elsevier, and the payment terms and conditions.

All payments must be made in full to CCC. For payment instructions, please see information listed at the bottom of this form.

Supplier	Elsevier Limited
	▓▓▓▓▓▓▓▓▓▓
Registered Company Number	1982084
Customer name	Quanzhi Ye
Customer address	▓▓▓▓▓▓▓▓▓▓
License number	3874350514327
License date	May 22, 2016
Licensed content publisher	Elsevier
Licensed content publication	Icarus
Licensed content title	When comets get old: A synthesis of comet and meteor observations of the low activity comet 209P/LINEAR
Licensed content author	Quan-Zhi Ye (叶泉志),Man-To Hui (许文韬),Peter G. Brown,Margaret D. Campbell-Brown,Petr Pokorný,Paul A. Wiegert,Xing Gao (高兴)
Licensed content date	15 January 2016
Licensed content volume number	264
Licensed content issue number	n/a
Number of pages	14
Start Page	48
End Page	61
Type of Use	reuse in a thesis/dissertation
Portion	full article
Format	both print and electronic
Are you the author of this Elsevier article?	Yes
Will you be translating?	No
Title of your thesis/dissertation	Aging comets and their meteor showers
Expected completion date	Aug 2016

Estimated size (number of pages)	200
Elsevier VAT number	GB 494 6272 12
Permissions price	0.00 USD
VAT/Local Sales Tax	0.00 USD / 0.00 GBP
Total	0.00 USD
Terms and Conditions	

INTRODUCTION

1. The publisher for this copyrighted material is Elsevier. By clicking "accept" in connection with completing this licensing transaction, you agree that the following terms and conditions apply to this transaction (along with the Billing and Payment terms and conditions established by Copyright Clearance Center, Inc. ("CCC"), at the time that you opened your Rightslink account and that are available at any time at http://myaccount.copyright.com).

GENERAL TERMS

2. Elsevier hereby grants you permission to reproduce the aforementioned material subject to the terms and conditions indicated.

3. Acknowledgement: If any part of the material to be used (for example, figures) has appeared in our publication with credit or acknowledgement to another source, permission must also be sought from that source. If such permission is not obtained then that material may not be included in your publication/copies. Suitable acknowledgement to the source must be made, either as a footnote or in a reference list at the end of your publication, as follows:

"Reprinted from Publication title, Vol /edition number, Author(s), Title of article / title of chapter, Pages No., Copyright (Year), with permission from Elsevier [OR APPLICABLE SOCIETY COPYRIGHT OWNER]." Also Lancet special credit - "Reprinted from The Lancet, Vol. number, Author(s), Title of article, Pages No., Copyright (Year), with permission from Elsevier."

4. Reproduction of this material is confined to the purpose and/or media for which permission is hereby given.

5. Altering/Modifying Material: Not Permitted. However figures and illustrations may be altered/adapted minimally to serve your work. Any other abbreviations, additions, deletions and/or any other alterations shall be made only with prior written authorization of Elsevier Ltd. (Please contact Elsevier at permissions@elsevier.com)

6. If the permission fee for the requested use of our material is waived in this instance, please be advised that your future requests for Elsevier materials may attract a fee.

7. Reservation of Rights: Publisher reserves all rights not specifically granted in the combination of (i) the license details provided by you and accepted in the course of this licensing transaction, (ii) these terms and conditions and (iii) CCC's Billing and Payment terms and conditions.

8. License Contingent Upon Payment: While you may exercise the rights licensed immediately upon issuance of the license at the end of the licensing process for the transaction, provided that you have disclosed complete and accurate details of your proposed use, no license is finally effective unless and until full payment is received from you (either by publisher or by CCC) as provided in CCC's Billing and Payment terms and conditions. If full payment is not received on a timely basis, then any license preliminarily granted shall be deemed automatically revoked and shall be void as if never granted. Further, in the event that you breach any of these terms and conditions or any of CCC's Billing and Payment terms and conditions, the license is automatically revoked and shall be void as if never granted. Use of materials as described in a revoked license, as well as any use of the materials beyond the scope of an unrevoked license, may constitute copyright infringement and publisher reserves the right to take any and all action to protect its copyright in the materials.

9. Warranties: Publisher makes no representations or warranties with respect to the licensed material.

10. Indemnity: You hereby indemnify and agree to hold harmless publisher and CCC, and their respective officers, directors, employees and agents, from and against any and all claims arising out of your use of the licensed material other than as specifically authorized pursuant to this license.

11. No Transfer of License: This license is personal to you and may not be sublicensed, assigned, or transferred by you to any other person without publisher's written permission.

12. No Amendment Except in Writing: This license may not be amended except in a writing signed by both parties (or, in the case of publisher, by CCC on publisher's behalf).

13. Objection to Contrary Terms: Publisher hereby objects to any terms contained in any purchase order, acknowledgment, check endorsement or other writing prepared by you, which terms are inconsistent with these terms and conditions or CCC's Billing and Payment terms and conditions. These terms and conditions, together with CCC's Billing and Payment terms and conditions (which are incorporated herein), comprise the entire agreement between you and publisher (and CCC) concerning this licensing transaction. In the event of any conflict between your obligations established by these terms and conditions and those established by CCC's Billing and Payment terms and conditions, these terms and conditions shall control.

14. Revocation: Elsevier or Copyright Clearance Center may deny the permissions described in this License at their sole discretion, for any reason or no reason, with a full refund payable to you. Notice of such denial will be made using the contact information provided by you. Failure to receive such notice will not alter or invalidate

the denial. In no event will Elsevier or Copyright Clearance Center be responsible or liable for any costs, expenses or damage incurred by you as a result of a denial of your permission request, other than a refund of the amount(s) paid by you to Elsevier and/or Copyright Clearance Center for denied permissions.

<div align="center">LIMITED LICENSE</div>

The following terms and conditions apply only to specific license types:

15. Translation: This permission is granted for non-exclusive world English rights only unless your license was granted for translation rights. If you licensed translation rights you may only translate this content into the languages you requested. A professional translator must perform all translations and reproduce the content word for word preserving the integrity of the article.

16. Posting licensed content on any Website: The following terms and conditions apply as follows: Licensing material from an Elsevier journal: All content posted to the web site must maintain the copyright information line on the bottom of each image; A hyper-text must be included to the Homepage of the journal from which you are licensing at http://www.sciencedirect.com/science/journal/xxxxx or the Elsevier homepage for books at http://www.elsevier.com; Central Storage: This license does not include permission for a scanned version of the material to be stored in a central repository such as that provided by Heron/XanEdu.

Licensing material from an Elsevier book: A hyper-text link must be included to the Elsevier homepage at http://www.elsevier.com . All content posted to the web site must maintain the copyright information line on the bottom of each image.

Posting licensed content on Electronic reserve: In addition to the above the following clauses are applicable: The web site must be password-protected and made available only to bona fide students registered on a relevant course. This permission is granted for 1 year only. You may obtain a new license for future website posting.

17. For journal authors: the following clauses are applicable in addition to the above: Preprints:

A preprint is an author's own write-up of research results and analysis, it has not been peer-reviewed, nor has it had any other value added to it by a publisher (such as formatting, copyright, technical enhancement etc.).

Authors can share their preprints anywhere at any time. Preprints should not be added to or enhanced in any way in order to appear more like, or to substitute for, the final versions of articles however authors can update their preprints on arXiv or RePEc with their Accepted Author Manuscript (see below).

If accepted for publication, we encourage authors to link from the preprint to their formal publication via its DOI. Millions of researchers have access to the formal publications on ScienceDirect, and so links will help users to find, access, cite and use the best available version. Please note that Cell Press, The Lancet and some

society-owned have different preprint policies. Information on these policies is available on the journal homepage.

Accepted Author Manuscripts: An accepted author manuscript is the manuscript of an article that has been accepted for publication and which typically includes author-incorporated changes suggested during submission, peer review and editor-author communications.

Authors can share their accepted author manuscript:

- immediately
  - via their non-commercial person homepage or blog
  - by updating a preprint in arXiv or RePEc with the accepted manuscript
  - via their research institute or institutional repository for internal institutional uses or as part of an invitation-only research collaboration work-group
  - directly by providing copies to their students or to research collaborators for their personal use
  - for private scholarly sharing as part of an invitation-only work group on commercial sites with which Elsevier has an agreement
- after the embargo period
  - via non-commercial hosting platforms such as their institutional repository
  - via commercial sites with which Elsevier has an agreement

In all cases accepted manuscripts should:

- link to the formal publication via its DOI
- bear a CC-BY-NC-ND license - this is easy to do
- if aggregated with other manuscripts, for example in a repository or other site, be shared in alignment with our hosting policy not be added to or enhanced in any way to appear more like, or to substitute for, the published journal article.

Published journal article (JPA): A published journal article (PJA) is the definitive final record of published research that appears or will appear in the journal and embodies all value-adding publishing activities including peer review co-ordination, copy-editing, formatting, (if relevant) pagination and online enrichment.

Policies for sharing publishing journal articles differ for subscription and gold open access articles:

Subscription Articles: If you are an author, please share a link to your article rather than the full-text. Millions of researchers have access to the formal publications on ScienceDirect, and so links will help your users to find, access, cite, and use the best available version.

Theses and dissertations which contain embedded PJAs as part of the formal submission can be posted publicly by the awarding institution with DOI links back to the formal publications on ScienceDirect.

If you are affiliated with a library that subscribes to ScienceDirect you have additional private sharing rights for others' research accessed under that agreement. This includes use for classroom teaching and internal training at the institution (including use in course packs and courseware programs), and inclusion of the article for grant funding purposes.

Gold Open Access Articles: May be shared according to the author-selected end-user license and should contain a CrossMark logo, the end user license, and a DOI link to the formal publication on ScienceDirect.

Please refer to Elsevier's posting policy for further information.

18. For book authors the following clauses are applicable in addition to the above: Authors are permitted to place a brief summary of their work online only. You are not allowed to download and post the published electronic version of your chapter, nor may you scan the printed edition to create an electronic version. Posting to a repository: Authors are permitted to post a summary of their chapter only in their institution's repository.

19. Thesis/Dissertation: If your license is for use in a thesis/dissertation your thesis may be submitted to your institution in either print or electronic form. Should your thesis be published commercially, please reapply for permission. These requirements include permission for the Library and Archives of Canada to supply single copies, on demand, of the complete thesis and include permission for Proquest/UMI to supply single copies, on demand, of the complete thesis. Should your thesis be published commercially, please reapply for permission. Theses and dissertations which contain embedded PJAs as part of the formal submission can be posted publicly by the awarding institution with DOI links back to the formal publications on ScienceDirect.

Elsevier Open Access Terms and Conditions

You can publish open access with Elsevier in hundreds of open access journals or in nearly 2000 established subscription journals that support open access publishing. Permitted third party re-use of these open access articles is defined by the author's choice of Creative Commons user license. See our open access license policy for more information.

Terms & Conditions applicable to all Open Access articles published with Elsevier: Any reuse of the article must not represent the author as endorsing the adaptation of the article nor should the article be modified in such a way as to damage the author's honour or reputation. If any changes have been made, such changes must be clearly indicated.

20. Other Conditions:

v1.8

Curriculum Vitae

Name: Quanzhi Ye

Post-Secondary   Ph.D. Astronomy, 2013–2016
Education and   The University of Western Ontario
Degrees: London, Ontario, Canada

                     M.Sc. Astronomy (Planetary Science), 2011–2013
                     London, Ontario, Canada

                     B.Sc. Atmospheric Sciences, 2006–2010
                     Guangzhou, Guangdong, China

Honours and   National Award for Outstanding Youth in STEM (China), 2007
Awards:
                     Gene Shoemaker Near-Earth Object Grant, 2007

Related Work   Manager, The 7Timer! Project, 2005–
Experience:
                     Graduate Research and Teaching Assistant,
                     The University of Western Ontario, 2011–2016

                     Researcher, Lulin Sky Survey, 2006–2009

Peer-Reviewed Publications:

- Man-To Hui, **Quan-Zhi Ye**, and Paul A. Wiegert (2016): Constraints on Comet 332P/Ikeya-Murakami. ApJ (in review).

- **Quan-Zhi Ye**, Peter G. Brown, and Petr Pokorný (2016): Dormant Comets Among the Near-Earth Object Population: A Meteor-Based Survey. MNRAS (in press).

- Jan T. Kleyna, **Quan-Zhi Ye**, Man-To Hui, Karen J. Meech, Richard Wainscoat, Marco Micheli, Jacqueline V. Keane, and Harold A. Weaver (2016): The catastrophic fragmentation of Comet P/2010 V1 (Ikeya-Murakami). ApJ Letters (in press).

- **Quan-Zhi Ye**, Meng Su, Hong Li, and Xinmin Zhang (2016): Tibet's Ali: Asia's Acatama? MNRAS Letters, 457, 1.

- **Quan-Zhi Ye**, Peter G. Brown, and Paul A. Wiegert (2016): Comet 252P/LINEAR: born (almost) dead? ApJ Letters, 818, L29.

- **Quan-Zhi Ye**, Man-To Hui, Peter G. Brown, Margaret D. Campbell-Brown, Petr Pokorný, Paul A. Wiegert, and Xing Gao (2016): When comets get old: A synthesis of comet and meteor observations of the low activity comet 209P/LINEAR. Icarus, 264, 48.

- Nalin H. Samarasinha, Beatrice E.A. Mueller, Matthew M. Knight, Tony L. Farnham, John Briol, Noah Brosch, John Caruso, Xing Gao, Edward Gomez, Tim Lister, Carl Hergenrother, Susan Hoban, Roy Prouty, Mike Holloway, Nick Howes, Ernesto Guido, Man-To Hui, Joseph H. Jones, Tyler B. Penland, Samuel R. Thomas, Jim Wyrosdick, Nikolai Kiselev, Aleksandra V. Ivanova, Thomas G. Kaye, Jean-Baptist Kikwaya Eluo, Betty P.S. Lau, Zhong-Yi Lin, José Luis Martin, Alexander S. Moskvitin, Martino Nicolini, Brian D. Ottum, Chris Pruzenski, David C. Vogel, Leo Kellett, Valerie Rapson, Joel Schmid, Brandon Doyle, Frank Dimino, Stephanie Carlino, Margarita Safonova, Jayant Murthy, Firoza Sutaria, David G. Schleicher, Colin Snodgrass, Cihan T. Tezcan, Onur Yorukoglu, David Trowbridge, Dennis Whitmer, and **Quan-Zhi Ye** (2015): Results from the worldwide coma morphology campaign for comet ISON (C/2012 S1). Planet. Space Sci., 118, 127.

- **Quan-Zhi Ye**, Peter G. Brown, Charles Bell, Xing Gao, Martin Mašek, and Man-To Hui (2015): Bangs and Meteors from the Quiet Comet 15P/Finlay. ApJ, 814, 79.

- Man-To Hui, **Quan-Zhi Ye**, Matthew Knight, Karl Battams, and David Clark (2015): Gone in a Blaze of Glory: the Demise of Comet C/2015 D1 (SOHO). ApJ, 813, 73.

- **Quan-Zhi Ye**, Man-To Hui, Rainer Kracht, and Paul A. Wiegert (2014): Where are the Mini Kreutz-family Comets? ApJ, 796, 83.

- **Quan-Zhi Ye** and Man-To Hui (2014): An Early Look of Comet C/2013 A1 (Siding Spring): Breathtaker or Nightmare? ApJ, 787, 115.

- **Quanzhi Ye**, Paul A. Wiegert, and Peter G. Brown et al. (2014): The Unexpected 2012 Draconid Meteor Storm. MNRAS, 437, 3812.

- **Quanzhi Ye** and Paul A. Wiegert (2014): Will Comet 209P/LINEAR Generate the Next Meteor Storm? MNRAS, 437, 3283.

- **Quanzhi Ye**, Peter G. Brown, Margaret Campbell-Brown, and Robert J. Weryk (2013): Radar Observations of the 2011 October Draconid Outburst. MNRAS, 436, 675.

- **Q.-Z. Ye** and S.S. Chen (2013): The ultimate meteorological question from observational astronomers: how good is the cloud cover forecast? MNRAS, 428, 3288.

- **Q.Z. Ye** (2011): Forecasting Cloud Cover and Atmospheric Seeing for Astronomical Observing: Application and Evaluation of the Global Forecast System. PASP, 123, 113.

- **Q. Ye** (2011): BVRI photometry of 53 unusual asteroids. AJ, 141, 32.

- **Quanzhi Ye**, Liaoshan Shi, Wentao Xu, Hung-Chin Lin, and Junfeng Zhang (2009): Photometric Observations and Lightcurve Analysis of Near-Earth Asteroids (136849) 1998 CS1, 2006 SZ217, and 2008 UE7. Minor Planet Bull., 36, 180.

- **Quanzhi Ye**, Liaoshan Shi, and Hung-Chin Lin (2009): CCD Lightcurve Analysis of (53430) 1999 TY16. Minor Planet Bull., 36, 126.

- Brian D. Warner, **Quanzhi Ye**, Liaoshan Shi, Hung-Chin Lin, and Robert D. Stephens (2009): The Curious Case of (162900) 2001 HG31. Minor Planet Bull., 36, 56.

- **Quanzhi Ye**, Liaoshan Shi, Wing-Huen Ip, and Hung-Chin Lin (2009): Multi-color Photometry of 1998 BE7. Minor Planet Bull., 36, 41.